UNIVERSITY OF SOUTHAMPTON

FACULTY OF ENGINEERING AND THE ENVIRONMENT

Energy Technology Research Group

Lightweight ceramic nanotubes reinforced polymer composite coatings and electrospun microfibres

by

Ruben Porras Ortigosa

Thesis for the degree of Doctor of Philosophy

March 2016

UNIVERSITY OF SOUTHAMPTON

ABSTRACT

FACULTY OF ENGINEERING AND THE ENVIRONMENT

Energy Technology Research Group

Thesis for the degree of Doctor of Philosophy

LIGHTWEIGHT CERAMIC NANOTUBES REINFORCED POLYMER COMPOSITE COATINGS AND ELECTROSPUN MICROFIBRES

by Ruben Porras Ortigosa

The reinforcement of soft ductile polymers with hard brittle ceramic materials in order to improve mechanical and tribological properties of such composites has been explored since the dawn of the polymer technology. The recent advances in synthesis of nanosized materials have further extended the range of suitable fillers for polymer matrices, with particular attention focused on lightweight ceramic elongated nanomaterials. This research is concerned with a prospective approach to enhance mechanical and tribological properties of novel polymer composites by incorporation of titanate nanotubes and other metal oxide elongated nanostructured materials which could also enable the introduction of several responsive functionalities to new nanocomposites such as controlled release of encapsulated chemicals after a specific stimulus.

In this work, methods for isolation of single nanotubes from their agglomerates are developed by long-term mechanical stirring in a choice of suitable solvents with/without ultrasound treatment as well as nanotube surface modification (e.g. addition of CTAB). Colloidal suspensions of titanate nanotubes are affected disparately under ultrasound depending on the surrounding media, resulting in a different extent of shortening. Besides, it has been demonstrated that encapsulation of ibuprofen can be accomplished via polypyrrole sealing followed by its controlled release under short duration of ultrasonication.

A comprehensive study of mechanical and tribological properties of polyethylene oxide/chitosan (PEO/CS) composites reinforced with different content of various elongated nanofillers incorporated from stable aqueous suspensions is shown in addition to a systematic investigation of such properties as a function of length in titanate nanotubes controlled by ultrasound. It is demonstrated that increasing of the concentration of titanate nanotubes (TiNT) leads to improvement in hardness, Young's modulus, friction coefficient and residual depth. Short duration of sonication of colloidal suspensions of TiNT in the presence of polymer prior to drop-casting has resulted in enhanced mechanical and tribological properties probably due to better dispersion.

However, further ultrasound treatment of the mixture leads to deterioration of properties in composites along with nanotube shortening, as observed by TEM.

Subsequent investigations into the manufacture of titanate nanotubes embedded in poly ethylene oxide microfibres via electrospinning technique reveal that although our initial attempts to incorporate TiNT into electrospun microfibers have resulted in poor dispersion, long mechanical stirring of nanotubes in aqueous suspensions of the cationic surfactant CTAB has been essential for the manufacture of electrospun microfibres with high loads of single isolated TiNT (up to 13 wt %) aligned parallel to the electrospinning direction, as confirmed by TEM data.

Table of Contents

List of Tables

List of Figures

DECLARATION OF AUTHORSHIP

I, Ruben Porras Ortigosa declare that the thesis entitled **Lightweight ceramic nanotubes reinforced polymer composite coatings and electrospun microfibres** and the work presented in the thesis are both my own and have been generated by me as the result of my own original research. I confirm that:

- This work was done wholly or mainly while in candidature for a research degree at this University;
- Where any part of this thesis has previously been submitted for a degree or any other qualification at this University or any other institution, this has been clearly stated;
- Where I have consulted the published work of others, this is always clearly attributed;
- Where I have quoted from the work of others, the source is always given. With the exception of such quotations, this thesis is entirely my own work;
- I have acknowledged all main sources of help;
- Where the thesis is based on work done by myself jointly with others, I have made clear exactly what was done by others and what I have contributed myself;
- Parts of this work have been published as:

1. R. Porras, D.V. Bavykin, J. Zekonyte, F.C. Walsh, R.J. Wood, Effect of the quantity and the length of titanate nanotubes incorporated into a polyethylene oxide-chitosan mixed matrix on the mechanical properties of composite films. Composite Week @ Leuven and Tex-Comp-11 Conference, September 2013.

2. R. Porras, D.V. Bavykin, J. Zekonyte, F.C. Walsh, R.J. Wood, Titanate Nanotubes for Reinforcement of a Poly(Ethylene Oxide)/Chitosan polymer matrix. Nanotechnology. **2016**. 27, 195706.

3. R. Porras, D.V. Bavykin, J. Zekonyte, F.C. Walsh, R.J. Wood, Titanate nanotubes embedded in electrospun polyethylene oxide microfibres. *In preparation*.

4. C. Harito, R. Porras, D.V. Bavykin, F.C. Walsh, Electrospinning of in-situ and ex-situ synthesised polyimide fibres reinforced by titanate nanotubes. RSC Advances. *Submitted.*

Signed: .....

Date:.....

Acknowledgements

First and foremost, I would like to express my sincere gratitude to my main supervisor Dr. Dmitry Bavykin and my second supervisor Dr. Jurgita Zekonyte for giving me the opportunity to carry out this project, for their continuous patience and support, for many helpful discussions, and for the invaluable expertise they have shared with me. I would also like to thank my advisor Professor Frank Walsh for the advice he has giving me on writing my thesis. I gratefully acknowledge the Defence Science and Technology Laboratory (Dstl) for their financial support and Dr. Garry Wells for his contributions during our progress meetings.

I would also like to thank some of my laboratory colleagues for helping me in one way or another. Special thanks go to Dr. Rachel White for her support since the very beginning, for her patience, and for her willingness to help me with the electron microscopes at the beginning of my PhD. I would also like to acknowledge Dr. Irene Merino-Jimenez for indirectly bringing me the opportunity to start this PhD. I wish to thank Dr. Carlos Ponce-de-Leon Albarran for his proof-reading and useful comments during my Nine-month and Transfer Report assessments. I am grateful to my colleagues in my office and laboratory for their friendship and support.

A thank you to the “Cierrabares” crew for all the experiences and adventures we have lived over the last four years in the United Kingdom, Galicia, Corfu and Malaga. I am extremely grateful to all the members of the “Victoria’s Wolves” futsal team for having made me feel part of such a big team. I would like to thank all the guys of the University of Southampton Futsal Club for giving me the opportunity to train and play over the last two years. I also would like to thank the members of the “HK Chef” futsal team who allowed me to play in the Veterans league in the last semester of my PhD.

Last but by no means least, I would like to thank my partner Sara for her patience during my PhD, for being a strong supporter of mine through good and bad times, and for having given me the most beautiful thing in my life, my son Yoel. I wish to express my gratitude to my parents and all the rest of my family for their continuous support despite the distance, as always. I would also like to thank my friends in Spain for their long conversations on Skype, who have demonstrated how much I mean to them.

List of Abbreviations

A	projection of the contact area
ABS	acrylonitrile butadiene styrene
AcOH	acetic acid
AFM	atomic force microscopy
AgNP	silver nanoparticles
AMTES	aminomethyltriethoxysilane
APES	aminopropyl triethoxysilane
APS	ammonium persulfate
APTES	3-aminopropyltriethoxysilane
APTS	3-aminopropyltrimethylsiloxane
atm	atmosphere
ATRP	atom transfer radical polymerisation
AuNR	gold nanorods
BBT	2,5-bis (2-benzoxazolyl) thiophene
BET	Brunauer-Emmett-Teller
BJH	Barrett-Joyner-Halenda
BST	barium strontium titanate nanofibre
^{o}C	degree Celsius
CB	carbon black nanoparticles
Ce-TiNT	cerium-doped titanate nanotube
CF	carbon fibre
cm	centimetre
CMC	carboxymethyl cellulose
CNT	carbon nanotube
Col-	collagen
C_p	specific heat
CPP	chlorinated polypropylene
CS	chitosan
CTAB	cetyltrimethylammonium bromide
CVD	chemical vapour deposition

ΔQ	thermal energy
ΔT	Temperature rise
DCM	dichloromethane
DEF	diethyl fumarate
dm	decimetre
DMF	dimethylformamide
DMSO	dimethyl sulfoxide
ε	molar extinction coefficient
E	elastic modulus
E_r	reduced Young's modulus
EDS	energy-dispersive X-ray spectroscopy
ERP	elastic recovery parameter
EtOH	ethanol
eV	electron volt
FA	formic acid
FKM	fluoroelastomers
FS	flexural strength
g	gram
GA	glutaraldehyde
Ge-Imo	germanium modified imogolite nanotube
GO	graphene oxide
GPa	gigapascal
H	hardness
h	hour
Hap	hydroxyapatite
h_c	intercept of the tangent drawn from the linear elastic part of the unloading curve
HDI	hexamethylene diisocyanate
h_{max}	maximum displacement of indenter
HNT	halloysite nanotube
h_r	residual depth
HTPMDS	hydroxyl-terminated poly-dimethylsiloxane
IB	ibuprofen

Imo	imogolite nanotube
K	Kelvin
kHz	kilohertz
kJ	kilojoule
kV	kilovolt
L	average length
λ	wavelength
LDH	layered double hydroxide
LDPE	low density polyethylene
l-TiNF	long titanate nanofibre
m	metre
MA	maleic anhydride
mbar	millibar
MCB	monochlorobenzene
MEK	methyl ethyl ketone
MG	glycerol α-monolaurate
mg	milligram
MHz	megahertz
MMA	methacrylic acid
mmol	millimole
mN	millinewton
mPa	millipascal
MPa	megapascal
μ	viscosity
µm	micrometre
µl	microlitre
µs	microsecond
m-TiO_2	titanium dioxide microparticles
Mw	molecular weight
MWNT	multi-walled nanotube
NC	nanocrystals
ND	nanodiamonds

nm	nanometre
NMP	N-methyl-pyrrolidone
n-TiO_2	titanium dioxide nanoparticles
ν	Poisson's ratio
ODA	4,4'-oxydianiline
o-DCB	orthodichlorobenzene
P	pressure
P_0	ambient pressure
PA-6	polyamide 6
PA-66	polyamide 66
PAA	polyamic acid
PAN	polyacrylonitrile
PANI	polyaniline
PBI	polybenzimidazole
PBO	polybenzobisoxazole
PC	polycarbonate
PCL	polycaprolactone
PDDA	poly (diallyldimethylammoniumchloride)
PEEK	polyether ether ketone
PEG	polyethylene glycol
PEI	polyethylenimine
PEO	polyethylene oxide
PET	polyethylene terephthalate
PFA	perfluoroalkoxy polymer
PFSA	perfluorosulfonic acid
P-HEMA	2-acidphosphoxyethyl methacrylate
phr	parts per hundred parts of resin
PI	polyimide
Ph-	phenoxy
PMDA	pyromellitic dianhydride
PLA	polylactide
PLGA	poly(lactic-co-glycolic acid)

Pmax	maximum applied load
PMMA	polymethyl methacrylate
PP	polypropylene
PPESK	poly(phthalazine ether sulfone ketone)
PPF	poly(propylene fumarate)
PPy	polypyrrole
PPS	poly(phenylene sulphide)
PS	polystyrene
PTFE	polytetrafluoroethylene
PTW	potassium titanate whiskers
PU	polyurethane
PVA	polyvinyl alcohol
PVAc	polyvinyl acetate
PVB	poly(vinyl) butyral
PVC	polyvinyl chloride
PVDF	polyvinylidene fluoride
PVK	poly(N-vinyl carbazole)
Py	pyrrole
ρ	density
RAFT	reversible addition-fragmentation chain transfer
ROP	ring opening polymerisation
rpm	revolutions per minute
S	stiffness
s	second
SEM	scanning electron microscopy
s-TiNF	long titanate nanofibre
t	time
TCP	tricalcium phosphate
TEM	transmission electron microscopy
TEMS	triethoxymethylsilane
TEOS	tetraethyl orthosilicate
TFA	trifluoroacetic acid

THF	tetrahydrofuran
TiNF	titanate nanofibre
TiNT	titanate nanotube
TPa	terapascal
TS	tensile strength
SWNT	single-walled nanotube
SBR	butadiene styrene rubber
UHMWPE	ultra-high molecular weight polyethylene
UV-vis	ultraviolet-visible
V	volume
VH	Vickers hardness
W	watt
wt	weight
xSBR	carboxylated butadiene styrene rubber

Chapter 1: Introduction

1.1 Background and motivation

The development of synthetic composite materials with enhanced mechanical and tribological properties continually attracts researchers' attention due to their high relevance to improve the stability and capabilities of such composites, which is crucial for potential applications where impact resistance and degradation are involved [1]. Addition of lightweight ceramic nanotubes [2] and nanofibres [3] to polymer matrices via electrospinning or drop-casting opens up a possibility not only for enhancement of mechanical stability but also could allow the introduction of several responsive functions such as drug delivery [4] or "self-healing" [5].

The reinforcement of polymer matrices with elongated nanostructures such as nanotubes, nanorods and nanofibres has been extensively investigated in the past fifteen years. Some nanotubular materials such as carbon [6] or tungsten sulphide (WS_2) [7] have already demonstrated good mechanical response. However, the high cost in the manufacture of carbon nanotubes and the excessive weight of WS_2 nanotubes encourage us to the employment of alternative nanostructured elongated materials. Titanate nanotubes (TiNT) are characterised by multi-walled structure, mesoporous inner diameter and an average length that can exceed a few hundreds of nanometres [8]. The facile and cost-effective alkaline hydrothermal synthetic route, the low weight compared to other ceramic nanostructures as well as the high strength of such nanotubes provides them with promising features for the manufacture of alternative resistant polymer-based composites.

It is worth noting that the development of methods for separation of nanotubes from aggregates is needed in order to achieve homogeneous dispersions within matrices. Long-term stirring, utilization of ultrasound and a choice of suitable solvents are essential to accomplish a uniform distribution of fillers within matrix. TiNT polymer composite films are produced as a first attempt to gain a good understanding on the distribution of nanotubes via drop-casting or spin-coating. A comprehensive study of mechanical and tribological properties including strength, hardness, friction and wear have been systematically investigated as a function of type, content and length of the filler within the matrix, which are assessed via nanoindentation and nanoscratch testing. The use of ultrasonic treatment has been found beneficial for the nanotube debundling, although a reduction in mean length occurred depending on the experimental conditions.

Much effort has been put into the investigation of composite materials reinforced with inorganic nanotubes. As a part of our project, polymer composites have been filled with other elongated nanostructures, for example, titanate nanofibres (TiNF) synthesised by the alkaline hydrothermal method and aluminosilicate nanotubes such as halloysite and imogolite. Unlike the hollow-like structure in nanotubes (Figure 1.1b), length of the solid nanofibres can easily exceed a few microns, which differs by an order of magnitude. Such variation in both morphology and size has been worth investigating due to the distinct tribological behaviour found in composites reinforced with such TiNF (Figure 1.1c).

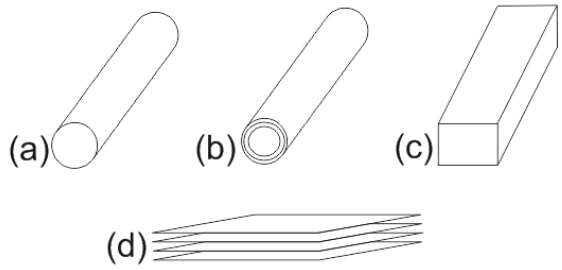

Figure 1.1. Most common elongated nanostructures found in polymer composite materials: (a) nanorod, (b) nanotube, (c) nanofibre and (d) nanosheet.

Experimental conditions have been optimised in the manufacture of composite films as well as microfibres filled with nanotubes have been simultaneously produced via electrospinning. The introduction of a new critical variable such as high electric field developed in the needle during electrospinning varies significantly the experimental conditions, where the negatively charged nanotubes might undergo an electrophoretic motion causing their coagulation. The incorporation of new additives for surface modification of nanotubes is essential in order to achieve well-dispersed and oriented nanotubes embedded into the polymer electrospun microfibres.

TiNT are robust hollow containers that could be filled with certain chemicals. Future research should be focused on the encapsulation/sealing of these selected molecules in the mesoporous nanotubes and their controlled release after a mechanical stimulus, which would open up a wide range of novel applications in the field of drug-delivery or “self-healing” properties. For instance, ibuprofen molecules have been encapsulated in titanate nanotubes.

1.2 Aims and objectives

The aims of the project are to develop a synthetic approach for an effective dispersion of elongated nanostructures previously dispersed as colloids within the polymer matrices, and to characterise the mechanical and tribological response of such composites. The research therefore pursued the following objectives:

- development of methods of isolation of single nanotubes from agglomerates and their uniform dispersion as stable colloidal suspensions in various solvents by modification of the nanotube surface, ultrasound and long-term stirring.
- manufacture of polymer composite films reinforced with homogeneously dispersed TiNT within matrices. Mechanical and tribological properties are assessed as a function of content of nanotubes. Furthermore, ultrasound can be an appropriate tool for the isolation of nanotubes that are obtained mainly in the form of bundles. However, long-term sonication can damage nanotubes, reducing their aspect ratio. Both effects are evaluated as a function of ultrasound duration maintaining a fixed content of TiNT.
- production of polymer nano/microfibres via electrospinning. Elaboration of methods to control orientation of nanotubes embedded into polymer matrices, considering that both nanotube length and orientation can affect the mechanical performance of the electrospun fibres, which can be examined using transmission electron microscopy.
- incorporation of selected substances into the inner pores of the nanotubes and study a controlled release of such molecules induced by various stimuli. Encapsulation of chemicals catalysing cross-linking polymerisation would enable responsive "healing" of the polymer composite. In different circumstances, non-woven electrospun mats containing nanotubes filled with drugs would be liberated for drug delivery purposes.

1.3 Thesis outline

This thesis is divided into seven chapters including the introduction and literature review (Chapters 1 and 2), experimental methodology (Chapter 3), results and analysis (Chapter 4, 5 and 6) followed by the conclusions (Chapter 7), in which the results are summarised and suggestions for further work are made. In Chapter 2, a thorough literature review of

synthesis, physical/chemical properties of inorganic nanotubes as well as manufacture processing of their polymer composites is presented. Mechanical and tribological characterisation of composite materials is also included in the last part of the literature review alongside nanotube dispersion/scission within polymer matrices caused by ultrasound treatments.

The Chapter 3 describes the experiments designed to address the thesis aims previously mentioned in Section 1.2 of this chapter. The results of these experiments together with discussions are presented in Chapters 4-7. In Chapter 4, results of ultrasound treatment of colloidal suspensions of titanate nanotubes in various solvents and its effect on the scission rate are presented with the aid of electron microscopy techniques. In addition, encapsulation of a selected molecule ibuprofen can be sealed by a polymer coating of polypyrrole, which can be released under sonication. Chapter 5 presents results of the dispersion of titanate nanotubes within the polymer matrix polyethylene oxide / chitosan (PEO:CS=6:1), which are characterised by electron microscopy, nanoindentation and nanoscratch testing techniques. Mechanical and tribological properties are investigated as a function of titanate nanotubes content and length controlled by duration of ultrasound. Moreover, mechanical and tribological properties of composite thin films reinforced with various elongated metal oxide nanostructured materials such as titanate nanofibres, germanium-modified imogolite nanotubes and titanate nanotubes stirred in the presence of pyrrole are studied.

In Chapter 6, polymer microfibres with a composition of PEO:CS=6:1 and filled with surface modified titanate nanotubes are produced via electrospinning technique. In the last part of Chapter 6, results of polyimide (PI) electrospun microfibres loaded with titanate nanotubes are presented. Finally, the results are compiled into a set of conclusions and suggestions for further work in Chapter 7.

Chapter 2: Literature Review

The term nanomaterials refers to materials which have an internal or surface structure in the nanoscale, that is, a single unit in at least one dimension is sized between 1 and 100 nanometres [9]. Over the last twenty five years, development in technology has allowed the synthesis of novel nanostructures characterised by unique physical-chemical properties that differ from those as bulk materials, which renders the former with a new range of potential applications.

This section focuses on synthetic elongated nanostructures as well as naturally occurred nanotubes, which are further used in the manufacture of a great variety of polymer based composite materials. Special attention has been paid to polymers such as polyethylene oxide, chitosan and polyimide, which have been used in the experimental part of this research. Manufacture of polymer composite materials studied in this work can range from mere drop cast films and coatings or alternatively they can be stretched into fibres via electrospinning. It is believed that enhanced mechanical and tribological properties at the nanoscale can improve the complete robustness in the bulk material. Due to the nanometric nature of the fillers incorporated into the polymer matrix, techniques including nanoindentation and nanoscratch must be introduced in order to characterise their physical properties along with electron microscopy to investigate the distribution of the reinforcing phase within the matrix. Ultrasound is widely applied for the purpose of obtaining an adequate dispersion of independent nanostructures, although their total length can be reduced as a side effect (see Chapter 4).

2.1 Elongated nanostructures in polymer composites

Elongated nanostructures can be defined as shapes with aspect ratio greater than 10, where aspect ratio is determined by the proportion between the two characteristic dimensions of a structure, length and diameter for elongated materials [8]. These one-dimensional nanostructures are named differently in literature, which can be classified as a function of their shape. Nanotubes have a long cylindrical shape containing a hollow cavity along their full length, usually structurally concentric with a relatively constant diameter. Their walls can be single or multi-layered, with their ends either open or closed depending on the type of nanotube or synthetic method. Nanowires or nanorods are long linear structures with a

preferable growth direction, but their cross-sectional shape are not well defined, being nanorods much shorter than nanowires [10]. Nanoribbons, nanobelts or nanofibres are parallelepiped with well-defined sides, cross-section and good crystallinity. Their aspect ratio is normally quite large.

This review focuses on carbon nanotubes due to their remarkable properties in addition to the alternative nanostructures that have been used during our research because of their low-weight and cost-effective synthesis or mining, in other words, titanate nanotubes (TiNT), titanate nanofibres (TiNF) and aluminosilicate nanotubes such as imogolite (Imo) and halloysite (HNT).

2.1.1 Carbon nanotubes

Carbon nanotubes are one of the best examples of novel synthetic nanomaterials that have been attracting the scientific community for the last two decades. They were first published in the Journal of Physical Chemistry of Russia in 1952 [11], where some TEM images show evidence of tubular nanostructure. However, the Western World was not aware of such publication due to the Cold War and the use of Russian language. It was reported later in 1976, the discovery of carbon nanotubes described as concentric sheets like the "annual ring structure of a tree" [12], which were obtained by pyrolysis of a mixture of benzene and hydrogen at high temperature. The publication of the illustrious work about multiwalled carbon nanotubes produced via arc-discharge evaporation method by Iijima in 1991 [13] stimulated researchers to investigate such nanotubes in most areas of science and engineering due to their fascinating properties such as thermal conductivity, electrical conductivity, strength and hardness.

A carbon nanotube can be viewed as single atomic layers of graphene rolled up into a seamless, hollow cylinder, with each end capped with half of a fullerene [14]. The lattice vector (n,m) in the graphene plane determines both diameter and chirality of the nanotube [15]. There are infinite possibilities in the type of carbon nanotube although two limiting cases occur where the chiral angle is at 0˚ or 30˚ [16]. Zig-zag nanotubes are those which their chiral angle equals zero and the roll-up vector is referred as (n,0). The structure where n = m (n,n) is called armchair (30˚) based on the symmetry of the carbon bonds around the perimeter of the nanotube. The chirality predetermines physical behaviour such as electrical, mechanical, optical and other properties [17]. For example, electrical properties

in single walled nanotubes can vary from metallic or semi-metallic to semiconductor [18], being the band gap inversely proportional to the diameter. However, physical properties in multiwalled carbon nanotubes are more difficult to predict.

This statement leads us to a second classification of carbon nanotubes as a function of the number of layers. Single walled nanotubes (SWNTs) by definition are a single sheet of graphene rolled up in the shape of a cylinder with a diameter between 1 and 2 nm and a length up to a few millimetres whereas multiwalled nanotubes (MWNTs) consist of an array of concentric graphene cylinders fitted one inside another, with a central hollow core and an interlayer distance of approximately 0.34 nm [18], which is similar to the basal plane separation in graphite [19]. Diameter in MWNTs can range from 2 to 100 nm and lengths close to millimetres.

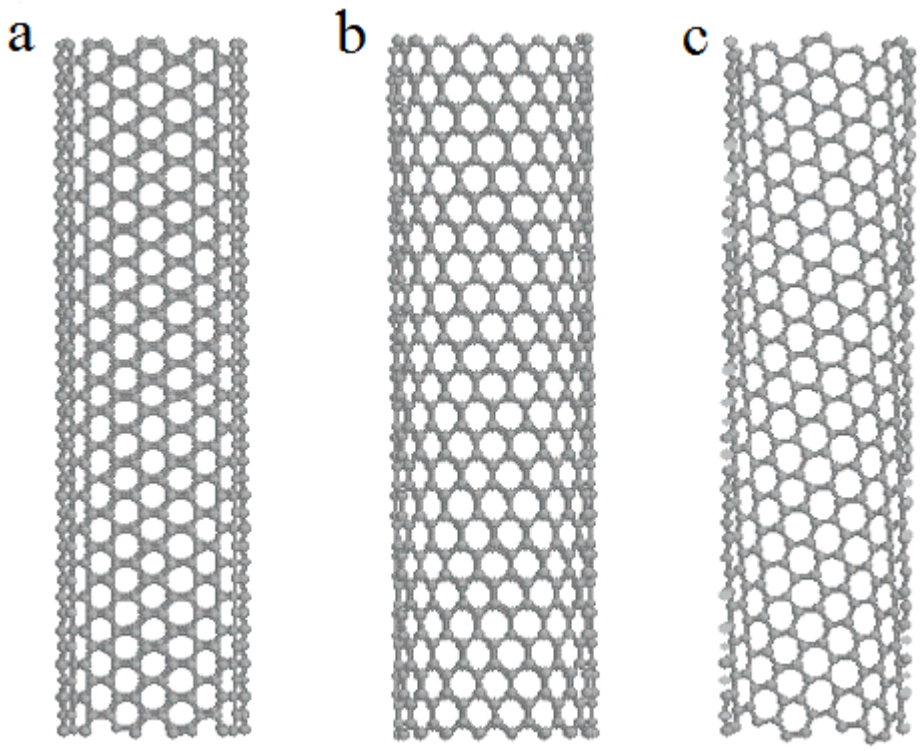

Figure 2.1. Illustration represents three types of single-walled carbon nanotubes. Armchair (a), zigzag (b) and chiral (c) structures respectively [15]. Adapted with permission from American Chemical Society.

It is believed that the carbon-carbon covalent bond is one of the strongest bonds in nature; hence a structure composed of such bonds along the longitudinal axis of the nanotube gives rise to a solid with extremely high strength. Reduced Young's moduli have been measured in SWNTs via atomic force microscope (AFM) obtaining values greater than 1 TPa, which

make them one of the stiffest materials ever made [20]. A higher compressive strength along with their quite low density (1.3 g cm^{-3}) results in a nanostructure 100 times as strong as steel per unit weight. The most attractive feature is the combination of high flexibility and strength with high stiffness. Due to the fact that their fracture strains can reach up to 30% before fracture failure and their aspect ratio can be as high as 10000 [14], carbon nanotubes can be used as promising materials for polymer composites. Thermal conductivities are highly anisotropic, being conductive along the length of the nanotubes and insulating in the orthogonal directions.

Currently all synthetic methods yield a random distribution of chiralities, lengths, diameters and number of layers as well as impurities contaminating the samples such as graphite, amorphous carbon, fullerenes and metals that were introduced as catalysts. Therefore, the availability of pristine and isolated either SWNTs or MWNTs is virtually unachievable, which hinders their experimental study at the same time that their fully exploitation has yet to come. Due to their high flexibility and aspect ratio coupled with London dispersion interactions, carbon nanotubes tend to appear in the form of large bundles or ropes, which are extremely difficult to separate. The properties of such bundles or ropes are inferior to those of isolated nanotubes.

Another issue in the real application of carbon nanotubes is the high manufacture cost along with their scaling-up. Thus far the known synthetic methods cannot produce very large quantities at a competitive price. The most commonly used techniques in the synthesis of carbon nanotubes are arc discharge, laser ablation and chemical vapour deposition (CVD), being the latter more cost-effective. Furthermore, certain parameters such as orientation, alignment, length, diameter and purity can be controlled to some extent in CVD method [17].

Direct current and high temperature over 1700 ˚C are used in the synthesis of carbon nanotubes via arc discharge method, from which both SWNTs and MWNTs are produced after vaporization and condensation of graphite on the cathode, with fewer structural defects. The preparation is carried out in a chamber filled with helium, argon, hydrogen, methane, ethanol, acetone or hexane under reduced pressure. A higher yield is obtained in the organic media owing to the fact that they can be ionized and decomposed into hydrogen and carbon. The presence of catalyst is required for the manufacture of SWNTs whereas MWNTs are generated even in the absence of transition metals. A slightly variation such as pulsed arc discharge has been introduced in order to increase the yield of SWNTs [21].

Synthesis via laser ablation, the laser removes a graphite target containing a metal catalyst in argon at lower temperature in the range of 1200 ˚C. The principles are similar to arc discharge with the only difference that the energy is provided by a laser, which can range from single or dual pulsed to continuous [21]. CNTs require further purification in this technique, whose morphology is strongly dependent on the experimental conditions such as type of laser, catalyst composition, growth temperature, gas, pressure and so on.

Chemical vapour deposition (CVD) is the most common method nowadays for the production of carbon nanotubes, either thermal or plasma enhanced. Unlike laser ablation or arc discharge methods, this gas-phase process tends to yield higher nanotube purity at lower temperature (between 500 and 1000 ˚C) and is more viable in the large-scale processing since the carbon source is continuously replaced by flowing gas, although a large number of defects are found in the structure [19]. There are certain modifications in CVD technique such as hot-filament, microwave plasma, water assisted or oxygen assisted. The mechanism by which carbon nanotubes are formed is the decomposition of the carbon source into free radicals followed by the new nucleation within the proximity of the catalyst surface to initiate their growth onto a huge variety of substrates.

An alternative promising production of carbon nanotubes is a bottom-up organic approach, which consists of the utilisation of hoop-shaped carbon macrocycles that preserve information with respect to chirality and diameter [22]. It can be described as a two-step method: the synthesis of macrocycle templates and the extension of the CNTs via polymerisation. Zig-zag, arm-chair and chiral carbon nanotubes with various diameters have already been synthesised.

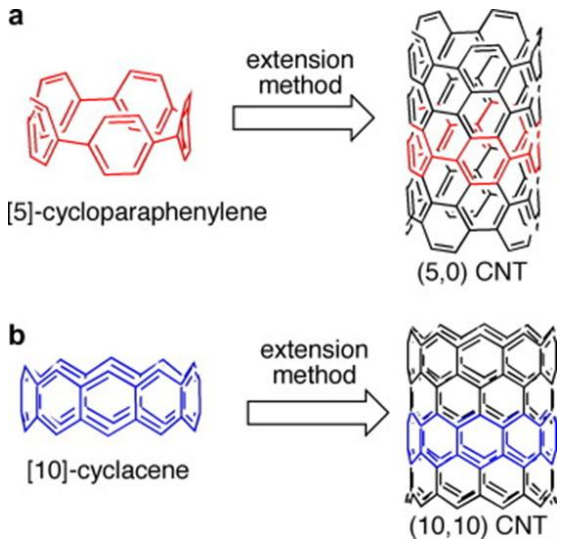

Figure 2.2. CNT bottom-up organic synthesis approach with discrete chirality after ref. [22].

2.1.2 Titanate nanotubes and nanofibres

The rapid advancement in nanotechnology has also catalysed the synthesis of nanostructured titanium dioxide and titanate nanomaterials. Historically, titanium dioxide (TiO_2) has been used as a pigment in paints from ancient times; photocatalytic properties under UV light were discovered afterwards in the late 1970s [23]. Initially, nanostructured TiO_2 materials were synthesised mainly via sol-gel techniques, from which rounded nanoparticles were obtained for applications such as photocatalysis and dye sensitised solar cells. It was later in 1998 when Kasuga *et al*. [24] reported the discovery of titania or titanate nanotubes (TiNT) synthesised by the alkaline hydrothermal method, in which both starting materials and manufacture process are cost effective unlike their carbon nanotube counterparts. Other elongated nanostructured titanates such as nanosheets and nanofibres have also been found [25].

Elongated TiO_2 nanostructures can be prepared by three synthetic methods. The first one is called template-assisted route, which consists of a two-step method: deposition and template removal. This ingenious technique has become less popular due to the development of new routes which are less expensive. For example, titanate nanotubes are spontaneously formed under the single-stage alkaline hydrothermal route, which gives rise to a wide distribution of randomly oriented nanotubes in terms of size. The third general method, the anodic oxidation synthesis produces arrays of larger titanium dioxide nanotubes immobilised onto the substrate in the presence of fluoride-containing electrolytes.

It has previously reported that Kasuga *et al*. [24] prepared for the first time TiNT via the alkaline hydrothermal method, involving the treatment of amorphous TiO_2 mixed with a strong alkaline aqueous solution of NaOH (10 mol dm^{-3}) at high temperature (110 ˚C). The nanotubes were washed with an aqueous solution of HCl (0.1 mol dm^{-3}) and water to ion-exchange Na^+, obtaining the protonated form. The morphology of TiNT is characterised by a multi-layered structure ranging between 2 and 10 layers -although generally they have four- and whose interlayer distance is 0.72 nm approximately in the protonated form. They are shaped as open-end cylinders with a hollow cavity along their full length, which can be up to a few hundreds of nanometres and a constant diameter in the range from 2 to 20 nm [8]. Nanotubes are usually presented as large aggregates after synthesis which can be separated into stable colloidal suspensions after being treated with surfactants, ultrasound or long-term mechanical stirring.

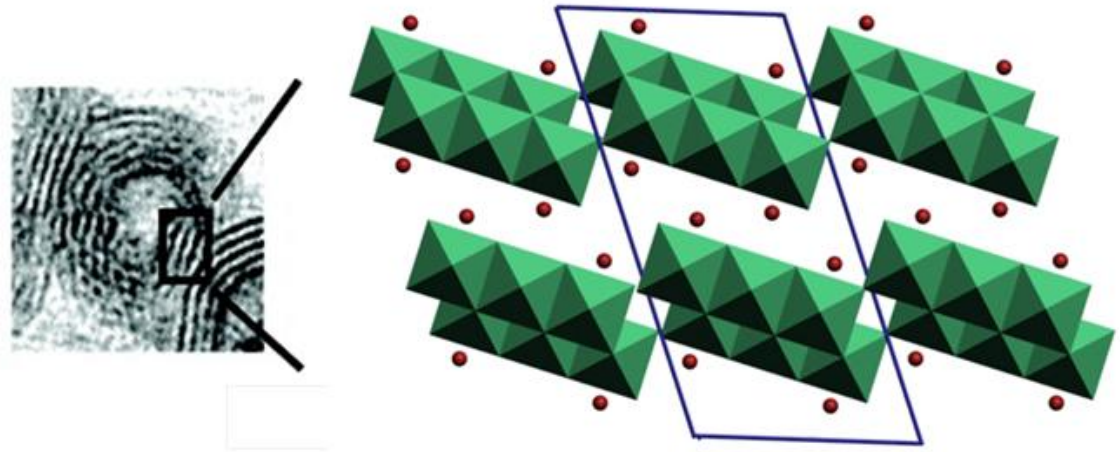

Figure 2.3. Crystal structure of trititanic acid ($H_2Ti_3O_7$) extracted from the orthogonal projection on the TEM micrograph adapted from references [26, 27]. The illustration represents TiO_6 edge-sharing octahedra in green and ion-exchangeable protons in red. Adapted with permission from American Chemical Society.

Nanofibres can be produced via alkaline hydrothermal method starting from the same materials (e.g. NaOH 10 mol dm^{-3} and TiO_2) by increasing temperature up to 170 ˚C. These titanate nanofibres have also a multi-layered structure with an interlayer distance of 0.72 nm in the protonated form and can easily exceed several microns in length and up to 200 nm in width. It has been discovered that dissolution of TiO_2 can be increased by incorporation of KOH at reduced temperature. Therefore, titanate nanosheets, nanotubes and nanofibres can be obtained by the alkaline hydrothermal method at reduced temperature and atmospheric pressure by modification of the ratio KOH:NaOH for a concentration of 10 mol dm^{-3}. Besides, an increase in temperature can vary the final synthetic product. For example, short titanate nanofibres are produced in pure KOH (10 mol dm^{-3}) at lower temperature whereas long titanate nanofibres can be made in NaOH (10 mol dm^{-3}) at much higher temperature (190 ˚C) [25, 28]. It is agreed that chemical composition in every nanostructure can be described as the hydrated form of titanium dioxide, with the stoichiometric formula $H_2Ti_3O_7$ [29].

It is believed that the intermediate single-layered and multi-layered titanate nanosheet plays an important role in the nanotube formation under alkaline hydrothermal conditions [30]. These nanosheets can curve, scroll or fold into a nanotubular structure, which is explained from various points of view. On the one hand, an imbalance of Na^+ and H^+ ion concentration on both sides of the nanosheet creates an uneven chemical environment with

an excess of surface energy, thus the system tends to move to a minimum of energy resulting in nanosheet bending [31]. Mechanical tensions occur during the dissolution-crystallisation events in nanosheet growth causing their bending. The width in consecutive layers can vary due to rapid crystallisation. This imbalance in layer width might result in a sliding movement of the topmost layer over the adjacent layer in order to decrease the excess of surface energy, which leads to curving of multi-layered nanosheets [29, 32].

Various types of nanotubes are found depending on the method of loop closing in nanosheets. In the case that layers ends match, a seamless cross-section is produced with a number of concentric layers. However, non-matching layers give rise to either onion-like structures or scrolled helical layers known as snail-type [30, 33].

It was earlier mentioned that an increase of temperature above 170 ˚C or the addition of KOH can lead to an increase in the local concentration of titanium in aqueous media, which in turn may result in a faster growth rate in the intermediate. As a consequence, the scrolling effect in nanosheets can be reduced, favouring the crystallisation so the thickness is sufficiently large to suppress the bending effect. This will lead to the synthesis of titanate nanofibres rather than nanotubes [8]. The preferred direction in nanofibre growth is along the crystallographic axis c, which is the actual length of a nanofibre whereas the width of the fibre corresponds to the axes a and b. Under lower temperature or certain conditions that favour a lower concentration of titanium in solution, an imbalance in the width of the nanosheet along the axis c results in bending around the axis b until the loop is closed, which is when the fastest growth direction disappears. In terms of energy, nanofibres are the thermodynamically stable product.

Titanate nanostructures and especially nanotubes have quite exceptional surface area due to their reduced size and diameter, which increases the ratio between accessible atoms at the surface to bulk atoms. The BET (Brunauer–Emmett–Teller) method is a well-established technique for the characterisation of specific surface area in porous materials obtained from the isotherm of nitrogen adsorption at -195 ˚C. In the case of titanate nanotubes, values for BET specific surface area can oscillate between 200 and 300 m^2 g^{-1} [30]. The pore volume distribution is obtained from the desorption part of the nitrogen curve using the BJH algorithm, which shows the mesoporous nature of these nanotubes with a diameter ranging between 4 and 20 nm.

Both ionic charge and adsorption in aqueous solutions are affected by the fact that titanate nanotubes develop a negative zeta potential due to the dissociation of the polytitanic acid

($H_2Ti_3O_7 \leftrightarrow [HTi_3O_7]^- + [H]^+$) [34, 35]. Therefore, adsorption of charged species will be affected according to the electric charges: positive or negative [36]. For example, adsorption of cationic species (e.g. cetyltrimethylammonium bromide (CTAB)) will be favoured due to the electrostatic interactions between adsorbent and adsorptive in aqueous solution, which can even switch zeta potential from negative to positive [37].

The semiconductive character of titanium dioxide is suitable for several applications in the field of photocatalysis, solar cells, sensors and electronic devices. Spectroscopic studies conducted in aqueous colloidal suspensions of titanate nanotubes suggest that the estimated value for the band gap is approximately 3.87 eV, which does not depend on the internal diameter [38]. Besides, the reversible ion-exchange reaction in TiNT mainly favoured for monovalent alkaline cations suggest that they have notable proton conductivity (see Section 2.2.2). The cations located between titanate layers (both in nanotubes and nanofibres) and on the nanotube surface can be easily replaced with protons in an acid aqueous media. This method of ion-exchange allows the decoration of TiNT with metal precious, acting nanotubes as a support for catalysts [39].

The large quantity of OH groups on the surface of titanate nanotubes enables a much easier functionalization compared with their carbon counterpart. Several strategies have been followed in order to make their surface more hydrophobic such as the controlled hydrolysis of trialkoxysilanes in anhydrous solvents [40], in which covalent bonds are formed; or weaker electrostatic interactions after addition of cationic surfactants in aqueous solution (e.g. CTAB) [37].

The high aspect ratio coupled with the physical and chemical properties of the elongated titanate nanostructures such as high specific surface area, ion-exchange behaviour, semiconductive electric properties and facile functionalization render these materials with high versatility for numerous applications in the realm of energy conversion and storage for dye-sensitized solar cells [34], lithium batteries [41], fuel cells [42], hydrogen storage [43]; catalysis for isomerisation of organic compounds [44], supercapacitors [45], photocatalysis [46]; magnetic materials [47]; drug delivery [48] and composites [40, 49].

2.1.3 Aluminosilicate nanotubes: Imogolite and Halloysite

The name of “halloysite” was first used by Berthier [50] in honour of Omalius d’Halloy, who first discovered it in a mineral deposit in Belgium. Halloysite occurs as a result of

long time weathering of a wide variety of silicon-rich rocks mainly in tropical and subtropical areas with a high moisture regime such as Brazil, China, New Zealand, Japan and South Korea; although they are also mined from natural deposits in France, Belgium and Turkey [51, 52]. This aluminosilicate clay of the kaolin group presents a dioctahedral 1:1 layer structure whose chemical stoichiometric formula corresponds to $Al_2(OH)_4Si_2O_5(2H_2O)$ for its hydrated form, giving a water content of approximately 12 wt % [53, 54]. Its crystal structure is formed by a corner-sharing block of [SiO_4] tetrahedra and an edge-sharing block of [AlO_6] octahedral where 2/3 of the octahedral sites are occupied by aluminium (shown in Figure 2.4) [52]. Interlayered water molecules are located between two consecutive layers, having a basal spacing of 10 Å that can be irreversibly reduced to 7 Å during dehydration process, after which its chemical composition is similar to kaolinite.

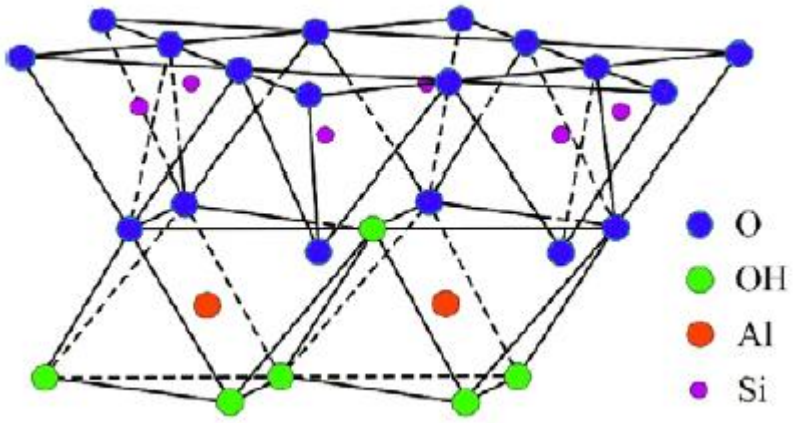

Figure 2.4. Illustration represents the crystal structure of halloysite after reference [55]. Blue, green, red and purple circles represent oxygen, hydroxyl, aluminium and silicon, respectively.

Due to the large variety of geological deposits as well as the different crystallisation conditions, real chemical composition is subject to little variations, being iron oxides the most common impurities [53]. For the same reasons, morphology of halloysite can vary from one mine to another. The most common and valuable structure is the tubular morphology, which is formed by layer rolling due to a dimensional misfit between octahedral and tetrahedral sheets. The long axis in halloysite nanotubes coincides with the crystallographic b axis most of the times. Typical dimensions are 1-100 nm in inner diameter, 10-120 nm in outer diameter and 2-2000 nm in length, resulting in nanotubes with a high aspect ratio [51, 54]. However, short tubular structure, spheroidal onion-like

nanoparticles with diameter in the range of 50-500 nm and 2-dimensional platy structures with high content of iron have been also reported. It has been observed that long term progressive alterations via hydration of kaolinite might induce plate curving, giving rise to curled hydrated halloysite at the edges of laminar kaolinite [53].

It has been reported that inner and outer surface on HNTs are rather different. The inner lamella consists of aluminum atoms coordinated by oxygen atoms and hydroxyl groups and its properties are associated with Al_2O_3 whereas the outer surface is formed essentially of O-Si-O groups and a few silanol groups located at the edges of the nanotube and on the surface due to defects [51, 55]. Therefore, in terms of reactivity, the outer surface of HNTs is more inert owing to their low density of hydroxyl groups while the rich aluminol inner surface and the end of the nanotubes are much more reactive. The zeta potential of HNTs in aqueous solution depends on the pH, which is slightly negative for very low pH and decreases sharply as the pH values are higher [53, 56]. As it has been previously mentioned, the surface is made mainly of silica, thus the negative zeta potential in a wide range of pH in aqueous solution. A less negative zeta potential is found at a very low pH due to a small contribution of the amphoteric oxide alumina in the inner part of the nanotubes [57].

It should be noted that halloysite nanotubes have been used in a wide range of applications. For instance, corrosion has been prevented by encapsulation of inhibitors in the hollow cavity of nanotubes, which are released after a mechanical stimulus (damage) or internal corrosion trigger (change in concentration of certain chemicals). Nanotubes are dispersed within coatings, playing the role of nanocontainer [58]. Following the same principle, other additives have been entrapped such as pesticides [59] and contaminants [60]. These nanotubes have been used as biomimetic nanoreactors to produce inorganic nanoparticles via enzymatic loading in the inner lumen [61] as well as supports for catalysts [62]. Special attention will be paid on polymer halloysite nanocomposites and their properties in various polymeric matrices below in Section 2.2.3.

Imogolite are single-walled nanotubes clay associated with volcanic ash soils where increased rainfall contributes to silica percolation [63]. Natural imogolite was first discovered in Japan in 1962 [64]. The hollow tubular nanostructure is formed of an outer curved gibbsite sheet ($Al(OH)_3$) where the inner hydroxyl surface has been replaced by O_3SiOH groups [65]. Therefore, the outer surface can be positively charged depending on the solution pH (below 5) [66, 67]. Such a structure has a stoichiometric formula $(OH)_3Al_2O_3SiOH$, which corresponds to the distribution of atoms encountered from the

outer surface down to the inner part [68]. Typical dimensions for such nanotubes are internal diameter of approximately 1 nm, external diameter between 2 and 2.5 nm and length which ranges from 100 nm to a few microns [69]. Therefore, imogolite nanotubes have a larger specific surface area compared to halloysite [67] and titanate nanotubes [8].

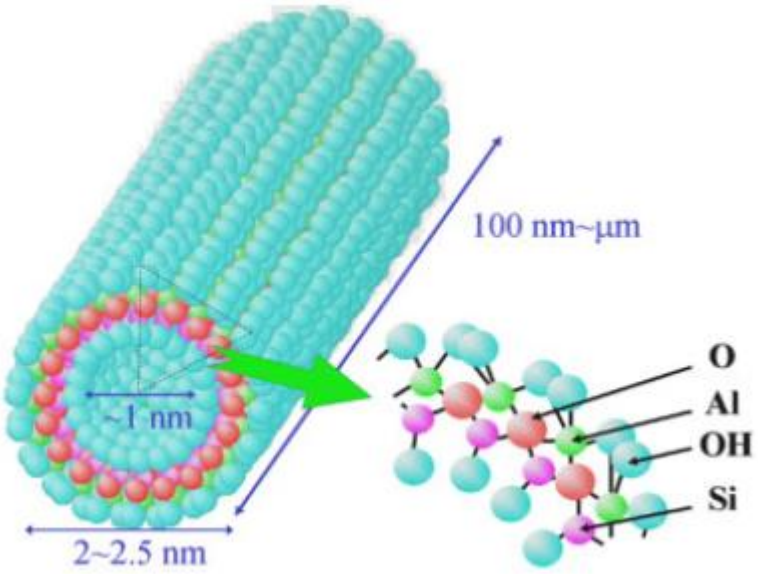

Figure 2.5. Schematic representation of the structure and dimensions of imogolite nanotubes after reference [69]. Oxygen, aluminium, hydroxyl and silicon are drawn in different colours.

Although the formation mechanism of imogolite has not been understood yet, it has been suggested that isolated and inverted silicate tetrahedra are bound to the gibbsite layer, after which the pulling strain associated with the Si-O-Al bonding is accommodated by bending, leading to nanotubular structure [68, 70]. Several theoretical studies on various tubular nanostructures have stated that the strain energy to roll a sheet into a single-walled nanotube decreases as the nanotube radius increases. However, exclusively for imogolite, there is a minimum in the strain energy for the optimum structure, which corresponds to a circumference composed of 12 gibbsite units with a zig-zag chirality, outer diameter around 2.3 nm and inner diameter of 1.0 nm [71].

Extraction of naturally occurred imogolite involves a purification process in order to separate the tubular clay from organic and inorganic impurities. The first synthetic approach to artificially produce imogolite from diluted solutions of aluminium chloride and the precursor of orthosilicic acid under very mild conditions was described in 1977

[66, 70]. An increase in the concentration of precursors always ended up with the formation of allophane instead, a clay with the same composition of imogolite but spherical morphology [72]. It is also possible to synthesise a germanium analogue of imogolite, in which silicon atoms have been partly replaced by germanium. Tubular morphology is found although length in aluminogermanate imogolite is reduced down to 10 nm with an external diameter of 3.3 nm [73]. A reduction in curvature occurs due to a longer distance in the O-O bonding in GeO_4 [70].

Both naturally occurred and synthetic imogolite have been used for several applications in the fields of catalysis [74], gas storage [75] and as adsorbents [76, 77], as a coagulant [78] as well as for membranes [79]. Functionalization of imogolite nanotubes along with the preparation of novel polymer hybrids is further discussed in the Section 2.2.3.

2.2 Polymer composite materials filled with elongated nanostructures

The incorporation of elongated nanostructures into polymer matrices leads to the manufacture of composite materials with improved properties, for example, mechanical, electrical, thermal, optical and catalytic properties; which enhance the total performance of the composite with respect to the neat polymer. Furthermore, the high aspect ratio of 1-dimensional elongated materials can provide extra structural stability, resulting in robust composites which are exploited for diverse applications.

2.2.1 Carbon nanotube polymer composites

Carbon nanotubes have been integrated in a vast number of materials due to their extraordinary properties such as high aspect ratio, mechanical, electrical and thermal properties, which make them the ideal candidate for fillers in composite materials. Research on carbon nanotubes composite materials is a subject of great interest, which is corroborated by a great deal of publications and financial support in this field over the last decade. This section focuses on the fabrication and enhancement of mechanical properties of composite materials reinforced with carbon nanotubes, including pre-treatment of nanotubes before composite processing as well as the different approaches that have been followed for their manufacture.

Effective reinforcement in nanotube polymer composites is governed by four main requirements: large aspect ratio, homogeneous dispersion, alignment (depending on the morphology of the composite; e.g. fibres, bulk composites) and interfacial stress transfer [19]. Carbon nanotubes are used for polymer strengthening owing to their large aspect ratio which can reach a value as high as 10000 [14]. However, dispersion of nanotubes is not a straightforward task. Ideally, a uniformly distributed dispersion of independently separated nanotubes in contact with polymer chains must be achieved in order to improve nanotube/matrix adhesion for an effective stress transfer (see Figure 2.6). A poor dispersion causes an uneven distribution of stress concentration points associated to worse mechanical properties. Nanotube alignment within composite material makes mechanical properties anisotropic. Strength and stiffness will be maximised in the parallel direction of the alignment, which is beneficial for composite fibres. However, a random distribution of nanotubes in bulk enhances the total stability of the composite providing a good interfacial bonding between nanotubes and matrix.

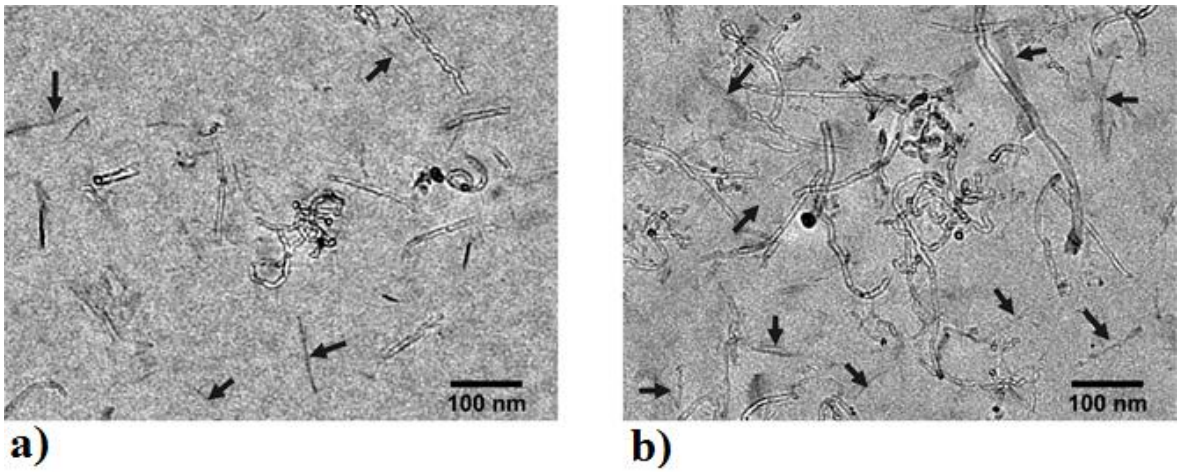

Figure 2.6. TEM images show random distribution of multiwalled carbon nanotubes and alpha-zirconium phosphate nanoplatelets within an epoxy matrix for low (0.2 wt % MWCNT, 1 wt % Zr) (a) and high (0.4 wt % MWCNT, 2 wt % Zr) (b) concentration reproduced from reference [80]. Adapted with permission from American Chemical Society.

All of the aforementioned requirements are futile in the case that external stresses applied to composites are not efficiently transferred to the nanotubes. The force exerted over the composite is linearly proportionate to the stress felt by a nanotube [19]. However after a threshold value of shear stress, nanotube matrix bonding will collapse resulting in

delamination. A crack was induced in order to study fracture mechanisms occurring during composite failure, which are nanotube pull-out, nanotube fracture (usually sword-in-sheath failure) and cracks bridged by nanotubes [81, 135].

Pre-treatment of carbon nanotubes precedes their incorporation within polymer matrices. Many carbonaceous species are found after carbon nanotube synthesis contaminating the sample, for example, fullerenes, graphite, carbon nanoparticles and catalysts. Impurities are removed by several methodologies. Thermal annealing in the presence of oxygen followed by acid treatment is the most common approach, which eliminates any remaining amorphous carbon and catalyst [14]. Purification of carbon nanotubes reduces significantly the total amount of final product, which is one of the reasons why scaling up is not economically viable yet.

The high surface area along with dispersion forces causes nanotube agglomeration. SWNT tend to form aligned hexagonal conformation of ropes uniform in diameter whereas MWNT are usually randomly entangled as bundles [18]. Ultrasound baths or horns have been employed to disperse aggregates of nanotubes, although long-term treatment or high energy output can lead to nanotube shortening with a reduction of their aspect ratio [82].

Chemical surface modification of carbon nanotubes enables an improvement in the processability of polymer composites. Non-covalent physical adsorption or wrapping of conjugated polymers and surfactants can be achieved due to π-interactions between the graphitic sidewalls and the adsorptive, leading to supramolecular adducts. This non-destructive approach preserves the structural integrity as well as the conjugated system on the surface. Therefore, structural properties are not affected by this type of functionalization [83].

The second method is the covalent functionalization known as grafting, which may be divided into two subgroups: “grafting to” and “grafting from” [83]. A polymer chain is attached to the pristine or pre-functionalized nanotube surface by radical or carbanion addition reactions in the “grafting to” approach such as ester linkage [84, 85], amide linkage [86], radical grafting [87], nucleophilic addition via carbanions [88], azide-cycloaddition [89], polyurethane condensation [90] and sonochemical reactions via ultrasound [91]. Reactivity in carbon nanotubes is higher compared to graphene, caused by the intrinsic strain in the curved lattice of carbon sp^2. The main disadvantage of this method is the low reactivity due to steric impediment at the polymer chains.

Alternatively, polymerisation of monomers through the "grafting from" approach allows an easy growth of high molecular weight polymers covalently attached to nanotubes, which have been previously modified with a wide variety of functional groups and monomers. Several methods fall into these methodologies such as two-step procedure atom transfer radical polymerisation (ATRP) [92], two-step reversible addition-fragmentation chain transfer (RAFT) [93], ring opening polymerisation (ROP) [94], free radical polymerisation [95], cationic/anionic polymerisation [96, 97], condensation [98], reduction/oxidation polymerisation [99], metallocene catalysis [100], electrochemical grafting [101], nitroxide-mediated radical polymerisation [102] and endohedral filling [103]. Low molecular weight of precursors favours a high grafting density on the nanotube surface due to a less steric impediment compared to the "grafting to" approach [83].

In order to maximise mechanical properties in carbon nanotubes composite films, it has been agreed that dispersion of single nanotubes within matrices is essential for good interfacial interactions. Several processing methods have been attempted for the manufacture of such composites, which may be mainly classified into three groups, namely, solution processing, melt blending and in-situ polymerisation. Figure 2.7 shows a schematic diagram of nanotube modification and the different processing methods for the manufacture of polymer composites. Dealing with low viscosity makes the solution-based method as the most commonly extended and versatile method, which have been used for both thermoset and thermoplastic polymers [14]. For example, epoxy resins and carbon nanotubes have been mixed sometimes in a solvent in order to improve their dispersion followed by evaporation and curing.

Solution processing involves three steps: nanotube dispersion in an appropriate solvent, addition of a polymer solution in order to achieve a homogeneous blend and composite casting or precipitation under controlled evaporation. Generally, mechanical agitation of nanotubes and polymer facilitates the dispersion in the solvent, which is provided by magnetic stirring, shear mixing or ultrasound. Mild sonication might be not sufficient to disintegrate nanotubes bundles whereas high power sonication shortens nanotube length [82], reducing their aspect ratio which is not desirable for polymer reinforcement. Therefore, sonication conditions must be optimised in order to obtain a good dispersion of nanotubes with a high aspect ratio.

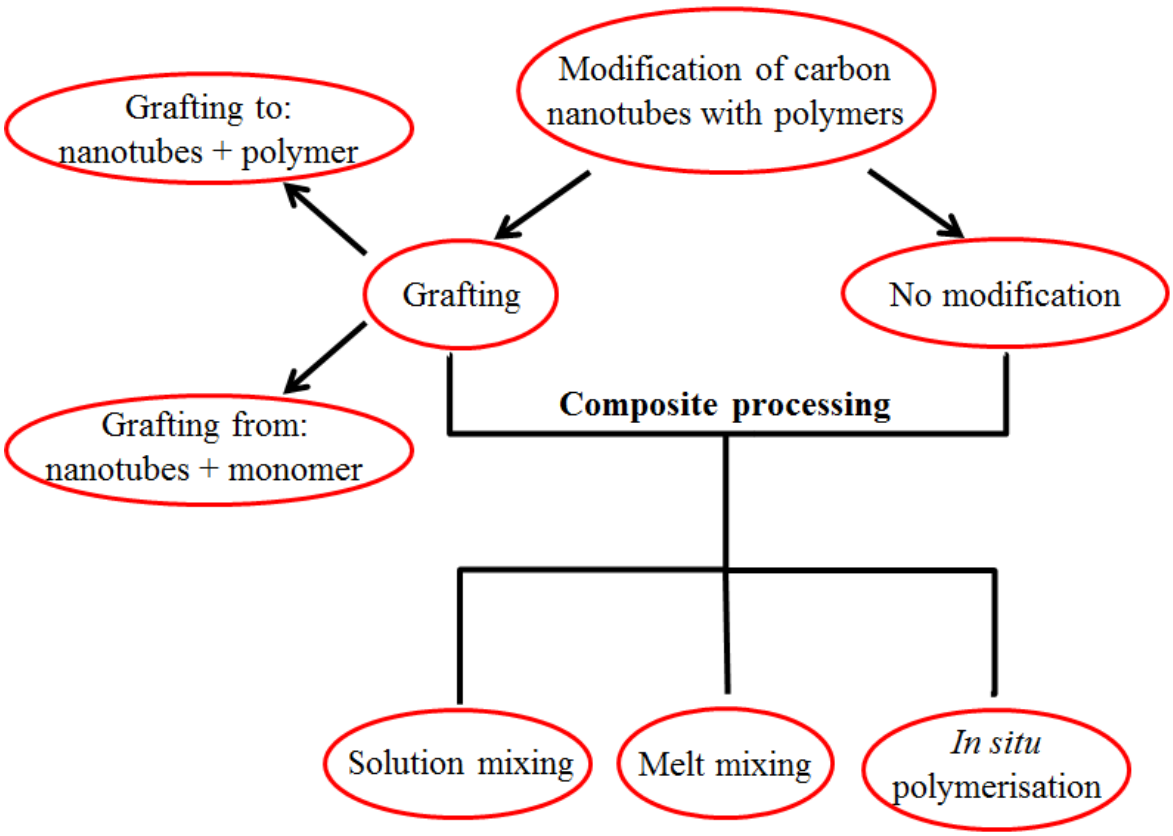

Figure 2.7. Schematic summary of modification of carbon nanotubes with polymers before composite processing adapted from reference [83].

Note that carbon nanotubes are hard to disperse in any solvent, hence the solvent is chosen as a function of the solubility of the polymer. In fact, carbon nanotubes have been successfully dispersed in aqueous solutions of water soluble polymers such as polyvinyl alcohol (PVA) [104]. Sometimes, incorporation of surfactants can help in the dispersion of nanotubes [105, 106]. However, the surfactant remains in the composite film and might deteriorate certain properties [18].

Slow solvent evaporation may lead to nanotube aggregation, resulting in an uneven distribution of carbon agglomerates. Two different approaches have been used to tackle this issue. The evaporation duration can be reduced by the spin coating technique [107], which consists of a device with a rotary disk. Also, the evaporation rate can be controlled by drop-casting onto a hot surface to prevent re-aggregation [18]. Secondly, coagulation in the presence of dispersed nanotubes can be induced after addition of a large amount of a bad solvent (non-solvent). Precipitation of polymer chains entrapping carbon nanotubes occurs instantly [108].

Melt mixing is a suitable technique for thermoplastic polymers that are insoluble in common solvents. A thermoplastic matrix softens when heated above their melting point. Nanotubes are less effectively dispersed due to the high viscosity experienced during manufacture at high loadings, which can affect nanotube aspect ratio and degrade polymer matrices under high shear rate [109]. Therefore, the content of nanotubes is limited to low concentration to optimise viscosity. Fabrication involves shear mixing of the melt containing polymer chains and nanotubes followed by compression moulding, injection moulding, extrusion and blow moulding. High speed processing, compatibility with the established industrial techniques along with recyclability of such composites are among the main advantages of melt blending [19].

In situ polymerisation has been intensively studied for the production of polymer composite materials. It is related to some extent to nanotube grafting and enables the incorporation of high nanotube loadings owing to the low viscosity of the media formed of monomers dispersed in a proper solvent, resulting in considerably homogeneous composites. Polymers can be grafted to modified nanotubes or helically wrapped around nanotubes. It is a quite appropriate method for insoluble or thermally unstable polymers that cannot be processed by other methods [19]. A singular case is epoxy resins, which are in its liquid state and are cured after addition of a catalysing agent or hardener. Nanotubes are usually dispersed by sonication before the hardener is added.

To recapitulate, tensile strength and Young's modulus are enhanced with nanotube loading, dispersion and alignment, at the same time as strain at break, toughness and flexibility are reduced. Solution and in situ polymerisation methods show the best results for processed composites caused by a good interfacial stress transfer. In fact, both dispersion and shear strength are improved after functionalization of nanotubes via polymer grafting. Incorporation of long nanotubes with small diameter results in a better reinforcement for composite films, although their dispersion is much harder. Aligned nanotubes give rise to anisotropic composite materials that are superior for energy absorption applications. Sword and sheath failure mechanism proves a strong nanotube matrix interaction. The main advantage of melt processing is the compatibility with industrial techniques. However, as a downside, poor dispersion and interfacial stress transfer lead to poor reinforcement.

Table 1. Mechanical properties of CNT polymer composites.

Matrix	CNT type	Max CNT content (%)	Method	Mechanical properties (% increase)	Reference
Epoxy	SWNT	2	Ultrasound dispersion & Polymerisation	VH 250	[110]
Epoxy	MWNT	1	Mixing	E 100	[111]
Epoxy	MWNT	4	Mixing	TS 150, E 300	[112]
Epoxy	MWNT	3	Solution mixing	TS 50, E 100	[113]
Epoxy	MA-MWNT	1	Grafting & Solution mixing	TS 45, E 100	[114]
Kevlar	MWNT	4	Yarn soaking	TS 26, E 80	[115]
LDPE	MWNT	10	Melt mixing	TS 56, E 89	[116]
LDPE	MWNT	3	Ball milling	TS 150, E 30	[117]
Nylon 6	MWNT	1	Melt mixing	TS 124, E 71, H 67	[118]
Nylon 6	PA-SWNT	1.5	Grafting & Polymerisation	E 127	[119]
Nylon 6	MWNT	2	Melt mixing	TS 162, E 214	[120]
Nylon 6	PA-SWNT	0.5	Grafting & Polymerisation	TS 150, E 250	[121]

Table 1. (Continued)

Matrix	CNT type	Max CNT content (%)	Method	Mechanical properties (% increase)	Reference
Nylon 6	MWNT	1	Melt extrusion	TS 164, E 220	[122]
UHMWPE	MWNT	5	Gel-spinning	TS 19, E 12	[123]
PAN	MWNT	5	Electrospinning	TS 75, E 72	[124]
PAN	MWNT	5	Solution mixing & Spinning	TS 74, E 40	[125]
PANI	SWNT	0.76	Solution mixing & Spinning	TS 50, E 110	[126]
PBO	SWNT	10	Polymerisation & Spinning	TS 60, E 20	[127]
PC	MWNT	0.5	Solution mixing	TS 47, E 46	[128]
PCL	SWNT	0.2	Solution mixing & Melt drawing	E 562	[129]
PEI	SWNT	50	Layer-by-layer deposition & Crosslinking	TS 2700, E 3000	[130]
PEO	Ph-MWNT	1.5	Grafting & Solution mixing	TS 442, E 228	[131]
PET	NH_2-MWNT	2	Grafting & Polymerisation	TS 350, E 290	[132]
PI	MWNT	0.38	Grafting & Solution mixing	TS 60, E 50	[133]

Table 1. (Continued)

Matrix	CNT type	Max CNT content (%)	Method	Mechanical properties (% increase)	Reference
PI	C18-MWNT	7	Grafting & Solution mixing	TS 46, E 250	[134]
PMMA	PMMA-MWNT	20	Grafting & Solution mixing	E' 1100	[135]
PMMA	PMMA-MWNT	5	Grafting & Solution mixing	TS 360, E 94	[136]
PMMA	C8-MWNT	5	Electrospinning	TS 160	[137]
PMMA	SWNT	8	Solution & melt mixing, melt spinning	E 100	[138]
PP	SWNT	0.75	Shear mixing	TS 15, E 39	[139]
PP	SWNT	1	Solution mixing & Spinning	TS 45, E 150	[140]
PP	MWNT	1	Melt spinning	TS 400, E 270	[141]
PP	SWNT	10	Melt mixing polymerisation	TS 173, E 133	[142]
PS	Kevlar-MWNT	0.5	Grafting & Solution mixing	TS 20, E 11	[143]
PS	CPP-MWNT	0.5	Grafting & Solution mixing	TS 100, E 100	[144]
PU	Ester-SWNT	3	Grafting & Electrospinning	TS 104, E 250	[145]

Table 1. (Continued)

Matrix	CNT type	Max CNT content (%)	Method	Mechanical properties (% increase)	Reference
PU	NH_2-MWNT	4	Grafting & Solution mixing	TS 270, E 70	[146]
PU	MWNT	4	Polymerisation	TS 40, E 130	[147]
PU	APES-MWNT	0.5	Grafting & Solution mixing	TS 60, E 160	[148]
PU	PU-SWNT	0.7	Grafting & Polymerisation	TS 23, E 178	[149]
PVA	MWNT	1	Solution mixing	E 78, H 56	[150]
PVA	MWNT	1	Solution mixing	TS 330, E 267	[151]
PVA	Col-SWNT	4	Solution mixing	TS 300, E 260	[152]
PVA	MWNT	0.2	Solution mixing	TS 100, E 200	[153]
PVK	MWNT	8	Solution mixing	E 200, H 100	[150]

Abbreviations: Vickers hardness (VH), Young's modulus (E), tensile strength (TS), maleic anhydride (MA), low density polyethylene (LDPE), hardness (H), nylon (PA), ultra-high molecular weight polyethylene (UHMWPE), polyacrylonitrile (PAN), polyaniline (PANI), polybenzobisoxazole (PBO), polycarbonate (PC), polycaprolactone (PCL), polyethylenimine (PEI), polyethylene oxide (PEO), phenoxy (Ph-), polyethylene terephthalate (PET), polyimide (PI), polymethylmethacrylate (PMMA), polypropylene (PP), chlorinated polypropylene (CPP), polystyrene (PS), polyurethane (PU), aminopropyl triethoxysilane (APES), polyvinyl alcohol (PVA), collagen (Col-) and poly(9-vinylcarbazole) (PVK).

A collection of carbon nanotube polymer composites have been summarised in Table 1, which is organised in 6 columns: type of polymer matrix, type of CNT (single or multi-walled), maximum content of CNT, processing method, increase of mechanical properties compared to the neat polymer matrix and reference. Due to the large amount of literature available, only a few papers have been selected according to the enhancement in their mechanical properties. It is observed that polymer grafting before solution mixing improves the dispersion of nanotubes at the same time that enables a better stress transfer within the composite. Furthermore, composites processed by the in situ polymerisation method show enhanced stiffness as a consequence of proper mixing of the initial components. Large interfacial shear stress is transferred as a result of effective polymer nanotubes interactions.

2.2.2 Titanate nanotubes/nanofibres polymer composites

Reinforcement of composite materials based on elongated titanate nanotubes or nanofibres provide additional functionalities at the same time as structural enhancement, due to the impressive mechanical properties of titania with Young's modulus and tensile strength of 230 GPa and 680 MPa respectively [40]. A wide range of polymer matrices have been used in the manufacture of titanate composite materials depending on potential applications. For example, alkyl siloxane modified TiNT were incorporated to polystyrene matrix via solution casting in order to increase their hydrophobicity [40]. An effective dispersion of TiNT was achieved within the matrix, resulting in an improvement of both Young's modulus and tensile strength at low nanotube loading relative to neat polymer. Polystyrene matrix has been used for intumescent flame retardant materials. Thermal stability and burning behaviour were significantly improved in a composite made of pentaerythritol, microencapsulated ammonium polyphosphate and polystyrene after addition of 0.1 wt % of cerium-doped titanate nanotubes (Ce-TiNT), which leads to residual char more compact and stronger [154].

Tribological behaviour in composite materials based on polyurethane has been investigated by incorporation of elongated titanate nanostructures. Friction coefficient was considerably reduced after a PU matrix was filled with 1 wt % of unmodified and hexamethylene diisocyanate (HDI) modified TiNT [49]. The wear life was improved by nearly 200 % and 250 % in composites reinforced with TiNT and HDI-TiNT, respectively. It is believed that

grafting of HDI onto TiNT enhances the interfacial interaction and dispersion of such nanotubes within the matrix, which contributes to a reduction in friction and an improvement in wear resistance. Mechanical and tribological properties were studied in blends of polyurethane and high molecular weight hydroxyl-terminated polydimethylsiloxane (HTPDMS) reinforced with potassium titanate nanowhiskers (PTW) [155]. Tensile strength and friction coefficient increased with higher content of PTW while wear rate decreased in the composite film loaded with PTW 7 wt % under dry conditions. A reduction in friction coefficient occurred as the sliding speed was increased under water lubrication in every sample, thus it is advisable to reinforce polyurethane under aqueous environment. Mechanical behaviour along with wear resistance and thermal deformation were enhanced in polytetrafluoroethylene (PTFE) composites reinforced with large and small size surface modified PTW, which makes such composite an ideal candidate to be used under a strong alkaline environment [156].

Conductive polymers such as polyaniline (PANI) have been loaded with 1-dimensional titanate nanostructures. Synthesis of PANI was carried out on the surface of TiNT by chemical oxidative polymerisation of aniline [157]. The presence of the triblock copolymer Pluronic 123 as a structure-directing agent assisted polymerisation of aniline by micellization, giving rise to an extremely stable polymer due to strong hydrogen bonds between PANI and TiNT. A composite material with improved thermal stability and high UV-visible absorption has been also produced by addition of long titanate nanofibres (TiNF) via aniline in situ polymerisation in anhydrous ethanol [158]. Such combination of electroconductive polymer and proton-conductive nanotubes might be used in sensors, ion-exchange materials, solar cells or batteries.

Similar conductive composites have been prepared by polypyrrole (PPy) coating of titanate nanotubes and nanofibres, which exhibit conductive properties along with chemical and environmental stability. PPy/TiNF composites have been prepared via chemical oxidative polymerisation with [159] or without [160] the presence of the surfactant cetyltrimethylammonium bromide (CTAB) assisting the reaction. Both composites showed an enhanced thermal stability and chemical integrity due to hydrogen bonds between matrix and nanofibres as well as π-π interaction in polymer chains [159]. Composites oxidise by $FeCl_3$ show higher conductivity compared to APS oxidised PPy counterparts probably due to the lower redox potential of $FeCl_3$ [160]. PPy/TiNT coatings were electrodeposited onto stainless steel, decreasing dramatically corrosion rates to electrodeposited neat PPy [35]. Electrostatic affinity of pyrrole towards the surface of

TiNT originated nucleation centres to polymerise thin coatings of PPy. Such strong interfacial interactions are responsible for the 53 % increase of hardness for the composite loaded with 10 wt %.

A slightly different approach has been made to reinforce dental resin based cements. TiNT were annealed and modified with methacrylic acid (MMA) before their addition to cement, which was cured by free radical polymerisation technique [161]. Strong interfacial interactions due to functionalization were confirmed by an increase in fracture toughness (73 %), flexural strength (42 %) and flexural modulus (56 %) when 1 wt % of the modified MMA/titania nanotubes were added to the resin. Thermal stability and electric conductivity were enhanced in comparable hybrid PMMA/sodium titanate nanofibres composites prepared by in situ chemical oxidative polymerisation in the presence of CTAB as surfactant [162].

The relationship by which high aspect ratio fillers enhance mechanical properties in composite materials is supported by melt mixed polyamide 6 (PA6) composites filled with 5 wt % of the following titania nanostructures: microparticles (m-TiO_2), nanoparticles (n-TiO_2) and TiNT. It has been reported an enhancement in the elastic modulus in all composites compared to neat polymer. Modulus increased 35 % in PA6/TiNT, 14 % in PA6/n-TiO_2 and 9 % in PA6/m-TiO_2, which coincides with worse particle dispersion in reverse order: microparticles < nanoparticles < nanotubes [163]. It is thought that the lack of free hydroxyl groups on the nanotube surface will improve nanotubes dispersion. Therefore, 3-aminopropyltriethoxysilane (APTES) was grafted onto TiNT [164] in order to be incorporated to a nylon 11 matrix. It was found that functionalization was favoured in aqueous ethanol medium for TiNT with low content of sodium, which have higher density of hydroxyl groups available and can be more efficiently grafted.

Proton conductive Nafion/titanates composites have presented a better performance in membranes for fuel cells. Although proton conductivity can decrease with the nanotube content caused by nano-channels blocking, a lower permeability provides such membranes with a higher selectivity, and therefore they can outperform pure Nafion [165]. It was found that proton conductivity in Nafion/TiNT composites at high temperatures is much higher than in clean membranes, although mechanical strength is a bit lower for composites [166]. Figure 2.8 shows titanate nanotubes well dispersed within the Nafion matrix. Incorporation of sulfonic acid functionalised TINT was studied in composites based on an alternative perfluorosulfonic acid (PFSA) matrix similar to Nafion with the commercial name of Fumion, which enhanced its conductivity compared to Nafion

ionomer [167]. Amino-tailored TiNT have been also introduced to improve their compatibility with the polymeric resin via 3-aminopropyltrimethylsiloxane (APTS) grafting [168], followed by solution casting process.

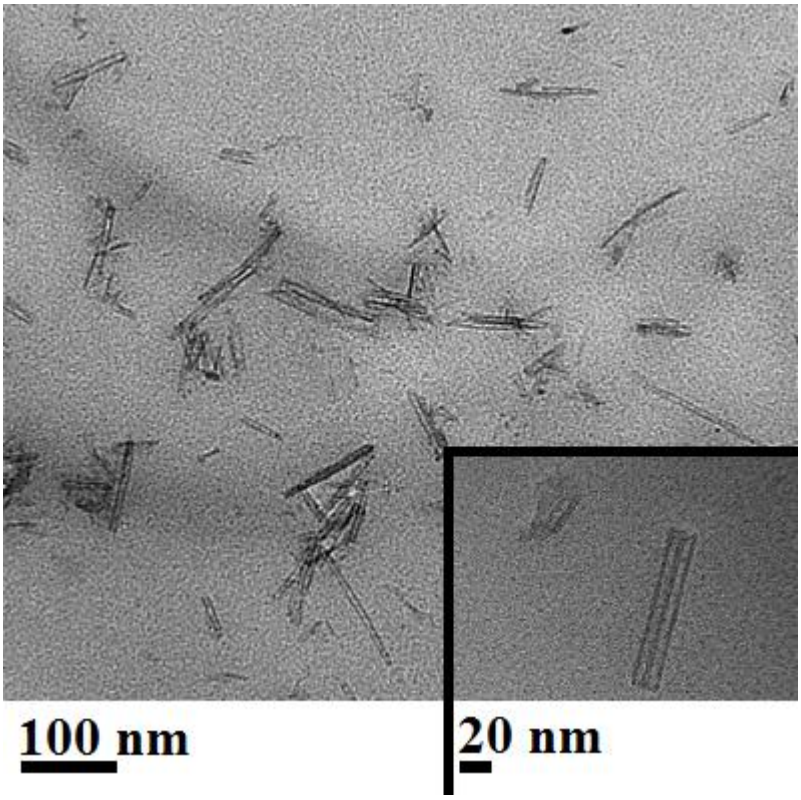

Figure 2.8. TEM image shows Nafion with a content of TiNT 5 wt % reproduced from reference [166]. The bottom right inset TEM micrograph shows hollow-like structure of titanate nanotubes dispersed in Nafion.

The cationic polymer chitosan (CS) has been used in fuel cells as a promising material for proton exchange membranes. Methanol permeability and proton conductivity in CS/TiNT composites produced by solution casting were reduced [169]. However, mechanical strength was substantially improved, hence the utilization of such composite membranes as an alternative for Nafion. A denser polymer chain packing was achieved in CS/TINT composites by nanotube phosphorylation prior to casting [170]. It is believed that phosphoric acid facilitated proton transfer in the membrane, which yielded a much better performance compared to neat CS membrane and Nafion.

Titanate nanostructures can be cast into membranes to be used as a filter, absorber or catalyst. For example, TiNF were treated with the surfactant plutonic 127 in order to

oxidise organic compounds retained in the membrane filter [171]. It has been mentioned before the affinity of TiNT towards cationic compounds, which can be applied to remove chemicals from aqueous media. The cationic dye thionine was adsorbed and electrochemically polymerised via a substrate-less approach onto Co-TiNT synthesised by the alkaline hydrothermal method [172]. "Sandwich" multi-layered polymer catalyst composites made of precious metal decorated TINT (Ag, Au) were fabricated via layer-by-layer deposition technique. The substrate made of quartz or silicon wafers was pre-coated with a thin layer of PEI, after which nanotubes were confined between layers of poly (diallyldimethylammoniumchloride) (PDDA) [173]. This approach might be applied for the fabrication of thin composite films in the field of photocatalysis, solar cells or self-cleaning surfaces.

Several methods have been used for the manufacture of TiNT composite films for some other engineering applications. By way of illustration, modified barium strontium titanate nanofibres (BST) with a stoichiometric formula $Ba_{0.2}Sr_{0.8}TiO_3$ were dispersed in a poly (vinylidenefluoride) matrix (PVDF) [174]. It was reported the highest breakdown strength and energy storage properties to date, outperforming the polypropylene composite counterparts that are already used as capacitors. Because of ion-exchange properties, TiNT were dispersed in N-methyl-pyrrolidone (NMP) and blended with acetylene black prior to mixing with PVDF matrix for electrodes in lithium batteries produced by the doctor blade technique [175, 176]. They exhibited a high rate capability, a large charge/discharge capacity and enhanced cycling stability. Nanostructured inorganic materials have been used recently for bioengineering purposes. A thin layer of biocompatible TiNT was homogenously spin-coated over a biopolymer scaffold composed of poly(propylene fumarate)/diethyl fumarate blend (PPF:DEF, 7:3), which showed an enhanced cell growth and proliferation compared to the uncoated films [177].

2.2.3 Aluminosilicate nanotube polymer composites

The number of scientific publications on polymer nanocomposites containing halloysite nanotubes has experienced a sudden increase in the last decade. The experimental elastic modulus of HNT equals 140 GPa, which differs from the theoretical value between 230 and 340 GPa [178]. However, this feature could yield high performance polymer composites providing an optimised interfacial stress transfer within the polymeric matrix. It was previously mentioned that inner and outer surfaces in HNT are chemically different,

hence the fact that selective covalent or non-covalent functionalization can be applied to change polarity/hydrophobicity, shield hydroxyl groups or attach new functional groups in order to improve compatibility with polymer matrices. Figure 2.9 shows three examples of polymer composites filled with halloysite nanotubes obtained with various processing techniques: electrospinning (Figure 2.9a), casting (Figure 2.9b) and injection moulding (Figure 2.9c).

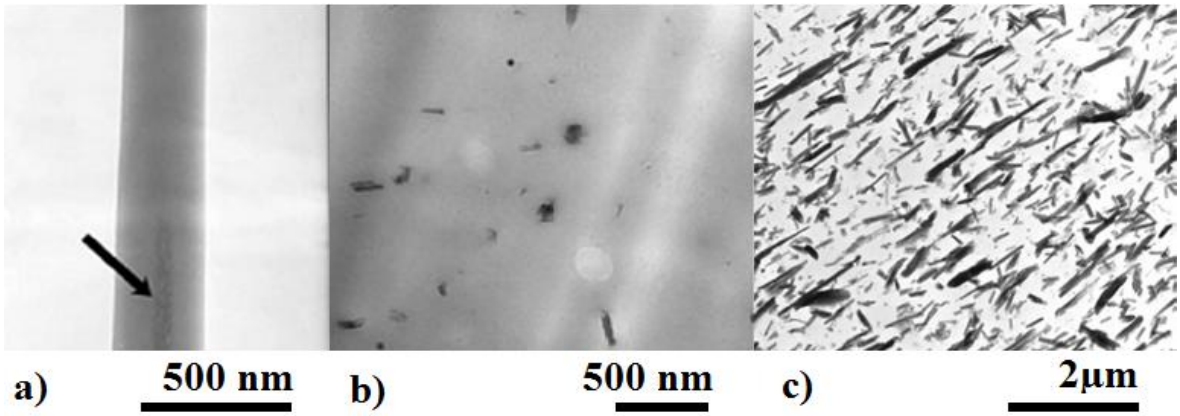

Figure 2.9. TEM micrograph showing an independent halloysite nanotube aligned with the electrospinning direction in poly(lactic-co-glycolic acid) (PLGA) matrix with a content of 5 wt % (a). TEM image illustrates randomly oriented halloysite nanotubes in fluoroelastomers (FKM) matrix for halloysite content of 5 phr (parts per hundred parts of resin) (b). TEM micrograph shows high orientation of halloysite dispersed in polylactide (PLA) injection moulded composite with a content of 30 phr (c). Images adapted from reference [178].

The solution processing method is the most commonly extended procedure to manufacture HNT polymer composites. HNT are previously dispersed in a suitable solvent and then cast onto moulds. Although halloysite can be easily suspended in aqueous solutions by mechanical stirring, use of ultrasound is sometimes required in various solvents. However, a good distribution of nanotubes can reassemble during drying, giving rise to stress concentration points that negatively affect mechanical and tribological properties (see Figure 2.10). Polyvinyl alcohol (PVA) can be mixed with HNT in solution with several polar solvents to obtain composite films. Coagulation is induced by addition of an excess of acetone resulting in precipitation, which hinders nanotube re-aggregation [179].

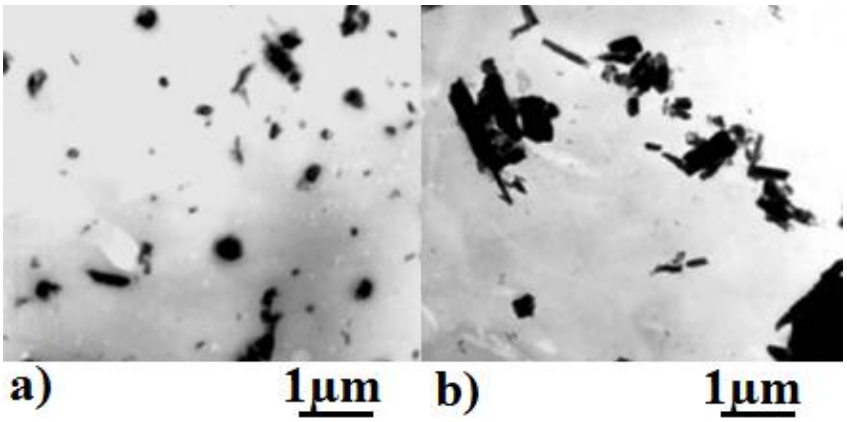

Figure 2.10. TEM images show halloysite nanotubes dispersed in polyvinyl alcohol matrix. Halloysite was induced to coagulate, giving rise to a uniform dispersion within the composite (a). Nanotubes tend to reassemble as the solvent evaporate for cast films (b). Micrographs adapted from reference [179].

Chitosan (CS) has been blended with HNT to produce composite membranes because of good interactions between hydroxyl and amine groups in the polymer chain and the hydroxyl groups at the edge and on the surface of the nanotubes, resulting in hydrogen bonding. Therefore, stress can be transferred to the reinforcing phase. Incorporation of only 5 wt % of HNT improved Young's modulus and tensile strength by 21 % and 34 %, respectively [180]. Mechanical properties were also enhanced in blends with a composition of PVA:CS 80:20 after reinforcement with 0.5 wt % of HNT. Further addition of nanofiller resulted in nanotube agglomeration, effect which is more prominent for high filler loadings [180, 181]. Aqueous suspensions of CS containing HNT were cast via the freeze-drying method, which consists of water sublimation at low temperature under reduced pressure to produce highly porous composite films. A better compressive behaviour and thermal stability coupled with biocompatibility was found in such materials used in tissue engineering as scaffolds and drugs carriers [182].

Halloysite nanotubes have been modified to improve adhesion with both pure PVA and their blends. For instance, mechanical properties were enhanced after HNT were treated with sulphuric acid for less than 2 hours. Long term treatment led to dissolution of Al^{+3}, worsening interfacial adhesion and total strength in the composite [183]. A different approach was made to improve mechanical properties in old corrugated container paper. A remarkably increase in tensile, tear and burst index was achieved for blends containing PVA/SBR/CMC filled with titanate modified halloysite used for surface coating reinforcement [184]. A third alternative method consists of PVA/HNT composites

crosslinked by addition of glutaraldehyde (GA). Aldehyde groups react with the hydroxyl groups in PVA via condensation assisted by halloysite nanotubes, which caused orientation and crystallisation of polymer chains, leading to an enhancement of 80 % in tensile strength for composites filled with 7.5 wt % of HNT [185].

Polyethylene glycol (PEG) [186] and its heavier molecular weight analogue polyethylene oxide (PEO) [187] can be mixed with HNT and cast by the solution processing method too. It has been demonstrated that PEO chains can be nano-confined within halloysite due to their ability to interact with the hydroxyl-rich inner surface of the nanotubes. Water molecules act as a bridge linking polymer chains and nanotubes via hydrogen bonding [187]. PEG composites filled with HNT 30 wt % exhibited a higher elastic modulus [186].

It has been demonstrated a significant enhancement in mechanical properties in xSBR rubber composites reinforced with HNT via mixing and co-coagulation process (see Figure 2.11) [188]. Such process consists of the following: (i) mixing fillers with water, (ii) adding the polymer while stirring, (iii) coagulating the filled dispersion and (iv) drying followed by compression moulding [189]. Remarkable reinforcing effects were associated with strong hydrogen bonding after vulcanization of the xSBR rubber filled with HNT, which yield an increase in Young's modulus, tensile strength and hardness of 265 %, 53 % and 45 % respectively in composites loaded with HNT 30 wt % [188].

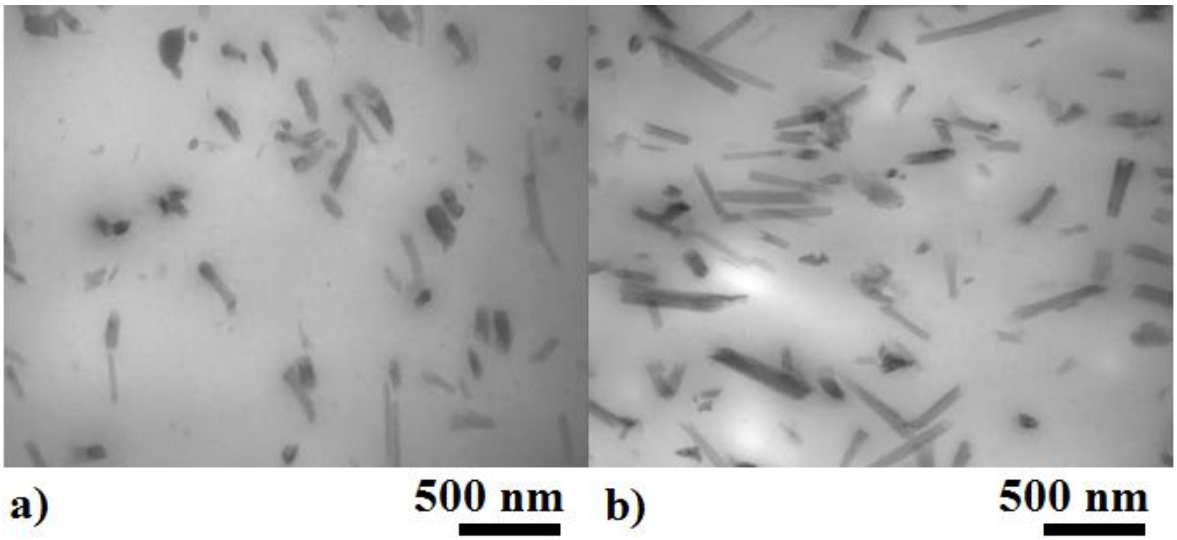

Figure 2.11. TEM images illustrate randomly oriented halloysite nanotubes in a carboxylated styrene-butadiene rubber matrix (x-SBR) for low (a) and high (b) concentration of nanotubes (5 and 20 wt% respectively). Photographs adapted from reference [188].

A peculiar approach has been recently made in the preparation of polyurethane (PU) hybrid composites with MWCNT and HNT. Acid treated multi-walled carbon nanotubes were grafted onto silane-modified halloysite and incorporated to a PU matrix via hot solution mixing and casting [190]. Stiffer and tougher composites materials were prepared arising from optimum stress transfer to the elongated nanostructures via hydrogen bonding. Addition of only 1 wt % of grafted nanotubes increased tensile strength, Young's modulus and elongation at break by 140 %, 35 % and 68 % respectively.

Melt processing technique is an alternative method for thermoplastic matrices as it was previously mentioned in the section on polymer/carbon nanotubes composites. The main downsides of melt mixing are polymer degradation due to high temperature, use of strong shear force due to high viscosity which leads to poor dispersion of nanotubes and therefore the content of fillers is limited to low loadings. On the other hand, its simplicity and compatibility with standard processing techniques established in industry make this method a realistic candidate to scale-up polymer composite manufacture.

For example, mechanical properties were significantly enhanced in composites based on polyamide 6 (PA 6) matrices with a more pronounced effect at low nanofiller fractions without any loss of elongation at break. Such effect is even more noticeable above the glass transition temperature [191, 192]. The incorporation of HNT was investigated in order to improve the fire retardant behaviour of PA 6 composites. For such systems, a relatively high concentration of halloysite over 15 wt % is needed to achieve the best degree of flame inhibition [193]. Besides, hydrophobicity in HNT was maximised after silane groups were grafted onto halloysite to better both interfacial bonding and dispersion within PA 6 matrix [194]. Thermal and mechanical behaviour in such composites were improved at low modified-nanotube content.

Extrusion processing is one of the most extended manufacture methods in melt mixing technique. Unmodified and quaternary ammonium salt treated halloysite were dispersed within PP [54] and PLA [195]. Incorporation of both nanotubes enhanced thermal, tensile, bending and impact properties although treated halloysite was better distributed within the matrix and hence the higher strength and stiffness in their composites at very low nanofiller concentration (see Figure 2.12), in which 6 wt % appears to be optimum [54, 195]. Thermal stability and flame retardant properties were also investigated in both neat and silane modified halloysite incorporated to PP matrix. It is speculated that a better dispersion of modified halloysite along with the content of iron in their structure leads to an enhancement owing to an entrapment mechanism while thermal decomposition [196].

The interfacial electron donor modifier 2,5-bis (2-benzoxazolyl) thiophene (BBT) was used in the preparation of PP/HNT composites. It was found that formation of BBT fibrils in the presence of HNT improved interactions with the polymer matrix as well as crystallinity of PP, hence the higher tensile and flexural behaviour [197].

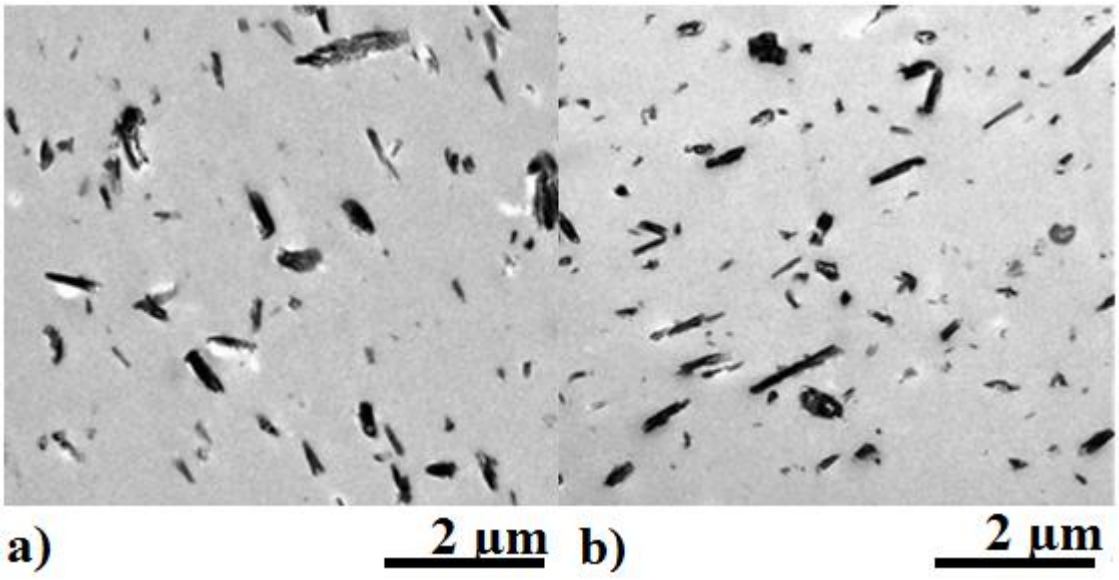

Figure 2.12. TEM images illustrate PLA nanocomposites prepared by melt extrusion reinforced with neat halloysite nanotubes 4 wt % (a) and modified halloysite nanotubes 4 wt % (b). Images adapted from reference [195].

Nanofillers and monomers are better dispersed in solvents before in situ polymerisation occurs in comparison to solution mixing. Interfacial reactions can occur on the surface of halloysite between silanol/aluminol functional groups, epoxy resins and hardeners during polymerisation [55]. Nanotubes can be covalently attached to the matrix and therefore quite strong hybrid materials are created. Unmodified HNT improved unexpectedly impact strength by 400% as well as flexural modulus and tensile modulus mainly due to nanotube bridging, mechanism by which energy is dissipated and at the same time crack propagation is hindered within the composite [198].

Mechanical and tribological properties were also investigated in epoxy composite materials reinforced with PMMA [199] and silane [200] chemically grafted halloysite. Toughness, hardness and wear resistant were enhanced at low content of modified HNT. Unsaturated PS matrix was polymerised in the presence of silane modified halloysite nanotubes in order to study tribological behaviour in such materials, which exhibited lower wear rate and

friction coefficient compared to untreated HNT [201]. The polymer PANI has been also polymerised in situ, giving rise to new potential applications of HNT composite materials where conductivity is involved [202]. The affinity of the monomer aniline towards the nanotube surface facilitates its adsorption after which polymerisation occurs by chemical oxidation.

Several attempts have been made in order to incorporate naturally occurred or synthetic imogolite nanotubes into polymer matrices, being PVA the first polymer reinforced with imogolite [203]. More recently, crosslinked PVA membranes containing a high loading of synthetic imogolite (up to 40 wt %) were prepared by solution casting [204]. Such nanocomposites showed an excellent dispersion of isolated single nanotubes within the polymer matrix for relatively high concentration of fillers (30 wt %). Further addition of imogolite resulted in the formation of bundles of approximately 3-4 nanotubes. Mechanical and optical properties were significantly enhanced in polymer nanohybrids containing imogolite synthesised in situ in the presence of PVA [66]. In situ synthetic method favoured dispersion of imogolite within the matrix reducing significantly the amount of aggregates. Young's modulus in the PVA film loaded with imogolite 16.7 wt % was increased by 57 %.

In order to provide imogolite nanotubes with functional groups in either the inner or the outer surface, different one-step approaches have been reported. Amino-methyl groups were immobilised at the inner surface of imogolite with 15 % of hydroxyl group substitution by direct synthesis of aminomethyltriethoxysilane (AMTES) and tetraethylorthosilicate (TEOS) in the presence of a source of aluminium [205]. Silanol groups were substituted with Si-methyl groups when triethoxymethylsilane (TEMS) was used as a source of silicon. Larger pores and much higher surface area were found in the chemically modified imogolite, which outperformed the unmodified nanotubes for methane adsorption purposes [206]. The precursor glycerol α-monolaurate (MG) was added during the synthesis of imogolite. In this particular case, the aluminium in the outer sheet of gibbsite is complexed by laureate. Modified imogolite exhibited hydrophobic behaviour as it was confirmed by extraction with 1-nonanol [207].

The outer surface of imogolite is populated with aluminol groups that can be functionalised via phosphonic bonding. Dyes based on terthiophenes were attached to imogolite via phosphonic acid moiety which acts as an anchoring group [208]. Optical properties as well as conductivity changed after surface modification. Moreover, hydrophobic alkyl outer surface modified imogolite nanotubes were obtained in aqueous solutions by grafting of

octadecylphosphonic acid [209] and dodecylphosphonic acid [210], which dispersed in hexane and toluene respectively. A similar approach has been made to graft PMMA onto imogolite. Previously, 8-(2-bromo-2-methylpropanoyloxy) octyl phosphate was chemisorbed onto the nanotube surface via metal-oxygen-phosphorous (Al-O-P), from which MMA was subsequently polymerised via atom transfer radical polymerisation (ATRP) [211].

It is believed that such modification will help the dispersion of nanotubes in organic solvent as well as within polymer matrices. In fact, PVC-PMMA-grafted-imogolite composite was prepared by solution mixing. Grafting of PMMA onto nanotubes was prepared following the aforementioned ATRP procedure. It was observed that mechanical properties were inferior at low and room temperature owing to weak interfacial adhesion with the PVC matrix whereas tensile performance was superior at high temperature (90 °C) [212]. Methacrylate groups in the 2-acidphosphoxyethyl methacrylate (P-HEMA) moiety were grafted onto the imogolite outer surface following a similar procedure. In a second step, PMMA hybrid nanocomposite was prepared by free radical polymerisation [213]. The reinforcement effect together with the high transparency of the composite can be associated to the high compatibility between PMMA matrix and PMMA-grafted imogolite.

Easy availability coupled with its low cost have stimulated research on imogolite for some other applications that have been reported in literature such as flocculant/coagulant of latex particles [214], reinforcement in hydrogels [215, 216] and PVA nanocomposite thin membranes cast on polysulfone for removal of hardness in water [217].

2.3 Electrospinning

2.3.1 Introduction

The fabrication of one-dimensional submicron size electrospun fibres has experienced an exceptional progress in the last 20 years especially after Reneker *et al*. [218, 219] focused their efforts on electrospinning due to its potential in the field of nanoscience and nanotechnology. Such versatile technique enables the production of fibres with uniform diameter ranging from several tens of nanometres to a few microns, large surface area to volume ratio and high porosity with small pore size [220]. Therefore, electrospun nanofibres are promising materials for applications in several areas of expertise such as

filtration [221], composite materials [222], tissue scaffolds [223, 224], drug delivery [225], solar cells [226, 227], protective clothing [228, 229], wound dressings [230, 231] and fuel cells [232].

The electrospinning process is based on the uniaxial stretching of a polymer solution that has been previously loaded in a syringe which is in turn connected to a spinneret (a metallic needle). A pump feeds the syringe at a constant and controllable rate and thereafter an electric field is applied between the needle and the metallic collector in order to induce a surface charge on the fluid drop pending from the nozzle [233]. Once this electric field has overcome a threshold value, the electrostatic repulsion forces surmount the surface tension of the polymer solution, causing the liquid to stretch into a fibre. The drop from which the fibre is ejected has a conical shape commonly known as Taylor cone [234]. The charged jet is then exposed to a stretching and whipping journey as the solvent evaporates until is randomly deposited on the collector (see Figure 2.13). When the current stops oscillating the deposition becomes stable, and therefore it can be used to monitor the spinning process [235].

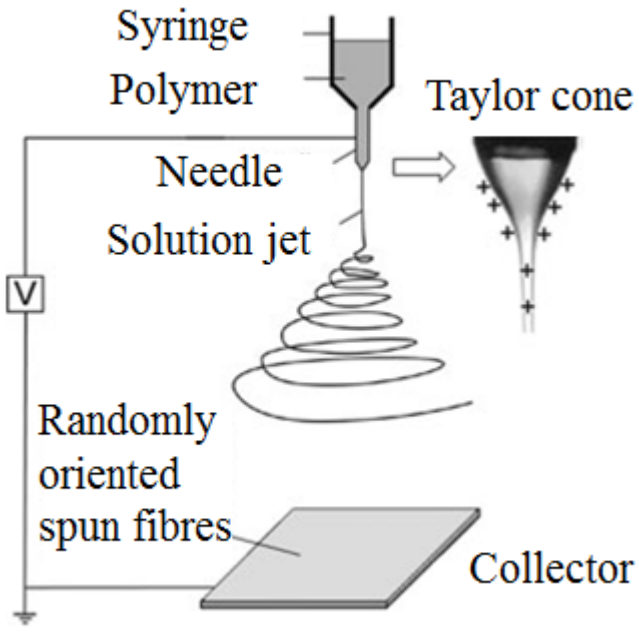

Figure 2.13. Sketch illustrates a basic electrospinning arrangement. The polymer solution is pumped through the syringe with a constant flow rate. Image adapted from reference [233] is not drawn to scale.

The morphology of electrospun fibres not only depends on the intrinsic properties of the polymer solution such as type of polymer, conformation of polymer, viscosity, concentration, elasticity, conductivity, polarity, surface tension and solvent but also other important variables can be controlled such as applied electric field, distance between needle tip and collector, feeding rate, type of collector and diameter of the needle. Ambient parameters must also be taken into account, e.g. humidity and temperature. Solution properties are intimately correlated since a small variation in one parameter generally affects other properties [236].

For instance, solution viscosity is a function of both concentration and polymer molecular weight [237], which in turn is proportional to the electrospun fibre diameter obtaining an average small diameter for lower concentration [238]. However, a minimum viscosity is needed for the formation of electrospun fibres since electrospraying or beaded fibres are produced below a certain value of viscosity (or concentration). It has been reported that chain entanglements play a key role in fibre formation during electrospinning. It has been identified four concentration regimes depending on viscosity, namely dilute, semidilute unentangled, semidilute entangled and concentrated [239]; which results in the following morphologies as a function of concentration: beads (or electrospraying), beaded fibres and bead-free fibres at a minimum of 2.5 entanglements per chain [237]. Further increase in concentration leads to unspinnable solutions due to extremely high viscosity [236]. Despite chain entanglement is commonly used to prognosticate fibre formation, viscosity is a more acceptable variable to take into account due to the fact that not only polymers can be electrospun but also precursors with low molecular weight [238].

Morphology and size in electrospun fibres can be also affected by changes in surface tension. Generally, addition of certain solvents can reduce surface tension in the solution from which fibres are electrospun, hence a decreased presence of beads. A different approach in the production of uniform fibres is to increase the solution charge density by incorporation of an appropriate salt [240, 241] or surfactant [242, 243]. A decrease in surface tension along with an increase in charge density facilitates electrospinning of bead-free fibres at low voltage or field strength, as long as the electric force overcomes surface tension. There is a correlation between electric field and beading. Stability of the solution will be weakened as the applied voltage is increased, which causes a recession of the Taylor cone [233, 236]. Fibres with a larger diameter are produced and eventually both multiple jets and beading take place in the case that voltage is further increased, which might lead to fibres with a decreased diameter.

Solvent evaporation rate during electrospinning is also involved in the morphology of the as-spun fibres. A circular cross-section is usually collected, although flat rectangular cross-section can be also obtained due to a rapid solvent evaporation on the outer part of the fibre followed by further collapse of the solvent molecules entrapped in the fibre [233]. In addition, an optimum distance between tip and collector is essential for the fibre to dry during its journey to the collector since beading has been observed when the distance is too short or too long. Likewise, the solution flow must be pumped at the correct rate. Lower feeding rate usually yields fibres with smaller diameter or even can cause flow recession followed by diameter narrowing, discontinuous fibre or beading if the drawing rate is higher than the flow rate. On the other hand, too high flow rates result in dripping or beading because there is not sufficient time for the fibre to dry.

Ambient conditions can also affect the electrospinning process. For example, an increase in temperature can decrease fibre diameter probably due to lower viscosity, as viscosity in polymer solutions are rather sensitive to a slight variation of temperature. Furthermore, a fluctuation in the relative humidity not only can modify diameter in electrospun fibres due to a slower evaporation rate but also can lead to beading if relative humidity has been increased beyond a critical concentration [244].

The geometry of the collector affects significantly both morphology and properties of the electrospun fibres. A conductive metal plate is normally used as a collector, on which randomly oriented fibres are deposited in the form of non-woven mats. Since microfibres are usually made of non-conductive polymers, the conductive collector helps in the dissipation of residual charges that build up during electrospinning. However, repulsive forces raise at the collector as the nanofibre mat becomes thicker, which might lead to uneven loosely fibre packing or disruption in the process [235, 245]. Several collector arrangements have been developed to obtain highly ordered aligned fibrous meshes such as rotary drum, parallel electrodes and disk collector [238]. Rotational speed must be controlled in rotary drum collectors since high speed improves fibre alignment but the electrospinning jet can be disrupted when velocity is too high [245]. Disk collectors outperform drum collectors in terms of alignment although the amount of fibres collected is limited due to its small area [238].

Highly aligned nanofibres have been produced with a simple pair of static parallel electrodes with a gap or insulating section between them. Such a set-up forces electrospun fibres to traverse the distance between electrodes obtaining aligned arrays of fibres which can be easily transferred to another substrate [238]. However, this arrangement presents

certain limitations such as thickness of the electrospun layer and maximum gap size between electrodes. Nanofibres are unable to support their own weight coupled with electrostatic repulsions induced by other fibres might end in a collapse of the fibre array beyond a maximum gap [246]. A slightly variation was introduced to collect yarns on the edge of two parallel steel blades connected to a negative high voltage followed by dipping in water to compact stray fibres in the yarn [247]. High negative voltage helps deposition of fibres at the tip of the blades although a higher negative voltage is counterproductive beyond a certain limit possibly due to ionization of the air. Most of the times, yarns are twisted to enhance its mechanical strength. A wide range of continuous yarn manufacture methods via electrospinning are summarised in the following review [235].

It is worth noting that external auxiliary electrodes can be added to more sophisticated electrospinning set-ups in order to guide, steer or focus the fibre as it is being electrospun. A prime example of a demonstration that it is possible to narrow down the collection target was studied by Deitzel *et al*. [248]. It was demonstrated that a secondary external positive field (same charge sign as the needle) can indeed diminish the collecting area as well as reduce bending instability during electrospinning drawing. Such multiple field apparatus is able to produce parallel fibres collected on wooden splints that were afterwards twisted into yarns.

Coaxial electrospinning or co-electrospinning technique has evolved from conventional electrospinning in the last decade [249]. Core-shell nanofibres have been manufactured following this novel approach, which allows the encapsulation of target materials within a sheath polymer coating that can be eventually removed by calcination [250]. A core-shell needle attached to a two different compartments which are in turn connected to two separate syringe pumps is needed, although it has been also demonstrated that core-shell polymer nanofibres can be made from an emulsion of two polymer solutions spun from a standard single needle [249]. Coaxial electrospinning opens up the possibility to produce hollow-like structures by selectively removal of the undesired core polymer [251] or, alternatively, if the sheath polymer is used as a template and removed afterwards, one can electrospin polymers that would be difficult to make otherwise [252]. The use of the same solvent in the two solutions usually favours the electrospinning process due to low interfacial tension, although it has been demonstrated that a stable coaxial jet can be successfully achieved with two immiscible liquids [253, 254].

2.3.2 Electrospun polymer blends/composites

Nanostructured metal oxide ceramics have been produced via electrospinning for many fields of applications such as sensors, membranes, catalysts and biomedicine reviewed in the following reference [255]. However, we will focus on the production of electrospun nanofibres which have been synthesised from polymers, blends or in which nanostructured fillers have been incorporated to the matrix prior to electrospinning. Special attention is paid to the cationic polymer chitosan since it has been used in the production of polymer composite films and it will be further discussed in Chapter 5.

Chitosan is the deacetylated derivative of chitin, which is a natural polysaccharide synthesised by a vast number of natural organisms such as crabs, shrimps, fungi and yeast [256, 257]. The name of chitosan is given after the degree of deacetylation is over 50 %. This polymer dissolves in aqueous media at pH < 6 by protonation of the amine group at the C2 position of the D-glucosamine repeat unit, giving rise to a cationic polyelectrolyte. Trifluoroacetic acid and acetic acid are the most commonly used solvents although formic acid and dichloromethane have been used too [257].

It is found that electrospinning of polyelectrolytes is extremely difficult, albeit blends of chitosan and other compatible polymers such as PEO, PVA or PA-6 have been successfully electrospun [258]. Alternatively, different approaches such as incorporation of surfactants [259] or employment of a voltage of opposite polarity [260] have facilitated the electrospinning of chitosan. The utilisation of crosslinkers with chitosan improves both chemical and mechanical stability [261] although some of them are cytotoxic in their unreacted form, encouraging a search for a biocompatible alternative [262].

The structural arrangement taking place during electrospinning affects significantly mechanical performance of the fibres due to local domains with specific molecular orientation and crystallinity, where the amorphous phase confers an elastomeric response and areas with high crystallinity are responsible for the stability of the fibre [245]. It has been found that oriented and stretched polymers do not display necking in the stress-strain curves in contrast to bulk samples. Besides, mechanical properties have been substantially enhanced in highly aligned polymer nanofibrous scaffolds [263] and polymer fibres twisted into yarns [264]. A slightly different approach has been proven to reinforce non-woven electrospun PA-6 bound by PVA, giving rise to void-free polymer-polymer composite material [265].

Mechanical integrity of polymer electrospun nanofibres can be further enhanced by embedding other functional materials such as nanoparticles [266, 267], combination with 2-dimensional planar nanosheets [268, 269] or incorporation of high strength and high aspect ratio elongated materials such as nanorods [270] or nanotubes [271] (see Figure 2.14). Carbon nanotubes are the most commonly used elongated nanofillers to improve mechanical and electrical properties in electrospun composite nanofibres [272, 273]. It is worth noting that properties in polymer solutions might change after addition of nanofillers which in turn can affect the morphology of the as-spun nanofibres. For instance, a variation of conductivity results in narrower fibres [274] or larger diameter [271]. In addition, further increase of nanofiller beyond a threshold concentration leads to aggregation, worsening mechanical stability since agglomerates act as stress concentration points.

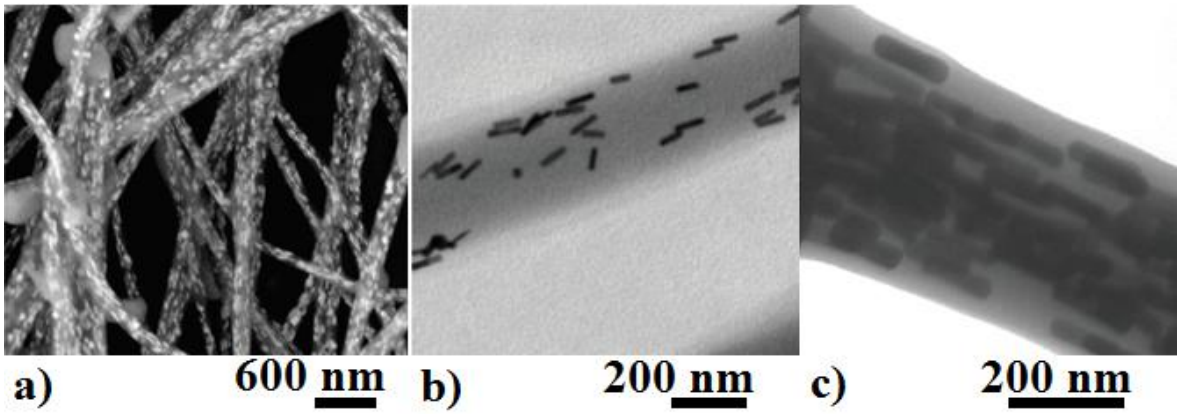

Figure 2.14. Electron microscopy images illustrate gold nanorods (AuNR) distributed within electrospun PVA nanofibres. SEM micrograph of a nanofiber mat (a), TEM micrographs of PVA nanofibres filled with aligned AuNR at low (b) and high (c) concentration respectively; adapted from reference [270].

A representative review of electrospun polymer composite materials is summarised in Table 2, which is divided in 6 columns as follows: polymer matrix, type of filler, filler content, type of solvent, enhancement of properties and reference number. Only some relevant papers published in the last 8 years have been selected as examples due to the increasing literature available on electrospinning of polymer composites.

Table 2. Electrospun polymer composite nanofibres.

Matrix	Filler	Content %	Solvent	Properties (% enhancement)	Reference
PEO	MWCNT	1	EtOH/water	TS 240	[222]
PS/PEO	AgNP	2.2	AcOH	TS 40, E 440	[266]
PVA/CS	AgNP	1	AcOH	Improved antibacterial activity	[267]
PVA	GO	0.2	Water	TS 50 times higher	[268]
PVA	GO	1	Water	TS 21	[269]
PVA	AuNR	200 nM	Water	Tunable optical properties	[270]
PLGA	HNT/CNT	5	THF/DMF	HNT: TS 20, E 40; CNT: TS 22, E 41	[271]
PU	MWCNT	3	THF/DMF	TS 19, E 17	[272]
PVA/CS	MWCNT	1	AcOH	TS 27, E 133	[273]
Silk	MWCNT	2	FA	E 140	[274]
PA 66	MWCNT	7.5	FA/DCM	Mechanical enhancement by tensile testing and nanoindentation	[275]
PLGA	HNT	1	THF/DMF	TS 57, E 19	[276]

Table 2. Continued.

Matrix	Filler	Content %	Solvent	Properties (% enhancement)	Reference
PVA	MWCNT	3	Water	TS 40	[277]
PVA/CS	MMT	5	Water	TS ~ 30	[278]
PEO	Cellulose NC	20	Water	TS 180, E 152	[279]
PMMA in PCL	Al_2O_3	10	DMF	TS 76, E 49	[280]
PCL	HAp	30	DMF/$CHCl_3$	TS 30, E 10	[281]
PCL	HAp/TCP	30	DCM/DMF	TS 12, E 14	[282]
PLA	HNT	3	DCM/DMF	Enhanced thermal properties	[283]
PU	MWCNT	1	DMF/MEK	TS 64, E 32	[284]
PVA	ND	2	Water	TS 89, E 155	[285]
UHMWPE	MWCNT	0.8	o-DCB	TS and E ~100 times higher	[286]
PEO	MWCNT	20	$CHCl_3$	E 5 times higher, enhanced conductivity	[287]
PVA	CB	8	Water	E 100, worse TS	[288]

Table 2. Continued.

Matrix	Filler	Content %	Solvent	Properties (% enhancement)	Reference
PVA	LDH	5	Water	TS ~ 200	[289]
PVA	MWCNT	1	Water	TS 60	[290]
PANI/PEO	MWCNT	5	Water	E 190	[291]
PEO	MWCNT	1	Water	E 200, worse TS	[292]
PAN	MWCNT	5	DMF	TS 75, E 72	[124]

Abbreviations: polyethylene oxide (PEO), ethanol (EtOH), tensile strength (TS), polystyrene (PS), silver nanoparticles (AgNP), acetic acid (AcOH), Young's modulus (E,) polyvinyl alcohol (PVA), graphene oxide (GO), gold nanorods (AuNR), poly(lactic-co-glycolic acid) (PLGA), halloysite nanotubes (HNT), tetrahydrofuran (THF), dimethylformamide (DMF), polyurethane (PU), formic acid (FA), polyamide 66 (PA 66), dichloromethane (DCM), nanocrystals (NC), polymethylmethacrylate (PMMA), polycaprolactone (PCL), hydroxyapatite (Hap), tricalcium phosphate (TCP), methyl ethyl ketone (MEK), nanodiamonds (ND), ultra-high molecular weight polyethylene (UHMWPE), orthodichlorobenzene (o-DCB), carbon black nanoparticles (CB), layered double hydroxide (LDH), polyaniline (PANI), Polyacrylonitrile (PAN).

2.4 Mechanical and tribological characterisation

2.4.1 Tensile testing

Tensile tests are performed to characterise materials for engineering applications since their strength is a fundamental concern, be it the stress necessary to cause permanent plastic deformation or the maximum strength that a material can withstand [293]. Tensile properties extracted from such tests can be used to predict the behaviour of materials under real conditions. A normalised specimen is tightly gripped on to the machine, which in turn is subjected to tension forces while it is being pulled so that deformation or failure occurs. Tensile strength and elongation at break are directly measured whereas Young's modulus and Poisson's ratio are determined from the load-displacement curve or its equivalent strain-stress curve, which is independent of the specimen dimensions (see Figure 2.15). Nominal stress is defined as the tensile force divided by the initial cross-sectional area of the gauge section and nominal strain is defined as the change in gauge length divided by the initial length.

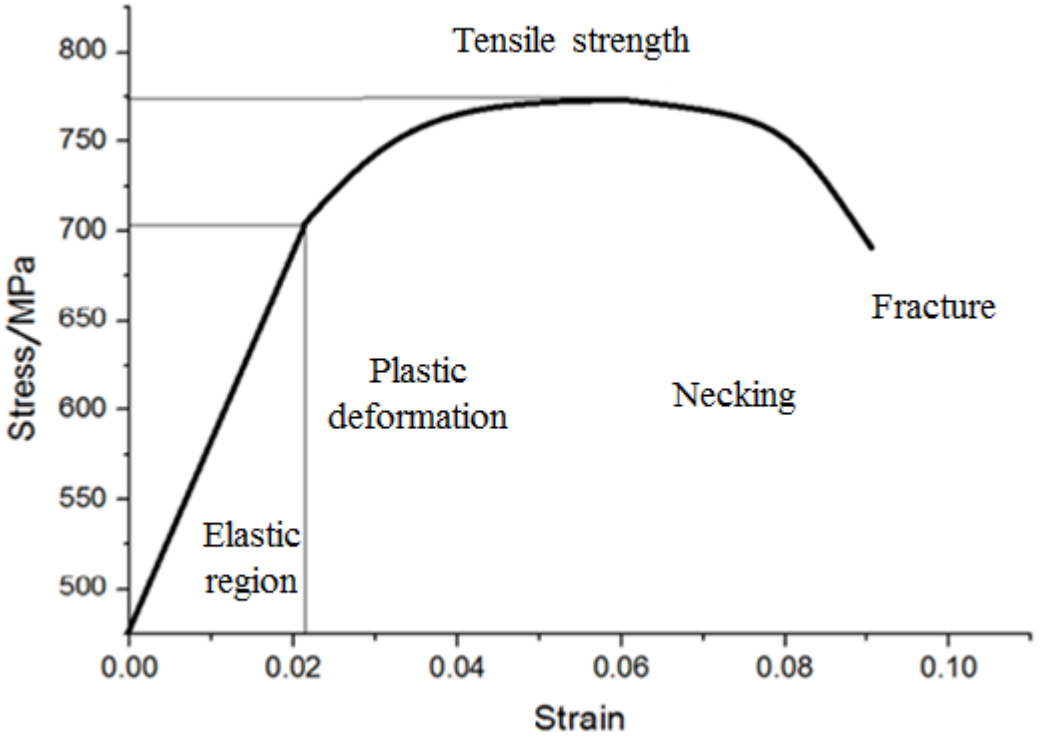

Figure 2.15. Stress-strain diagram. The elastic linear region obeys the Hooke's law, after which irreversible plastic deformation occurs. The tensile strength is the maximum on curve. Ductile materials experience necking until failure.

Elastic deformation is produced when the material undergoes small stresses so that bonds between atoms are stretched. When the stress is removed, the sample returns to its original shape. This initial section of the stress-strain curve is usually linear and obeys the Hooke's law, that is, the extension is proportional to the force [294]. The slope of this curve is called elastic modulus or Young's modulus (E), which is numerically calculated as the ratio of the tensile stress over the tensile strain along the same axis. The elastic modulus is a characteristic parameter to measure a material's stiffness. In this elastic range, a contraction occurs in the perpendicular direction to the applied tension force at the same time as the sample is being stretched known as the Poisson's ratio (ν), which is defined as the negative ratio of the lateral contraction to the axial strain.

Stress-strain curve deviates from its linear behaviour for higher stresses, when the strain does not disappear completely and permanent plastic deformation occurs after unloading. The onset of the plasticity behaviour is described as the offset of the yield strength. A straight line parallel to the linear region is built for a given value, which results in the yield strength at the intersection with the stress-strain curve. The tensile strength sometimes also known as ultimate tensile strength is described as the maximum value for engineering stress. In ductile materials, which are the ones that elongate under tensile stress prior to failure, the tensile strength coincides with the formation of a mode of irreversible plastic deformation called neck. Percent elongation and reduction in area are typical parameters of ductility [293]. In contrast, brittle materials do not yield and hence their tensile strength will be close to the linear elastic region or at the end of it. In the latter case, tensile strength coincides with fracture strength.

It should be noted that the rate at which strain is applied in tensile testing affects significantly the stress-strain curve. The strain rate dependence increases with an increment in temperature. Furthermore, a material's behaviour can vary from brittle to ductile and vice versa as temperature changes. Due to the high anisotropy in some composite materials, the design of the specimen must be taken into account since mechanical properties are strongly dependent on the orientation of the reinforcing phase.

2.4.2 Nanoindentation

Mechanical characterisation at the very surface of thin films and samples with small volume using depth-sensing nanoindentation tests has been developed in the last two

decades. The main purpose of this technique is to determine properties such as elastic modulus and hardness of a material of interest with another material whose properties are well characterised [295]. The load-displacement curve is built as an indenter is being pressed into the flat surface of the specimen with a steady increasing load. Both load and depth are recorded in real time followed by a constant removal of the load, which is also used to determine indirectly the area of contact and hence the hardness of the sample whereas the elastic modulus is analytically calculated through the contact equations [294]. An initial elastic contact takes place at the very beginning after which plastic yield is caused at higher applied loads. A residual impression is usually left at the surface owing to the plastic yield, which results in a different path for the load-displacement curve. Both loading and unloading curves are employed to calculate not only the plastic behaviour but also elastic and viscoelastic-plastic responses of the material.

The compliance method has overcome the limitations associated with the imaging techniques that relied on the measurement of the residual indent cross section, especially when a great deal of polymeric materials tested has a complex viscoelastic-plastic response [296]. The determination of mechanical properties at the nanoscale can be affected by errors within an order of magnitude equivalent to the penetration depths and consequently a good estimation of potential inaccuracy has to be rectified such as tip defects, initial contact of the indenter, residual stress and the like.

Data analysis is based on the Oliver and Pharr method [297]. Figure 2.16 shows typical load-displacement data for a viscoelastic-plastic material reproduced from reference [296] where h_{max} describes the maximum displacement of the indenter under the maximum applied load, P_{max}, h_r corresponds to the final or residual depth and h_c describes the intercept of the tangent drawn from the linear elastic part of the unloading curve whose slope illustrates the contact stiffness, S, and represents the elastic deformation effects. The difference between h_{max} and h_c quantifies the elastic recovery of the material and the relationship between stiffness and reduced Young's modulus can be defined as

$$S = k E_r (A)^{1/2} \quad (1)$$

where A is the projection of the contact area at h_{max}, k is a parameter which is dependent on the indenter geometry and E_r is the reduced elastic modulus which is also defined as

$$E_r = \left(\frac{1-\nu_s^{\,2}}{E_s} + \frac{1-\nu_i^{\,2}}{E_i} \right)^{-1} \qquad (2)$$

where E and v are with subscripts 's' and 'i' are the elastic moduli and the Poisson's ratios of the specimen and indenter respectively. The difference between h_c and h_r corresponds to the viscoelastic recovery followed by the elastic depth recovery. In addition, hardness can be described as a material's ability to resist penetration or permanent deformation at the surface [295], which is calculated as the ratio between the maximum load to surface area of indentation at full depth delimited by h_{max}.

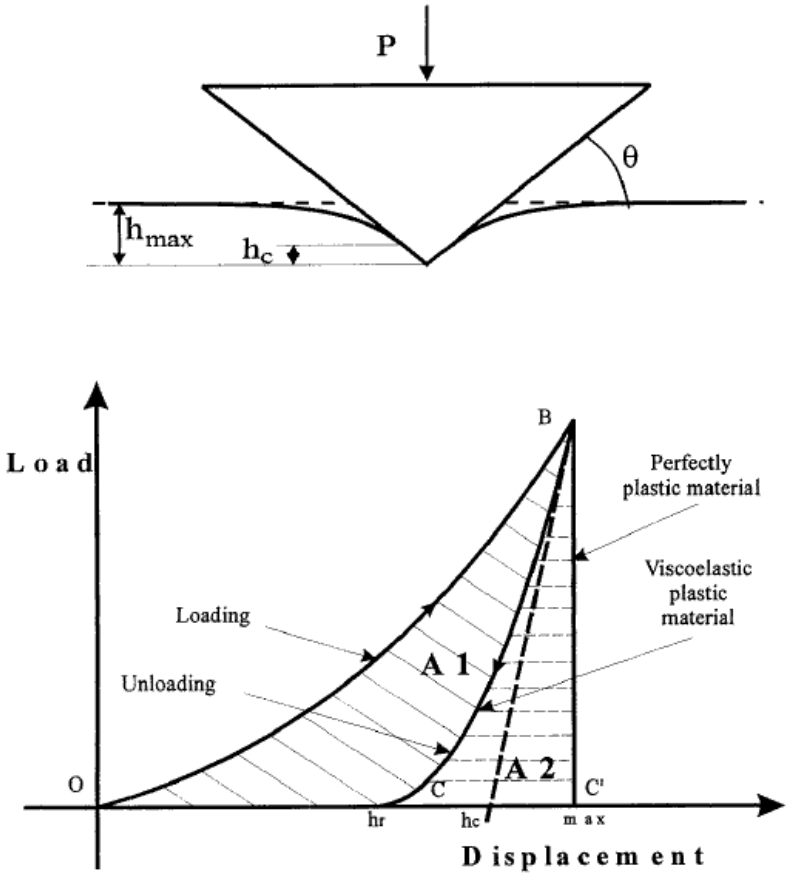

Figure 2.16. Schematic diagram of indentation load-displacement data after Briscoe [296]. A1 corresponds to the viscoelastic-plastic work while A2 represents the elastic work after unloading.

The plasticity index is a dimensionless parameter related to the deformation in contacts which provides the relative elastic and plastic behaviour of a material under external

stresses and strains [298]. For polymers, it has been described as the as the ratio of the irreversible plastic work to the total work, in other words, the area contained within the loading and unloading curves to the total area including the projection drawn from the maximum load which represents the viscoelastic recovery (see Figure 2.16) [296]. Deformation is mainly elastic for low plasticity index whereas plastic deformation occurs for high plasticity index. Complementary to the plasticity index, the elastic recovery parameter (ERP) is defined as the difference between maximum depth and plastic depth divided by the plastic depth [299]. Both plasticity index and ERP are linearly related to the ratio H/E_r which is often correlated to tribological properties such as wear resistance. Most of the times, high H/E_r ratio results in a lower plasticity index (and ERP) and therefore a more elastic behaviour which in turn leads to lower wear rate [300].

The apparatus consist of a pendulum-based depth-sensing system with a magnet, a coil and a current source. When a current is applied in the coil an electromagnetic motion is induced, causing the indenter to penetrate the specimen. The voltage is measured with a parallel-plate capacitor and translated into displacement with nanometre resolution [301]. A sharp and symmetric shaped three-sided pyramid Berkovich tip made of diamond is normally used as an indenter [302]. A reference material with constant elastic moduli throughout a wide range of depths (frequently fused silica) is indented at high maximum loads in order to calibrate the tip [296]. The maximum load preferred in the determination of hardness is that for which a fully plastic deformation takes place. However, in nanoindentation testing of thin films, the total depth must not exceed 10 % of the thickness of the specimen to avoid contributions from the substrate that could lead to inaccurate results [294].

The measurement of the contact area under maximum loading can be sometimes affected by a material's response to tip penetration which can either expand or reduce the actual contact area, phenomenon known as pile-up and sink-in respectively. Figure 2.17 depicts contact area for a material with elastic-plastic behaviour with a sink-in phenomenon shown on the right and pile-up on the left [303]. Piling-up usually occurs in materials with viscoelastic behaviour and low ratio H/Er. The real contact area is larger and therefore the material can accommodate a larger load which leads to a larger stiffness [304]. Such effect can also cause the development of an undesired "nose" in the unloading section of the load-displacement curve. High loading rates, shallow depths and long holding time at maximum loading can potentially minimise pile-up and viscoelasticity. On the other hand,

the surface of the sample in fully elastic materials is pulled inwards and downwards underneath the nanoindenter, which gives rise to a pronounced sinking-in effect [295].

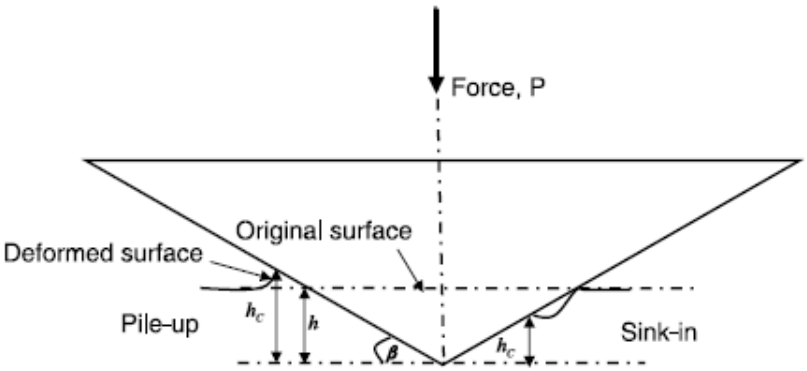

Figure 2.17. Contact area on the surface of the indenter tip. Pile-up (left) and sink-in effects (right) are shown after reference [303].

Creep is defined as a delayed time-dependent response under indentation loading in which depth varies with a constant force applied in viscoelastic materials [305]. Polymeric materials are characterised by a free void volume available for chain motion which is dependent on the glass transition temperature. Such volume enables the material flow from underneath the indenter towards the sample, along the interface and also in bulk when the indenter is pressed onto the specimen for a certain dwell time [295]. Similar to pile-up and sink-in phenomena, sufficiently long dwell time to reach its mechanical equilibrium and a high loading rate can prevent the "nose" feature in the unloading curve [301]. In addition, since indentation depth increases during dwell, the contact area is larger too and thus lower hardness and higher stiffness is extracted from data [306].

Thermal drift along with creep are two sources of potential errors difficult to identify in nanoindentation. Generation of heat due to the electronics of the apparatus leads to thermal expansion of the components which varies the dimension of the contacts, be it the indenter, the indenter tip or the actual specimen [294]. A thermally insulated chamber together with a sufficiently long time for the sample to reach its thermal equilibrium before indentation testing is essential to minimise errors. Furthermore, thermal drift can be amended by introducing a new holding time at low loadings at the end of the unloading curve which monitors change in indentation depth [307].

2.4.3 Tribology: friction, wear and lubrication

Contrary to what the naked eye can discern at the macroscopic scale, surfaces in the vast majority of materials are comprised of ridges and troughs with steep slopes and large valleys sometimes. Such undulated topography can significantly affect a material's performance, which is reflected in its properties such as adhesion, optics, and tribology [308]. For instance, surface structure in polymer nanocomposites and nanocoatings which combine a soft matrix with ceramic nanofillers at the nanoscale is intimately related to their performance.

Proximity between two bodies and actual area of contact between two surfaces depend on both surface topographies. When two relatively flat surfaces come into contact with each other, the actual contact area is only a small part of the nominal contact area. At the micro/nanoscopic level, domains of contact are minuscule asperities of one solid squeezed against the other, which are deformed plastically and elastically or even fracture might occur depending of the nature of the materials and conditions [309]. For example, if a rubbery material is pushed into a substrate with different scale roughness, the rubber fills out large cavities although it is unlikely that both surfaces are in contact at small-sized cavities. In addition, pressure at the bottom of the cavity will be lower compared to pressure at the top of the asperity.

In this section, interactions between two surfaces in relative motion so-called tribology will be discussed, including the principles of friction, wear and lubrication.

(i) Friction

Friction can be defined as the force that resists motion when a surface of a body slides over the surface of other. It is noted that two different phenomena are coined under the term "friction", namely static (sometimes known as stiction) and kinetic friction. Static frictional force is the minimal force at which sliding starts to occur whereas kinetic frictional force is the force required to maintain two bodies sliding against each other. The two Amontons' laws that describe the motion resistance between two solids in contact were postulated in late 17^{th} century [310]:

1. The frictional force is directly proportional to the applied load and independent of the apparent area of contact. Moreover, if two objects have the same mass and different surface area, they will exert the same frictional force.

2. The frictional force is independent of the driving velocity, provided that the speed is not zero.

This second law implies that the study of friction can be split in static and kinetic friction as it has been previously mentioned. In general, the static force required to initiate sliding is considerably larger than the kinetic force employed to maintain the body in motion, both of which are dependent on the nature of the sliding surfaces [311]. Due to the roughness of dry surfaces in the absence of lubricant (or third bodies), the real contact area is small in comparison with the visible contact area and proportional to the load, that is, area of contact linearly increases at high loads occasioned by plastic deformation [310].

There is interdependence between adhesion and friction especially in soft materials such as polymers. It has been stated that plastic deformation occurs at the outermost layers of two objects brought into contact whereas elastic stresses take place deeper in the bulk [312]. The point at which the load is released, the elastic recovery underneath the very surface causes a rearrangement of external molecular groups, which strengthen contacting bonds at the interface [313]. Such localised adhesion equals the shearing force needed to surmount friction and might result in wear.

Let us visualise the interface at the microscale illustrated in Figure 2.18a. If an asperity slides against another asperity sticking out of the opposite surface, a rapid slip motion occurs so the friction force decreases. On the other hand, if an asperity is dragged over a valley on the other side, the transition is hindered by a higher friction force. Therefore, static frictional force is dependent on the duration of stationary contact. Such periodic transitions between various dynamic states during steady-state sliding are defined as stick-slip regime shown in Figure 2.18 [314]. Frequency of stick-slip increases with driving velocity until a transition to smooth motion in the kinetic state is reached. Stick-slip regime is observed in soft systems or at low velocities whereas smooth sliding occurs in stiff systems or high velocities.

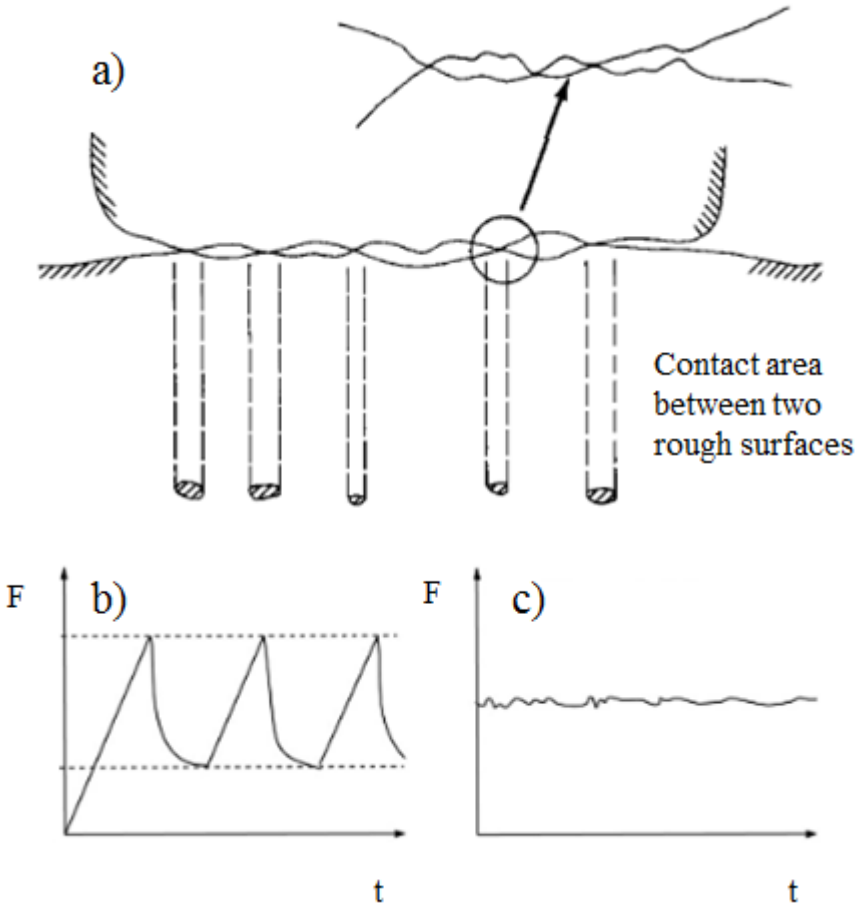

Figure 2.18. Schematic representation of real contact area between two rough surfaces (a) and friction force versus time diagrams in the stick-slip and smooth sliding regimes (b, c); adapted from references [310, 311].

Local high temperature is developed at the surface contact as a consequence of the kinetic energy dissipated as heat, which depends on the load, sliding velocity and heat conductivity of the materials involved, leading to a variation on the friction force.

(ii) Wear

Removal or erosion of material from the surface of a solid including plastic deformation caused by the mechanical actions of another surface is known as wear [315]. Interfacial conditions such as normal load, geometry, relative surface motion, sliding speed, surface roughness, type of material, system rigidity, temperature, stick-slip regime, humidity, lubrication and vibration can affect friction and wear rate [316]. Such wear rate varies through consecutive stages. It has been previously stated that both surfaces at the interface

deform and readjust to each other at the microscale in an early stage while wear occurs at a fluctuating rate. Thereafter, a period of mild progressive wear takes place on the components at a relatively steady rate. A last stage with rapid rate of ageing causes severe damage on the specimen followed by the onset of cracking, shearing or delamination which results in catastrophic failure. Wear mechanisms are further discussed as detailed below:

1. Adhesive wear. Interactions between two bodies that slide over each other via a rolling contact might lead to micro-junctions by welding. The softer material will be transferred to its counterpart due to shearing during motion. Adhesive wear is also termed as scuffing [317, 318] or galling [319]. Few parameters can be adjusted to lower adhesive wear rate such as low loading, material hardening and the presence of third bodies like contaminants, lubrication oils and other additives.

2. Delamination wear. Asperities of the softer surface are primarily worn until a smooth surface is created. In addition, micro-cracks are generated underneath the interface and propagate parallel to the surface direction at the same time. They eventually reach the surface causing delamination of thin worn sheets [320].

3. Abrasive wear. The two-body abrasive wear occurs when asperities of a harder material plough grooves on a softer material followed by removal of the softer material. This type of wear can be improved by reducing the hardness difference between the surfaces [319]. Conversely, three-body abrasive wear is caused by free particles (third body) in the interface of both surfaces [317].

4. Corrosive wear. Aggressive environments and protective coating failure can lead to corrosive or oxidational wear [321]. Increase in sliding speed, temperature and humidity in the presence of oxygen can accelerate chemical or electrochemical reactions and hence severe corrosive wear takes place [319].

5. Fatigue wear. Large fragments are detached from the worn surface after a critical number of cycles of loading and unloading. Unlike other wear mechanisms where a steady degeneration is observed, fatigue wear leads to a sudden failure after the incubation period [317]. Fretting is described as a type of fatigue wear where contact surface is tangential to the other surface and subject to a minor motion of small amplitude or vibration [319].

6. Erosive wear. This type of wear is caused by the impingement of gas, liquid or solid particles on the surface [320]. The erosive wear rate, which might be intensified by corrosion [319], mainly depends on the shape of the impacting particles, hardness, impact velocity and impingement angle.

7. Thermal wear. Wear rate can be affected by temperature rise due to softening, melting or evaporation phenomena at the contact surface [319].

(iii) Lubrication

Lubrication is the process by which wear and friction can be reduced in one or both bodies in contact moving relative to each other after a substance is introduced into the system so-called lubricant. Such lubricant can be in a solid state (e.g. graphite), composed of a solid dispersed in a liquid (PTFE dispersed in oil), a liquid phase (oil), liquids dispersed in other liquids (grease, additives in fuels) or even a gas. Although the main purpose of lubrication is to reduce friction and wear rate between two sliding surfaces, heat transfer is additionally improved at the same time as contaminants are carried away. Three different regimes are observed with respect to the mode of lubrication as a function of load (see Figure 2.19):

1. Boundary lubrication. This mode of lubrication usually occurs at high load or low sliding speed. Contact between both sliding surfaces takes place due to reduced thickness of the lubricant film, which is smaller than surface roughness. Therefore, micro-asperities on both surfaces are in full contact, which will lead to an increase in temperature, high wear rate and eventually failure. At this regime, load is supported by surface asperities rather than the lubricant [322].

2. Mixed lubrication. It is defined as an intermittent contact regime in between boundary and hydrodynamic lubrication, that is, asperity contact and fluid film mode respectively. Both bodies undergo elastic strains at the interface that creates a load-bearing volume gap for the fluid to flow. For an extreme case in which the lubricating film breaks down, only high spots protruding out the surface will be in contact with its counter-body and friction will be comparable to the boundary regime [323].

3. Hydrodynamic lubrication. Direct contact does not occur at the interface since the lubricant film completely isolates friction surfaces. Providing both load and sliding speed are steady, the friction coefficient decreases as viscosity does decrease too owing to the

fact that the load is fully supported by the lubricant within the gap between the surfaces in relative motion [322]. Tribological properties are determined therefore by the lubricant, which can vary as a function of temperature. In this regime, one can define a mode of lubrication in between mixed and hydrodynamic lubrication called elastohydrodynamic lubrication in which elastic strains occur at both surfaces without a lubricant film breakdown [322].

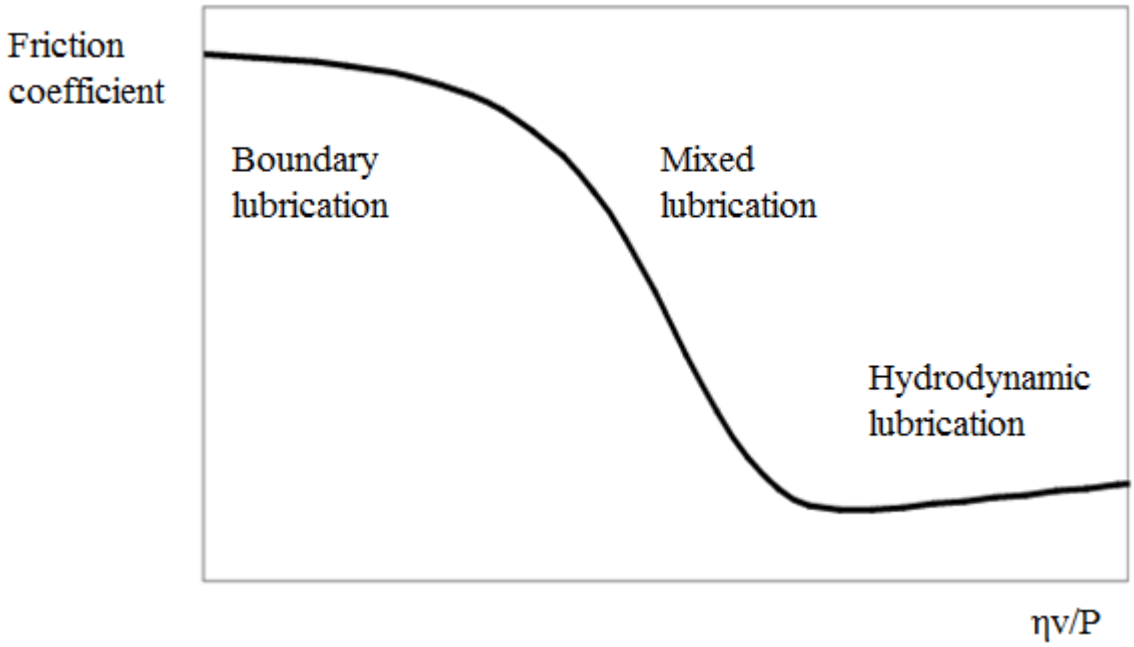

Figure 2.19. Stribeck curve diagram illustrates the three lubrication regimes. Friction coefficient is plotted as a function of the lubrication parameter, which equals viscosity times sliding speed over normal force; adapted from reference [323].

An external pressure is pumped into the system sometimes in order to create a bearing fluid film that can accommodate heavy loads at low relative motion. Otherwise, a fluid disruption would lead to compressed surfaces at the boundaries. Furthermore, a peculiar feature worth noting is the self-lubrication phenomenon, where usually dry surfaces experience a micromaterial transfer that gives rise to a lubricant film at the surface, and hence a reduction in both friction and wear rate. Such particles entrapped in the porous material can reach the sliding surfaces and consequently the lubricating effect is enhanced [324].

2.4.4 Nanoscratching

Nanoscratch testing is amongst the most widely used techniques for the characterisation of tribological properties at the surface of polymers and composite materials nowadays. It is known that composition and properties near the surface of coatings or thin films might differ from the properties in the bulk [325]. This scratch method enables the study and characterisation of deformation in coatings, thin films and paints; bulk property correlations are extracted from the scratch width as well as some features such as cracks, crazes and plastic flows. Alongside the extreme complexity of the study, one must also take into account that scratch behaviour not only depends on the near surface properties but also it is a function of both the bulk material's properties and experimental conditions such as normal load, scratch velocity and indenter geometry [326].

Experiments are usually performed by applying a normal load supported by the contact area between the indenter and the specimen with a steady lateral displacement across the sample. At the same time, the material's response against deformation occurs in the tangential direction of the scratch track, which is the friction force. Several diamond indenter geometries are commercially available such as Berkovich, three-sided cubic, spherical and spheroconical.

Testing is based on alternate repetition of off-load and on-load multi-pass cycles. An initial topographic scan is carried out at low load after which the probe is returned to the starting position of the track. Then, either a constant or ramp load is applied along the track previously scanned, thus a scratch profile curve is obtained. The residual depth is obtained from the third off-load scan as well as additional information such as elastic/plastic deformation and permanent damage. In the first and third scans, the applied load is sufficiently low for wear not to occur. Data are corrected during analysis according to the initial slope/topographic scan and compliance in the instrument software [327]. Multi-pass scratch cycles can be performed in order to investigate wear behaviour in thin films.

There are four critical transition points that can be identified via scratching: the onset of the plastic behaviour, the onset of cracking, unloading failure behind the indenter and total film failure [327]. In addition, material is accumulated on the sides of the scratching track as ridges or as a prow in front of the indenter due to a ploughing effect, which can be confirmed by using complementary tools of characterisation such as atomic force microscopy (AFM) along with the conventional optical microscopy [326]. Microscopy techniques can be also applied to determine the appearance of coating delamination,

penetration depth and possible cracks in or around the track as well as other type of plastic and brittle deformations [328].

Let us analyse how the energy supplied by the indenter is consumed in various simultaneous processes in the course of scratching. A part of the energy in the normal component is assigned to support the indenter over the sample whereas another part is employed for the resistance to tangential deformation which can be divided in a ploughing component and a traction component. The last part of the energy is dissipated as thermal energy. From the forces perspective, scratch testing is divided in a normal component which is the applied load and a perpendicular component friction force which is the resistance against scratch deformation [326].

Failure on the surface of the sample is produced due to compressive stress at the front of the probe and tensile stress at the rear while the indenter is traversing the material. For this reason, it is wise to think that mechanical properties are involved in the scratch behaviour of materials. Indeed, mechanical properties of the materials such as the elastic modulus or the ratio H/E considered by other authors [329] can affect significantly the residual depth and the type of failure produced during scratching, which is also related to the aforementioned plasticity index in the nanoindentation section. For instance, high modulus or low H/E ratio decreases residual depth in ductile materials although it is subject to the applied load [327]. On the other hand, the same high modulus can be detrimental for brittle materials, resulting in cracking [326]. Besides, high friction coefficient leads to failure of the material due to stress concentration at the rear of the probe.

A ductile response to scratching is usually found in polymer materials with a reduced scratch hardness and deeper residual depths, in which failure requires much more energy compared to brittle glass or ceramics. Figure 2.20 depicts a schematic representation of the different modes of response to scratching. It is worth noting that thermal changes in polymer materials may cause a transition in the deformation response from brittle to ductile due to a softening effect whether the operating temperature is close to the glass transition temperature [326]. A collection of polymer nanocomposites with enhanced tribological properties reinforced with a wide variety of nanofillers are gathered together in some reviews [330, 331], in which is highlighted once again the importance of dispersion and how the use of nanomaterials at very low content outperforms their counterparts at the microscale.

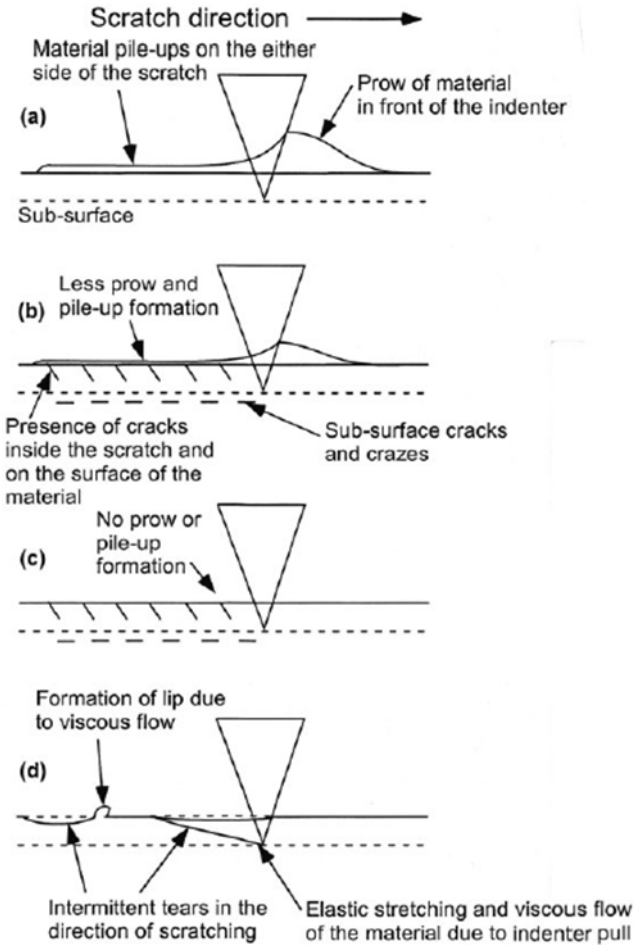

Figure 2.20. Representation of the response modes to scratching: (a) ductile, with ridges and a prow formed on the sides and at the front of the indenter; (b) ductile/brittle mixed response; (c) brittle response and (d) elastomeric response; reproduced from reference [326].

2.5 Ultrasound: dispersion of nanotubes

2.5.1 Introduction to ultrasound

It is known that dispersion of nanomaterials within solvents and polymer matrices is not a straightforward task because of their large specific surface area. Elongated nanostructured materials with high aspect ratio, be it carbon nanotubes, titanate nanotubes or aluminosilicate nanotubes previously mentioned in this review, are affected by increased dispersion forces which can cause formation of large bundles, ropes or entangled aggregates after their synthesis [28, 332]. Ultrasound sonication has been widely used to

disperse nanomaterials in liquid media. However, ultrasonic treatment can lead to shorter nanotubes with reduced aspect ratio [41, 333].

Ultrasound is defined as sound waves with frequency higher than the upper audible limit of human hearing, which is approximately 20 kHz although it can vary from person to person [334]. The phenomenon by which nanoparticle aggregates can be disintegrated and even nanotubes can be exfoliated or cut is known as acoustic cavitation. This event occurs when ultrasound waves pass through a liquid, which induces a sudden pressure variation in it. In the first instance, nucleation of gas bubbles takes place followed by their growth through diffusion of dissolved gas, liquid evaporation and coalescence. After critical size is reached, bubbles implosively collapse inducing high strain rates in the liquid. The intensity of the cavitation effect is amplified as the bubble volume increases, which cannot only exfoliate bundles of nanotubes but also can be applied for surface cleaning due to induced surface erosion. At the end of the cycle, a rapid expansion occurs where microcavities are formed as new potential nucleation sites within the liquid phase. The lifetime of the bubble is typically 100 μs [335]. Temperature as high as 5000 K [336] and pressure around 500 atm [337] can be developed locally during bubble formation.

Cavitation can occur at frequencies ranging 20 kHz to 1 MHz. This process is dependent on the nature of the solvent which includes parameters such as viscosity, surface tension, vapour pressure, gas solubility and type of radicals formed under sonication which are described hereunder [338]. Generally, nanotube aggregation fraction is reduced significantly for solvents with low vapour pressure, high viscosity and high surface tension. However, some solvents present an anomalous behaviour. DMSO is known to be highly hygroscopic thus it is observed as an outlier. Besides, it has been reported that chlorinated solvents can decompose into chlorine and hydrochloric acid or polymerise on the surface of nanotubes in case of haloaromatic compounds [339]. However, fully chlorinated solvents such as CCl_4 do not decompose probably due to the absence of hydrogen atoms. Moreover, the presence of ethanol can quench solvent decomposition which is thought to occur via radicals [340].

The nature of the gas dissolved in the solvent can also affect the number of cavitation events and the quantity of gas. Temperature and pressure can alter liquid properties and gas solubility. Intensity delivered by the ultrasound equipment can be manually controlled. Larger intensity implies larger acoustic amplitude and collapse pressure as well as higher probability of cavitation events per volume unit. Ultrasound frequency is inversely proportional to the size of the cavitation bubbles. For instance, low frequency signifies

higher maximum bubble size and thus higher cavitation intensity. Conversely, high frequency in the range of MHz implies low power cavitation, which can be applied for diagnostic purposes. The duration of the sonication will determine the total energy input.

Ultrasound treatments are conducted in two different arrangements, namely ultrasonic bath and ultrasonic tip, horn or wand. Baths usually work at higher frequency (40-50 kHz), delivering a lower energy input. In consequence, smaller bubble size will be formed during cavitation, thus nanotube length will be slightly affected. However, cavitation is concentrated in a confined volume when ultrasound is applied through a horn [341]. The conical geometry of the tip is designed for this purpose, which leads to nanotube debundling as well as scission. Frequency in this apparatus is usually fixed in the range of 20-25 kHz whereas the energy output released by the sonicator can be manually modulated. Vibration of the wand tip generates a cavitational domain as well as a recirculating flow within the liquid medium.

2.5.2 Nanotube scission under sonication

Several models and mathematical functions have been reported in order to explain length distribution and scission kinetics of elongated nanostructured materials under ultrasound. These kinetic rate models can predict how length distributions change as a function of time. It is agreed that mean length distribution exhibits a power law decay dependence on the sonication time which varies as the nanotubes are fragmented. As a general rule, fragmentation rates decrease as the nanotube length shortens. It is worth noting that the amount of energy dissipated in nanotube motion, compression, buckling, temperature rise and some other mechanisms will increase as size is reduced [341]. Length-dependent comminution rates are interpreted to first order process in terms of continuum physics approach, based on the assumption that only one fragmentation event occurs at a time as well as the nanostructure is split into two parts for a single event, which is a precise approximation except in cases with high degradation rates due to extremely long nanotubes or polymer chains [342].

It is assumed that the yet unclear mechanisms involved in cavitation-induced polymer scission are similar to nanotube shortening under ultrasound. Supposing that the distance of the nanotube from the centre of the cavity is sufficiently short, strong solvent drag forces are created within the proximity of the nanotube surface during sudden bubble

implosion. Due to a radial velocity profile near the cavity, linear velocity at the leading end of the nanotube will be much higher than linear velocity at the trailing end of the nanotube. Flow-induced stretching and eventually scission occurs because of friction between solvent and nanotube [343]. A relative displacement within an individual nanotube is caused by accumulative drag forces that are balanced by mechanical tensile stresses, which is maximum in the centre and therefore scission takes place around the middle of the nanotube providing the stress exceeds tensile strength [344]. Strain rates in aqueous dispersions of nanotubes sonicated with an acoustic ultrasound frequency of 20 kHz can be as high as 10^9 s^{-1} and the nanotube will move at a velocity up to 2500 m s^{-1} [345].

Experiments report a power law relation between average length L and sonication time t, which scales as $L \sim t^{-0.49}$. The strain force associated with the cavitation scales with the square of the nanotube length [345]. In this kinetic model, some effects have not been considered for simplification such as dependence of fragmentation rate on nanotube diameter. Moreover, drag forces in the presence of surfactants, nanotube bundles and defect density are strongly dependent on the diameter. Logarithmic corrections are necessary for small aspect ratio materials. On the other hand, this model predicts that scission will stop after a long experimental time, which is needed to reach terminal length. This limiting length is highly dependent on the material properties, therefore sonication-induced scission can be used as a statistical approach to calculate tensile strength of a wide range of elongated nanostructured materials [346].

Nevertheless, it is essential to know the diameter of the particles because the total force needed to fracture a nanotube equals to its tensile strength times its cross section [347]. A later work by Lucas *et al.* [347] considers the probability of the nanotubes to be in the proximity of collapsing bubbles, which takes place in a short span of time of 4 μs with a radius of 30 μm approximately [348]. Larger nanotubes sweep out a larger volume and thus the larger the probability of a nanotube to be near a cavitation bubble. Mean length was plotted as a function of sonication energy delivered to the sample in a logarithmic plot. Results fit into a linear curve where the terminal length is not yet achieved. Experimental data does not follow the previously scaling behaviour $L \sim t^{-0.5}$ [345] but the power law behaviour is $L \sim t^{-0.21}$. It is thought that efficiency of sonication depends mainly on the acoustic pressure, which must overcome the cavitation threshold. Above this threshold, sonication energy determines nucleation rate of cavitation bubbles.

Nanotube bending and other effects can occur as bubbles collapse. For instance, bubbles experience a rapid expansion followed by a sudden collapse, which might induce nanotube

motion and radial alignment with respect to the bubble surface. In this configuration, bubble collapse might induce nanotube rotation or buckling [347]. Furthermore, turbulence regime could modify scission kinetics due to the high collapse velocity.

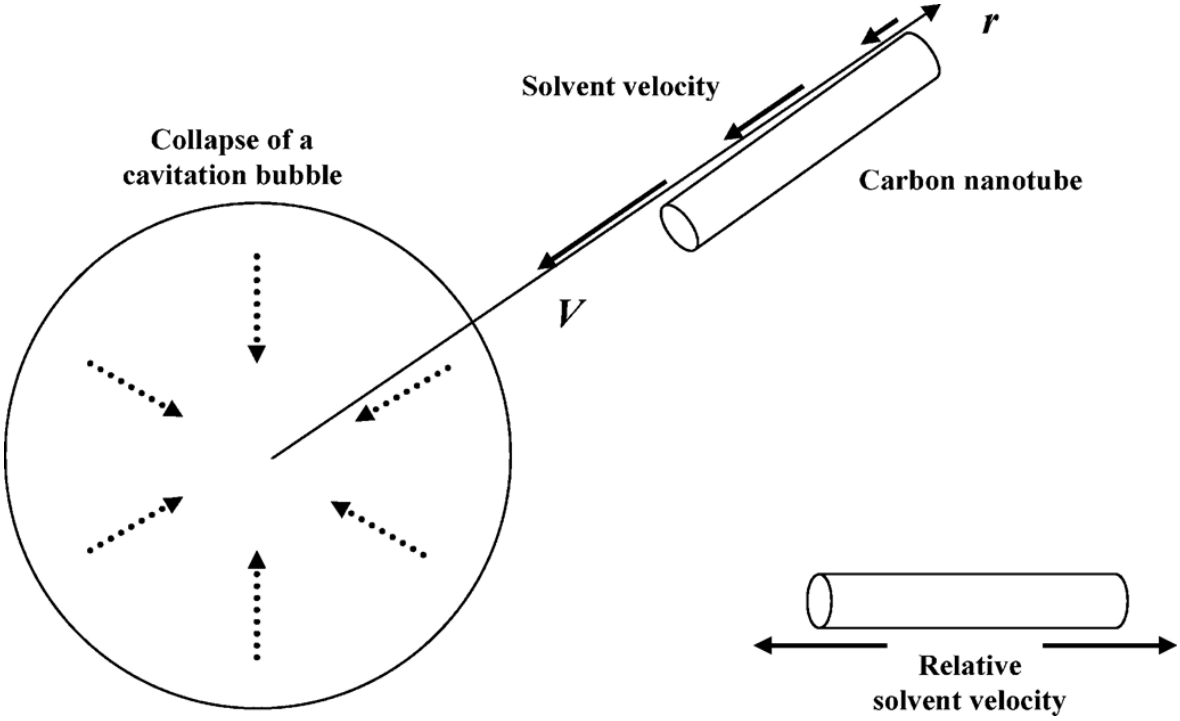

Figure 2.21. The upper representation shows a nanotube close to an imploding cavitation bubble whilst the bottom right image illustrates the relative motion within a nanotube causing scission; reproduced from reference [347]. Reprinted with permission from American Chemical Society.

Contrary to the theories previously mentioned about possible mechanisms of nanotube scission under ultrasound such as tension, local high temperature and sonochemical free radical reactions, it has been reported that fragmentation of single walled carbon nanotubes (SWNT) befalls via axial compression [348]. Almost half of the nanotube circumference is split as a result of compressive atom ejection, which ends up with bonding rearrangement within the graphene layer causing local kinks along the length of the nanotube.

Thus far, although the principles behind scission mechanisms are not fully understood, experiments reported on the literature show that there is a power law relation between maximum or average length of nanotubes and sonication time or energy delivered into the sample, which scales as $L \sim t^{-m}$. The exponent m varies from 0.2 to 0.5 according to literature. Pagani *et al.* [335] proposed a combined model in order to conciliate between

such discrepant experimental results. In this model, it is suggested that nanotubes oriented parallel to the bubble surface could either rotate and align radially to the bubble or buckle (see Figure 2.22). Regions are defined in the surroundings of a growing bubble at the beginning of sonication with respect to bubble centre. Most of the nanotubes affected by the sonication flow are distributed within a volume in between 40 and 250 μm radius. The volume below 40 μm is so small that it is considered negligible because only a tiny fraction of nanotubes is contained. Besides, the volume beyond 250 μm is not affected by cavitation.

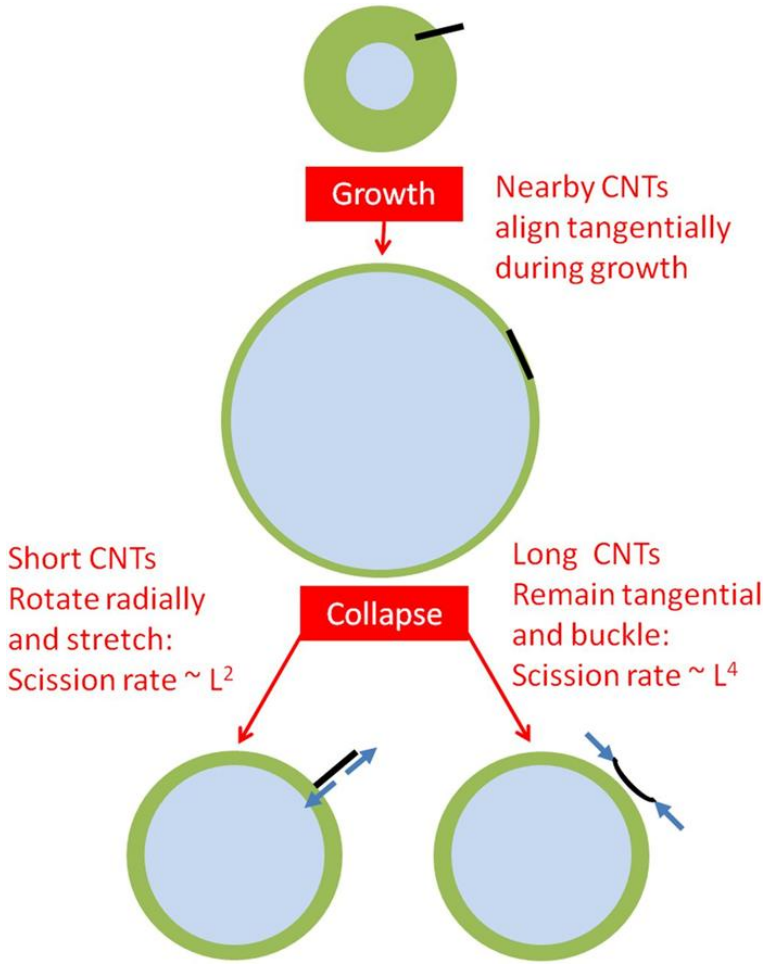

Figure 2.22. Growth and bubble collapse illustration reproduced from reference [335]. Nanotubes align tangentially during growth, after which they may rotate radially or buckle depending on their length.

Nanotubes adopt a tangential orientation during bubble growth, after which bubble collapse exerts strong drag forces that grows inversely to the distance from the bubble. Then, they are subjected to a compressive force that makes them bend eventually followed by bucking or rotating for a radial orientation. Depending on the nanotube length, several

situations are observed as follows. Long nanotubes usually buckle into bent shapes, which can cause fragmentation as long as compressive forces surpass the compressive strength. Therefore, scission exclusively happens when the local curvature is amply high. Intermediate nanotubes curve into U shapes and, as length decreases, they slightly bend or simply align into radial orientation. At certain nanotube length, the fragmentation mechanism will change from compressive buckling to tensile stretching. Both mechanisms can coexist and follow a power law decay that scales with m in the range of 0.41-0.5 for long tubes and 0.205-0.25 for short tubes [335].

Chapter 3: Experimental methodology

In this thesis, metal oxide elongated nanostructured materials have been incorporated to polymer matrices to produce both thin films and electrospun microfibres with enhanced mechanical and tribological properties. In addition, the hollow-like morphology of ceramic titanate nanotubes enables the introduction of several additional functionalities depending on the molecule encapsulated in the inner pores, which can be released after mechanical stimulus (e.g. controlled ultrasound treatment). This chapter describes in detail experimental procedures followed in laboratories throughout the development of this research. Section 3.1 reports titanate nanostructures synthesised by the alkaline hydrothermal method, sonication of colloidal suspensions of titanate nanotubes in several solvents, both polymer and ceramic coatings of titanate nanotubes and encapsulation of the selected molecule "ibuprofen" released after ultrasonication. Section 3.2 describes the preparation of polymer composite films consisting of: (i) different content of ceramic nanostructures added to polymer matrices, (ii) length in titanate nanotubes controlled by duration of ultrasound. Besides, CTAB-modified titanate nanotubes are embedded in polymer microfibres via electrospinning. Section 3.3 outlines the techniques used to characterise the solid and liquid (colorimetric analysis to determine solution concentration) products obtained from the previous Section 3.1 and 3.2.

3.1 Synthesis procedures

3.1.1 Alkaline hydrothermal synthesis of titanate nanotubes (TiNT)

The alkaline hydrothermal method was used to synthesise TiNT based on the procedure described elsewhere [28]. A mass of 25 grams of raw titanium dioxide (TiO_2) was added to an alkaline aqueous solution of sodium hydroxide (NaOH) and potassium hydroxide (KOH) 10 mol dm^{-3} (with respect to hydroxide ions) with a ratio of NaOH:KOH 50:1. The reaction was carried out in a perfluoroalkoxy polymer (PFA) round bottom flask at atmospheric pressure and 100 ºC for 4 days. The nanotubes were washed with an aqueous solution of hydrochloric acid (HCl) 0.1 mol dm^{-3} until pH 2. Distilled water was used to return to pH 5 – 6. After washing, TiNTs were filtered and dried under vacuum at room temperature (25 ºC) overnight.

3.1.2 Alkaline hydrothermal synthesis in the presence of oleic acid

A similar procedure as for titanate nanotubes was followed with the only difference that 25 grams of oleic acid was incorporated into the reactive mixture prior to the initiation of the chemical reaction by heating. This approach was attempted for the purpose of improving the dispersion of TiNT in organic solvents before sonication, which will be further discussed thereafter. A higher reflux temperature (as high as 115 ˚C) was reached after the addition of oleic acid.

3.1.3 Alkaline hydrothermal synthesis of titanate nanofibres (TiNF)

A synthesis procedure was adapted from a method of preparation of sodium titanates reported in reference [30]. 5 grams of titanium dioxide (TiO_2) was added to 60 cm^3 of a concentrated aqueous solution of sodium hydroxide (NaOH) 10 mol dm^{-3} in a beaker under vigorous stirring. The solution was transferred into a PTFE (Teflon)-lined autoclave and heated for 4 days at a controlled temperature of 190 ˚C. The white titanate nanofibres (TiNF) were rinsed with distilled water several times until the solution reached pH 7. The powdered TiNF were washed with an aqueous solution of hydrochloric acid (HCl) 0.1 mol dm^{-3} until pH 2 followed by distilled water to return to pH 5 – 6. The white powdered was filtered and dried in vacuum at room temperature 25 ºC.

3.1.4 Preparation of stable colloidal suspensions by long term mechanical stirring

Stable colloidal suspensions of TiNT and TiNF were prepared as follows. 400 mg of powdered elongated nanostructured material was mixed with 200 cm^3 of distilled water and allowed to stir at ambient temperature for 2 weeks using a magnetic stirrer with stirring rate 700 rpm. Then the suspension was allowed to settle for one day, the supernatant liquid was decanted while the precipitate at the bottom was discarded. Suspensions of TiNT were prepared following the same procedure in ethanol.

In order to investigate the comminution rate of nanotubes in various solvents, suspensions of TiNT were systematically prepared in organic solvents such as dichloromethane, chloroform and bromoform. Unlike hydrophilic solvents such as water and ethanol, titanate nanotubes cannot be well dispersed in halogenated solvents. The surfactant

cetyltrimethylammonium bromide (CTAB) has been used to modify the nanotube surface as a thin coating. TiNT were soaked in an aqueous solution of the surfactant CTAB 0.02 mol dm^{-3} and mechanically stirred for 24 h. The nanotubes were filtered and dried at room temperature 25 ºC overnight. CTAB-TiNT were subsequently stirred in the halogenated solvents for investigation of the effect of the solvent density on the fragmentation rate of nanotubes.

3.1.5 Sonication of titanate nanotubes in various solvents

To study the effect of solvent density on the scission rate of TiNT, 25 cm^3 of TiNT suspended in various solvents such as ethanol, water, dichloromethane, chloroform and bromoform were consecutively treated with ultrasound for 0.5, 1, 2 and 3 hours (total time) using a HD3200 Sonopuls Ultrasonic Homogenizer (purchased from Monmouth Scientific Ltd, UK) with a 6 mm diameter titanium alloy probe KE76. Sonication parameters are: 0.005 s pulses, frequency of 20 kHz and 50 % of the energy output of 100 W. The probe was immersed 1.2 cm into the liquid suspensions, which were treated sequentially every 3 minutes and kept in an ice-bath to avoid overheat and reduce the temperature. Figure 3.1 shows a schematic representation of the experimental arrangement.

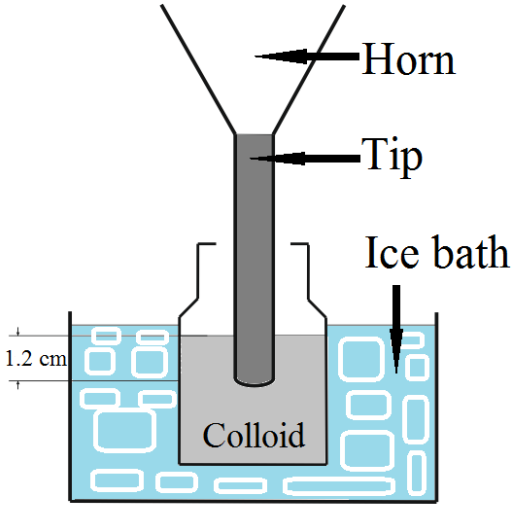

Figure 3.1. Arrangement for ultrasound treatment of colloidal suspensions of nanotubes in various solvents. The figure is not drawn to scale.

3.1.6 Acoustic energy absorbed under ultrasound treatment

The purpose of this experiment was to investigate whether the amount of acoustic energy absorbed by a given solvent is correlated with its density. Such effect might vary thermal energy added to the solution, the regime of cavitation and the size of the bubbles under ultrasound treatment in different solvents which in turn might affect scission rate of titanate nanotubes. 25 cm^3 of all solvents were sonicated for 1 minute in adiabatic conditions. The initial temperature of the solvents was 25 ºC to avoid an error due to evaporation. Temperature rise (ΔT) during sonication was measured, from which the acoustic energy converted into thermal energy can be estimated as $\Delta Q = \rho\ V\ C_p\ \Delta T$, where ρ is density, V is volume and C_p is specific heat of the solvents.

3.1.7 Polymer and ceramic coating on titanate nanotubes

The intention of this series of experiments was to measure indirectly the strength of nanotubes prior and subsequent to polypyrrole (PPy) and silica (SiO_2) coating by sonication of colloidal suspensions of neat / coated nanotubes. One can speculate beforehand that a brittle ceramic coating would not affect significantly stiffness in titanate nanotubes whereas a ductile polymer coating would decrease the scission rate of nanotubes under ultrasound and therefore an effective reinforcement would be achieved. The approach followed was to obtain colloidal suspensions of polypyrrole / silica coated titanate nanotubes by mechanical stirring, which would be sonicated thereafter.

Four different procedures were designed for polypyrrole coating of TiNT. Firstly, white powdered titanate nanotubes were added to a concentrated aqueous solution of hydrogen peroxide (H_2O_2) 30 wt % and mechanically stirred for 30 minutes. The yellow coloured peroxide nanotube complex was thoroughly washed with distilled water and filtered under vacuum. It is thought that peroxo groups attached to the nanotube surface can initiate polymerisation of pyrrole. 200 cm^3 of an aqueous solution containing pyrrole 0.1 mol dm^{-3} and oxalic acid ($H_2C_2O_4$) 0.05 mol dm^{-3} was added dropwise to 0.02 moles of peroxo-nanotubes and stirred with a magnetic stirrer overnight. A dark solid powder was washed and dried at reduced pressure (100 mbar). Polymerisation cycles were repeated three times to ensure a uniform thin layer of polypyrrole on the nanotube surface.

An alternative route in the preparation of polypyrrole coated titanate nanotubes was performed by mechanical stirring of 1 g of the yellow peroxo-TiNT complex in water for 1

week. Pyrrole (6.6 mmol) and oxalic acid (3.3 mmol) were added into the colloidal suspension and stirred overnight. The grey solid obtained was centrifuged, filtered and dried under reduced pressure (100 mbar).

The third approach consists of the incorporation of pyrrole (6.6 mmol) to the stable aqueous colloidal suspension of TiNT, which was mechanically stirred for a week afterwards. Based on the curve of pyrrole adsorbed on TiNT as a function of equilibrium concentration reported by Herrasti *et al*. [35], the solution has reached the saturation region of the curve when 1.6 mmol of pyrrole are adsorbed onto the nanotubes whereas the remaining excess of pyrrole will be in solution. A semi-molar quantity of oxalic acid and equimolar hydrogen peroxide were added and stirred overnight followed by filtration and drying of the grey solid under reduced pressure at room temperature.

A fourth synthetic method was followed considering equivalent volumes of pyrrole and titanate nanotubes (density equals 0.967 and 3.12 g cm^{-3} respectively). 200 mg of TiNT and 62 mg of pyrrole were stirred in 100 cm^3 of water for 1 week. Hydrogen peroxide equimolar and oxalic oxide semi-molar with respect to pyrrole were added and stirred overnight followed by filtration and drying of the black solid under reduced pressure at room temperature.

A comparative set of experiments was performed for titanate nanotubes coating with the ceramic species silica (SiO_2) by two different procedures. Firstly, a colloidal suspension of CTAB-TiNT in chloroform ($CHCl_3$) was obtained by vigorous mechanical stirring of 200 mg of nanotubes in 200 cm^3 of $CHCl_3$ for 1 week. Then, a solution composed of 1.4 cm^3 of ammonia (NH_3) 30 wt % and 0.6 cm^3 of tetraethyl orthosilicate (TEOS) dissolved in 28.6 cm^3 of ethanol was added dropwise and stirred overnight. The white powdered solid was collected and dried for further characterisation.

The ceramic silica coating was alternatively produced in ethanol media. 20 g of powdered neat titanate nanotubes was stirred in 20 cm^3 of ethanol for 1 week. A solution consisting of 0.06 cm^3 of TEOS and 0.14 cm^3 of NH_3 30 wt % in 2.86 cm^3 of ethanol was added dropwise to the colloidal suspension of nanotubes and stirred overnight. The white solid was filtered and dried under reduced pressure at room temperature for further characterisation.

3.1.8 Ibuprofen encapsulated in titanate nanotubes released by ultrasound

The molecule ibuprofen was selected to be encapsulated inside the pores of titanate nanotubes and sealed with polypyrrole via *in situ* chemical polymerisation of the monomer pyrrole. This compound could be released in a controlled manner should nanotubes covered with polypyrrole break upon ultrasonication. Ibuprofen sodium salt was precipitated after addition of hydrochloric acid (HCl) 0.1 mol dm^{-3} followed by filtration in a Büchner funnel under reduced pressure. The incipient wetness impregnation technique was used for ibuprofen to be adsorbed on the nanotube surface. 1 g of the dried powdered white solid was dissolved in 5 cm^3 of ethanol and poured into 3 g of titanate nanotubes. The solution was stirred until the solvent completely evaporated at room temperature. Nanotubes loaded with ibuprofen (TiNT-IB) were filtered and dried under reduced pressure and room temperature.

Pyrrole polymerisation was performed following the first method described in the previous Section 3.1.7. 10 cm^3 of hydrogen peroxide (H_2O_2) 30 wt% were added to 1 g of TINT-IB and allowed to stir for 30 minutes. The yellow coloured peroxo complex was washed with distilled water. 0.519 g of pyrrole (Py) and 0.483 g of oxalic acid ($H_2C_2O_4$) were added to the peroxo nanotubes loaded with ibuprofen and allowed to stir in 50 cm^3 of distilled water for 24 h. Two polymerisation cycles were performed to ensure a thorough polypyrrole coating.

Concentration of ibuprofen in aqueous solutions of NaOH 0.1 mol dm^{-3} was determined by UV-visible spectrometry in 3 different sets of samples (see Section 3.3.5): uncoated titanate nanotubes loaded with ibuprofen (TiNT-IB), titanate nanotubes filled with ibuprofen and coated by polypyrrole (TiNT-IB-PPy) and the latter dispersed in 25 cm^3 of NaOH 0.1 mol dm^{-3} after being treated in an ultrasonic bath for 1 minute (TiNT-IB-PPy-Us).

3.2 Preparation of polymer composite materials

3.2.1 Polymer composite films

(i) Polyethylene oxide / chitosan filled with titanate nanotubes

The purpose of these experiments was to study the distribution of TiNT within the polymer matrix along with the mechanical and tribological performance of such composite materials as a function of nanotube content prepared by drop-casting. Aqueous colloidal suspensions of TiNT were obtained following the procedure described in Section 3.1.4. Polymer composite films were prepared by mixing of aqueous solutions of nanotubes with polymers blends followed by slow evaporation of the solvent. 300 mg of Polyethylene Oxide (Aldrich, Mw = 400 k) and 50 mg of Chitosan (Aldrich, medium Mw, 75-85% degree of deacetylation) were dissolved in 25 cm^3 of acetic acid 2 wt % at room temperature. A *y* cm^3 of stable aqueous colloidal solution of TiNT (where *y* was varied in range from 50 to 500 cm^3) was added to the solution of polymer under stirring. The solvent was then slowly evaporated in a rotary vacuum evaporator under reduced pressure (ca. 100 mbar), moderate temperature in the bath (55 ºC), and constant spinning (100 rpm) until the final mass of the viscous solution was ca. 5g, which corresponds to the 6 wt % and 1 wt % of PEO and CS in solution respectively. The samples were cast into flat glass slide moulds and dried at room temperature (22 ºC) and atmospheric pressure. Thickness of the films measured with the optical 3D microscope (Infinite Focus, Alicona, Austria) varied in a range from 20 to 180 µm. The ratio between nanotubes and polymers was calculated using the quantity of added TiNT that varied from 0 to 30 wt % with respect to solid polymers. The dried films were peeled off, turned upside down and fixed to a glass slide with epoxy resin, after which they were used for further studies on mechanical and tribological properties (see Section 3.3.5).

(ii) Polyethylene oxide / chitosan filled with inorganic elongated nanostructured materials

Incorporation of elongated ceramic metal oxide nanostructured materials to mixed matrices composed of polyethylene oxide / chitosan was systematically studied in order to investigate their mechanical and tribological performance following the procedure aforementioned in the section above. The elongated materials used in the preparation of

PEO/CS composite thin films were: naturally occurred halloysite nanotubes (Sigma Aldrich, cat. no. 685445), synthetic germanium-imogolite nanotubes produced and kindly supplied by White *et al*. [349], short titanate nanofibres synthesised by the alkaline hydrothermal method in potassium hydroxide, long titanate nanofibres synthesised by the alkaline hydrothermal method in sodium hydroxide and titanate nanotubes stirred in an aqueous solution of pyrrole 3 mol dm^{-3}. The concentration of elongated materials with respect to dry polymer varied between 0 and 7.5 wt %.

(iii) Polyethylene oxide / chitosan / TiNT as a function of nanotubes length

The length in nanotubes was controlled by breaking initial long nanotubes via ultrasound treatment of colloidal suspension of TiNT [29]. The solutions of TiNT with polymer were sonicated for 0.25, 0.5, 1, 2 and 3 hours, in an ice bath sequentially every three minutes to avoid overheat using a HD3200 Sonopuls Ultrasonic Homogenizer (purchased from Monmouth Scientific Ltd, UK) with a 6 mm diameter titanium alloy probe KE76 prior to casting. Sonication parameters were: 0.005 s pulses, frequency of 20 kHz and 50 % of the energy output of 100 W.

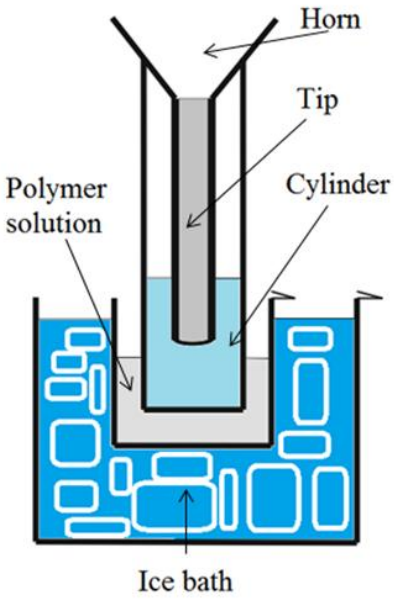

Figure 3.2. Arrangement for ultrasound treatment of colloidal suspensions of nanotubes in the presence of polymers. A glass cylinder is placed in between the sample and the probe to avoid debris contamination. The figure is not drawn to scale.

For the purpose of avoiding crossed contamination of the sample with debris from the eroded probe tip during ultrasound treatments, the tip and the liquid samples were separated by a glass tube filled with 30 cm^3 of distilled water. The concentration of TiNT was fixed at 4.7 wt % in a mixed matrix PEO:CS 6:1. Further mechanical and tribological characterisation was performed on drop-cast films as a function of ultrasound duration (see Section 3.3.5). Figure 3.2 depicts an illustration of the experimental arrangement.

3.2.2 Polymer composite electrospun fibres

(i) Polyethylene oxide based electrospun microfibres

Aqueous colloidal suspensions of TiNT obtained by long term stirring were added to polymer solutions composed of PEO:CS 6:1 following the procedure reported in the previous Section 3.2.1 prior to electrospinning. It is known that TiNT are characterised by negative zeta potential when pH is higher than 2 whereas the cationic polymer chitosan develops a good affinity towards such nanotubes, which improves the interactions polymer-nanotube and the dispersion of nanotubes within the matrix as it will be further discussed in Chapter 5. However, the presence of an electric field within the proximity of the needle wall during electrospinning might result in an electrophoretic motion which affects adversely the dispersion of nanotubes within the matrix as it will be explained in Chapter 6.

Alternatively, a different strategy was simultaneously pursued in order to improve the dispersion of titanate nanotubes within electrospun polymer microfibres by the introduction of new additives (e.g. a cationic surfactant). Firstly, colloidal suspensions were produced by long-term mechanical stirring of TiNT in aqueous solutions of the cationic surfactant CTAB 10 mmol dm^{-3} as described in Section 3.1.4. Meanwhile, 400 mg of Polyethylene Oxide (Aldrich, Mw = 400 k) was dissolved in 25 cm^3 of distilled water at room temperature. A *z* cm^3 of stable aqueous colloidal solution of TiNT in CTAB (where *z* was varied in the range from 25 to 200 cm^3) was added to the solution of polymer under vigorous stirring overnight. The solution was concentrated in a rotary vacuum evaporator under reduced pressure (ca. 100 mbar), moderate temperature in the bath (55 ºC) and constant spinning (100 rpm) until the final mass of the viscous solution was ca. 5g. The content of TiNT-CTAB varied in a wide range from 0 to 13 wt % with respect to dry PEO.

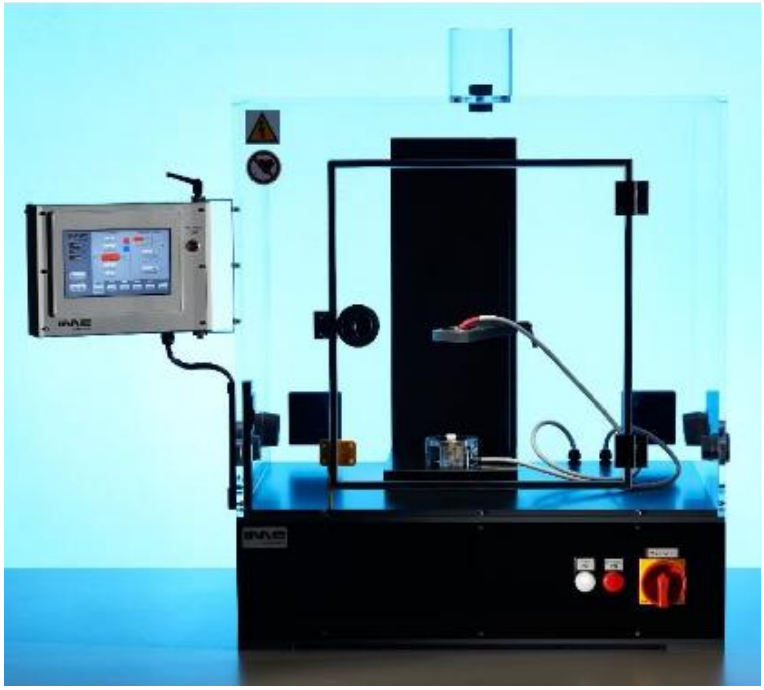

Figure 3.3. Electrospinning apparatus EC-DIG purchased from IME Technologies, The Netherlands. Image reproduced from the company brochure.

Solutions were loaded into a plastic syringe connected to a 0.80 x 22 mm, 21G x 7/8 " blunt tip needle prior to electrospinning. Polymer composite microfibres were produced using an electrospinning apparatus EC-DIG (purchased from IME Technologies, the Netherlands). The experimental parameters were: feeding rate from 0.15 to 0.5 cm^3 h^{-1}, electrospinning voltage from 15 to 21 kV, tip to collector distance from 15 to 25 cm and room temperature oscillated from 19 to 22 ˚C. Experiments were arranged both vertically and horizontally over a span of 2 to 45 minutes. Polymer composite microfibres were collected on aluminium foil, TEM copper grids and silicon wafers for subsequent characterisation. Figure 3.3 shows the commercially available electrospinning arrangement from IME Technologies.

(ii) Polyimide based electrospun microfibres

An alternative approach was made in the electrospinning of polyimide microfibres filled with titanate nanotubes. A polyamic acid intermediate (PAA) is produced by the polycondensation of an equimolar mixture of the monomers 4,4’-oxydianiline (ODA) and pyromellitic dianhydride (PMDA) in dimethylformamide (DMF). The PAA solution is electrospun followed by a chemical cyclodehydration in a mixture of acetic

anhydride/pyridine 8:7 and subsequently treated in a furnace at 120 °C for 1 hour. Electrospinning parameters were: polymer concentration from 15 to 25 wt %, applied voltage between 15 and 25 kV, tip to collector distance between 15 and 35 cm and feeding rate from 100 to 250 µl h^{-1}.

Two different methodologies were followed in the addition of TiNT-CTAB in electrospun polyimide microfibres namely *in situ* and *ex situ* polymerisation. TiNT-CTAB and a solution of the monomer ODA in DMF are stirred before polymerisation with the other monomer PMDA in the former whilst polymerisation of ODA and PMDA occurs before dispersion of titanate nanotubes within the PAA matrix (see Section 6.5). Chemical/thermal cyclodehydration in acetic anhydride/pyridine is carried out to obtain the final polyimide electrospun fibres in both cases.

3.3 Characterisation of samples

3.3.1 Transmission electron microscopy

All solid samples were examined via transmission electron microscopy (TEM). Copper grids with perforated carbon film (Agar Scientific) were covered with finely powdered sample several times whereas polymer composite fibres were electrospun directly onto the copper grids. Composite thin films were deposited directly onto copper grids by spin-coating from dilute solutions to investigate dispersion of nanotubes within the polymer matrix. An aliquot of 10 µL of a fourfold diluted PEO:CS:TiNT=6:1:1 solution was dropped onto a copper grid attached to double sided carbon tape and spun at 3000 rpm for 60 s. Providing that the thickness of the film is small enough for the electron beam to penetrate it, one can obtain the cross section of the composite film.

Furthermore, length distribution histograms of titanate nanotubes sonicated in aqueous media in the presence of polymer were built from TEM micrographs before and after 3 hours of ultrasound to confirm nanotube scission. The length of at least 100 nanotubes was measure at higher magnification using digital imaging software (Corel Draw). TEM micrographs were recorded with a JEOL 3010 transmission electron microscope operating at an accelerating voltage of 300 kV. It should be noted that transmission electron microscopy only characterises a small quantity of the sample. Therefore, a minimum number of 20 images from different areas are required to analyse each sample as well as

complementary techniques where possible to ensure that micrographs represented the entire sample as accurate as possible.

Moreover, randomly oriented fibrous non-woven mats produced by electrospinning were deposited directly onto TEM copper grids with perforated carbon film to investigate both dispersion and orientation of titanate nanotubes within the matrix in electrospun microfibres.

3.3.2 Scanning electron microscopy

Scanning electron microscopy (SEM) samples were prepared by depositing material onto silicon wafers attached to conductive studs through double-sided carbon conductive tape. SEM images were recorded using a JEOL 6500 FEG-SEM thermal emission scanning electron microscope operating at accelerating voltage of 15 kV.

Length distribution histograms of titanate nanotubes were built from SEM images in order to investigate both nanotube fragmentation and scission rate in various solvents (see Section 3.1.5). Colloidal suspensions of nanotubes were diluted under vigorous stirring for each data point. These suspensions were deposited onto ultrasonically-cleaned silicon wafers and were left in air until the solvents had totally evaporated. SEM images were analysed using digital imaging software (Corel Draw). The length of at least 100 nanotubes was measured for each sample in order to build length distribution histograms as well as to plot mean length of nanotubes as a function of duration of sonication for each solvent.

Morphology in both neat polymer and polymer composite electrospun microfibres was studied by scanning electron microscopy. For this purpose, solutions containing polymer and nanotubes were directly electrospun onto ultrasonically-cleaned silicon wafers and analysed thereafter without further gold coating. Imperfections along the length of as-spun microfibres such as beading which is related to low polymer chain entanglement or aggregations of nanotubes which might be associated with either poor initial dispersion of nanotubes or an electrophoretic effect developed during the electrospinning process (see Chapter 6) can be identified via SEM micrographs.

3.3.3 Optical microscopy

Surface topography and roughness measurements were performed on drop-cast polymer composite films with an optical 3D microscope (Infinite Focus, Alicona, Austria). Special attention was paid to the measurement of the thickness in polymer composite films, which is an indispensable preliminary analysis prior to nanoindentation since the penetration contact depth of the indenter in the determination of mechanical properties cannot exceed a tenth of the total specimen thickness (see Section 3.3.5 below). Residual depths and permanent plastic deformation as a result of nanoscratch and nanoindentation testing can be visualised and measured on the composite surface using the optical 3D microscope with a vertical resolution as accurate as 10 nm.

3.3.4 Nitrogen adsorption

Nitrogen adsorption isotherms were recorded at 77 K for analysis of specific surface area, pore volume and pore size distribution of a palladium catalyst supported on carbon lot A17Y002 (see Appendix B) using a Micrometrics Gemini 2375 Surface Area Analyser. The solid sample was heated to high temperature at 200 ˚C and outgassed under vacuum at evacuation rate of 100 mm Hg min^{-1} for 1 hour. The mass was then measured with a balance accurate to ± 0.5 mg. The ambient pressure, P_0, was measured and data points were collected for adsorption and desorption at various pressure, P, between $0 < P/ P_0 < 1$ using nitrogen gas (N_2). The adsorption and desorption isotherms were plotted as volume per unit mass of sample ($cm^3 g^{-1}$) using a nitrogen equation of state at 77 K.

Data points in the range 0.15 and 0.35 of relative pressure were used to calculate BET specific surface area on the N_2 adsorption isotherm. The specific total pore volume was calculated from the area under the desorption isotherm, which was defined as the volume of nitrogen adsorbed per gram of material ($cm^3 g^{-1}$) at relative pressure $P/P_0 = 0.97$.

Evaluation of BJH pore distribution was calculated with the Halsey formula to determine the thickness of liquid nitrogen [350]. Distributions were determined for both adsorption and desorption parts of the isotherm. However, the desorption isotherm is used in preference to determine pore-size distributions because of the spherical shape of the gas-liquid interface in desorption. Few analytical artefacts can be identified due to collapse of the nitrogen film at the interface. The cumulative specific pore volume of the sample was defined as the volume of nitrogen per gram of material ($cm^3 g^{-1}$).

3.3.5 UV-visible spectrometry

The concentration of titania (with respect to Ti (IV)) in colloidal suspensions was determined using a UV-visible spectrophotometer (Neosys-2000, Scinco) by measuring the characteristic absorbance band at 280 nm in fused quartz cuvettes using the molar extinction coefficient $\varepsilon = 5900$ dm^3 mol^{-1} cm^{-1} for TiNT at this wavelength. The obtained aqueous colloidal suspensions of TiNT are stable for more than a year at room temperature and the concentration of titania varies typically between 300 and 800 mg dm^{-3} (see Section 4.3.1).

The concentration of ibuprofen filled in titanate nanotubes both coated and uncoated by polypyrrole was determined in NaOH 0.1 mol dm^{-3} by the measurement of the characteristic absorbance band of ibuprofen at 225 nm wavelength [351] in fused quartz cuvettes. The molar extinction coefficient was calculated from the slope of the calibration curve $\varepsilon = 6460$ dm^3 mol^{-1} cm^{-1} at this wavelength. A blank solution of nanotubes coated by polypyrrole (TINT-PPy) in NaOH 0.1 mol dm^{-3} was subtracted from the samples TiNT-IB-PPy and TiNT-IB-PPy-Us.

3.3.6 Nanoindentation and nanoscratch testing

Mechanical and tribological properties of the polymer composite films (see Section 3.2.1 for film preparation details) were tested using a nanoindenter Nanotest Platform 3 (Micro Materials Ltd, UK), which is a pendulum-based depth-sensing system and the load is applied electromagnetically. When the electric current reaches the coil, the pendulum rotates so the indenter tip penetrates the specimen. Displacement is recorded using a capacitor with sub-nanometre resolution [301]. A three-sided pyramidal Berkovich indenter was used to measure hardness and elastic modulus of the films. Typical experimental conditions for indentations were: maximum load = 1.0 mN, loading rate = unloading rate = 20 mN s^{-1} with 30 s dwell at maximum load. A matrix of 14 x 14 (196) load-controlled indentations was arranged to ensure that measurement of mechanical properties represented the entire sample as accurate as possible. The load-displacement curves were analysed using the Oliver and Pharr method [297] with analytical software provided by Micro Materials Ltd.

Nanoscratch testing was performed with the same equipment. Scratching resistance was investigated by repeating alternate off-load and on-load scratch tests. A spherical diamond

tip with 10 μm radius was used in the tests. A low load of 0.1 mN was applied in the initial topographic scan, length of 500 μm, scan speed of 16.67 μm s^{-1}, after which the tip was moved back to the starting position. Nanoscratch tests were completed along the same track applying a ramp load within the first 90 μm of the total length followed by a constant load of 10, 20 and 50 mN throughout the last 410 μm of the track. After the on-load part of the experiments, the probe was returned to the initial position from which a final topographic scan was repeated at an applied load of 0.1 mN. In the first and third topographic scans, the load was sufficiently low that no wear takes place. Data were corrected during analysis according to the initial topographic scan using analytical software provided by Micro Materials Ltd. Experiments were spaced 100 μm apart and repeated to verify homogeneity of the films and to ensure that results represented the whole samples. Friction coefficient data were calculated from on-load experiments whereas the residual depth data were extracted from the final off-load topographic scans. This friction coefficient μ can be defined as

$$\mu = F_f / F_n$$

where F_f corresponds to the frictional force and F_n corresponds to the normal force.

Due to the unexpected enhanced tribological properties (see Chapter 5) found in PEO:CS=6:1 composite films filled with either long titanate nanofibres (l-TiNF) or short titanate nanofibres (s-TiNF) produced by the alkaline hydrothermal method in concentrated NaOH and KOH 10 mol dm^{-3} respectively (see Section 3.1.3), complementary nanoscratch tests were performed in a total of 24 drop-cast composite films (12 filled with l-TiNF, 12 filled with s-TiNF) with a content of TiNF that ranged between 0 and 7.5 wt % with respect to dry polymer mass in order to investigate such low friction coefficient. Experimental parameters for these nanoscratch tests were virtually identical as previously described with the only difference that a ramp load of 50 mN was applied throughout the full length of the scratch track 500 μm.

Chapter 4: Ultrasound treatment of titanate nanotubes suspended in various solvents

4.1 Introduction

The vast majority of synthetic methods for 1-dimensional nanomaterials yield entangled aggregates of high aspect ratio elongated nanostructures which are affected by high surface area and increased van der Waals forces [28, 332]. A systematic study on the dispersion of titanate nanotubes in various solvents until stable colloidal suspensions are achieved was our first objective. Long-term mechanical stirring coupled with ultrasound treatments is the most extended approach found in literature for a rapid dispersion of nanotubes in common solvents. Acoustic cavitation is the phenomenon by which nanomaterials can be exfoliated under ultrasound from their aggregates to independent nanoparticles. However, such effect can lead to nanotube shortening at the same time depending on several parameters such as temperature, pressure, ultrasound power, duration of ultrasound, solvent and so forth [29, 333].

In the first instance, colloidal suspensions of titanate nanotubes in various solvents were prepared and sonicated over various periods of time. Length distribution histograms of nanotubes were built from electron microscopy micrographs in water, ethanol, dichloromethane, chloroform and bromoform to investigate the solvent dependence on nanotube shortening under ultrasound. In addition, evolution of the scission rate of TiNT in respect of the duration of sonication was further studied.

Both polymer and ceramic coatings might alter mechanical properties of titanate nanotubes, and therefore ultrasound treatments of colloidal suspensions comprised of nanotubes coated by polypyrrole or silica could be used as an alternative method in the indirect measurement of strength of coated nanotubes. An approximate degree of reinforcement might be extracted by comparison with a reference scission rate of neat TiNT in a reference solvent.

The last part of this chapter shows results of ibuprofen encapsulated in titanate nanotubes sealed by polypyrrole and its controlled release under ultrasound treatment. Additional functionalities might be achieved depending on the encapsulated materials in other polymers such as responsive polymer matrix “self-healing” in the presence of a cross-linker released after ultrasonic/mechanical nanotube fragmentation.

4.2 Characterisation using electron microscopy

Titanate nanotubes synthesised by the alkaline hydrothermal method are obtained as large entangled aggregates as it was confirmed by SEM micrographs in Figure 4.1 at low and high magnification. These nanotubes are characterised by a multi-layered structure with a number of layers that can vary from 2 to 10, although 3 or 4 layers seem to be the most commonly found structures for these nanotubes, which was also in agreement with literature [8] and confirmed by TEM techniques as it is shown in Figure 4.2. Agglomerated nanotubes are shown on the TEM image at lower magnification (Figure 4.2a). A single titanate nanotube protruding the aggregate is shown on the TEM image at higher magnification (Figure 4.2b), where characteristic lattice fringes are observed in the multi-walled isolated nanotube (3 layers in this case). The interlayer distance in the protonated form of these nanostructured hydrated titanium dioxide nanotubes with stoichiometric formula $H_2Ti_3O_7$ is 0.72 nm [29]. Further details on characterisation and mechanisms of formation of titanate nanotubes are reported in Section 2.1.2.

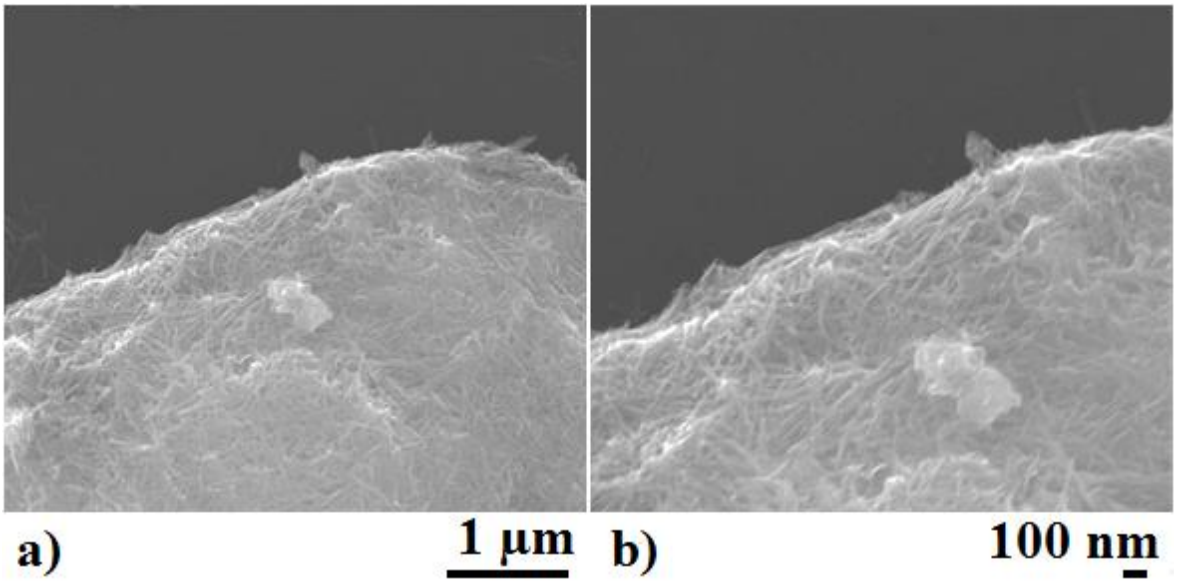

Figure 4.1. SEM micrographs show as-synthesised titanate nanotubes by the alkaline hydrothermal method at atmospheric pressure. They are presented as highly entangled aggregates of nanotubes at low (a) and high magnification (b).

The synthesis of titanate nanotubes in the presence of oleic acid was attempted in order to improve dispersion of such nanotubes in organic solvents such as dichloromethane,

chloroform and bromoform for further ultrasound treatments as it is discussed in Section 4.3.1. The addition of oleic acid *in situ* might result in functionalised nanotubes with hydrophobic tails around the surface in a 1-step reaction; hence more stable colloidal suspensions might be achieved in halogenated solvents.

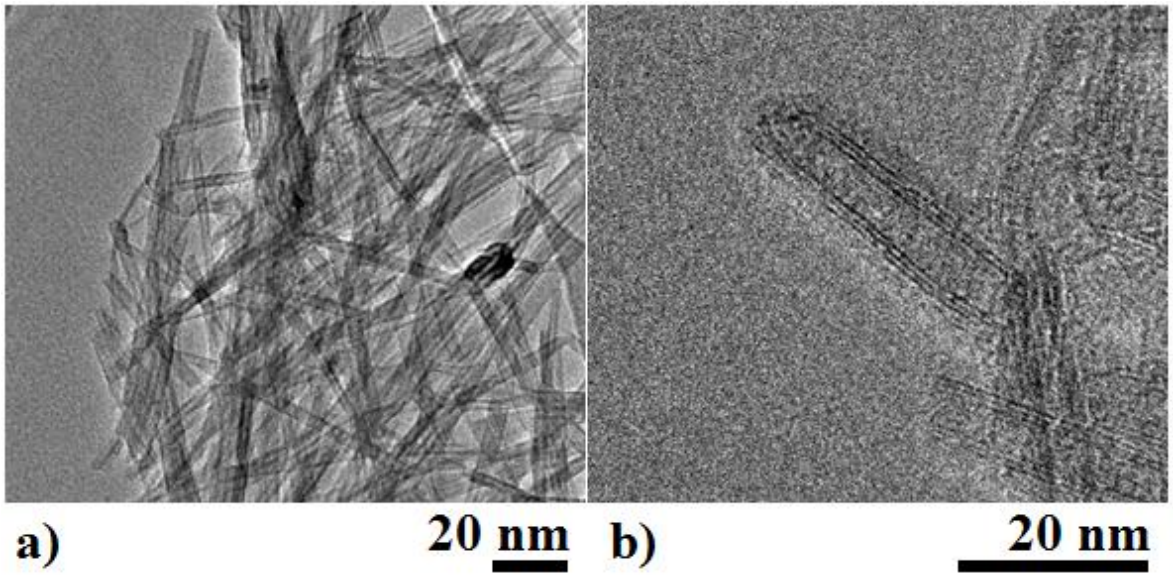

Figure 4.2. TEM micrographs show as-synthesised titanate nanotubes by the alkaline hydrothermal method at atmospheric pressure. Highly entangled aggregate is observed in the left TEM image at low magnification (a). A single titanate nanotube protruding the aggregate is observed in the HRTEM image at higher magnification (b).

However, a mixture of titanate nanofibres and nanotubes (mainly nanofibres) was obtained via the alkaline hydrothermal method confirmed by TEM analysis (Figure 4.3). The top left inset in Figure 4.3 shows a bundle of nanofibres with characteristic lattice fringes while the bottom right inset shows a long titanate nanotube protruding an aggregate. The presence of oleic acid increased the temperature at which reflux begins up to 115 ˚C, which might be a possible explanation for the production of titanate nanofibres. It is essential to maintain the concentration of Ti (IV) constant within a certain range in an alkaline mixture of sodium hydroxide and potassium hydroxide 50:1 [28]. One can speculate that even though the temperature reached during synthesis was not sufficiently high to produce titanate nanofibres, the presence of oleic acid *in situ* might alter the concentration of Ti (IV) in solution and modify the equilibrium of crystallisation of titanates during nanosheet-

nanotube transformation, resulting in titanate nanofibres which are the kinetically-favoured product.

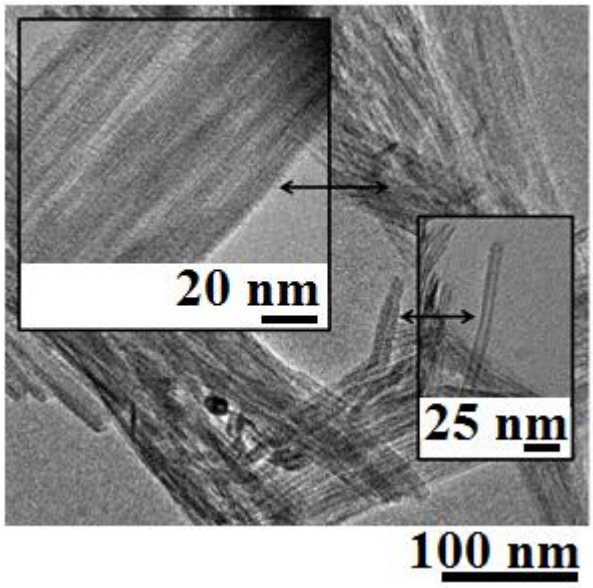

Figure 4.3. TEM micrographs show a mixture of titanate nanotubes and nanofibres produced by the alkaline hydrothermal method in the presence of oleic acid. The top left inset shows a bundle of nanofibres with characteristic lattice fringes. The bottom right inset shows an isolated titanate nanotube sticking out of the large mixture of nanotubes and nanofibres.

Therefore, a different approach was attempted in order to disperse titanate nanotubes in halogenated solvents. CTAB was used to treat all the samples that were then dissolved in halogenated solvents. Functionalization of nanotubes was achieved by adsorption of the surfactant cetyltrimethylammonium bromide (CTAB) on the surface of nanotubes, followed by washing with distilled water and drying prior to mechanical stirring in the selected solvents.

4.3 Ultrasound treatment of TiNT in various solvents

As synthesised titanate nanotubes are usually agglomerated as large bundles of randomly oriented nanotubes. In order to disassemble such several-micron-sized aggregates and disperse single nanotubes into the colloidal solution, ultrasound treatment of powdered TiNT suspended in the suitable solvent is widely used. However, such a treatment was found to result not only in disintegration of nanotube bundles but also in the breaking of individual nanotubes, leading to the reduction of their average length [29]. The average

length of nanotubes added to composite materials could affect mechanical properties of the final product. Therefore, in order to minimize nanotube shortening, the effect of experimental conditions during ultrasound treatment of suspended TiNT and their scission rate was studied. In particular, based on our previous observations that breaking rate is dependent on the nature of the solvent, the effect of the solvent density was systematically studied in a wide range of densities from 0.798 g cm^{-3} (ethanol) to 2.89 g cm^{-3} (bromoform).

4.3.1 Stable colloidal suspensions by long-term mechanical stirring

Stable colloidal suspensions of long nanotubes were prepared by applying minimal mechanical impact via several days stirring of TiNT suspended in various solvents. Figure 4.4 shows a SEM image of colloidal suspension of titanate nanotubes deposited on a silicon wafer after 2 weeks of mechanical stirring in distilled water. It can be seen that large aggregates obtained after synthesis were completely disintegrated as independent and isolated nanotubes. An insignificant percentage of the total amount of nanotubes might reassemble as the solvent evaporates shown in the SEM micrograph.

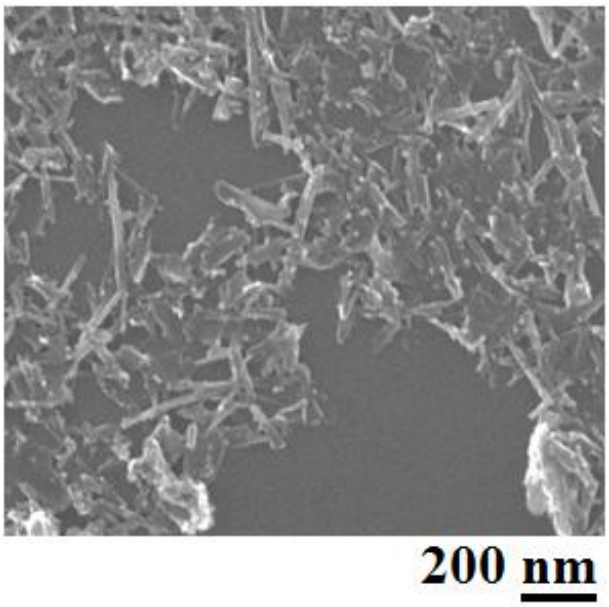

Figure 4.4. Independent titanate nanotubes stirred for 2 weeks in aqueous solution deposited from a colloidal suspension. Nanotubes might reassemble during solvent evaporation.

It was found that the kinetic curve of titania concentration in aqueous solution as a function of the stirring duration has a sigma shape with short induction time after which a rapid growth in concentration is observed followed by a plateau (see Figure 4.5). All samples of colloidal titanate nanotubes were obtained by 2 weeks stirring in various solvents.

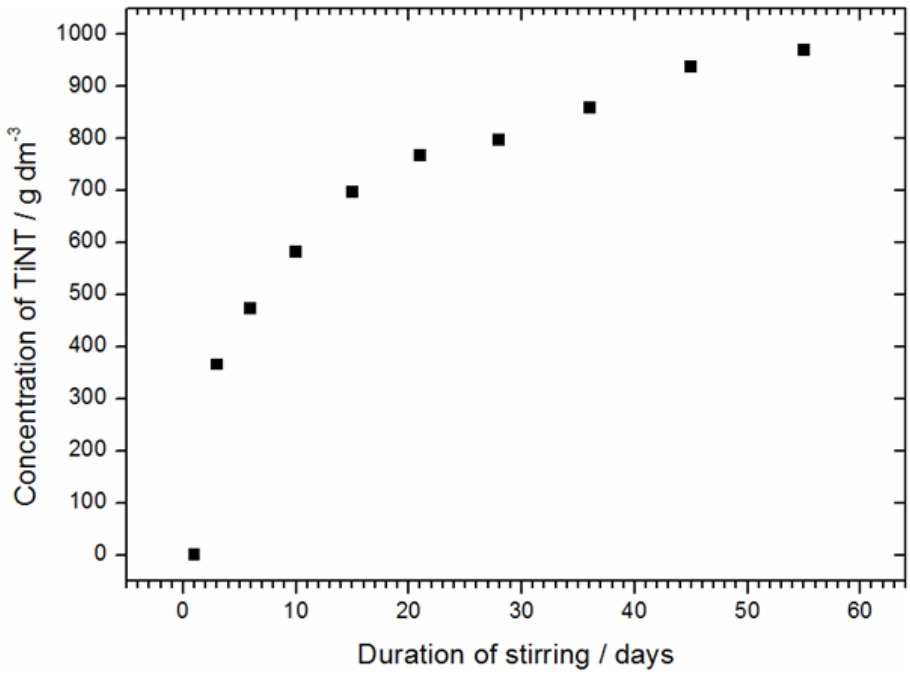

Figure 4.5. Kinetic curve of accumulation of isolated TiNT in distilled water during mechanical stirring of 400 mg of nanotubes suspended in 200 dm^3 of water using a cylindrical PTFE coated steel stirring bar 20 mm long and 5 mm diameter at a rotation rate of 700 rpm.

4.3.2 Nanotubes shortening under ultrasound treatment

Once the nanotubes were well dispersed, ultrasound was applied to the supernatant part of the samples while the sediment was previously discarded. Figure 4.6 shows SEM images of titanate nanotubes deposited on the surface of silicon wafers from colloidal solutions before and after their treatment with ultrasound for 3 hours. SEM data confirm that most of the nanotubes in the colloidal solutions are isolated from bundles. Only a small number of TiNT agglomerates can be found in the samples. Original nanotubes before treatment with ultrasound are characterised by relatively large length, which decreases when ultrasound treatment is applied for 3 hours, as shown in Figure 4.6b. Surprisingly, the same experimental conditions for colloidal nanotubes suspended in ethanol result in almost no change in length as seen in Figure 4.6c.

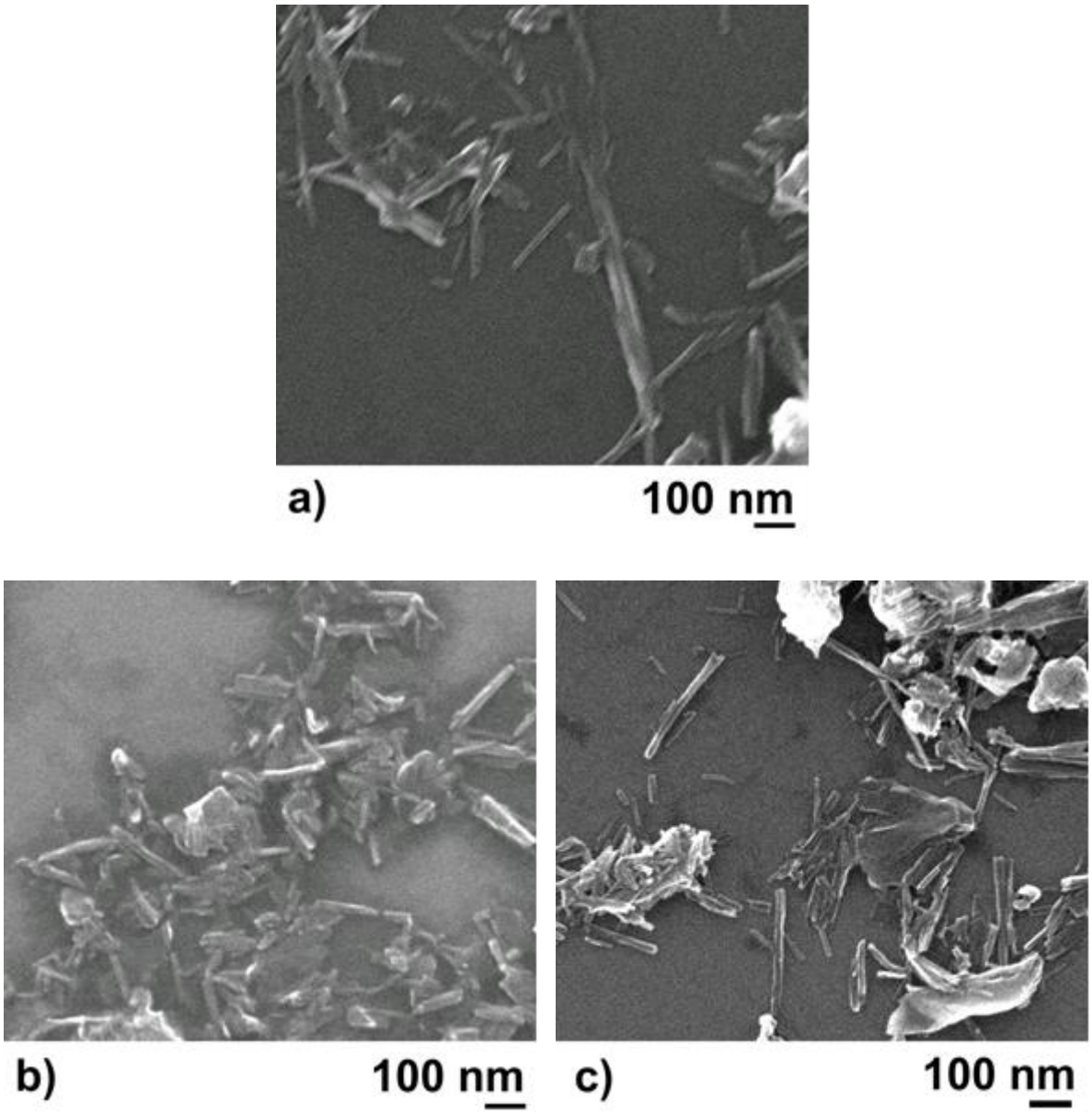

Figure 4.6. SEM images of titanate nanotubes deposited on silicon wafers from colloidal solutions: (a) original nanotubes from aqueous suspension, (b) after 3 hours of ultrasound treatment in water, (c) after 3 hours of sonication in ethanol.

Figure 4.7 shows length distributions of titanate nanotubes in various solvents before and after their treatment with ultrasound for 3 hours. These histograms were built by careful analysis of SEM images of titanate nanotubes deposited on the flat support (silicon wafer) with relatively low surface density of nanotubes (in order to avoid overlapping of nanotubes and their aggregation). The length of more than 100 individual nanotubes was digitally measured to make a statistically significant representation of each experimental

data point. All histograms are characterised by asymmetrical shape with relatively wide width and long tail at large length.

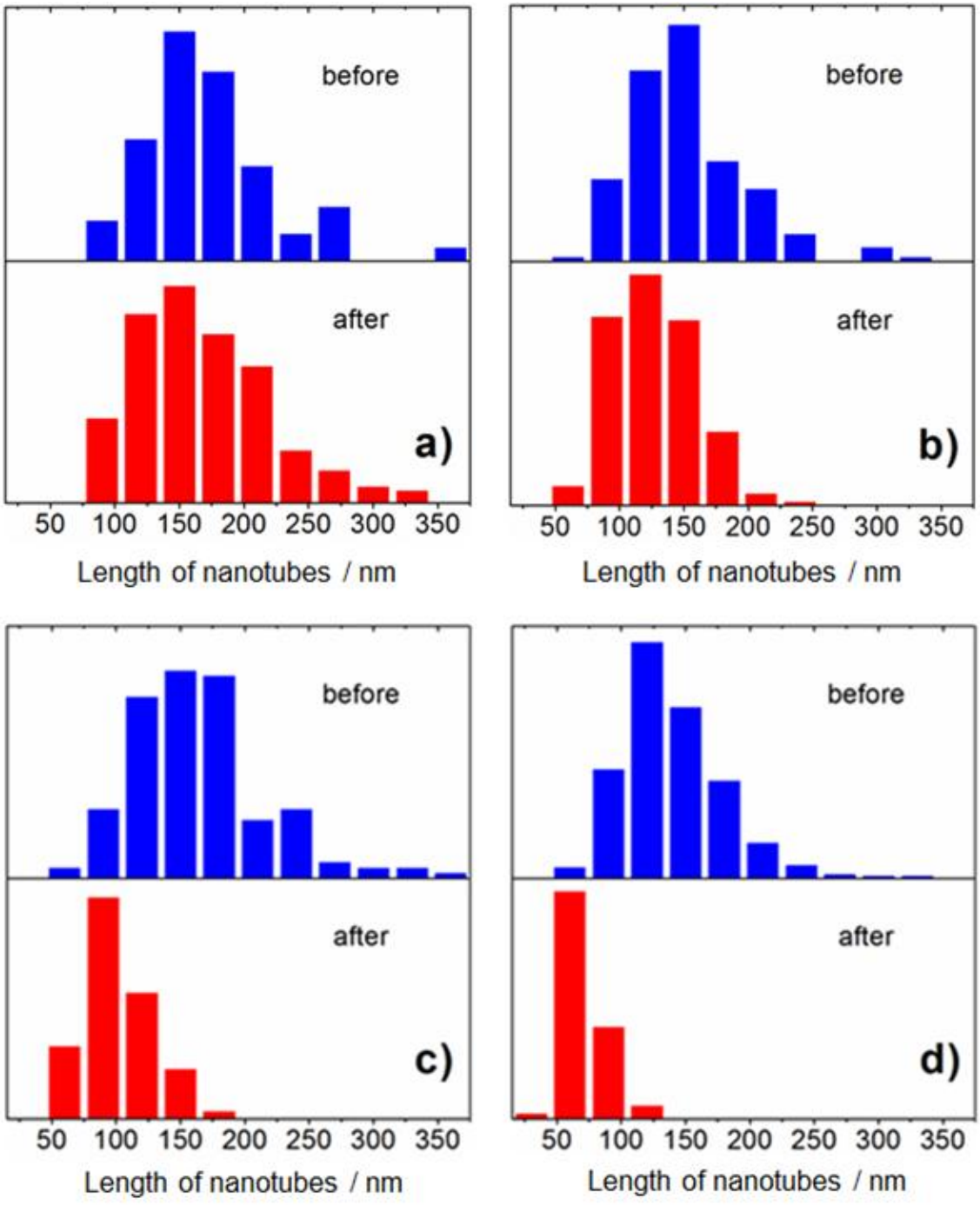

Figure 4.7. Length distribution histograms of titanate nanotubes before and after treatment with ultrasound for 3 hours suspended in (a) ethanol, (b) water, (c) dichloromethane, and (d) chloroform. The histograms were constructed by measuring the number of nanotubes of a particular length from SEM images.

When ethanol was used as a solvent for TiNT suspensions, its ultrasound treatment has resulted in almost no change in length distribution histograms (see Figure 4.7a). In contrast, the same ultrasonic treatment of an aqueous suspension of TiNT has shifted the length distribution towards lower values (see Figure 4.7b) indicating an efficient fragmentation of nanotubes in distilled water. In denser solvents, such as dichloromethane and chloroform (Figures 4.7c and 4.7d respectively), the effect of ultrasound is even more pronounced. For example, relatively long nanotubes (up to 250 nm) were observed after 3 hours treatment in water whereas only a few nanotubes longer than 150 nm could be detected quantitatively in dichloromethane and practically no nanotubes longer than 120 nm were found in chloroform after 3 hours of ultrasound treatment.

4.3.3 Scission rate as a function of duration of sonication in various solvents

Figure 4.8 shows a decrease in the average length of titanate nanotubes during ultrasonic treatment of colloidal TiNT in various solvents such as ethanol, water, dichloromethane, chloroform and bromoform. All kinetic curves follow a power law decay curve which stabilises at certain length. Initial average length of nanotubes decreased rapidly and after 2 hours of ultrasonic treatment there is no significant change in nanotubes length. This final length varies in different solvents and the observed tendency suggests that the denser the solvent, the shorter the terminal length of nanotubes.

Although the phenomenon of nanotubes scission under ultrasound treatment has been widely reported [341, 345], the exact mechanism of their fracture is not well understood. Generally it is considered that the viscous drag forces induced by bubble collapse during cavitation are balanced by mechanical tensile stresses, which are maximal near the centre of the nanotubes. Nanotubes can be broken when the stress exceeds the nanotube tensile strength and the average length of the nanotubes $L(t)$ in this case will be proportional to the time of sonication t^{-n} where $n \cong 0.2$ [347]. We have found, however, that kinetic curves of titanate nanotubes scission under sonication (see Figure 4.8) data do not fit such time power dependence probably due to the fact that it was derived for the nanotubes axially oriented towards centre of the collapsing bubble.

Recently, Pagani *et al.* [335] has reported that if nanotubes are oriented parallel to the surface of the collapsing bubble, the rate of the nanotube buckling is different and therefore $L(t)$ is proportional to the t^{-n} where $n \cong 0.5$. Usually, long nanotubes follow a

buckling mechanism of scission whereas short nanotubes are more likely to orient axially and break as they stretch. As a result, the overall kinetic curve of $L(t)$ decay has a rather steep initial part followed by the long tail where the rate on nanotubes shortening is reduced. Apparent kinetic curve of titanate nanotubes scission characterised by initial rapid decrease of average length probably demonstrate such switch from one mechanism of nanotubes scission to another.

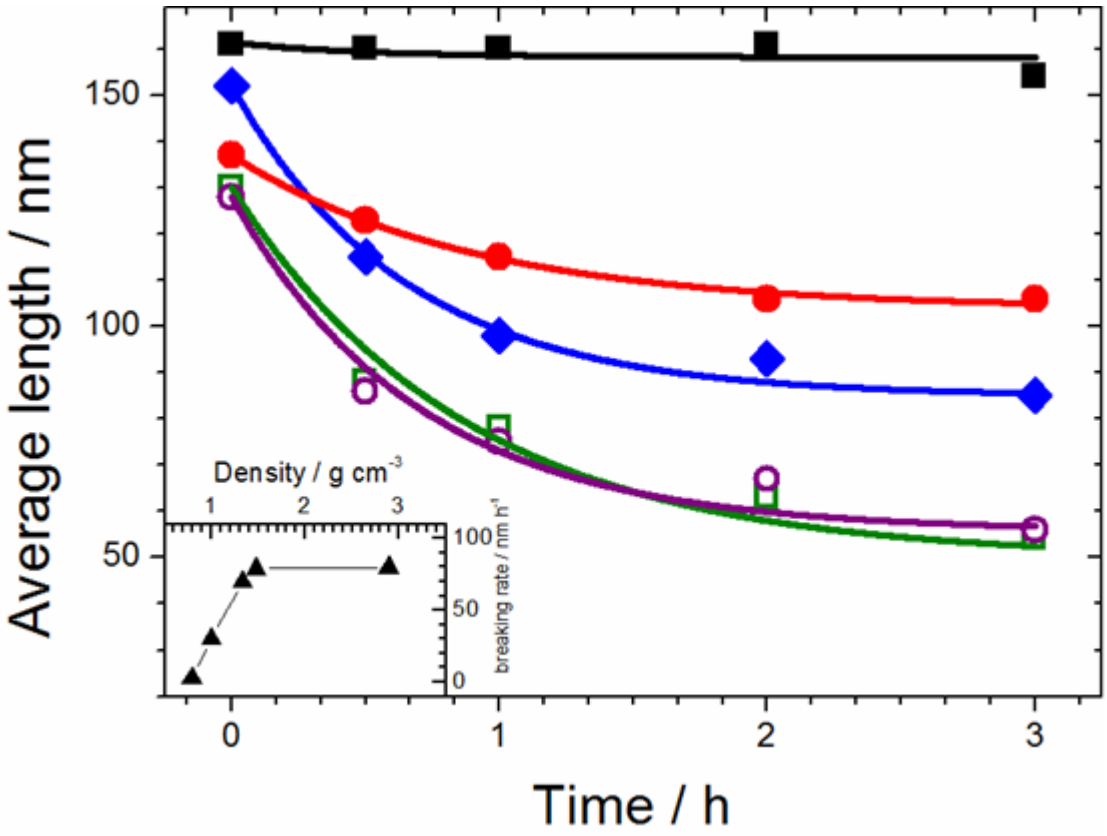

Figure 4.8. Nanotube mean length decay under ultrasonic treatment of ethanol (■), aqueous (●), dichloromethane (◆), chloroform (□) and bromoform (○) suspensions at room temperature. Inset: breaking rate vs. solvent density.

The initial rate of nanotubes shortening in various solvents under ultrasound is also correlated with the density of the media. Apparent initial breaking rate (in nm per hour) as a function of solvent density is shown in the inset in Figure 4.8. For the ethanol, water, dichloromethane and chloroform the rate of nanotubes breaking grows almost linearly with the density of the solvent. However, after chloroform, further increase in density has no effect on the breaking rate.

Such effect of solvent density on the rate of nanotubes scission has not been systematically investigated yet. There are several possible reasons for acceleration of nanotubes scission in denser solvents. Firstly, a switch in the solvent may change the maximal size of the bubbles, resulting in different level of forces occurring during their collapse [341]. Such alteration in the amount of acoustic energy absorbed by the solvent would eventually result in a variation of thermal energy added to the solution. Table 3 shows temperature rise (ΔT) during sonication of 25 cm^3 of all solvents for 1 minute in adiabatic conditions. The initial temperature of the solvents was 25 ºC to avoid errors due to evaporation. The amount of acoustic energy converted into thermal energy can be estimated as $\Delta Q = \rho\ V\ C_p\ \Delta T$ where ρ is density, V is volume and C_p is specific heat of the solvents (see Table 3). It was found that added heat during sonication of solvents varies between 0.35 and 0.76 kJ without correlation with density of the solvent. Such insignificant difference between solvents probably suggests that regime of cavitation and bubble size is almost the same in all selected media.

The second possible difference between solvents could be associated with the strength of the interaction between surface of the nanotubes and solvents affecting values of friction forces. In general, the value of drag force can be strongly affected by the type of the flow in the media. It was shown that at the range of nanotube sizes, a switch between laminar to turbulent flow is possible [352].

Table 3. Properties of the solvents, their temperature change (ΔT) during treatment of 25 cm^3 for 1 minute with ultrasound and estimated thermal energy delivered to the solution.

Solvent	**Density, ρ / g cm^{-3}**	**Viscosity,[a] μ/mPas**	**ρ/μ**	**C_p / J g^{-1} K^{-1}**	**ΔT/ K**	**ΔQ/ kJ**
Ethanol	0.789	1.082	0.729	2.44	11.9	0.570
Water	0.998	0.89	1.121	4.183	7.3	0.762
Dichloromethane	1.33	0.413	3.22	1.21	8.7	0.350
Chloroform	1.48	0.542	2.73	1.05	10.7	0.416

a) Viscosity taken at 25ºC

Table 3 shows values of density (ρ) and viscosity (μ) of the solvents at room temperature. The ratio of density over viscosity (ρ/μ) is growing from 0.73 to 2.73. Assuming that the size of the bubbles is the same for all solvents, the Reynolds number is increasing almost

fourfold from ethanol to chloroform. Such an increase not only changes the level of stress affecting the nanotubes during collapse of cavitation bubble but also can potentially transform laminar flow around the nanotubes to turbulent.

4.4 Polymer and ceramic coatings on TiNT

Ultrasound treatment could be a useful tool to measure indirectly strength in polymer and ceramic coatings of titanate nanotubes. For this purpose, colloidal suspensions of nanotubes were coated with polypyrrole (PPy) and silica (SiO_2) as it was previously mentioned in Section 3.1.7. The polymerisation of pyrrole on the nanotube surface was carried out in two steps. Firstly, hydrogen peroxide reacts with TiNT giving rise to yellow coloured titanate nanotubes species. The hydroxyl groups at the surface of nanotubes are converted into peroxo-complexes which will react with the monomers of pyrrole in the presence of oxalic acid in the second stage. The powdered solid shifted from yellow to dark green as the monomer polymerised. Further polymerisation resulted in a black solid composed of titanate nanotubes and polypyrrole.

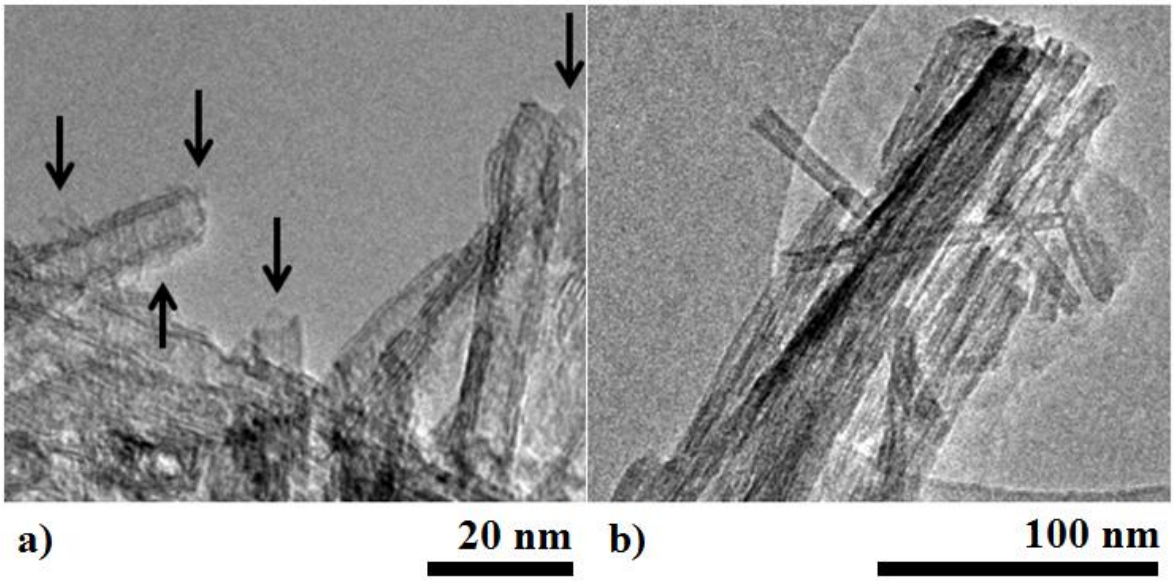

Figure 4.9. TEM images show titanate nanotubes sticking out of a polypyrrole particle. The majority of pyrrole polymerised in bulk. Black arrows (a) show polypyrrole coating on the surface of nanotubes. The TEM image at lower magnification (b) shows a bundle of nanotubes linked by polypyrrole.

The TEM micrograph in Figure 4.9a shows single nanotubes sticking out of a bulk particle of polypyrrole containing nanotubes. The black arrows point polypyrrole coating on the nanotube surface whereas the majority of the monomer polymerised in bulk leading to rather voluminous aggregates of nanotubes entrapped in a polypyrrole matrix and therefore their colloidal suspensions could not be achieved by long-term mechanical stirring due to large particle size. A large bundle of nanotubes joined by polypyrrole is observed on the TEM image at lower magnification in Figure 4.9b. On the left side of the micrograph, a single nanotube is sticking out of the bundle.

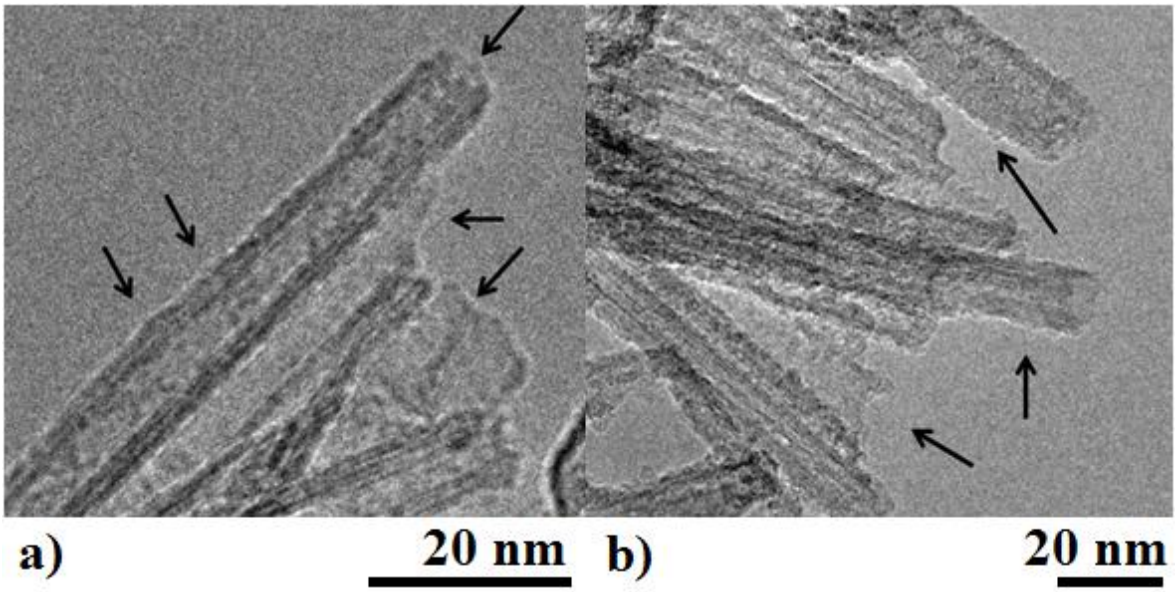

Figure 4.10. TEM micrographs showing thin silica coatings synthesised by the sol-gel method in chloroform (a) and ethanol (b), respectively. Silica grew on the surface and at the end of titanate nanotubes as well as in between nanotubes, filling the pores enclosed by nanotubes which results in large aggregates of TiNT-SiO_2.

An analogous approach was attempted in the sealing of both ends of titanate nanotubes by silica coating. Besides the hypothetical strength measurement via ultrasonication, this method along with polypyrrole coating would allow the encapsulation of selected molecules inside the pores of nanotubes providing new potential functionalities when the elongated carriers break upon ultrasound and release of such chemicals. The black arrows on the TEM images in Figures 4.10a and 4.10b show some thin silica coating synthesised by the sol-gel method in chloroform and ethanol respectively. It is observed ceramic silica

phase on the surface and at the end of the nanotubes emerging from a “lump” of nanotubes linked by silica on both TEM micrographs.

Similarly to nanotubes coated by polypyrrole, colloidal suspensions of titanate nanotubes coated by silica could not be prepared owing to large particle size which caused fast precipitation after long-term mechanical stirring. Therefore, comparable studies of nanotubes both coated and uncoated with silica and polypyrrole could not be explored.

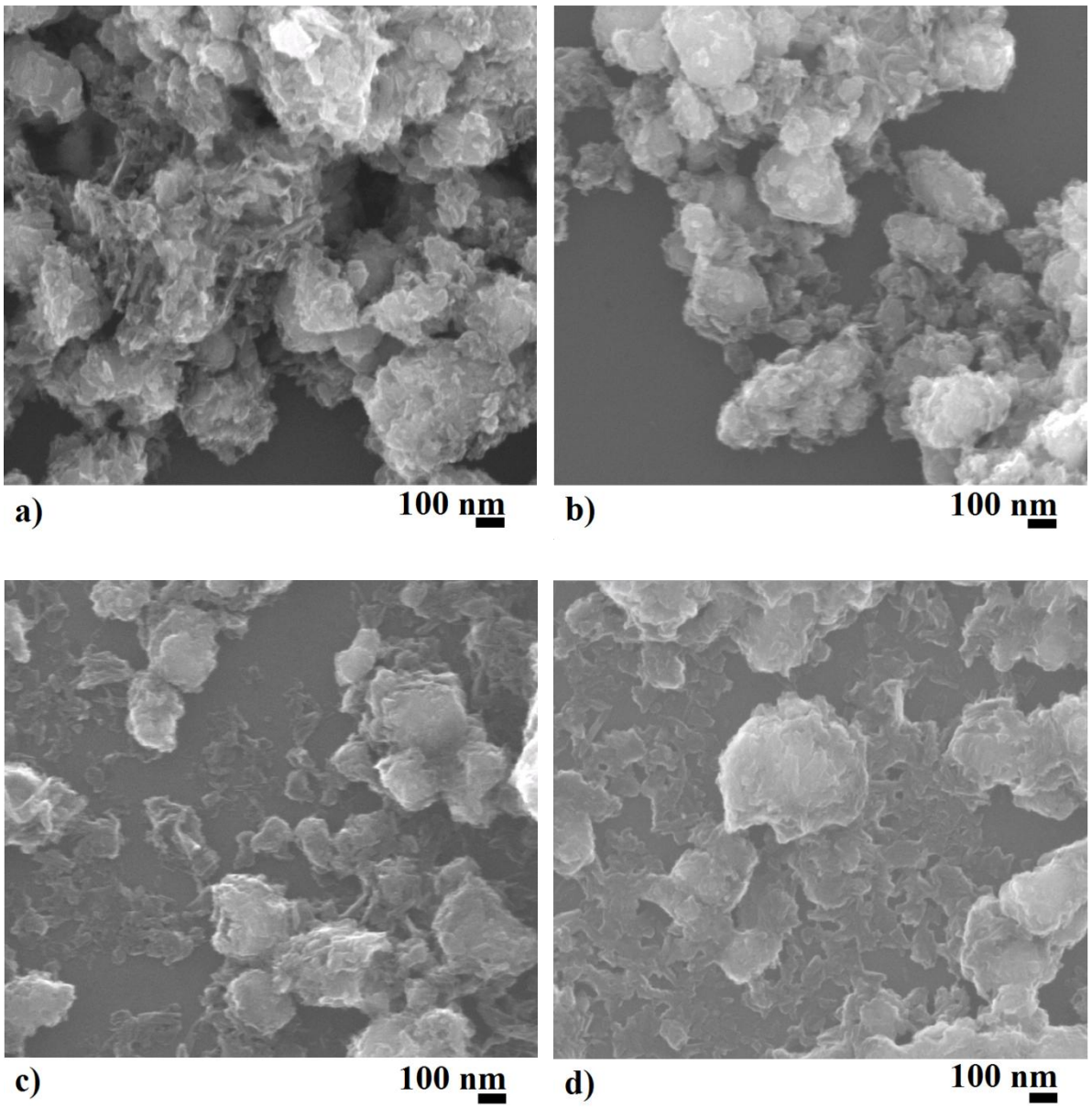

Figure 4.11. SEM images of titanate nanotubes coated by polypyrrole matrix and deposited on silicon wafers from chloroform solutions ultrasonicated for 0 (a, b), 0.5 (c) and 1 (d) hour. Colloidal suspension could not be prepared due to large particle size which induced precipitation. Nanotube fragmentation occurs probably due to a “shaving” effect.

Despite colloidal suspensions could not be made, the dark powdered solid made of titanate nanotubes confined in a polypyrrole matrix (TiNT-PPy) was stirred and ultrasonicated for 0, 0.5 and 1 hour in chloroform. It is believed that breakage of nanotubes occurs under ultrasound treatment at the edge of the polypyrrole bulk for those nanotubes sticking out, which has been termed "shaving effect", whereas the polypyrrole matrix might hinder the fragmentation of the embedded nanotubes acting as a shelter. SEM micrographs in Figures 4.11a and 4.11b show the large particle size of nanotubes fully covered with polypyrrole before ultrasound was applied. As the duration of ultrasound is increased up to 0.5 and 1 h (see Figures 4.11c and 4.11d respectively), the amount and size of TiNT-PPy particles is significantly reduced at the same time as nanotube debris are observed.

Although these results cannot be compared with the data shown in the previous Section 4.3.3, it suggests that nanotubes could be filled with selected molecules and sealed with a polymer matrix, leading us to the idea of controlled release of such chemicals after ultrasound treatment which is further discussed in the next section.

4.5 Encapsulation of ibuprofen in TiNT and release under ultrasound

Since ultrasonication has been confirmed to be an efficient method to fragment nanotubes embedded in polypyrrole matrix shaped as large nanoparticles, incorporation of selected molecules into the inner pores of the nanotubes followed by sealing of both ends of the nanotubes with polypyrrole could result in additional functionalities providing the encapsulated chemical is released after mechanical fracture of such microcapsules via ultrasound. It is worth noting that adsorption of chemicals onto the elongated hollow-like nanotubes can be classified in two types of phenomena (see Figure 4.12). Firstly, adsorption can occur on the surface of titanate nanotubes due to interactions between the free hydroxyl groups and some functional groups of the selected chemicals. A second type of phenomenon is the encapsulation of such chemicals in the empty volume inside nanotubes along their full length followed by nanotube sealing. A thin monolayer of the chemical can be adsorbed on the surface of titanate nanotubes whereas the inner available volume that can be filled is much larger. Moreover, a combination of both types of adsorption within titanate nanotubes is also possible.

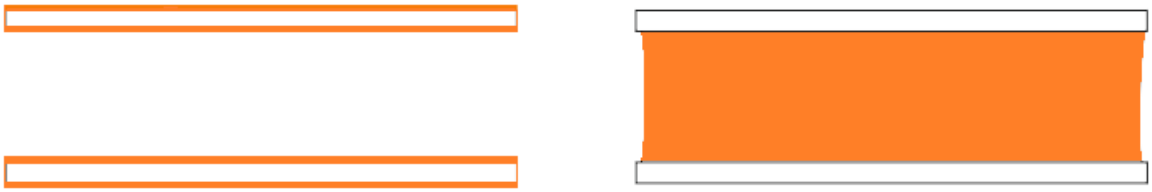

Figure 4.12. Schematic representation of a nanotube cross section with a monolayer of a selected molecule adsorbed on the surface (left) and encapsulated in the inner hollow nanostructure (right).

The molecule chosen to fill titanate nanotubes was ibuprofen or isobutylphenylpropanoic acid. A set of standard solutions of ibuprofen were prepared in order to determine the molar extinction coefficient in the linear part of the calibration curve [351], which corresponds to the slope of the curve at 225 nm ε = 6460 dm^3 mol^{-1} cm^{-1}. Titanate nanotubes were loaded with ibuprofen by the incipient wetness impregnation technique described in Section 3.1.8 after which 2 pyrrole polymerisation cycles were performed to encapsulate ibuprofen.

Concentration of ibuprofen was determined by the characteristic absorbance band of ibuprofen at 225 nm (see Section 3.3.5). Figure 4.13 shows the kinetic curve of ibuprofen release in NaOH 0.1 mol dm^{-3} of three sets of samples: uncoated titanate nanotubes loaded with ibuprofen (TiNT-IB), titanate nanotubes filled with ibuprofen and coated by 2 cycles of polypyrrole (TiNT-IB-PPy) and the latter dispersed in 25 cm^3 of NaOH 0.1 mol dm^{-3} after being treated in an ultrasonic bath for 1 minute (TiNT-IB-PPy-Us). All kinetic curves follow a non-linear saturation curve which reaches the maximum concentration within a short period of time. A rapid ibuprofen release occurs in uncoated TiNT-IB (black squares) dispersed in an alkaline solution reflecting the fact the absence of a protective polymer sealing enables desorption and dissolution of ibuprofen in the alkaline aqueous media.

The concentration of ibuprofen after nanotube sealing with polypyrrole (TiNT-IB-PPy) dropped significantly by a fifth (red circles). Ideally, polypyrrole sealed nanotubes should not release ibuprofen and its concentration in alkaline solution should equal zero. However, TEM micrographs in the previous Section 4.4 confirmed that even though three cycles of polypyrrole coating were performed on neat titanate nanotubes, polymerisation did not occur homogeneously on the nanotubes sticking out of the aggregates leading to bulk polymerisation and uneven coating on independent nanotubes. We can assume that TiNT-IB entrapped in large polypyrrole microparticles are fully sealed and therefore ibuprofen molecules might not be released. In contrast, a minority of open nanotubes at the

edge of the bulk microparticles might be responsible for the low concentration of ibuprofen found. Besides, ibuprofen might be adsorbed on the outer surface of the nanotubes interfering with polymerisation of pyrrole which could result in its rapid desorption in the presence of aqueous alkaline media.

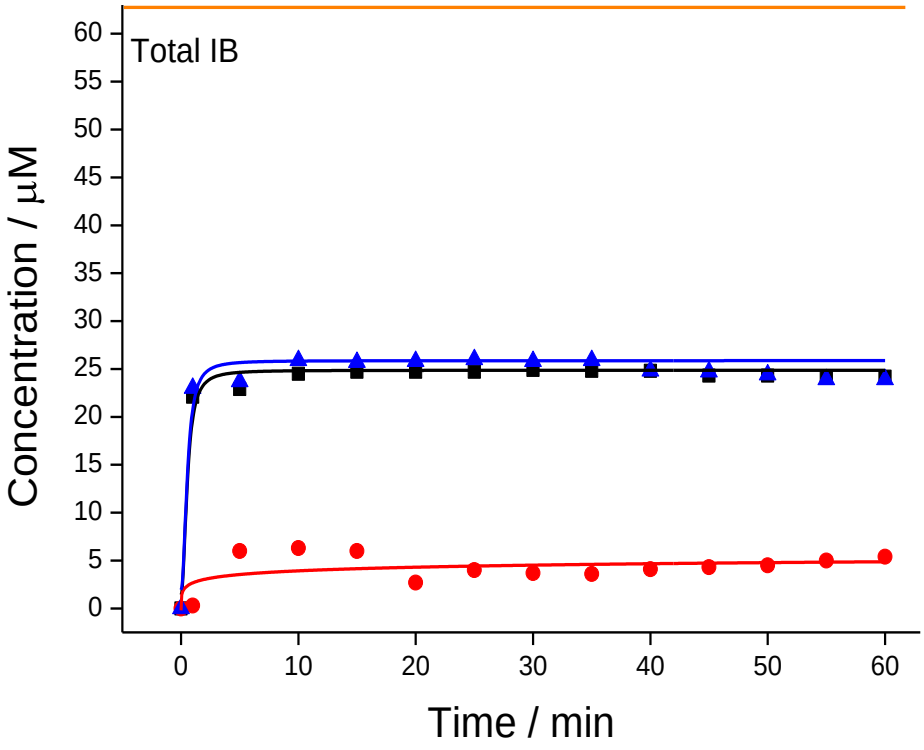

Figure 4.13. Saturation curves of ibuprofen release in NaOH 0.1 mol dm^{-3} for uncoated titanate nanotubes filled with ibuprofen (black squares), polypyrrole coated titanate nanotubes filled with ibuprofen (red circles) and polypyrrole coated titanate nanotubes filled with ibuprofen after 1 minute of ultrasound treatment in an ultrasonic bath (blue triangles). The orange straight line represents the real concentration of ibuprofen introduced in the experiment in the absence of other species.

Ultrasound was applied to filled nanotubes coated by polypyrrole dispersed in 25 cm^3 of NaOH 0.1 mol dm^{-3} in an ultrasonic bath for 1 minute (TiNT-IB-PPy-Us). The kinetic curve of uncoated TiNT-IB (black squares) is almost the same with respect to polypyrrole coated TiNT-IB after sonication (blue triangles), which demonstrates fragmentation of PPy-TiNT in agreement with data in the previous Section 4.4. The quantity of ibuprofen released into solution is virtually the same compared to the amount measured for uncoated titanate nanotubes, which supports the idea that ultrasound uncapped tubular nanocarriers

and opened up a path for ibuprofen to flow into solution. It remains uncertain why the concentration of ibuprofen in sonicated nanotubes is higher than the concentration of uncoated titanate nanotubes. Addition of oxalic acid during polymerisation of pyrrole might alter the dynamic adsorption equilibrium of ibuprofen on the nanotube surface. The chemical could be trapped within the polymer matrix followed by their release due to particle disintegration upon ultrasound. Another possible explanation is that the rapid initial release of ibuprofen might be caused by the resuspension of ibuprofen crystals in the basic media whilst the remainder stays irreversibly bound to the nanotubes.

The orange straight line drawn at 63 μmol dm^{-3} represents the starting concentration of ibuprofen before polymerisation considering the total quantity of the chemical loaded into titanate nanotubes. It is suggested that further experiments should be carried out in order to clarify such divergence in the concentration of ibuprofen found in solution for both uncoated and sonicated nanotubes (ca. 60 % difference). Although the affinity of certain functional groups for the hydroxyl groups on the surface of titanate nanotube (e.g. ammonium salts) could cause strong molecular binding due to interactions between nanotubes and chemicals, this idea can be discarded for the case of an organic acid as ibuprofen.

4.6 Conclusions

Stable colloidal suspensions of titanate nanotubes synthesised by the alkaline hydrothermal method under atmospheric pressure and low temperature (100 ˚C) were successfully achieved by long-term mechanical stirring in several solvents, although the incorporation of the surfactant cetyltrimethylammonium bromide (CTAB) was essential to disperse TiNT in dichloromethane, chloroform and bromoform. Ultrasound was applied in order to study fragmentation of such nanotubes dispersed in various solvents as colloids. Length distribution histograms of titanate nanotubes are strongly dependent on the solvent in which they are dispersed. It has been found that long ultrasound treatment of nanotubes in ethanol has resulted in almost no change in the length distribution whereas length distributions shifted towards lower values as the solvent density is increased in water, dichloromethane, chloroform and bromoform after 3 hours of sonication treatment.

Scission rate of titanate nanotubes suspended in various solvents was studied as a function of duration of sonication time. A rapid decrease in the average length of TiNT was found

in the first 2 hours of ultrasound followed by a lower breaking rate as the samples were further ultrasonicated except for nanotubes dispersed in ethanol where the average length of the nanotubes barely changed after 3 hours of ultrasound. Therefore, nanotube fragmentation is more likely to occur for longer nanotubes whilst it becomes much harder as the nanotube length is reduced. Terminal length varies in all different solvents, which has been found shorter in denser solvents. A clear correlation between the acoustic energy dissipated as heat and the acceleration of nanotubes scission in denser solvents could not be found. However, a switch between laminar to turbulent flows might be responsible for such a difference in the comminution of nanotubes due to a fourfold increase in the Reynolds number for the selected solvents, which might alter the collapse of bubbles during cavitation.

Ceramic and polymer coatings of titanate nanotubes have been prepared by the sol-gel method (silica coating) and *in situ* polymerisation (polypyrrole coating), respectively. Although indirect measurement of the strength of these coatings could not be investigated via sonication due to large particle size, we have demonstrated that ultrasound can disintegrate large aggregates of polypyrrole coated nanotubes. More interestingly, this approach could provide additional functionalities after incorporation of selected molecules into the inner pores of nanotubes, depending on the encapsulated chemical. In our experiments, we have sealed ibuprofen by coating both ends in nanotubes with a film of polypyrrole followed by their release after a mechanical fragmentation via ultrasound treatment. The concentration of ibuprofen found in alkaline aqueous solutions was significantly reduced by a fifth after nanotubes were coated by polypyrrole. Such polypyrrole coated nanotubes containing ibuprofen were subsequently treated in an ultrasound bath, after which particles were fragmented leading to ibuprofen release. The kinetic curve of ibuprofen release in alkaline aqueous media found in uncoated nanotubes was virtually the same as for ibuprofen encapsulated in polypyrrole after ultrasonication.

Chapter 5: Polyethylene oxide / chitosan composite films reinforced with titanates and various elongated materials

5.1 Introduction

Physical and chemical properties of composite materials made of two or more constituent materials differ significantly with respect to their individual components. The purpose of the combination of constituents usually is to enhance specific characteristics in the final material for a definite application. The development of nanotechnology in the last couple of decades has improved the study and investigation of inorganic nanofillers incorporated into polymer matrices. Among the wide range of nanostructured materials used in the manufacture of composites, we have focused on a particular morphology of nanofillers with high aspect ratio which is thought to be essential for the enhancement of mechanical properties.

Despite the fact that carbon nanotubes is the most common tubular nanostructure used in the fabrication of polymer composite materials due to their outstanding properties, certain limitations such as their homogeneous dispersion as independent and debundled nanotubes within the composite material along with their tendency to reassemble for high contents encourages the search for alternative cost-effective elongated nanostructured materials. Metal oxide elongated nanomaterials has been previously suggested as potential alternatives for the reinforcement of polymer matrices in Chapter 2 such as titanate nanotubes, titanate nanofibres and aluminosilicate nanotubes like halloysite and imogolite.

In this chapter, we will focus in the manufacture and systematic study of drop-cast polymer composites made up of both biocompatible and water soluble polyethylene oxide and chitosan mixed matrix reinforced with various elongated metal oxide nanostructured materials as a function of content of nanofillers and length controlled by ultrasonic fragmentation, which have been characterised by electron microscopy as well as mechanical and tribological characterisation at the nanoscale by nanoindentation and nanoscratch testing, respectively. Although PEO-based composites are less practical compared to commercial polymer mixtures, the established method of dispersion of nanofillers within soluble polymers allows us to obtain composites with a large range of composition. The found improvements of mechanical and tribological properties of

polymers such as hardness, Young's modulus and friction coefficient suggest the great potential of titanates as fillers for polymer composites.

5.2 Dispersion of titanate nanotubes within polymer matrix

Titanate nanotubes synthesised by the alkaline hydrothermal method and stirred in aqueous media to obtain stable colloidal suspensions were used in the preparation of polyethylene oxide / chitosan (PEO:CS=6:1) composite films following the procedure described in Section 3.2. To determine the degree of uniformity of TiNT dispersed within PEO/CS polymer matrix, a thin composite film has been deposited directly onto the holey carbon coated copper grid (TEM specimen) by spin coating from a diluted solution. Providing that the thickness of the film is sufficiently small for the electron beam in the TEM to penetrate it, one can obtain the cross section of the composite film, clearly identifying contrast dark titanate nanotubes embedded into the polymer matrix.

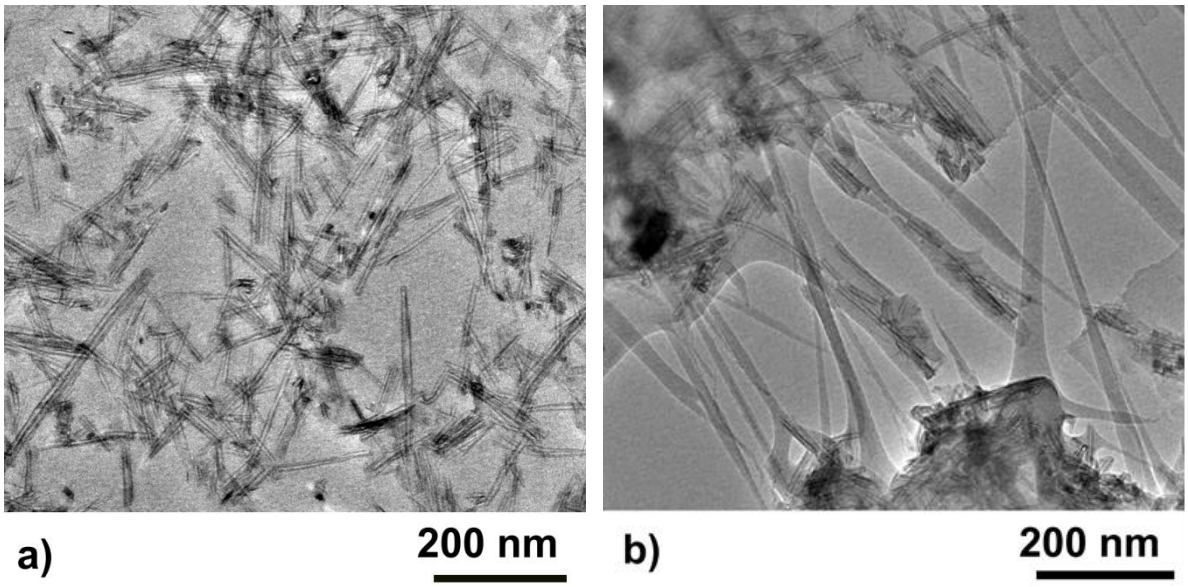

Figure 5.1. TEM images of titanate nanotubes (12.5 wt %) dispersed in the polymer matrix (PEO:CS=6:1 wt %); (a) representative homogeneous film, (b) crack in the film with debris.

Data indicate that nanotubes are randomly oriented and the majority of them are isolated as single tubes with several small aggregates, the percentage of which is insignificant. Figure 5.1a shows a representative TEM image of a thick composite film containing 12.5 wt%

TiNT uniformly distributed within the polymer blend (PEO:CS=6:1). The thickness of the film is relatively high, which results in an observation of nanotubes positioned one above the other and introduces extra difficulties in obtaining a good focus over all objects in the micrograph. Nevertheless, it is clear that the local density of nanotubes within the polymer matrix is approximately the same at different parts of the sample indicating good distribution of nanotubes.

Figure 5.1b shows a TEM image of a rare imperfection in the film (crack) probably induced by its mechanical tearing. Interestingly, the nanotubes are aligned in the perpendicular direction to the crack inside the stretched nanofibrils of the matrix. We can speculate here that improvement of the polymer's mechanical properties can be associated with the formation of such fibrils containing aligned nanotubes, which might hinder the propagation of such a crack and hold the stability of the composite film structure.

5.3 Polymer composite films as a function of TiNT content

Since we established a method of dispersion of TiNT in several solvents producing stable colloidal suspensions of principally isolated nanotubes (see Chapter 4), attempts of mixing such suspensions with polymer solutions were made. It was found that aqueous suspensions of nanotubes can be mixed at room temperature with aqueous acetic solutions of PEO and CS obtaining homogeneous mixtures without precipitation of nanotubes. Due to a limited TiNT concentration in the colloidal suspension, a relatively large volume has to be added to the polymer solution in order to incorporate a high proportion of ceramic nanostructures, which in turn dilutes the mixture. However, this mixture can be concentrated by slow evaporation rate of the solvent at reduced pressure also without coagulation of nanotubes until a desired concentration is achieved prior to drop-casting.

5.3.1 Mechanical analysis using nanoindentation

Hardness (*H*) and reduced Young's modulus (*Er*) of obtained composites have been measured using nanoindentation technique. Despite load-unloading curves were repeatedly measured many times for each sample (a nanoindentation matrix of 14 by 14 indents), results show that hardness or modulus values have a relatively wide standard deviation from their average, which were calculated from the unloading part of the load-

displacement curve. Still, the method of nanoindentation can be used for the investigation of polymer film uniformity at the nano-scale. Figure 5.2 shows the extracted values for hardness (*H*) and reduced Young's modulus (*Er*) as a function of concentration of TiNT with respect to dry polymer in the composite films. The content of TiNT in weight percent in solid films was calculated from the mass of nanotubes added to polymer mixture (PEO and CS in 6:1 mass ratio) which varied from 0 to 30 wt % as follows: 0, 3, 6, 9, 12.5, 15, 20, 25 and 30 wt %.

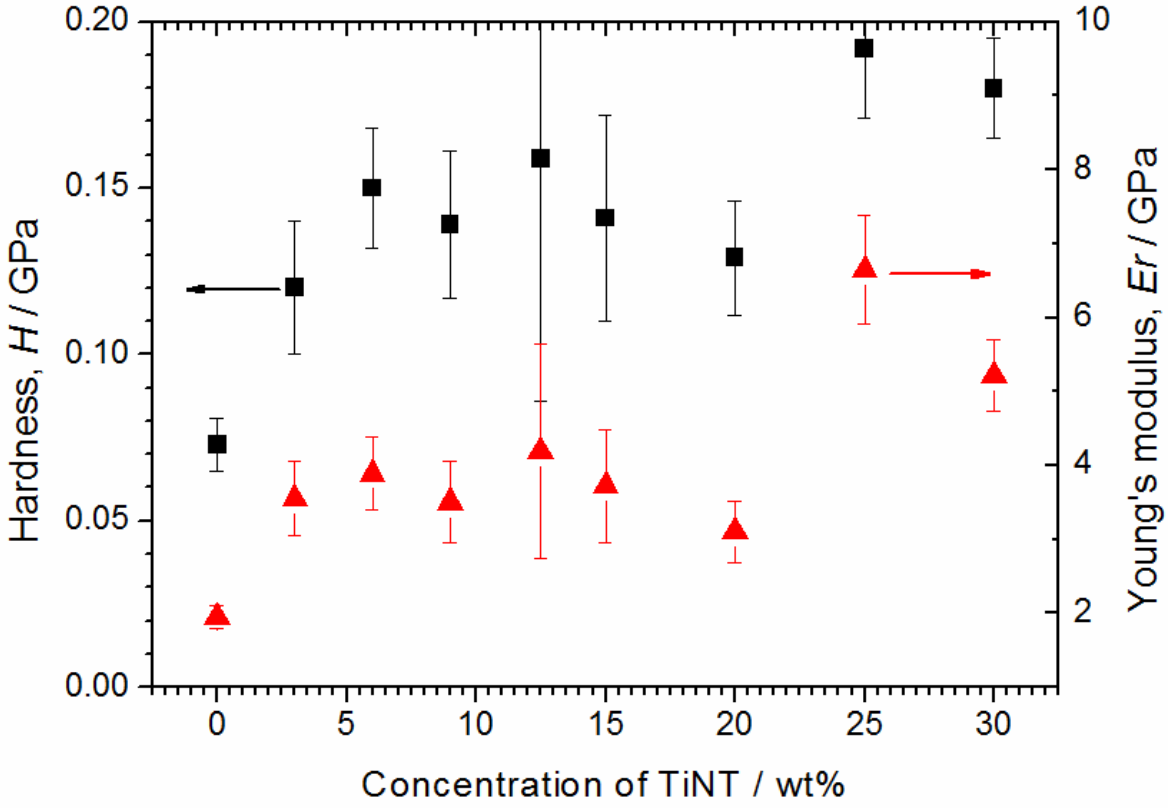

Figure 5.2. Hardness (left axis) and reduced Young's modulus (right axis) of composite films PEO:CS 6:1 reinforced with TiNT at the following concentration of nanotubes: 0, 3, 6, 9, 12.5, 15, 20, 25, 30 wt%. The number of repeat measurements was n=196 and the error bars show the standard deviation for each data point.

It was found that addition of TiNT to the polymer matrix resulted in an increase of its hardness and reduced Young's modulus for all concentration of added nanotubes compared to the pure polymer blend (first data point, 0 wt %). The composite film filled with 25 wt % of nanotubes was found to be approximately 2.6 times harder and 3.4 times stiffer with respect to the neat polymer blend (see Table 4). The composite films reached a

maximum when concentration of TiNT is 25 wt %. Further increase in the content of nanotubes in the polymer blend (30 wt %) resulted in a slight deterioration of mechanical properties probably due to particle aggregation and poor dispersion of the reinforcing phase at such high concentration of nanotubes.

Table 4. Hardness and reduced Young's modulus of composite PEO:CS (6:1) films at different quantities of added TiNT.

Composite Film	*H* / GPa	*Er* / GPa
PEO:CS 6:1	0.073 ± 0.008	1.948 ± 0.162
PEO:CS 6:1 + 3% TiNT	0.120 ± 0.020	3.551 ± 0.504
PEO:CS 6:1 + 6% TiNT	0.150 ± 0.018	3.891 ± 0.494
PEO:CS 6:1 + 9% TiNT	0.139 ± 0.022	3.505 ± 0.548
PEO:CS 6:1 + 12.5% TiNT	0.159 ± 0.073	4.193 ± 1.446
PEO:CS 6:1 + 15% TiNT	0.141 ± 0.031	3.725 ± 0.763
PEO:CS 6:1 + 20% TiNT	0.129 ± 0.017	3.102 ± 0.416
PEO:CS 6:1 + 25% TiNT	0.192 ± 0.021	6.646 ± 0.729
PEO:CS 6:1 + 30% TiNT	0.180 ± 0.015	5.218 ± 0.479

5.3.2 Tribological analysis using nanoscratch testing

All prepared composite samples made up of PEO:CS=6:1 with a content of TiNT ranging from 0 to 30 wt% have been subjected to nanoscratch testing. It was found that the surface in contact with the glass slides was much smoother, hence the tribological analysis was performed on this side in composite films after being detached, turned upside down and fixed with epoxy resin.

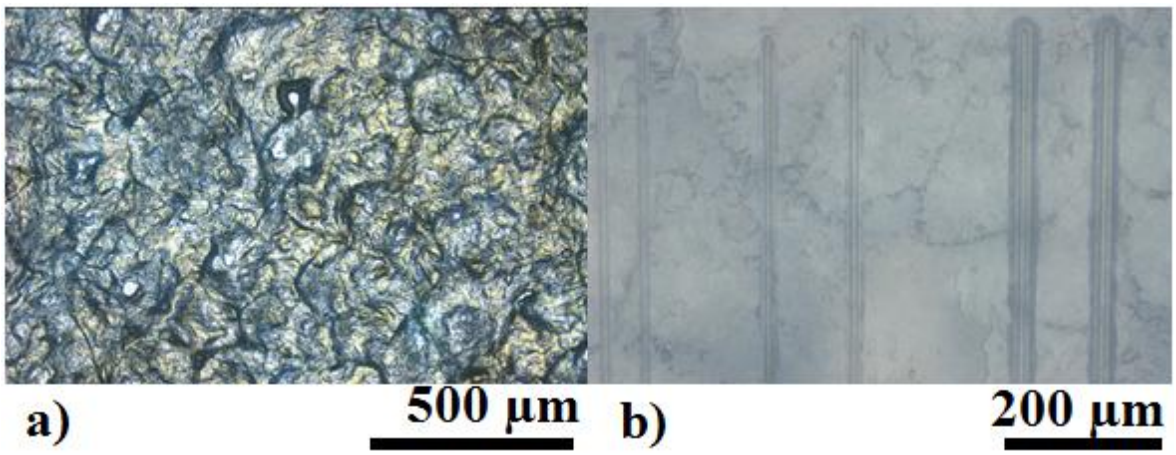

Figure 5.3. Optical micrographs of PEO:CS=6:1 composite films. Upper surface of a thin composite filled with TiNT 6 wt % (a) and the opposite surface in contact with the glass slide filled with TiNT 20 wt % (b); both were drop-cast on aluminium foil.

Figure 5.3 shows optical micrographs of the upper surface for the composite film PEO:CS=6:1 filled with TiNT 6 wt % (left image) and the opposite side underneath the thin composite film in contact with the glass slide with a content of TiNT of 20 wt % after the nanoscratch testing under three different loads (right image). In general, mechanical and tribological properties are correlated. For that reason, it might be assumed that films with improved hardness and modulus would exhibit the best scratch resistance. Figure 5.4 shows a graph of mean residual depths measured from the third topographic scan on scratched tracks as a function of TiNT content (0-30 wt %) under three different loads (10, 20 and 50 mN). The residual depth was found to be lower in films filled with TiNT 25 and 30 wt %, both of which exhibited the best mechanical properties in the nanoindentation analysis aforementioned in the Section 5.3.1. As the concentration of nanotubes is increased, the scratching track seems to be less damaged in the film containing TiNT 30 wt %, reflecting the fact that hardness and scratch resistance are related.

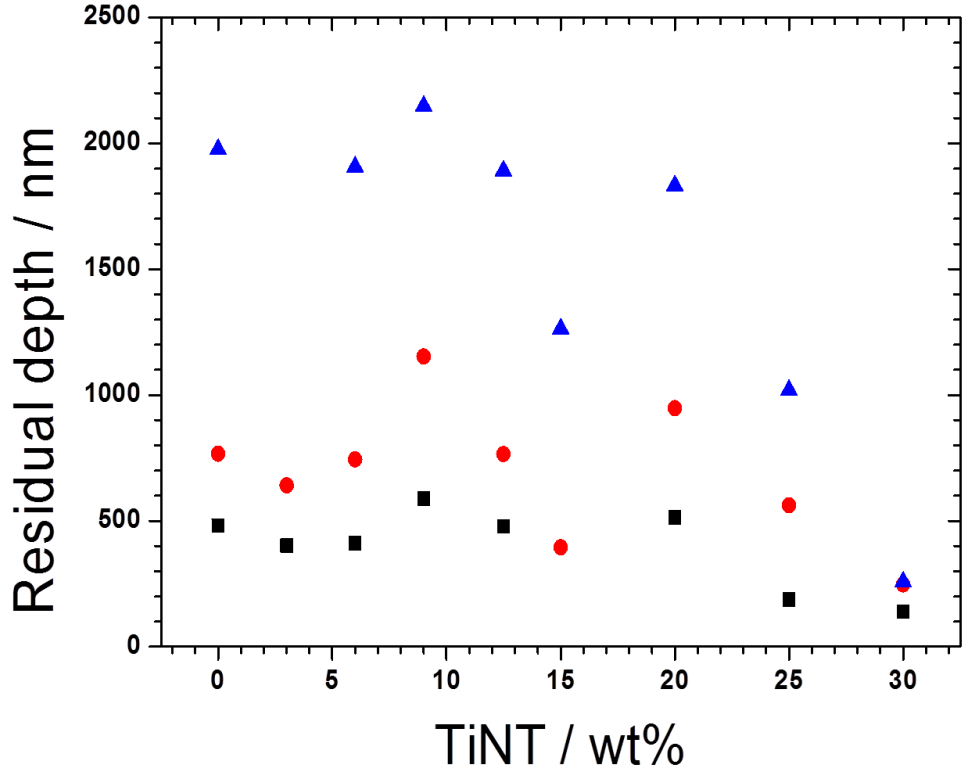

Figure 5.4. Residual depth vs. concentration of titanate nanotubes (wt %) in composite films under applied loads of 10 (■), 20 (●) and 50 (▲) mN respectively.

The slope of the fitted curve extracted from friction force as a function of normal force for three different loads (10, 20 and 50 mN) in composite films made of PEO:CS=6:1 with a content of TiNT ranging from 0 to 30 wt % is shown in Table 5 as friction coefficient. The experiments, which were repeated twice, show an increase of friction coefficient for low content of nanotubes, after which there is a monotonic decrease in the variable reaching the minimum value for the composite filled with TiNT 30 wt %. These results are in agreement with the data of residual depth showing that the composite film with a content of TiNT 30 wt % is more scratch resistant as well as exhibits the lowest friction coefficient.

Table 5. Friction coefficient of composite films PEO:CS=6:1 vs content of TiNT calculated from nanoscratch testing under various loads (10, 20 and 50 mN).

Composite Film	Friction coefficient
PEO:CS 6:1	0.322 ± 0.015
PEO:CS 6:1 + 3% TiNT	0.335 ± 0.011
PEO:CS 6:1 + 6% TiNT	0.363 ± 0.005
PEO:CS 6:1 + 9% TiNT	0.364 ± 0.004
PEO:CS 6:1 + 12.5% TiNT	0.302 ± 0.014
PEO:CS 6:1 + 15% TiNT	0.309 ± 0.015
PEO:CS 6:1 + 20% TiNT	0.313 ± 0.003
PEO:CS 6:1 + 25% TiNT	0.272 ± 0.014
PEO:CS 6:1 + 30% TiNT	0.097 ± 0.001

5.4 Polymer composite films sonicated before drop-casting

It is common practice during distribution of solid particles within polymer solution to use ultrasound to accelerate mixing and improve uniformity of the phase [81]. However, taking into account that such treatment can also reduce the average length of nanotubes [29], it is essential to know how alteration of the length in titanate nanotubes can affect physical properties of the composite. For this purpose, polymer solutions (PEO:CS=6:1) containing colloidal suspensions of TiNT were stirred overnight and then treated with ultrasound for 0, 0.25, 0.5, 1, 2 and 3 hours followed by drop-casting on glass slides. The concentration of TiNT in dry composites was fixed at 4.7 wt%.

5.4.1 Mechanical analysis using nanoindentation

The measured values of hardness and Young's modulus for the obtained composite films are shown in Figure 5.5. The blank data point represents hardness and Young's modulus for neat polymer blend without addition of nanotubes. After the incorporation of long titanate nanotubes with a content of 4.7 wt % into the polymer blend without ultrasound treatment, both hardness and Young's modulus increased by approximately 1.5 times. It is observed that short duration of sonication of aqueous mixtures of TiNT and polymers further improves the mechanical properties of the final drop-cast composite. The highest value of hardness (0.146 GPa) is observed in the sample treated for 30 minutes ultrasound whereas highest value of Young's modulus (3.97 GPa) was detected in the sample sonicated for 1 hour.

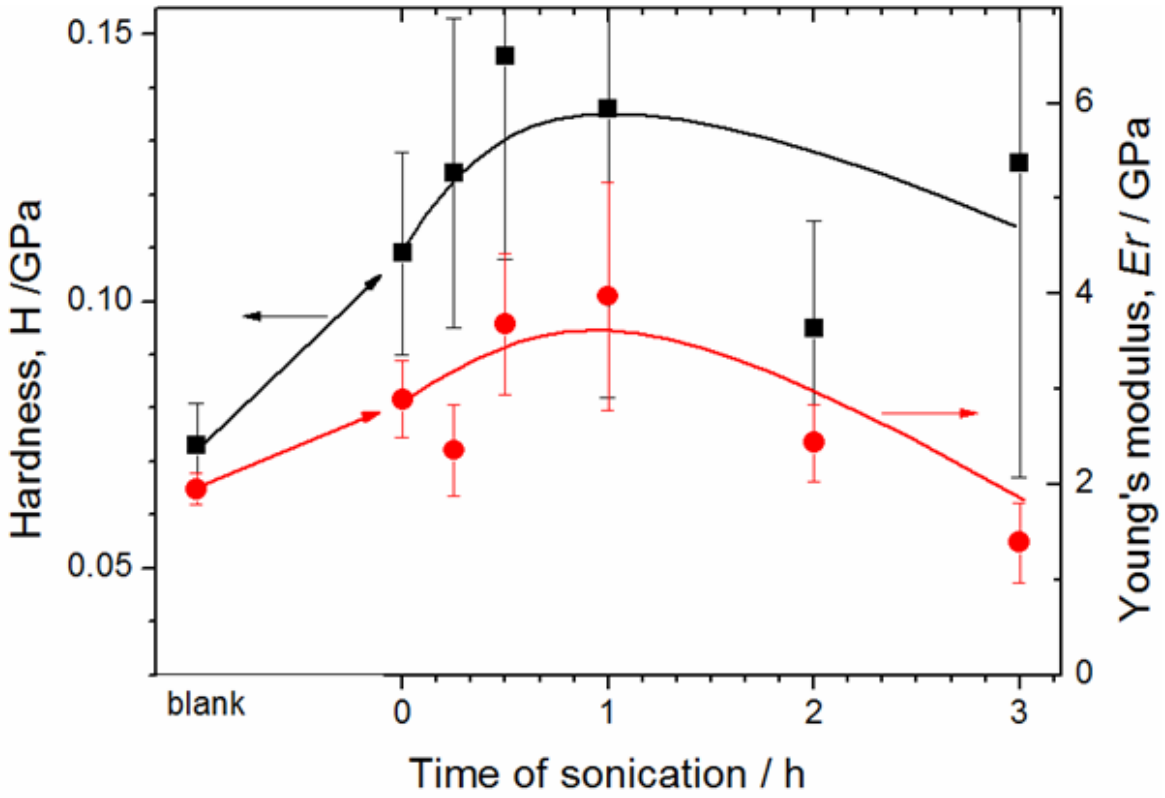

Figure 5.5. Hardness (left axis) and reduced Young's modulus (right axis) of composite films PEO:CS=6:1 reinforced with TiNT 4.7 wt % at the following duration of ultrasound treatment: 0.25, 0.5, 1, 2 and 3 hours. The first data point (blank) corresponds to pure polymer film. The number of repeat measurements was n=196 and the error bars show the standard deviation for each data point.

These tendencies somehow contradict the recently reported correlations suggesting that the longer carbon nanotubes, the better mechanical properties of their polymer composites [353]. As it was previously demonstrated in Section 4.3.3, sonication of colloidal suspensions of TiNT reduces the average length of nanotubes relatively fast and therefore one would expect rapid a deterioration of mechanical properties of composite under ultrasound due to nanotube scission. However, observed improvement of mechanical properties of the composite after short exposure to ultrasound suggests that the benefit of better dispersion of the reinforcing phase within the matrix surpasses the detrimental effect of nanotubes length reduction, at least for short duration of ultrasonic treatments.

In contrast, continuation of sonication reverses the effect. Samples obtained after 3 hour of ultrasound treatment apparently shows lower values of hardness and stiffness, which might be related to the reduction of length confirmed by TEM. Figure 5.6 shows length distribution histograms built from TEM images of composite films reinforced with TiNT 4.7 wt % for samples pre-treated in solution with ultrasound for 0 and 3 hours. The shift of the distribution after sonication indicates that despite the lower Reynolds number in polymer solution (compared to pure water), nanotubes still undergo scission under ultrasonic treatments, although probably with a lower rate.

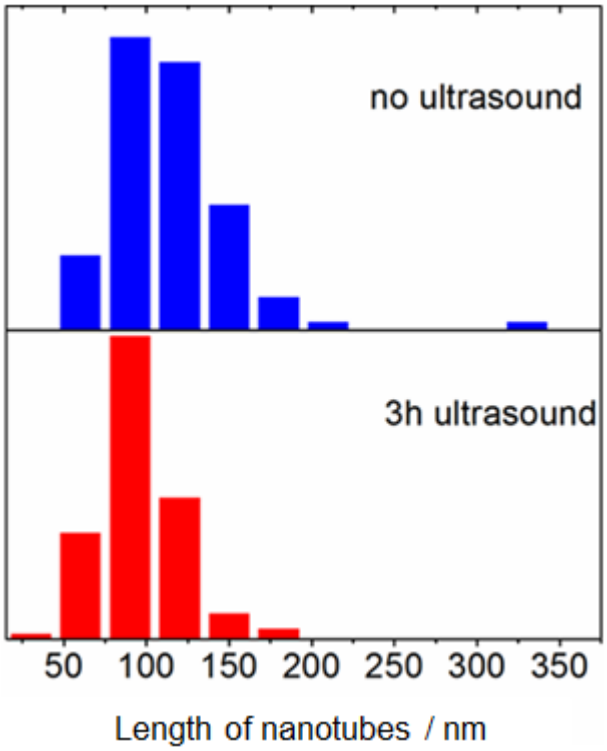

Figure 5.6. Length distribution histograms of 4.7 wt % TiNT dispersed in PEO:CS=6:1 without ultrasound (top) and after 3 hours of ultrasound treatment (bottom) built from TEM micrographs.

5.4.2 Tribological analysis using nanoscratch testing

Nanoscratch testing was also performed on PEO:CS=6:1 TiNT 4.7 wt % composite films as a function of the duration of ultrasonication. Figure 5.7 shows the average residual scratch depth under 10, 20 and 50 mN applied load as a function of sonication time. The first data points (blank) indicate the neat polymer film in which nanotubes were not added whereas the rest of data represent composite films filled with TiNT 4.7 wt % sonicated from 0 to 3 hours. A sudden rise in the residual depth takes place after incorporation of nanotubes compared to the unfilled polymer blend PEO:CS=6:1 followed by its reduction as the duration of the experiments are prolonged. One can speculate that a longer ultrasonication would improve the dispersion of nanotubes within the polymer matrix and might enhance their scratch resistance regardless of nanotube shortening caused by ultrasound. However, addition of nanotubes produced composite films with more pronounced residual depth for each sample compared to the unfilled polymer film.

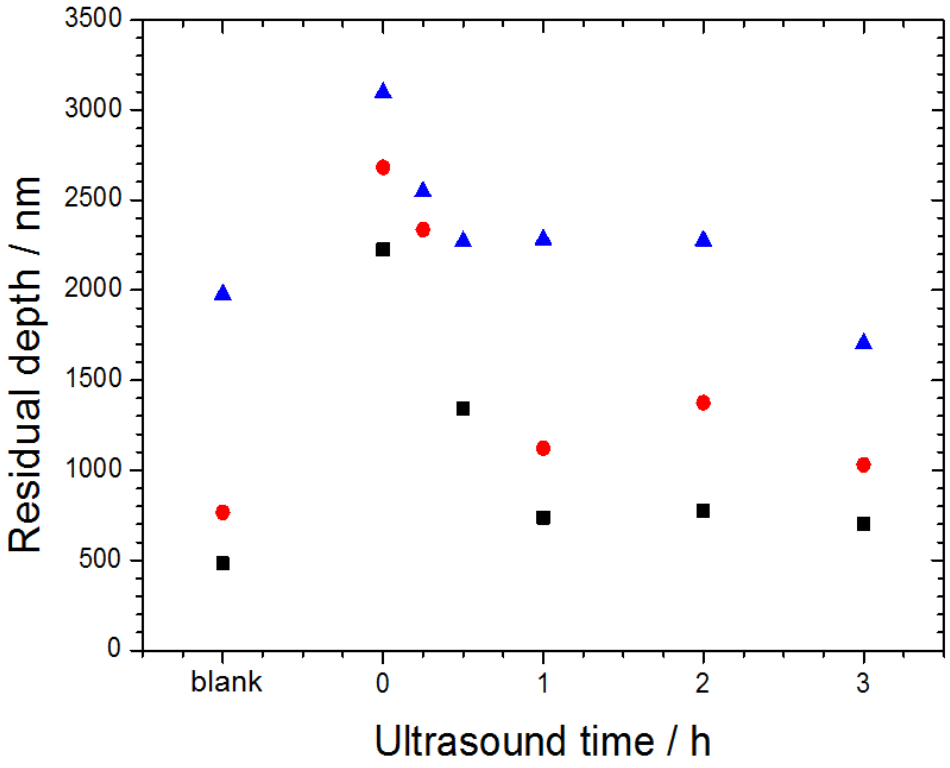

Figure 5.7. Residual depth vs. duration of ultrasound treatment of PEO:CS 6:1 TiNT 4.7 wt % composite films under applied loads of 10 (■), 20 (●) and 50 (▲) mN respectively.

Friction coefficient was calculated from the linear fitting (slope of the curve) of friction force versus normal force under various loads (10, 20 and 50 mN), which was extracted from the on-load scan of the nanoscratch track shown in Table 6. A steady decrease in friction coefficient is produced as the duration of sonication is extended until a minimum is reached for 1 hour of ultrasound treatment. Friction coefficient rises after a further use of ultrasound. Overall, the effect of ultrasound on the tribological properties of the composite is insignificant.

Table 6. Friction coefficient as a function of the duration of ultrasound treatment for a content of TiNT of 4.7 wt %. First data point corresponds to neat polymer blend PEO:CS=6:1.

Composite Film	Friction coefficient
PEO:CS 6:1	0.322 ± 0.015
4.7% TiNT No Usound	0.309 ± 0.003
4.7% TiNT 15 min	0.327 ± 0.005
4.7% TiNT 30 min	0.306 ± 0.000
4.7% TiNT 1 h	0.305 ± 0.002
4.7% TiNT 2 h	0.315 ± 0.002
4.7% TiNT 3 h	0.341 ± 0.005

5.5 Polymer composite films filled with various elongated materials

It has been proven that the incorporation of novel elongated nanotubular metal oxide nanomaterials into polymer matrices could improve not only physical properties in the composite (see Section 5.3) but also provide with additional functionalities by encapsulation of chemicals in the inner pores and controlled release after a mechanical stimulus (see Section 4.5). Titanate nanotubes are obtained by the alkaline hydrothermal method within a range of experimental conditions. However, subtle variations in the conditions of synthesis can lead to several elongated nanostructured materials. For example, an increase in temperature (190 ˚C) during the reaction of powdered titanium dioxide in NaOH 10 mol dm^{-3} results in large titanate nanofibres whereas shorter titanate nanofibres are obtained in KOH 10 mol dm^{-3} at lower temperature [25, 28].

Both long and short titanate nanofibres synthesised in NaOH and KOH respectively have been added to the blend of polymers PEO:CS=6:1 following the same procedure as for the production of drop-cast composite films reinforced with titanate nanotubes in order to study systematically mechanical and tribological properties of their composites. Besides, screening tests in the manufacture of composite films with additional elongated

nanomaterials such as naturally occurred halloysite nanotubes and germanium imogolite nanotubes kindly provided by White *et al.* [349] were performed for comparative purposes. Last but not least, promising results of mechanical properties were found in composite films filled with titanate nanotubes previously stirred in the presence of pyrrole monomers and incorporated to the polymer matrix from their stable aqueous colloidal suspensions, which are discussed at the end of this section.

5.5.1 Polymer composite films reinforced with titanate nanofibres

Aspect ratio in titanate nanofibres (TiNF) produced by the alkaline hydrothermal method can be tuned depending on the experimental conditions (see Section 2.1.2). The SEM micrograph in Figure 5.8a shows long nanofibres of up to several microns long which were obtained in NaOH 10 mol dm^{-3} at high temperature (190 ˚C) whilst the TEM micrograph in Figure 5.8b depicts short nanofibres of up to several tens of nanometres long which were synthesised in KOH 10 mol dm^{-3} at lower temperature.

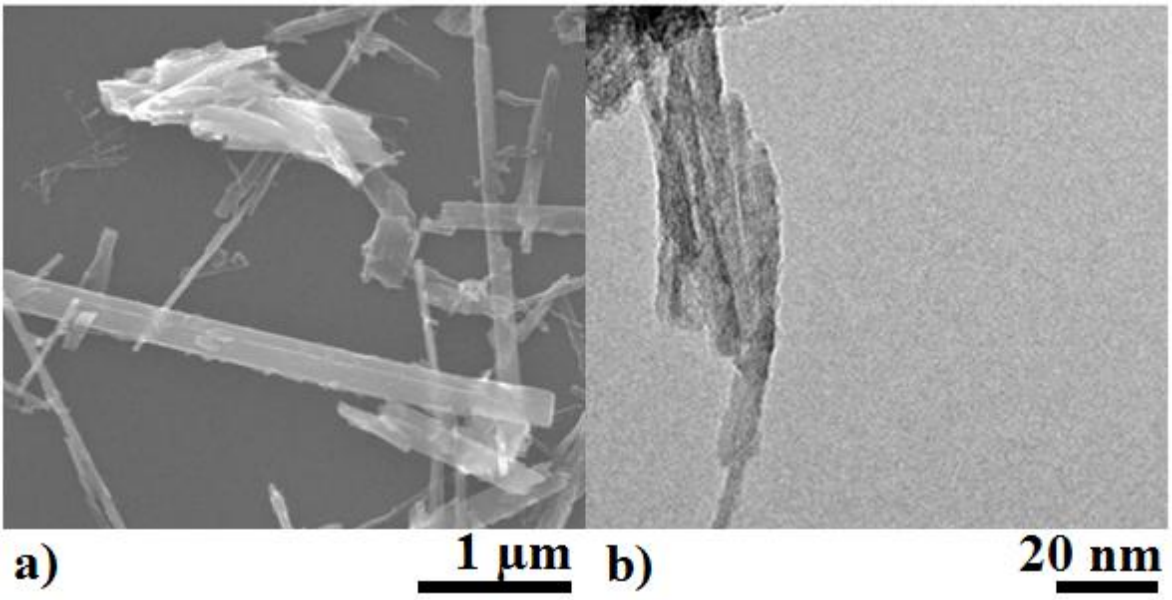

Figure 5.8. Electron microscopy micrographs of titanate nanofibres (TiNF). SEM image of long TiNF synthesised in NaOH at high temperature (a) and TEM image of short TiNF obtained in KOH at low temperature (b).

Preparation of composite films reinforced with nanofibres (TiNF) was carried out following the same procedure as for titanate nanotubes (TiNT). Colloidal suspensions of nanofibres were added to polymer solutions after which the solvent was evaporated and drop-cast on glass slides. Hardness (*H*) and reduced Young's modulus (*Er*) of composite films were determined by nanoindentation (14 by 14 indents). Similar to the results found for composites filled with nanotubes, *H* and *Er* present a relatively wide standard deviation from their average values. Figure 5.9 shows hardness and modulus data for composite films with a mass ratio PEO:CS=6:1 and a weight percent of long titanate nanofibres calculated from the total mass added to the polymer blend, which ranged from 0 to 7.5 wt %.

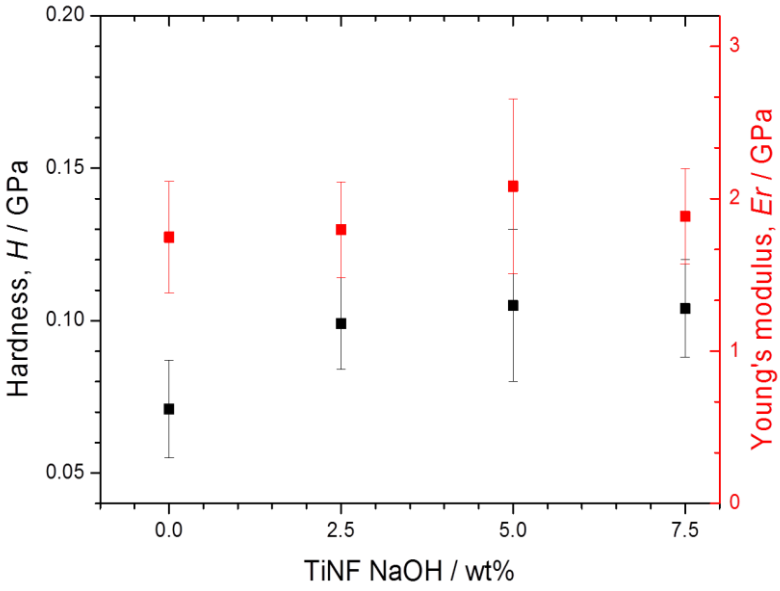

Figure 5.9. Hardness (left black axis) and reduced Young's modulus (right red axis) of composite films with a polymer ratio PEO:CS=6:1 reinforced with long titanate nanofibres produced in NaOH with the following content: 0, 2.5, 5 and 7.5 wt%. The number of repeat measurements was n=196 and the error bars show the standard deviation for each data point.

It was found that addition of TiNF to the polymer matrix resulted in an increase of its hardness for all concentration of incorporated nanofibres with respect to the neat polymer matrix. The presence of a low concentration of long nanofibres enhanced hardness in the composite filled with 2.5 wt %, after which further addition of nanofibres resulted in almost no change in hardness. The improvement of reduced Young's modulus in composites filled with long nanofibres was insignificant compared with the neat polymer

blend. The film with a content of long TiNF 5 wt % exhibited the best mechanical properties, being 48 % harder and 19 % stiffer.

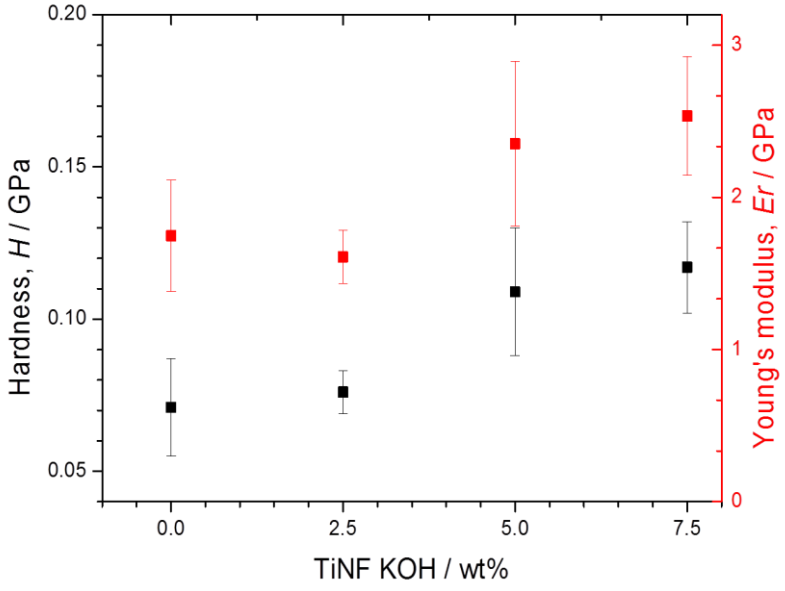

Figure 5.10. Hardness (left black axis) and reduced Young's modulus (right red axis) of composite films with a polymer ratio PEO:CS=6:1 reinforced with short titanate nanofibres produced in KOH with the following content: 0, 2.5, 5 and 7.5 wt %. The number of repeat measurements was n=196 and the error bars show the standard deviation for each data point.

Mechanical properties were also investigated in polymer films reinforced titanate nanofibres produced in KOH for comparative purposes. Short TiNF were incorporated to the polymer matrix with the same content ranging from 0 to 7.5 wt %. Enhancement of both H and Er is more pronounced after addition of short titanate nanofibres shown in Figure 5.10. The composite filled with a TiNF 7.5 wt % was found to be 65 % harder and 45 % stiffer compared to the unfilled polymer film. These series of data differ once again with the idea of the longer carbon nanotubes the better mechanical properties of their polymer composites [353] since our composites filled with long titanate nanofibres show slightly poorer mechanical performance in comparison with short titanate nanofibres.

Although mechanical behaviour found in our specimens reinforced with long and short titanate nanofibres are not as exceptional as the results previously reported for titanate nanotubes, tribological properties of such films show a significant enhancement even at low loadings. Averaged data on friction coefficient as a function of the content of titanate nanofibres for 3 different loads (10, 20 and 50 mN) are shown in Table 7. It is observed

that the friction coefficient is reduced for all samples after incorporation of the elongated reinforcing phase. Such beneficial effect is more profound for composites loaded with micron-sized titanate nanofibres. A remarkable reduction of 66 % and 53 % in friction coefficient was found for the composite filled with long TiNF 7.5 wt% and short TiNF 7.5 wt % respectively.

Table 7. Friction coefficient in composite films made of PEO:CS=6:1 filled with long TiNF produced in NaOH (top table) and short TiNF synthesised in KOH (bottom table) for various concentration (0-7.5 wt %). Experiments were duplicated for 3 different loads: 10, 20 and 50 mN.

Composite Film	Friction coefficient
PEO:CS 6:1	0.330 ± 0.002
2.5 % long-TiNF	0.322 ± 0.020
5 % long-TiNF	0.208 ± 0.019
7.5 % long-TiNF	0.199 ± 0.007

Composite Film	Friction coefficient
PEO:CS 6:1	0.330 ± 0.002
2.5 % short-TiNF	0.285 ± 0.013
5 % short-TiNF	0.299 ± 0.012
7.5 % short-TiNF	0.216 ± 0.013

A complementary set of nanoscratch experiments were performed on the same samples with the only difference that a ramp load of 50 mN was applied throughout the full length of the scratch track, that is, from 0 to 500 microns. Friction coefficient data as a function of the concentration of both long and short titanate nanofibres are shown in Table 8. It is observed that the friction coefficient dropped significantly for all specimens after addition of long and short titanate nanofibres. Composite films reinforced with different nanofibres (long and short TiNF) follow the same tendency, resulting in similar values of friction coefficient for composite films with the same content of nanofibres (although different length). For example, the best friction coefficient was obtained for the composite films reinforced with long and short TiNF 7.5 wt %, in which was found a reduction of 78 % and 94 % compared with the neat polymer blend made up of PEO:CS 6:1.

Unlike the hollow-like structure in titanate nanotubes, titanate nanofibres are characterised by superposition of solid nanoplatelets with a rectangular cross section. It is thought that such unexpectedly improved friction coefficient might be caused by exfoliation of these titanate nanoplatelets as the scratching probe is being pressed over the specimen during testing. Analogous to graphite, bonding between layers are weak whereas atoms within the

nanoplatelets are strongly bonded. Therefore, a sufficiently high shear stress applied by the nanoindentation tip might lead to collapse of such nanofibres by sliding of titanate nanoplatelets over each other.

Table 8. Friction coefficient in composite films made of PEO:CS=6:1 filled with long TiNF produced in NaOH (top table) and short TiNF synthesised in KOH (bottom table) for various concentration (0-7.5 wt %). Experiments were repeated three times with a ramp load of 50 mN throughout the full length of the three scratch tracks.

Composite Film	Friction coefficient
PEO:CS 6:1	0.330 ± 0.001
2.5 % long-TiNF	0.242 ± 0.022
5 % long-TiNF	0.220 ± 0.005
7.5 % long-TiNF	0.185 ± 0.012

Composite Film	Friction coefficient
PEO:CS 6:1	0.330 ± 0.001
2.5 % short-TiNF	0.255 ± 0.003
5 % short-TiNF	0.212 ± 0.006
7.5 % short-TiNF	0.170 ± 0.013

5.5.2 Incorporation of metal oxide elongated materials

All available elongated nanostructures available in our laboratory have been used in the reinforcement of PEO:CS=6:1 polymer matrix following the same methods of dispersion of single nanotubes in order to assess systematically their mechanical properties in manufactured composites as a function of the morphology and composition of the reinforcing phase. Brittle composite films filled with halloysite nanotubes could not be characterised by nanoindentation since all drop-cast samples broke as they were being detached from the glass slides. However, we have incorporated germanium-modified imogolite nanotubes (Ge-Imo) to the blend of polymers followed by mechanical characterisation. Table 9 shows hardness and reduced Young's modulus of composite films after incorporation of various content of Ge-Imo (0 to 7.5 wt %). An impressive enhancement in both *H* and *Er* is found in films loaded with Ge-Imo 7.5 wt % despite of their low aspect ratio and length, being 116 % harder and 70 % stiffer in comparison with the film made up of neat polymer blend.

Table 9. Hardness and reduced Young's modulus of composite PEO:CS (6:1) films at different quantities of added germanium imogolite nanotubes (Ge-Imo). The film loaded with Ge-Imo nanotubes 5 wt % could not be measured.

Composite Film	*H* / GPa	*Er* / GPa
PEO:CS 6:1	0.071 ± 0.016	1.748 ± 0.366
2.5% Ge-Imo	0.172 ± 0.044	2.691 ± 0.783
5% Ge-Imo	NA	NA
7.5% Ge-Imo	0.189 ± 0.036	2.972 ± 0.668

A new batch of PEO:CS=6:1 composite films reinforced with titanate nanotubes (0 to 7.5 wt %) were prepared as control samples in order to investigate the effect of the presence of pyrrole on the mechanical properties of such composite. For this purpose, titanate nanotubes were stirred in distilled water and in an aqueous solution of pyrrole 3 mmol dm^{-3} for 2 weeks respectively prior to their addition to polymer solutions as colloids. It was found that the concentration of colloids of titanate nanotubes in the aqueous solution of pyrrole was slightly higher compared with the nanotubes stirred in distilled water. In addition, nanoindentation characterisation shows that a small quantity of pyrrole results in an exceptional enhancement in both hardness and reduced Young's modulus as it can be observed in Figures 5.11 and 5.12.

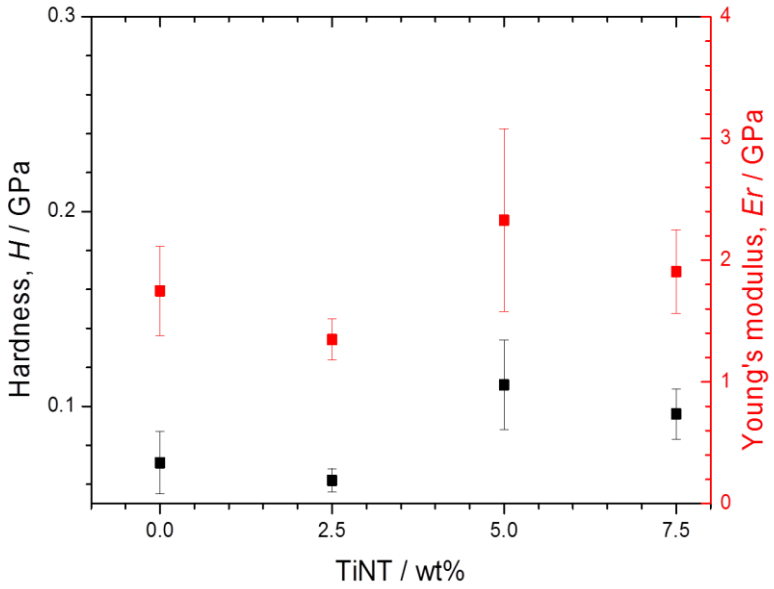

Figure 5.11. Hardness (left black axis) and reduced Young's modulus (right red axis) of composite films with a polymer ratio PEO:CS=6:1 reinforced with titanate nanotubes with the following content: 0, 2.5, 5 and 7.5 wt %. The number of repeat measurements was n=196 and the error bars show the standard deviation for each data point.

Mechanical properties were improved for all composite films after being loaded with nanotubes regardless of the presence of pyrrole with the exception of the composite filled with TiNT 2.5 wt % in Figure 5.11 (it might be an experimental artefact). Besides, composite films containing pyrrole outperformed their counterparts without such additive for the same content of titanate nanotubes. For instance, the best results were obtained for the composite film loaded with TiNT 5 wt % in the presence of pyrrole, which was 104 % harder and 51 % stiffer compared with the film reinforced with plain TiNT 5 wt%; and 218 % harder and 101 % stiffer compared with the neat polymer blend, respectively (see Figure 5.12).

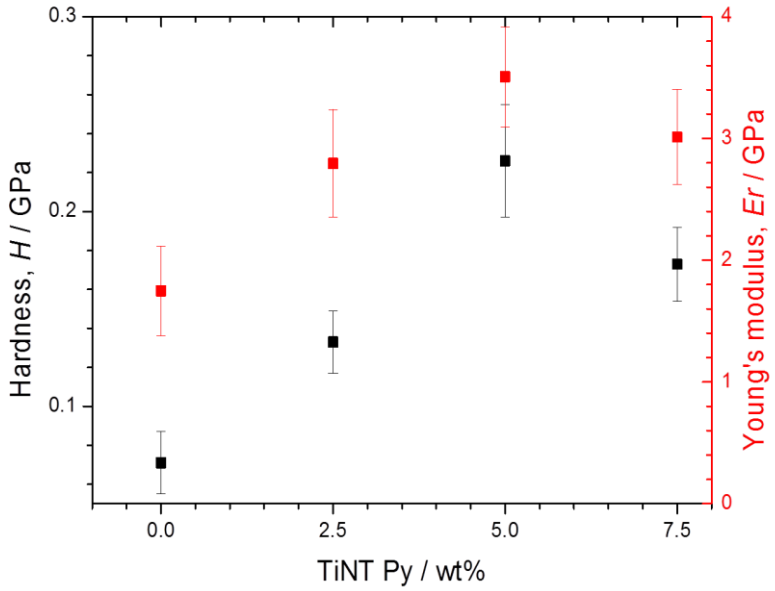

Figure 5.12. Hardness (left black axis) and reduced Young's modulus (right red axis) of composite films with a polymer ratio PEO:CS=6:1 reinforced with titanate nanotubes previously stirred in an aqueous solution of pyrrole 3 mmol dm^{-3} with the following content: 0, 2.5, 5 and 7.5 wt %. The number of repeat measurements was n=196 and the error bars show the standard deviation for each data point.

5.6 Conclusions

Titanate nanotubes synthesised by the alkaline hydrothermal method were used to reinforce PEO/CS polymer blends at controlled loadings. It has been demonstrated by TEM images that independent nanotubes were dispersed within the polymer matrix so well that they might hinder the propagation of cracks induced by mechanical tearing. We can

speculate that formation of nanofibrils of polymer and aligned nanotubes perpendicular to the crack direction might help to maintain stability of such composite films. The polymer composite film PEO:CS=6:1 with a content of TiNT 25 wt % was found to be approximately 2.6 times as hard as the neat polymer blend and 3.4 times stiffer. Further addition of nanotubes did not improve mechanical properties probably due to poor distribution and nanotube aggregation. Tribological properties were also enhanced and the composite film reinforced with TiNT 30 wt % exhibited the best scratch resistance and lower friction coefficient.

Titanate nanotubes dispersed in polymer solutions were treated with ultrasound prior to drop-casting. Although scission rate is expected to vary due to rather different experimental conditions (presence of polymer in aqueous solutions), it has been demonstrated that nanotubes break under ultrasound treatment confirmed by length distribution histograms of TiNT built from TEM micrographs. Both hardness and reduced Young's modulus are improved after short duration of ultrasound reflecting the fact that a better dispersion of nanotubes within the polymer matrix surpasses the detrimental effect of nanotubes shortening. One hour of ultrasound treatment gave rise to the composite film with the best mechanical properties, being 1.5 times harder and stiffer compared to the neat matrix. Besides, a lower friction coefficient was found for the same duration of sonication.

We found a significant reduction in the friction coefficient of polymer composite films filled with titanate nanofibres even though they exhibited an insignificant enhancement in their mechanical properties. It is thought that titanate nanoplatelets stacked on top of each other forming such elongated nanofibres might slide as the scratching probe is passed over the composite film, which might in turn lead to exfoliation and enhanced tribological properties.

Preliminary data on polymer composite films reinforced with germanium modified imogolite nanotubes show a significant enhancement in their mechanical properties despite their short length. In addition, the effect of the presence of a small quantity of the additive pyrrole during the preparation of polymer composite films loaded with titanate nanotubes on their mechanical properties has been investigated, resulting in a remarkable improvement in both hardness and reduced Young's modulus for composites containing pyrrole (and TiNT) compared with films reinforced with plain titanate nanotubes.

Chapter 6: Electrospinning titanate nanotubes polymer composite microfibres

6.1 Introduction

The development of the electrospinning technique in the last 20 years has enabled the manufacture of continuous micro/nanofibres with uniform diameter, large surface area to volume ratio and reasonably high porosity, which makes such fibres the ideal candidates for numerous applications in the area of nanoscience and nanotechnology determined by the type of precursors, experimental methodology and geometry previously mentioned (see Section 2.3.1).

The current challenges in the elaboration of materials with enhanced mechanical properties are insufficient strength of electrospun polymer fibres, degradation of the components due to external conditions, total weight of the components and manufacturing cost. In order to address all these hurdles, incorporation of inorganic nanofillers into the polymer matrices is known as an advantageous approach for the production of cost-effective 3-dimensional composite materials. Some nanotubular materials known for their high aspect ratio have demonstrated exceptional mechanical properties (e.g. carbon or tungsten disulphide nanotubes) which could contribute to the total integrity of the composite material providing good dispersion, enhanced polymer-nanotubes interactions and certain degree of orientation within the electrospun fibre to maximise the mechanical response in a required direction.

Proceeding along the methods for the incorporation of titanate nanotubes into polymer matrices as a cost-effective and lighter alternative (compared to other tubular nanostructures) in the reinforcement of polymer matrices, colloidal suspensions of these nanotubes were added to various polymers and subsequently electrospun. Despite the homogeneous distribution of individual titanate nanotubes within the polymer matrix found in drop-cast composite films in Chapter 5, the presence of a high electric field in the electrospinning process might cause independent nanotubes to reassemble due to a possible electrophoretic motion of such nanotubes negatively charged for pH above 2.

In this chapter, the influence of the selection of appropriate experimental conditions is studied for the manufacture of bead-free electrospun microfibres. The incorporation of titanate nanotubes dispersed within polymer fibres has been challenging owing to their

tendency to reassemble in the presence of an electric field. Combination of the most suitable conditions along with the incorporation of adequate additives has been fundamental in the manufacture of aligned and independent nanotubes dispersed along the full length of electrospun fibres, which were obtained even for high content of nanotubes.

6.2 Titanate nanotubes embedded in electrospun PEO:CS

Firstly, electrospinning of aqueous solutions of pure PEO was reproduced [279, 292] with concentration in the range between 4 and 6 wt %. Figure 6.1a shows a SEM micrograph of randomly oriented uniform PEO electrospun microfibres with a distribution of diameter ranging between 350 and 450 nm. Although PEO is soluble in aqueous solutions and their mixture with colloidal suspensions of TiNT can be obtained by mechanical stirring, our initial attempts to incorporate low content of TiNT (0.25 wt %) into electrospun PEO microfibres have resulted in a small change in the morphology and diameter.

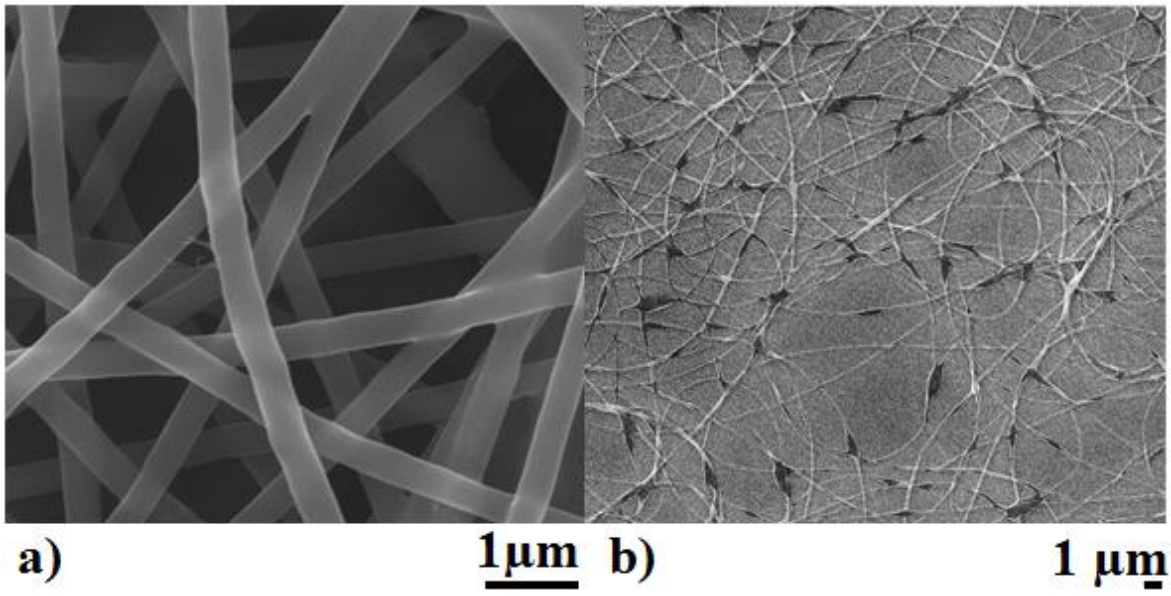

Figure 6.1. SEM images of randomly oriented PEO microfibres electrospun from an aqueous solution of PEO 6 wt% with a homogeneous diameter (a) and presence of beads in electrospun PEO microfibres filled with a small quantity of TiNT (0.25 wt %) (b).

The SEM image in Figure 6.1b shows the appearance of some beads in the intersection of two or more fibres along with a slightly reduction in the diameter of the electrospun

microfibres. The presence of nanotubes might reduce the number of entanglements per polymer chain [237] and might decrease viscosity of the solution prior to electrospinning [238], which leads to beaded fibres.

Further increase in the concentration of nanotubes up to 12.5 wt % has resulted in poor dispersion. The formation of numerous beads containing large bundles of nanotubes together with a decrease in the diameter of the microfibres is observed in Figure 6.2a. The SEM micrograph at higher magnification in Figure 6.2b shows a close-up of a titanate aggregate. Although TiNT are added from aqueous colloidal suspensions as independent items obtained after long-term mechanical stirring, they tend to reassemble during the electrospinning process.

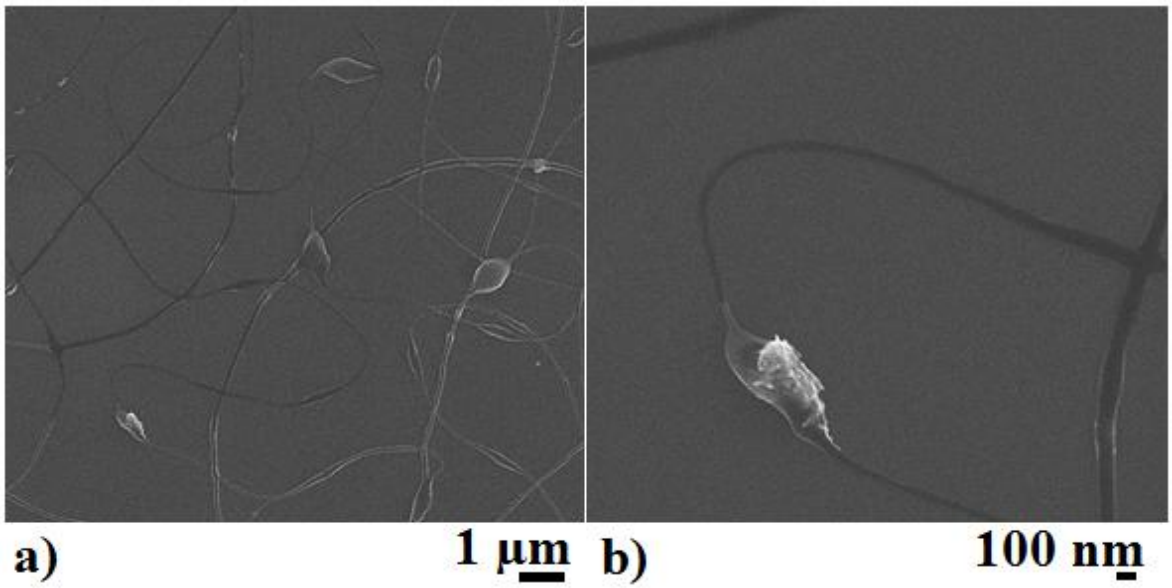

Figure 6.2. SEM images of electrospun PEO microfibres filled with TiNT 12.5 wt% at low (a) and high magnification (b). The close-up micrograph shows a bead in the fibre enclosing an aggregate of titanate nanotubes.

Since TiNT are characterised by a negative zeta potential when pH is over 2, addition of components with good affinity towards these nanotubes such as cationic polymers could potentially improve their dispersion within the polymer matrix due to better interactions between nanotubes and the protonated amine groups in the cationic polymer chitosan (CS) as it was previously reported in Section 5.2. Therefore, blends of polyethylene oxide and chitosan (CS) were prepared in aqueous solutions of acetic acid 2 wt % (CS is soluble in

acidic pH) at various concentrations with different mass ratio, from 4 to 6 wt % in PEO and from 0.5 to 1 wt % in CS.

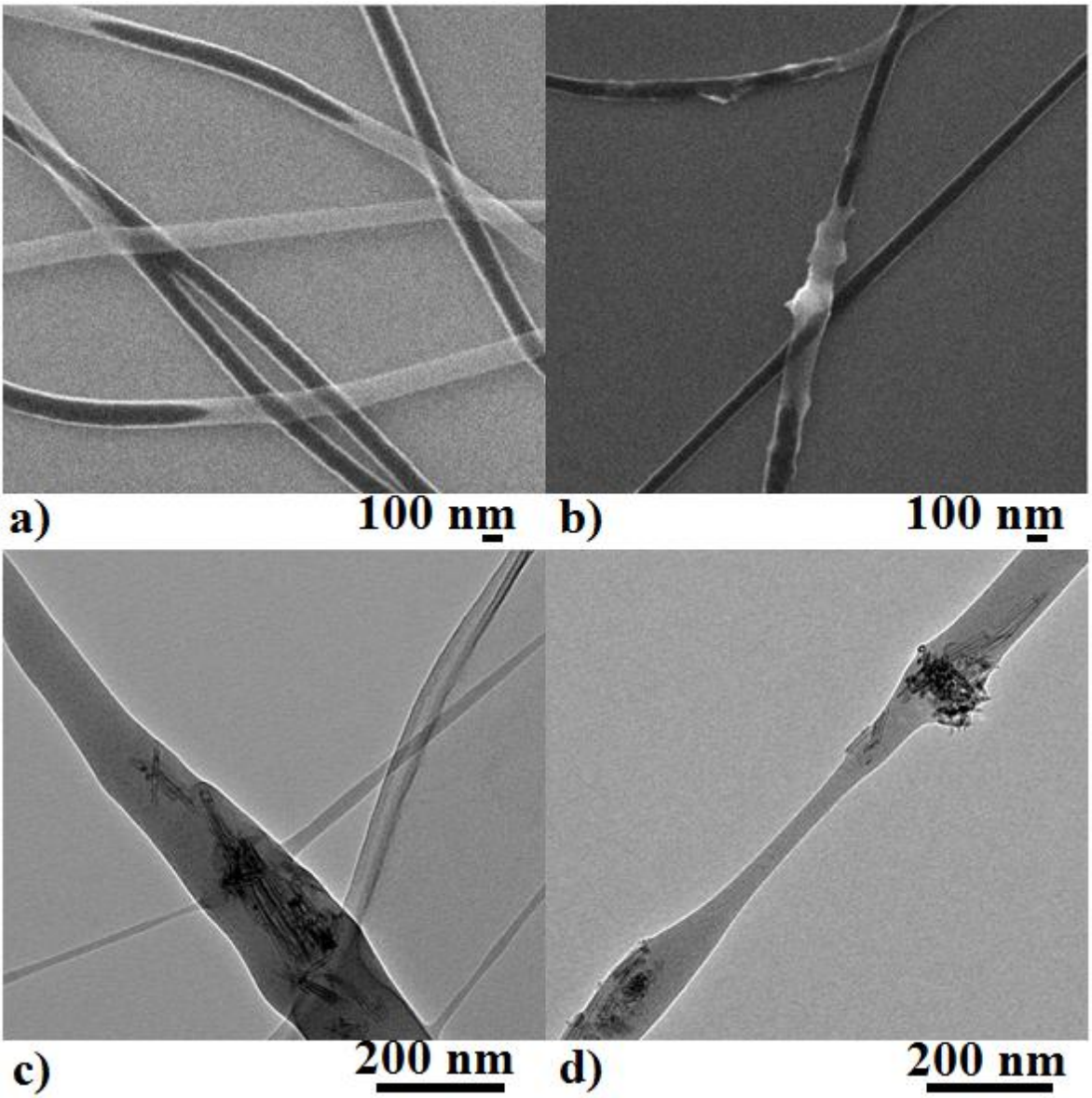

Figure 6.3. Electron microscopy images of PEO:CS=4:1 before (a) and after (b, c and d) incorporation of titanate nanotubes 12.5 wt %. The top left SEM image (a) shows unfilled polymer electrospun fibres with a diameter ranging from 100 to 200 nm. The top right SEM image (b) shows a nanotube aggregate within the spun fibres. Both bottom TEM images (c, d) show nanotube bundles within the electrospun fibres. A few nanotubes at the edge of the aggregates are aligned with the electrospinning direction.

Figure 6.3 shows four electron microscopy images of electrospun polymer microfibres with a ratio PEO:CS=4:1 before and after addition of titanate nanotubes. Homogeneous as-

spun fibres without titanate nanotubes are shown on the SEM image in Figure 6.3a with uniform diameter ranging from 100 to 200 nm. Some areas of the fibre in contact with the silicon wafer appeared darker probably due to fibre charging during acquisition of the image in the microscope. However, the incorporation of chitosan could not prevent the formation of aggregates of titanate nanotubes as it is shown in the SEM micrograph in Figure 6.3b. It is possible that the high electric field developed within the proximity of the wall of the needle during the electrospinning process might induce an electrophoretic motion causing the nanotubes to reassemble. Such electrophoretic effect surpasses the moderately weaker electrostatic interactions polymer-nanotubes leading to unevenly distributed agglomerates of nanotubes within the polymer electrospun microfibres.

TEM data in Figure 6.3c and 6.3d confirm our assumption that independent nanotubes added from colloidal suspension reassembled during electrospinning. The majority of the volume in the polymer microfibres was found to be unfilled despite the high content of TiNT (12.5 wt %). It is thought that individual nanotubes in the polymer solution are accumulated in the needle until a certain critical mass is achieved, which is when the whole aggregate is released as it can be seen in both TEM micrographs. Although most of the nanotubes are presented as bundles, a small quantity of them seems to be aligned with the electrospinning direction at the edge of the aggregates.

6.3 Incorporation of cetyltrimethylammonium bromide (CTAB)

The introduction of chitosan in the polymer/TiNT blend prior to evaporation and subsequently electrospinning resulted in a slightly improved distribution of such nanotubes within the electrospun microfibres, yet it is far from an ideal uniform dispersion throughout the whole sample. The addition of the cationic surfactant cetyltrimethylammonium bromide (CTAB) could have the following beneficial effects: (a) enhanced interactions between nanotubes and the polymer matrix due to a high affinity of the quaternary ammonium heads in the surfactant towards the negatively charged surface in nanotubes at the same time as the hydrophobic tails might be interconnected with the polymer chains; (b) a switch to a positive zeta potential [37], in other words, nanotubes can be enclosed in a cylindrical micelle supposing the concentration of surfactant is greater than the critical micelle concentration resulting in a switch in the zeta potential and inhibition of the electrophoretic motion of nanotubes in the needle; (c) decreased surface tension of the

polymer solution owing to the presence of surfactant, which reduces the energy required to enlarge the topmost surface of the solution and favours electrospinning (see Section 2.3.1).

Stable colloidal suspensions of titanate nanotubes stirred in aqueous CTAB at low and high concentration (3 and 10 mmol dm^{-3}, respectively) were poured into polymer solutions made up of PEO and chitosan and allowed to stir for 1 day. TEM data in Figure 6.4 show a significant enhancement in the distribution of nanotubes within electrospun polymer fibres with a composition of PEO:CS=6:1 and TiNT 6 wt % after the presence of CTAB at low (Figure 6.4a) and high (Figure 6.4b) concentration, respectively. Incorporation of the surfactant seems to be essential for titanate nanotubes to remain isolated along the polymer fibres unlike previous experiments without surfactant.

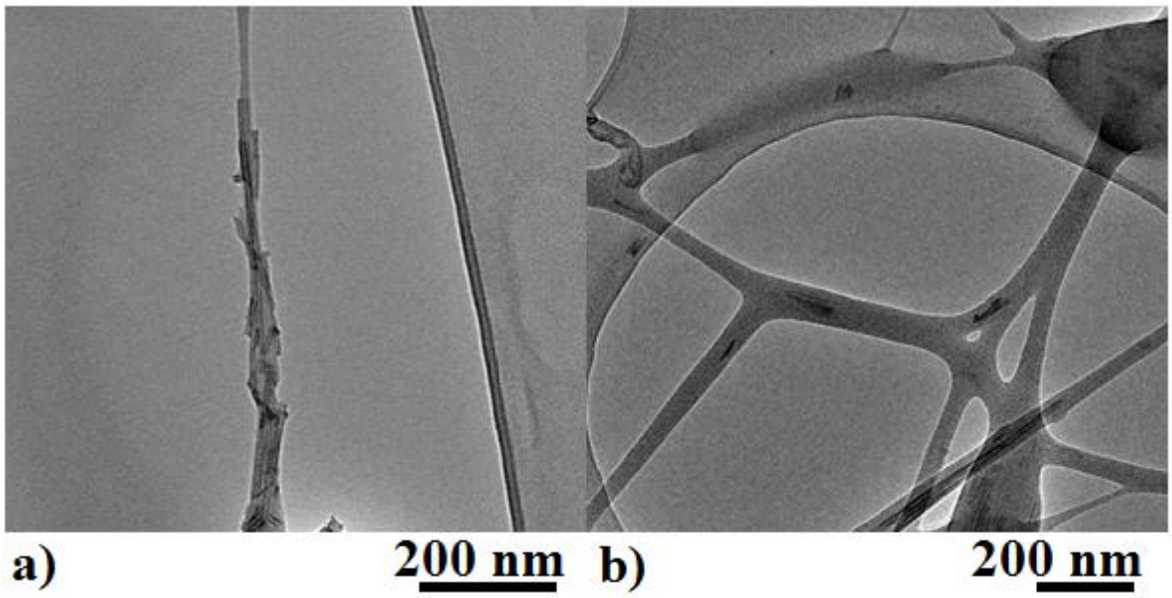

Figure 6.4. TEM images of PEO:CS=6:1 electrospun fibres filled with TiNT 6 wt % in the presence of CTAB at low and high concentration (a and b, respectively). Dispersion of independent nanotubes within fibres has improved after incorporation of CTAB.

6.4 Elimination of the cationic polymer chitosan

Although the incorporation of chitosan had a slightly positive effect on dispersion of titanate nanotubes within polymer electrospun fibres with respect to PEO/TiNT, the addition of the surfactant CTAB plays a more important role upon inhibition of the electrophoretic motion taking place during electrospinning. Thus, solutions were prepared

following the same procedure excluding chitosan. Colloids of titanate nanotubes were added to aqueous solutions of PEO containing different quantities of surfactant and allowed to stir for 24 h. Figure 6.5 shows SEM micrographs of PEO electrospun microfibres with a content of titanate nanotubes 6 wt % in the presence of added CTAB at low and high concentration (CTAB 0.7 and 1.7 wt %, respectively). The amount of aggregates of nanotubes confined in polymer beads along the electrospun microfibres was reduced significantly (see Figures 6.5a and 6.5b).

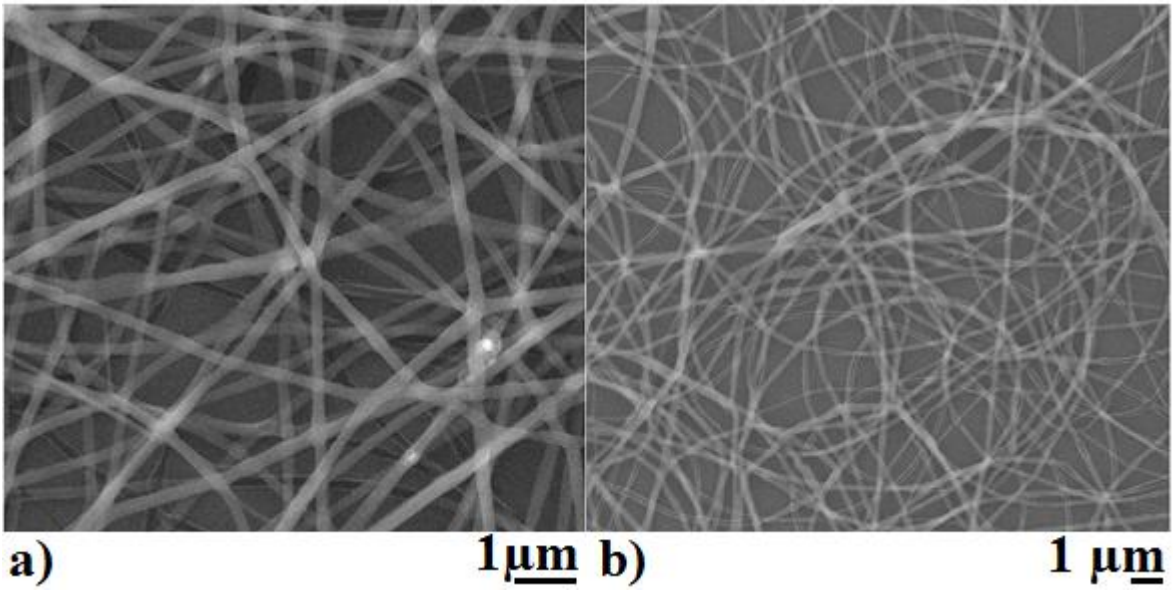

Figure 6.5. SEM micrographs show PEO electrospun microfibres with a content of TiNT 6 wt % and CTAB at low (a) and high (b) concentration with respect to the total weight (0.7 and 1.7 wt %, respectively). The cationic polymer chitosan was not added.

It is therefore confirmed that the addition of the cationic molecule aids the dispersion of titanate nanotubes. An analogous approach was followed to ensure surfactant saturation in solution before electrospinning. Titanate nanotubes were stirred in an aqueous solution of CTAB 10 mmol dm^{-3} for two weeks, after which UV-visible spectrometry measurements showed higher concentration of colloids in the presence of CTAB compared with the suspensions in distilled water. A known mass of TiNT-CTAB was added to aqueous solutions of PEO and subsequently evaporated under reduced pressure at a constant rate. The first batch of PEO electrospun microfibres were filled with TiNT-CTAB 4.8 wt %. Figures 6.6a and 6.6b show SEM micrographs of bead-free uniform and randomly oriented electrospun microfibres with a quite homogeneous distribution of diameter within the

whole sample at low and high magnification. Black arrows indicate few localised aggregation of nanotubes alongside interconnected microfibres as a result of wet as-spun fibre cohesion, giving rise to a non-woven polymer composite mat. Once again, exposure of fibres to the electron beam in direct contact with the silicon wafer results in darker areas probably due to fibre charging.

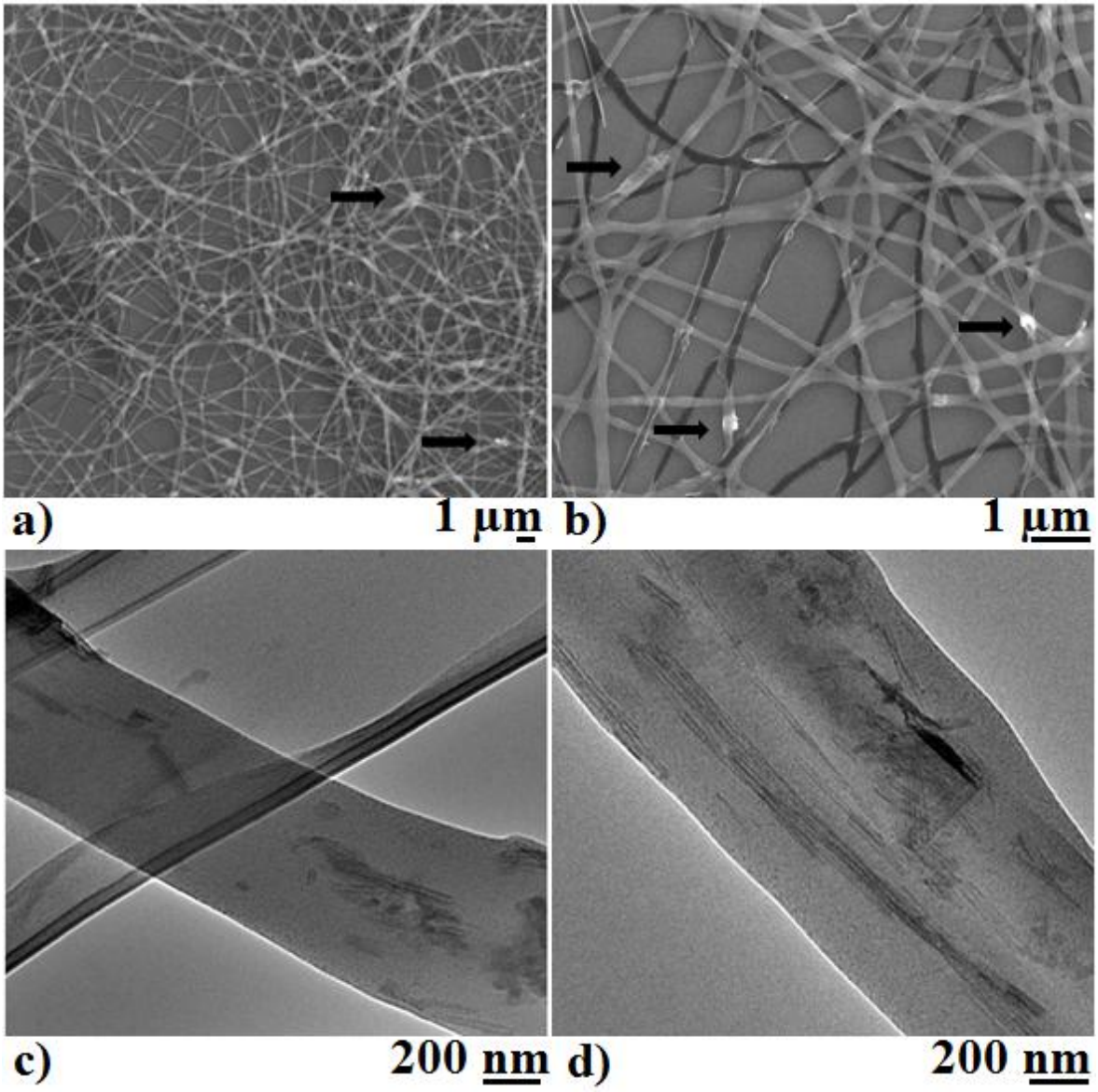

Figure 6.6. Electron microscopy images showing electrospun microfibres filled with TiNT-CTAB. SEM micrographs of PEO 6 wt % microfibres filled with TINT-CTAB 4.8 wt % at low (a) and high (b) magnification. TEM micrographs (c, d) exhibit independent nanotubes aligned with the electrospinning direction. TiNT were stirred in CTAB 10 mmol dm^{-3} for two weeks prior to electrospinning.

From TEM images in Figures 6.6c and 6.6d, it is clear that dispersion of titanate nanotubes along the full length of polymer microfibres was remarkably enhanced. TiNT saturated in aqueous CTAB are not affected by the electrophoretic motion within the proximity of the wall of the needle during electrospinning and remain independent. Transmission microscopy also confirmed orientation of such independent nanotubes, the majority of which are aligned with the electrospinning direction.

Simultaneously, microfibres of PEO with a content of TiNT 4.8 wt % were collected on a pair of static parallel electrodes with a gap of 2 cm apart between them. In addition to more sophisticated geometries in the collector which have been used for fibre alignment (e.g. rotary drum), such simple arrangement enables the production of an array of aligned electrospun fibres [238]. Although fibre alignment was enhanced to some extent (see Figure 6.7a), the TEM image in Figure 6.7b shows polymer microfibres perpendicular to the electrospinning direction within the fibre array collected on the parallel electrodes, suggesting the need of a more complex arrangement (e.g. rotary drum or disk collector) for the production of highly aligned electrospun polymer fibres (see Section 2.3.1).

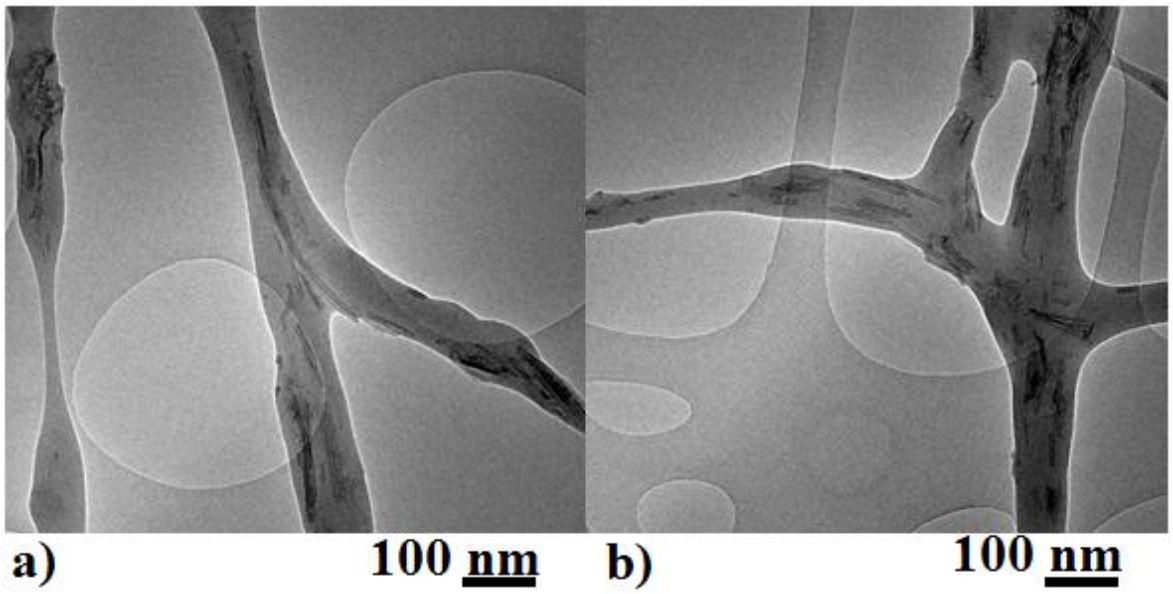

Figure 6.7. TEM images of PEO electrospun fibres loaded with TiNT-CTAB 4.8 wt % were collected on a pair of parallel static electrodes 2 cm apart. TEM micrographs showing a pair of aligned electrospun fibres with 2 merging fibres (a) and perpendicular electrospun fibres (b).

In contrast to the random orientation of nanotubes observed in cast films, we have observed that the majority of such independent nanotubes are oriented parallel to the

electrospinning direction (see Figure 6.6). Besides, mechanical reinforcement of polymer microfibres can be optimised as the content of nanotubes is increased within certain limits. An appropriate concentration of well distributed titanate nanotubes together with a great degree of fibre orientation could give rise to composite materials with rather anisotropic physical properties desired for reinforcements in a specific orientation. Following a similar approach as for drop-cast polymer composite films reinforced with titanate nanotubes previously reported in Chapter 5, we attempted to increase the content of TiNT-CTAB in electrospun PEO microfibres.

The TEM data in Figure 6.8 show that it is possible to increase the concentration of TiNT-CTAB up to 13 wt % with respect to the dry polymer preserving an excellent dispersion of independent nanotubes for such a high content. Once more, the majority of such titanate nanotubes are aligned with the considerably constant diameter electrospun microfibres (over 100 nm across) for 9 and 13 wt % analogous to the fibres with lower content shown in Figure 6.6.

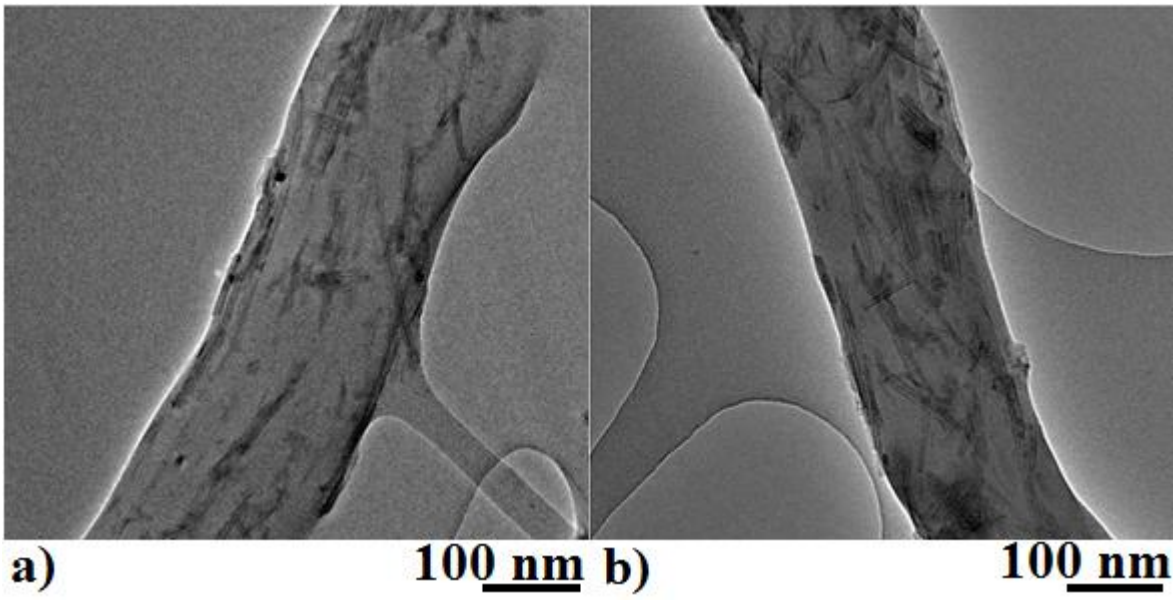

Figure 6.8. TEM images showing PEO electrospun microfibres filled with titanate nanotubes previously stirred in aqueous CTAB for low (a) and high (b) concentration (9 and 13 wt % with respect to the dry polymer).

The established method of dispersion of nanofillers in electrospun polymer fibres could be applied in the manufacture of composites with a diverse range of polymer matrices due to its great potential. In the same way as for composite films previously reported in Chapter

5, we can speculate that electrospun polymer microfibres might be reinforced after the incorporation of titanate nanotubes especially in the electrospinning direction although their mechanical characterisation will be needed to support such hypothesis.

6.5 Titanate nanotubes embedded in polyimide microfibres

The idea behind exchanging aqueous soluble blends of polyethylene oxide with polyimide is to manufacture a composite material with enhanced thermal stability, good chemical resistance and superior mechanical properties. In contrast to solution mixed electrospun microfibres, polyimide is produced in a two-stage reaction. Firstly, the polyamic acid (PAA) intermediate is generated by the polycondensation of an equimolar mixture of the monomers 4,4'-oxydianiline (ODA) and pyromellitic dianhydride (PMDA) in dimethylformamide (DMF) from which it is subsequently electrospun. The final product is obtained by chemical/thermal cyclodehydration of the as-spun polyamic acid microfibres by soaking in a mixture of acetic anhydride dissolved in pyridine. Samples are treated thermally in a furnace at 120 °C for 1 hour to ensure a complete dehydration. Figure 6.9 shows a schematic summary of the synthesis of polyimide electrospun microfibres (PI).

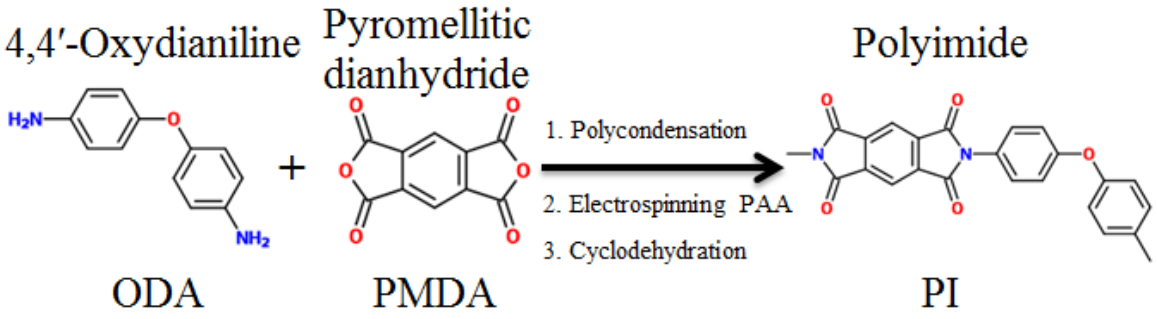

Figure 6.9. Schematic representation of polyimide electrospun microfibres produced from the monomers 4,4'-oxydianiline (ODA) and pyromellitic dianhydride (PMDA) in dimethylformamide (DMF). The intermediate polyamic acid (PAA) microfibres are treated with acetic anhydride in pyridine and heated at 120 °C to perform a whole cyclodehydration.

Polyimide microfibres were electrospun by slight modifications in the experimental parameters. For instance, concentration of the polymer varied from 15 to 25 wt %, high applied voltage was in the range between 15 and 25 kV, tip to collector distance was

adjusted between 15 and 35 cm and the polymer solution was pumped in a controlled rate from 100 to 250 µl h^{-1}. The SEM micrographs in Figure 6.10 show uniform electrospun polyimide microfibres at low and high magnification (6.10a and 6.10b, respectively) produced from a polymer solution of 20 wt % of polyamic acid in DMF, applied voltage of 20 kV, the tip to collector distance was fixed at 25 cm for a flow rate of 100 µl h^{-1}, which were collected directly onto silicon wafers and chemically/thermally dehydrated.

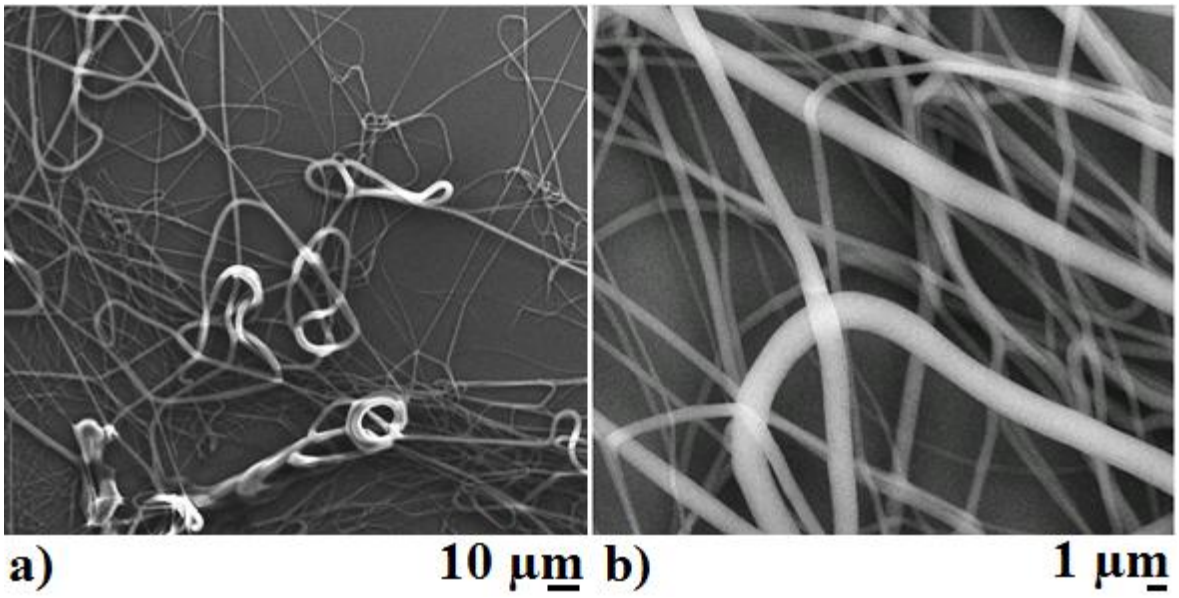

Figure 6.10. SEM images showing electrospun polyimide microfibres at low (a) and high (b) magnification. The concentration of the polyamic acid precursor solution in DMF was 20 wt %.

Two synthetic approaches were attempted for the incorporation of titanate nanotubes coated with the cationic surfactant cetyltrimethylammonium bromide (TiNT-CTAB) to electrospun polyimide microfibres. On the one hand, the *in situ* polymerisation consists of stirring of TiNT-CTAB in DMF in the presence of the monomer ODA for 1 day followed by the addition of PMDA. It is known the high affinity of the amine groups towards titanate nanotubes, which can aid their dispersion in the monomer solution although it might affect adversely polymerisation resulting in a reduction in the length of polymer chains. On the other hand, in the second method known as *ex situ* polymerisation, nanotubes are dispersed in a highly viscous solution of PAA after polymerisation of the monomers ODA and PMDA. It is thought that long polymer chains will hinder dispersion of nanotubes within the PAA matrix. Either method produces PAA electrospun fibres

which are cyclodehydrated into PI following the procedure previously described for unfilled PI.

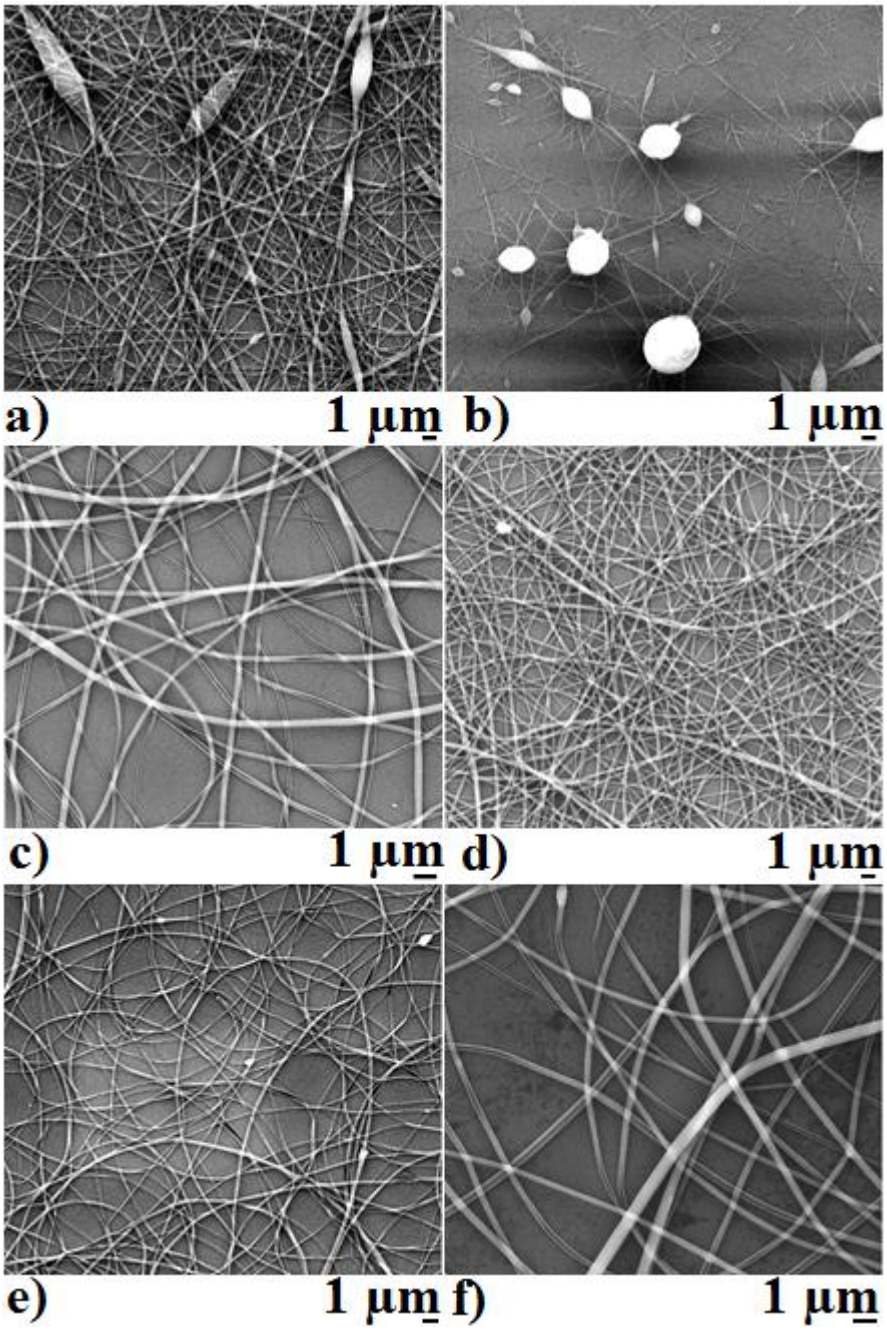

Figure 6.11. SEM micrographs of *ex situ* (a, c and e) and *in situ* (b, d and f) polymerised PI electrospun microfibres on the left and right column, respectively. Concentration of PI in DMF was 15 (a, b), 20 (c, d) and 25 wt % (e, f). The content of TiNT-CTAB was 5 wt % with respect to PI.

The diagram in Figure 6.11 illustrates SEM images of electrospun PI filled with TiNT-CTAB 5 wt% with respect to dry matrix. Rows are ordered as a function of the

concentration of PI with respect to DMF which varies from 15 (a, b), 20 (c, d) to 25 wt % (e, f) in the first, second and third row respectively whilst columns are classified according to the synthetic method, that is, the SEM images on the left column for *ex situ* polymerisation microfibres and *in situ* polymerised microfibres are shown on the right column.

The amount of beads in *ex situ* polyimide microfibres filled with nanotubes in Figure 6.11a is significantly reduced in comparison with *in situ* microfibres shown in Figure 6.11b despite the content of polymer was identical (15 wt %), which reflects the fact that the presence of titanate nanotubes hindered polymerisation. A decreased length in polymer chains for the same concentration of polymer leads to a reduction in viscosity and thus the appearance of beads along the electrospun microfibres. As concentration of PI is further increased up to 20 and 25 wt % (Figure 6.11 c, d, e and f), beads could not be identified. It seems that the minimum value of viscosity needed for polymer chain entanglement occurs for a concentration of PI 20 wt % in the presence of TiNT-CTAB 5 wt % for both *ex situ* and *in situ* methods, which yield bead-free microfibres electrospun from solutions in a semidilute entangled regime [237, 239].

SEM micrograph data show large protuberances of nanotube aggregates exceeding the polymer fibre diameter for both *ex situ* and *in situ* PI 15 wt %. The amount of such protuberances is negligible for higher content of PI, especially for *in situ* polymerised microfibres (Figure 6.11d and 6.11f) due to the fact that nanotubes are incorporated before polycondensation of monomers and hence their better dispersion.

TEM images of the same samples ordered by content of PI and synthetic method in rows and columns respectively are shown in Figure 6.12. It is noted that the scale bar in all micrographs is approximate due to technical issues during data acquisition. Unexpectedly, aggregates of nanotubes were observed in all samples regardless of the method of polymerisation. Moreover, protuberances containing nanotube aggregates surpassing fibre diameter were found in both *in situ* and *ex situ* samples for a content of PI 15 wt % in agreement with the aforementioned SEM data (see Figure 6.12a and 6.12b).

Analogous to aqueous colloidal suspensions of nanotubes previously reported in Chapter 4, it was assumed that suspensions of titanate nanotubes coated with CTAB in DMF were in the form of independent elongated nanostructures or small aggregates and consequently nanotubes might tend to reassemble owing to an electrophoretic motion within the proximity of the needle wall during the electrospinning process. In contrast, it was found

that large aggregates of nanotubes are still present in stable colloidal suspensions after long term mechanical stirring in DMF for two weeks. SEM images in Figure 6.13 show several examples of such aggregations exceeding micron-size together with independent isolated nanotubes at low and high magnification (Figure 6.13a and 6.13b, respectively).

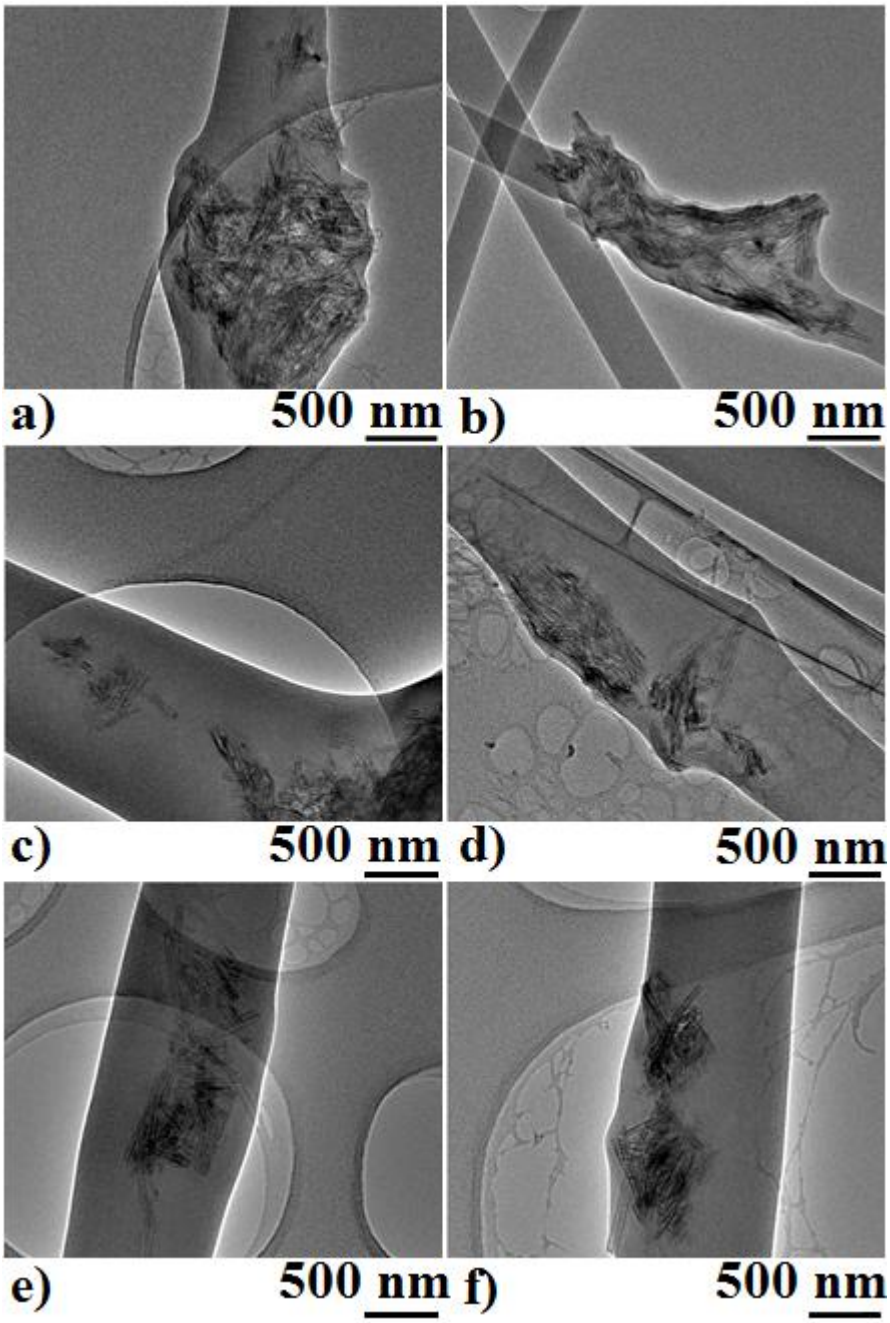

Figure 6.12. TEM micrographs of *ex situ* (a, c and e) and *in situ* (b, d and f) polymerised PI electrospun microfibres on the left and right column, respectively. Concentration of PI in DMF was 15 (a, b), 20 (c, d) and 25 wt % (e, f). The content of TiNT-CTAB was 5 wt % with respect to PI. Approximate scale bar due to technical issues during TEM data acquisition.

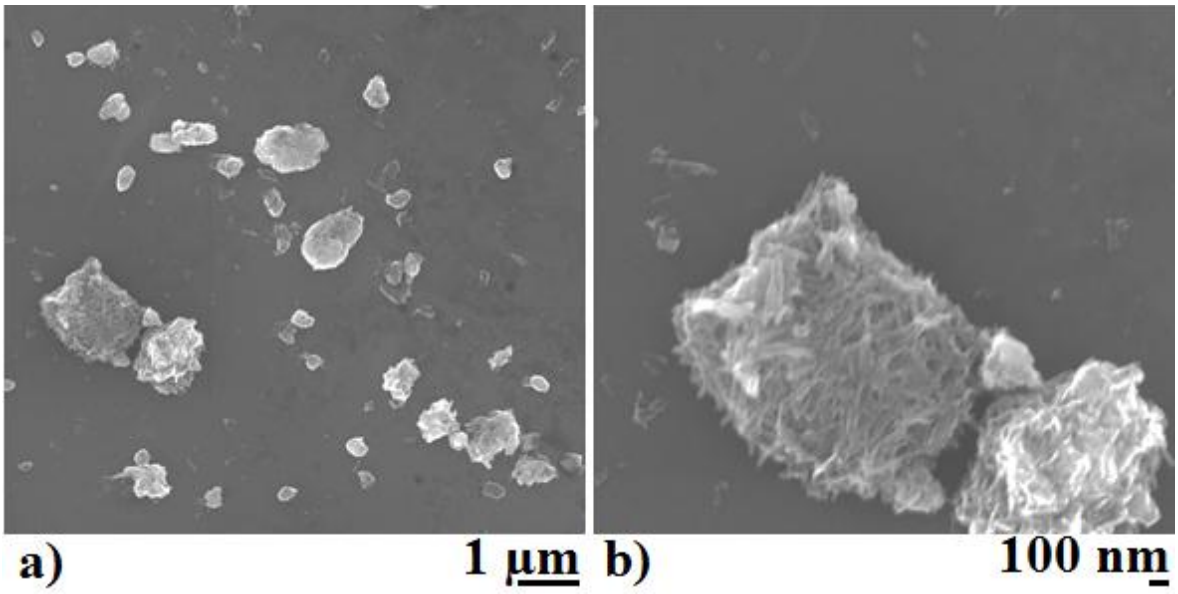

Figure 6.13. SEM micrographs of TiNT-CTAB mechanically stirred for 2 weeks in DMF at low (a) and high (b) magnification. Few aggregates exceed micron-size together with independent nanotubes.

It might be advisable a surface modification treatment on titanate nanotubes in order to improve solvent wetting in DMF as well as to maximise their dispersion in colloidal suspensions before their incorporation to the polymer matrix. Such modification should overcome the likely electrophoretic effect taking place during electrospinning due to the negative zeta potential in titanate nanotubes which causes them to reassemble.

6.6 Conclusions

Titanate nanotubes have been successfully incorporated to polymer electrospun microfibres. Our initial attempts to include nanotubes within the polyethylene oxide matrix have resulted in poor dispersion with the presence of large aggregates along the full length of the polymer composite. A mixed matrix made up of polyethylene oxide and the cationic polymer chitosan (PEO:CS=6:1) slightly improved the dispersion of titanate nanotubes. It is thought that the presence of a cationic polymer might enhance electrostatic interactions between polymer and nanotubes due to a negative zeta potential developed on the surface of such nanotubes coupled with their high affinity towards ammonium salts.

Although TEM micrographs data show few nanotubes aligned parallel to the electrospinning direction after the addition of chitosan, a stronger electrophoretic effect

occurring during electrospinning causes nanotubes to reassemble despite the fact that they were incorporated as independent nanotubes from aqueous colloidal suspensions. Such electrophoretic motion of titanate nanotubes (negative zeta potential) within the proximity of the needle wall (positively charged) during electrospinning leads to nanotube accumulation through the whole length of the needle until a certain amount is reached, which is when they are suddenly released within the continuous electrospun polymer microfibre.

The incorporation of the cationic surfactant cetyltrimethylammonium bromide (CTAB) was essential for a better dispersion and uniform distribution of titanate nanotubes, especially when they were mechanically stirred in an aqueous solution with relatively high concentration of the surfactant (10 mmol dm^{-3}) for 2 weeks. In addition to a high affinity of titanate nanotubes towards ammonium salts (CTAB), we can speculate that the lipophilic tail in the surfactant enhanced interactions with the polymer matrix along with a reduction of surface tension which facilitates the electrospinning process. Most importantly, CTAB might switch zeta potential to positive and therefore the electrophoretic motion might be supressed. The majority of titanate nanotubes were oriented parallel to the electrospinning direction within PEO bead-free microfibres even for high content of TiNT (13 wt %). However, few nanotubes aggregates were located at the interconnection between various microfibres.

Electrospinning of titanate nanotubes embedded in polyimide microfibres have been produced following two synthetic approaches, namely *in situ* polymerisation in which nanotubes are added to ODA prior to chemical reaction of an equimolar content of their monomers and *ex situ* polymerisation in which nanotubes are dispersed after the polycondensation of ODA and PMDA. The presence of a large number of beads in the *in situ* composite made up of PI 15 wt % and TiNT-CTAB 5 wt % suggests that titanate nanotubes might interfere with polymerisation, resulting in a decrease in the length in polymer chains as well as viscosity. Bead-free PI electrospun microfibres filled with titanate nanotubes are obtained in both methods when the content of polymer exceeds 20 wt %. In contrast to the exceptional dispersion of nanotubes in PEO electrospun microfibres, large aggregates of TiNT-CTAB have been observed in TEM micrographs for all samples. SEM data have confirmed that long term mechanical stirring in DMF for two weeks has not been a favourable methodology for the disintegration of nanotubes, hence surface modification is recommended.

Chapter 7: Conclusions and suggestions for further work

7.1 Conclusions

The work presented in this thesis considers a potential approach to improve mechanical and tribological properties of new polymer composite thin films and electrospun microfibres by the incorporation of ceramic elongated nanostructured materials which might also enable the introduction of responsive functions such as the controlled release of a target molecule after a mechanical stimulus.

In the first part of the project, methods for the isolation of independent nanotubes and nanofibres from their agglomerates obtained in alkaline hydrothermal synthesis were developed. A wide range of procedures for the dispersion of nanotubes were attempted, including long term mechanical stirring in a choice of suitable solvents. It was found that stable aqueous colloidal suspensions of titanate nanotubes are obtained after mechanical stirring. Although concentration of colloids continues growing with duration of stirring, 2 weeks was chosen as optimum stirring time due to a sufficiently high content of nanotubes measured via UV-visible spectrometry.

It is known that ultrasound treatment is used to disassemble aggregates of nanotubes. However, it was found that employment of ultrasound for a sufficiently long duration can lead to a decrease in the aspect ratio of titanate nanotubes, depending on the nature of the solvent in which they are dispersed. Scission of titanate nanotubes was systematically studied in a wide range of solvents: ethanol, water, dichloromethane, chloroform and bromoform. Surface modification on nanotubes was needed for their dispersion in halogenated solvents, which was performed by addition of the cationic surfactant CTAB.

Length distribution of titanate nanotubes suspended in ethanol had almost no change after 3 hours of ultrasonication. In contrast, length distribution of TiNT dispersed in distilled water shifted to lower values when the same ultrasound treatment was applied. This fragmentation effect was even more pronounced in denser solvents such as dichloromethane and chloroform, in which nanotubes longer than 150 nm could not be detected after 3 hours of ultrasound. Furthermore, the kinetic curve of average length in nanotubes as a function of time of sonication showed a rather steep initial part where fragmentation occurs fast followed by a long tail of a lower breaking rate with the only

exception of titanate nanotubes dispersed in ethanol, which seemed to be unaffected by ultrasound and presented almost the same average length after 3 hours of ultrasound. Although denser solvents exhibit a faster initial breaking rate, such effect might be associated with the Reynolds number, which was increased fourfold from ethanol to chloroform and might lead to a change in the flow around titanate nanotubes from laminar to turbulent.

Several methodologies were attempted for coating on the surface of nanotubes and sealing of nanotube's ends, namely ceramic silica coating and polymer polypyrrole coating. In both cases, ceramic and polymer phases were obtained in bulk, which gave rise to large particles of titanate nanotubes embedded in either silica or polypyrrole. Therefore, colloidal suspensions of coated titanate nanotubes could not be prepared due to such large particle size. However, it was confirmed that particles constituted of polypyrrole coated titanate nanotubes can be disintegrated under ultrasound treatment.

Such promising results lead us to the encapsulation of the target molecule *ibuprofen* to explore the possibility of functionalization of titanate nanotubes with responsive properties. It has been demonstrated that the concentration of ibuprofen dropped significantly close to zero in loaded nanotubes coated by polypyrrole. The concentration of ibuprofen in these same polypyrrole coated nanotubes treated with ultrasound returned to the same value as for uncoated titanate nanotubes loaded with the selected chemical.

Single and isolated titanate nanotubes were incorporated from aqueous colloidal suspensions into polymer matrices by the solution mixing manufacture processing, from which they were cast obtaining polymer composite thin films with randomly oriented nanotubes confirm by TEM data. Interactions between polymer and nanotubes were enhanced with the presence of the cationic polymer chitosan due to their electrostatic interactions with titanate nanotubes characterised by a negative zeta potential. Mechanical and tribological properties were systematically studied in PEO:CS=6:1 composite cast films as a function of TiNT content in a wide range from 0 to 30 wt % with respect to dry polymer. It was found that the composite filled with TiNT 25 wt % showed the best mechanical performance whilst the thin film with a content of TiNT 30 wt % showed the lowest friction coefficient and residual depth.

Mechanical and tribological characterisation was also carried out in PEO:CS=6:1 composite thin films with a fixed content of TiNT 4.7 wt % as a function of the length of titanate nanotubes controlled by duration of ultrasound. It was previously mentioned that

nanotubes are fragmented under ultrasound treatment depending on the nature of the media in which they are dispersed. TEM length distribution histograms show that titanate nanotubes break upon ultrasonication in polymer aqueous solutions, although experimental conditions are rather different. Two effects occur simultaneously: on the one hand, ultrasound enhances nanotube dispersion within the polymer matrix; on the other hand, longer ultrasonication results in nanotube shortening which is thought to be associated with worsening of mechanical properties. It was found that ultrasound applied prior to casting to titanate nanotubes dispersed in the polymer solution for 1 hour exhibited the best mechanical and tribological properties.

In addition to titanate nanotubes, several metal oxide ceramic elongated nanostructured materials including long and short titanate nanofibres (TiNF) and germanium modified imogolite nanotubes (Ge-Imo) were incorporated to the polymer blend PEO:CS=6:1 before casting. Although mechanical properties were slightly enhanced for all composites reinforced with long and short nanofibres, it is worth mentioning the remarkable reduction in friction coefficient for composite thin films reinforced with TiNF 7.5 wt % (both long and short nanofibres). It is thought that solid titanate nanoplatelets might slide and detach from titanate nanofibres as the nanoscratching probe is being passed over the polymer composite thin film, resulting in such exceptional reduction in the friction coefficient. In the case of PEO:CS=6:1 filled with germanium imogolite nanotubes, both hardness and reduced Young's modulus were enhanced in all samples, specially the film with a content of Ge-Imo 7.5 wt % which was found to be the hardest and stiffest.

It should be noted the significant enhancement in the mechanical properties of drop-cast composite films reinforced with titanate nanotube which were previously stirred in an aqueous solution of pyrrole. Not only concentration of their colloids was higher but also hardness and reduced Young's modulus were considerably improved for composite films produced in the presence of the monomer pyrrole compared to composite films with the same content of nanotubes added from plain aqueous solutions without pyrrole.

In the last part of this work, several approaches for the elaboration of polymer microfibres were attempted to control both the orientation and homogeneous dispersion of titanate nanotubes embedded into polymer microfibres produced by the electrospinning technique. Despite the exceptional dispersion of such nanotubes within the polymer matrix in composite thin cast films made up of PEO and CS, nanotubes reassembled during the electrospinning process for the same composition of polymers. It is believed that the high electric field developed within the proximity of the needle during electrospinning induces

an electrophoretic motion causing nanotube accumulation and sudden release. Such electrophoretic effect results in a heterogeneous distribution of nanotubes along the full length of electrospun fibres with densely populated areas of large nanotube aggregates enclosed within polymer beads whilst the majority of the polymer fibres remain unfilled. Insufficient enhancement in the dispersion and orientation of nanotubes occurred in the presence of chitosan due to better electrostatic interactions between the cationic polymer and negatively charged nanotubes compared with plain PEO electrospun fibres. To give an example, only a small quantity of nanotubes were observed independent and aligned parallel to the electrospinning direction.

The addition of the cationic surfactant CTAB to polymer solutions before electrospinning was crucial for homogeneous distributions of nanotubes within the polymer microfibres. It is believed that CTAB improves interactions polymer-nanotube, switches zeta potential to positive due to their affinity towards titanate nanotubes and reduces the surface tension of the polymer solution. Such favourable effects resulted in an increase in the number of isolated nanotubes along the length of electrospun fibres. It should be pointed out that the most prominent results were achieved after the elimination of chitosan, and in particular, when titanate nanotubes were stirred in an aqueous solution of CTAB for two weeks. An excess of the surfactant might cause a zeta potential switch, leading to elimination of electrophoretic motion. TiNT-CTAB-modified added from aqueous colloidal suspensions to polymer solutions before electrospinning resulted in PEO composite microfibres with an excellent dispersion of independent nanotubes, the majority of which were found to be aligned parallel to the electrospinning direction even for high content of nanotubes (TiNT-CTAB 13 wt %).

Titanate nanotubes modified with CTAB were embedded into polyimide electrospun microfibres following two methodologies: *in situ* and *ex situ* polymerisation. It is thought that the presence of titanate nanotubes might hinder polycondensation of monomers, resulting in shorter polymer chains and therefore decreased viscosity (*in situ*). For this reason, the number of beads present in PI 15 wt % synthesised by the *in situ* method was higher than for *ex situ* PI 15 wt %, both filled with TiNT-CTAB 5 wt %. However, TEM data show a poor dispersion of nanotubes within the polymer fibres for all samples. It seems that TiNT-CTAB are not well dispersed in DMF after 2 weeks of mechanical stirring, hence further research on nanotube surface modification should be carried out in order to improve their dispersion.

7.2 Suggestions for further work

7.2.1 Ultrasound treatment of titanate nanotubes suspended in various solvents

Although the work in Chapter 4 is a novel investigation on the scission effect of titanate nanotubes suspended as colloids in various solvents under ultrasound treatment, a systematic study with additional solvents in a wide range of density and Reynolds number would complement and validate our hypothesis. Furthermore, some drawbacks have been found in the synthesis of both polymer and ceramic coatings on the surface of titanate nanotubes which are associated with large particle size produced during polymerisation of pyrrole and sol-gel synthesis of silica. A uniform coating along with a reduction in the particle size would enable the dispersion of coated titanate nanotube in colloidal suspensions, after which ultrasound could be used as an indirect tool to measure strength of both ceramic and polymer coatings.

In addition to polypyrrole sealed titanate nanotubes used for the encapsulation of ibuprofen, other materials could be incorporated and released in a controlled mode induced by mechanical or chemical stimuli. For example, silica-sealed loaded nanotubes could release the encapsulated chemical after ultrasound treatment followed by their fracture as it has been previously confirmed whereas for the case of low molecular weight polypeptide sealing nanotube's ends, enzymatic digestion would be needed to liberate the selected molecule. Moreover, depending on the encapsulated materials, nanotubes will acquire additional functionalities. For instance, chemicals catalysing cross-linking polymerisation in a polymer matrix would facilitate responsive "self-healing" of the composite material providing that nanotubes release such chemical after a specific stimulus.

7.2.2 PEO/CS composite films reinforced with various elongated materials

The work in Chapter 5 is complete in that it shows a systematic study of mechanical and tribological properties by nanoindentation and nanoscratching characterisation in polymer composite thin films with a matrix composition of polyethylene oxide / chitosan PEO:CS=6:1 reinforced with titanate nanotubes in a wide range from 0 to 30 wt % with respect to dry polymer. TEM data confirmed an excellent distribution of titanate nanotubes within the polymer matrix probably due to enhanced interactions between the cationic polymer chitosan and the negatively charged nanotubes (negative zeta potential). It was

also established that the optimum duration of ultrasound treatment for PEO:CS=6:1 filled with TiNT 4.7 wt % is 1 hour, which is when nanotubes are better dispersed and shortening effect is negligible. However, there is scope for the work to be extended, particularly in the direction of studying systematically mechanical and tribological properties in composite films reinforced with various elongated nanostructures and different polymer matrices. Therefore, the following extension is suggested:

- Further research on PEO:CS mixed matrix with higher content of titanate nanofibres (both short and long) in order to investigate thoroughly the low friction coefficient found in our experiments. It is also recommended to study the possible sliding mechanism of titanate nanoplatelets in single nanofibres by AFM, which might be the reason for such low friction coefficient in polymer composite thin films.
- Extend concentration range of metal oxide ceramic nanotubes such as germanium imogolite and titanate nanotubes in the presence of pyrrole in PEO:CS mixed matrix in order to characterise mechanical and tribological properties using nanoindentation and nanoscratching techniques. Special attention should be paid into the additive pyrrole.
- Experiment with different polymer matrices depending on the pursued functionalities at the same time as mechanical properties are enhanced. For example: polymethylmethacrylate (PMMA) to obtain optically transparent composites, polyaniline (PANI) for electroconductive composite materials and nylon to produce low cost strong fibres.

7.2.3 Electrospinning titanate nanotubes polymer composite microfibres

The research in Chapter 6 display great results in that the electrophoretic motion causing nanotube to reassemble was completely eliminated after the incorporation of the cationic surfactant CTAB, giving rise to isolated nanotubes aligned parallel to the electrospinning direction within the full length even for high concentration of nanotubes (13 wt %). However, it is suggested mechanical microtensile testing characterisation of non-woven electrospun mats comprised of randomly oriented polymer microfibres obtained on a 2-dimensional collector, non-woven mats made up of aligned polymer microfibres collected on 2 parallel electrodes or a rotary drum/disk and twisted yarns built from electrospun

polymer microfibres; all of them filled with TiNT-CTAB in a wide range of concentration (up to 15 wt %)

Surface modification of titanate nanotubes is also suggested to improve their dispersion as single and isolated nanotubes in DMF colloidal suspensions. Once interactions between nanotubes and solvent are enhanced, long mechanical stirring of nanotubes for 2 weeks followed by their addition from colloidal suspensions to the solution of monomers before or after polycondensation (*in situ* or *ex situ* polymerisation, respectively) is recommended in the production of polyimide (PI) electrospun microfibres.

In the same manner with polymer composite thin films, it is advised the use of other metal oxide elongated nanostructures as fillers for electrospun polymer microfibres such as titanate nanofibres (long and short), halloysite nanotubes and germanium-modified imogolite nanotubes. Furthermore, we propose experimenting with a diverse range of polymer matrices combined with the aforementioned nanofillers although it is important to establish rapid screening tests to identify the most promising combination.

Appendix A Colorimetric data

Sample spectra ibuprofen

Figure A.1 is a sample spectrum collected over the ultraviolet range in a fused quartz cuvette for the molecule ibuprofen with a characteristic absorbance peak in the linear part of the spectrum at wavelength (λ) = 225 nm at 19.4, 48.5 and 97 mol dm^{-3} concentrations (4, 10 and 20 mg dm^{-3}, respectively) dissolved in an alkaline solution of sodium hydroxide (NaOH) 0.1 mol dm^{-3}.

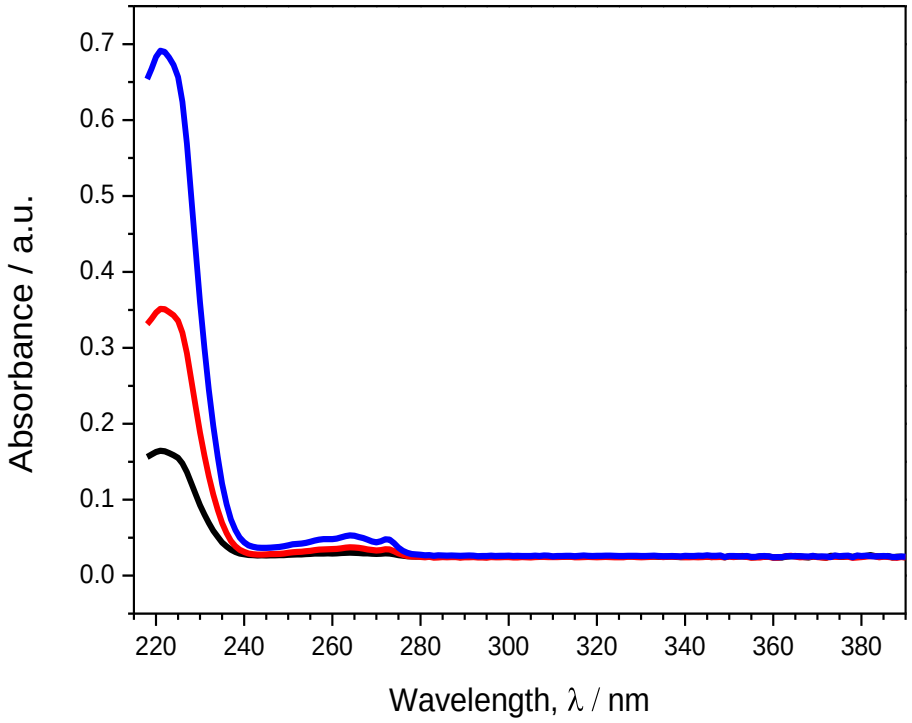

Figure A. 1. Sample ultraviolet spectrum of ibuprofen at 19.4, 48.5 and 97 mol dm^{-3} concentrations (4, 10 and 20 mg dm^{-3}, respectively) dissolved in NaOH 0.1 mol dm^{-3}.

Typical calibration curve

The calibration curve used to determine the concentration of ibuprofen in NaOH 0.1 mol dm^{-3} is shown in Figure A.2. In order to build the calibration curve, a stock solution containing a known concentration of ibuprofen (0.1 mol dm^{-3}) in NaOH 0.1 mol dm^{-3} was used, which had to be diluted several times by an appropriate amount to produce intermediate solutions and obtain the final solutions for the points of the calibration curve in this section. The molar extinction coefficient was calculated from the slope of the calibration curve $\varepsilon = 6460\ dm^3\ mol^{-1}\ cm^{-1}$ at 225 nm wavelength.

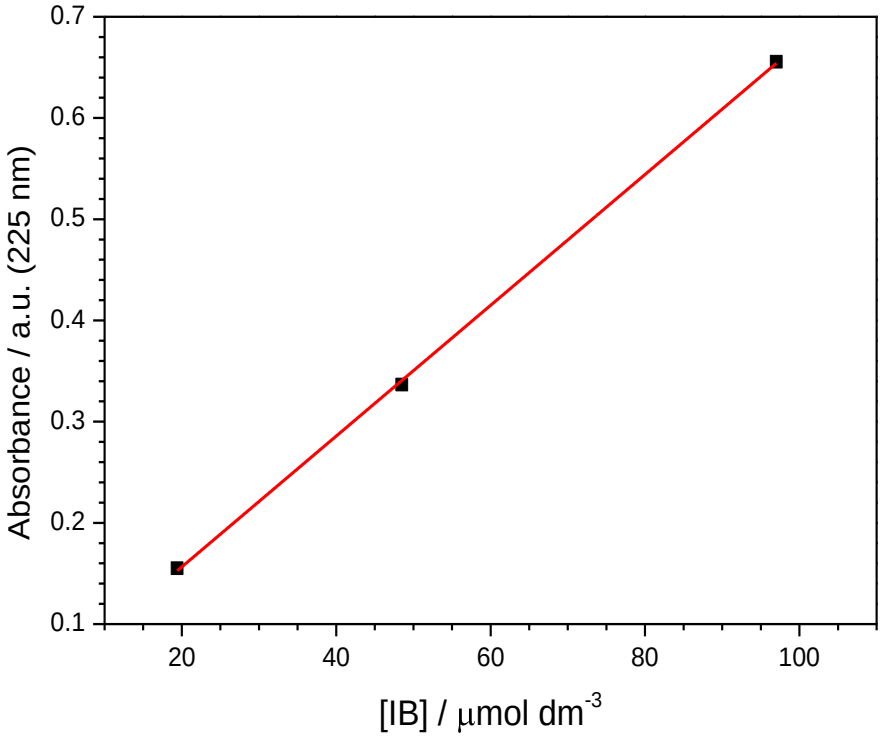

Figure A. 2. Calibration curve for ibuprofen concentration in NaOH 0.1 mol dm^{-3} vs. absorbance at 225 nm wavelength.

Appendix B Nitrogen adsorption of Pd/C catalyst

Isotherm of nitrogen adsorption

Nitrogen adsorption isotherms were analysed to calculate BET surface area and BJH pore size distribution on a catalyst of palladium supported by carbon lot A17Y002 in collaboration with Dr Irene Merino-Jiménez (unpublished). Figure B.1 shows the isotherms of nitrogen on the surface of the Pd/C catalyst. Black squares represent the adsorption isotherm whilst red circles depict the desorption isotherm. According to IUPAC recommendations [354], the isotherm follows H1 type of the curve indicating microporous nature of the sample. Small hysteresis (at $0.4 < P/P_0 < 0.95$) indicates small presence of mesopores.

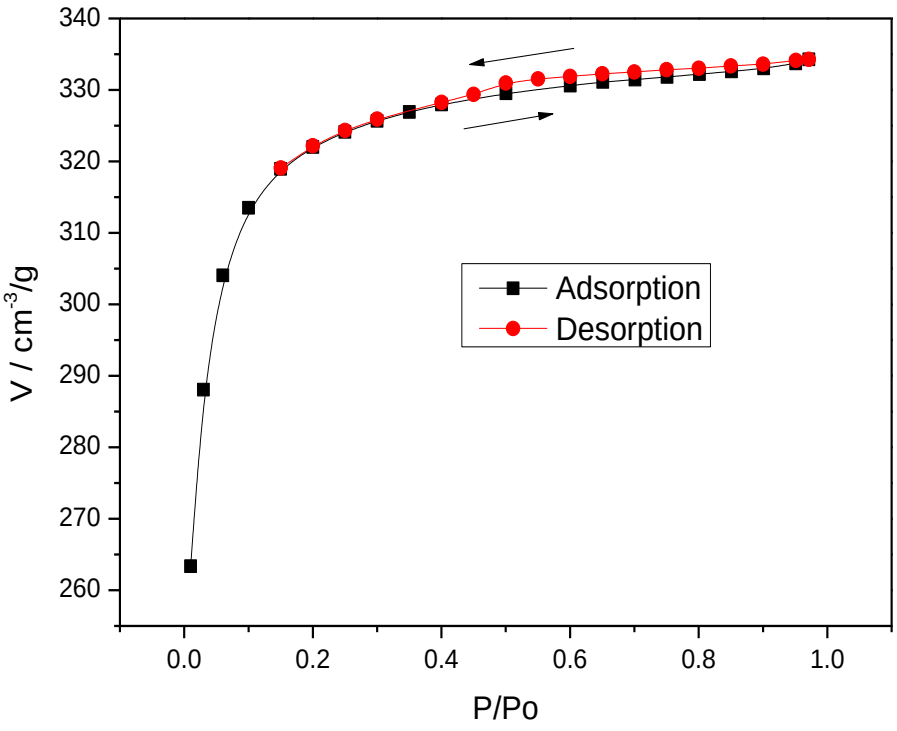

Figure B. 1. Isotherms of nitrogen adsorption-desorption on the surface of Pd/C catalyst at 77 K.

BET surface area

BET surface area was calculated from the N_2 adsorption isotherm for relative pressure between 0.1 and 0.3 and transformed into a linear form as shown in Figure B.2. The slope and intersect of the linear area were determined using least squared methods, which were found to be equal to 0.0048 g cm^{-3} and -1.542 10^{-4} g cm^{-3} for the slope and Y-Intercept, respectively. The calculated BET specific surface area corresponds to 934 m^2 g^{-1}.

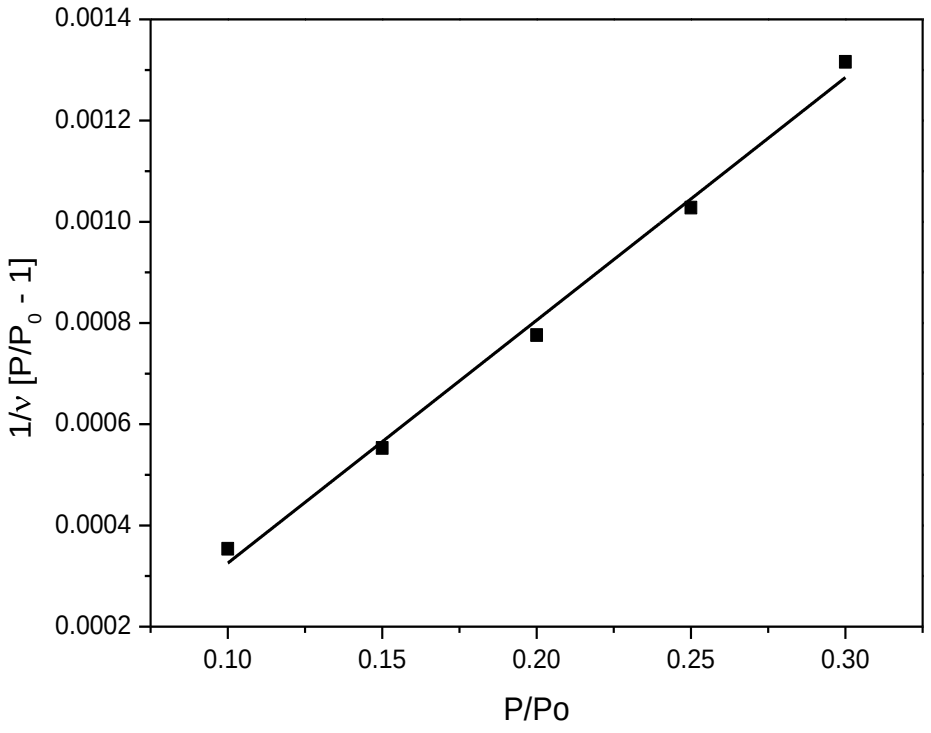

Figure B. 2. Linear transform of adsorption isotherm for determination of BET surface.

BJH pore size distribution

Figure B.3 shows a BJH pore size distribution of Pd/C catalyst determined from both adsorption and desorption branches of nitrogen isotherms. Both curves show monotonic growth of pore volume when the pore size is decreased. The peak on the desorption part of the curve at 3 nm < P/P_0 < 4 nm is to be attributed to a technical artefact associated with the collapse of the film of liquid nitrogen during desorption. The sample shows a significant number of micropores and some mesopores. The cumulative specific pore volume of the sample is 0.41 cm^3 g^{-1}.

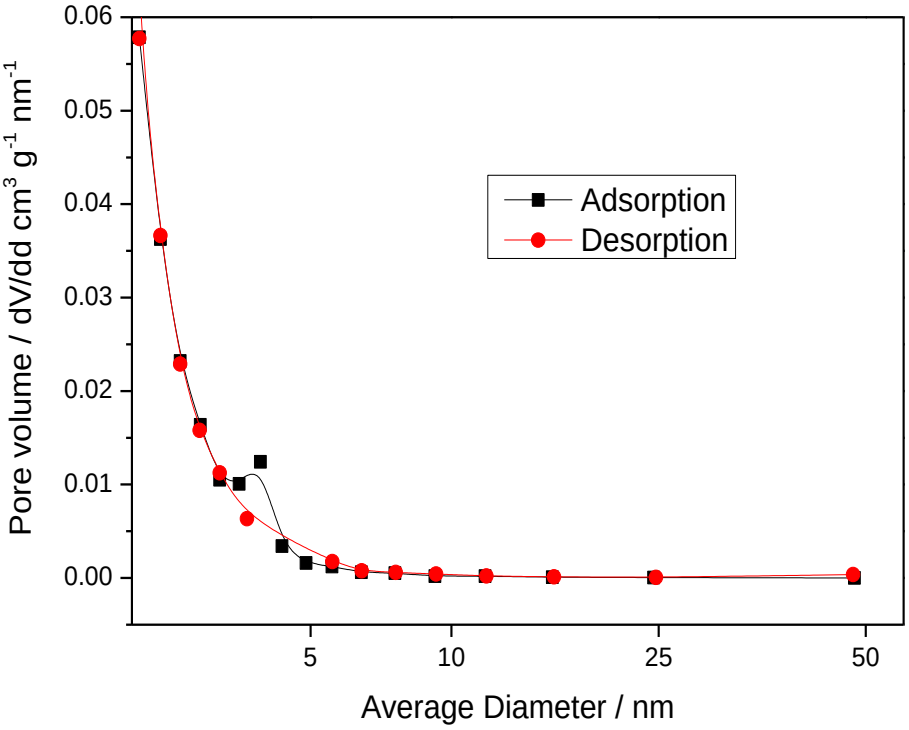

Figure B. 3. BJH pore size distributions of Pd/C catalyst determined from both adsorption and desorption branches of N_2 isotherms.

References

1. V. Mittal. *Advances in Polymer Nanocomposite Technology. Nova Science Publishers*. **2010**.

2. U. Khan, F.M. Blighe, J.N. Coleman. *J. Phys. Chem. C.* **2010.** 114, 11401.

3. L.R. Xu, V. Bhamidipati, W.-H. Zhong, J. Li, C.M. Lukehart, E. Lara-Curzio, K.C. Liu, M.J. Lance. *J. C. Mat*. **2004**. 38, 18.

4. M. Goldberg, R. Langer, X. Jia. *J. Biomater. Sci. Polym. Ed*. **2007**. 18, 3, 241.

5. R.P. Wool. *Soft Matter*. **2008**. 4, 400.

6. J.N. Coleman, M. Cadek, R. Blake, V. Nicolosi, K.P. Ryan, C. Belton, A. Fonseca, J.B. Nagy, Y.K. Gun'ko, W.J. Blau. *Adv. Funct. Mat*. **2004**. 14, 8, 791.

7. G. Lalwani, A.M. Henslee, B. Farshid, P. Parmar, L. Lin, Y.-X. Qin, F.K. Kasper, A.G. Mikos, B. Sitharaman. *Acta Biomaterialia*. **2013**. 9, 8365.

8. D.V. Bavykin, F.W. Walsh. *Titanate and Titania Nanotubes. RSC Publishing*, **2010**.

9. G.L. Hornyak, H.F. Tibbalis, J. Dutta, J.J. Moore. *Introduction to Nanoscience and Nanotechnology. CRC Press*. **2008**.

10. Y. Ding, Z.L. Wang. *J. Phys. Chem. B.* **2004**. 108, 12280.

11. L.V. Radushkevich, V.M. Lukyanovich. *Zurn. Fisic. Chim*. **1952**. 26, 88.

12. A. Oberlin, M. Endo, T. Koyama. *J. Cryst. Growth*. **1976**. 32, 3, 335.

13. S. Iijima. *Nature*. **1991**. 354, 56.

14. O. Breuer, U. Sundararaj. *Polymer composites*. **2004**. 25, 6, 630.

15. H. Dai. *Acc. Chem. Res*. **2002**. 35, 1035.

16. E.T. Thostenson, Z. Ren, T.-W. Chou. *Comp. Sci Tech*. **2001**. 61, 1899.

17. J. Prasek, J. Drbohlavova, J. Chomoucka, J. Hubalek, O. Jasek, V. Adamc, R. Kizek. *J. Mater. Chem*. **2011**. 21, 15872.

18. M. Moniruzzaman, K.I. Winey. *Macromolecules*. **2006**. 39, 5194.

19. J.N. Coleman, U. Khan, W.J. Blau, Y.K. Gun'ko. *Carbon*. **2006**. 44, 1624.

20. J.-P. Salvetat, G.A.D. Briggs, J.-M. Bonard, R.R. Bacsa, A.J. Kulik, T. Stöckli, N.A. Burnham, L. Forró. *Phys. Rev. Lett*. **1999**. 82, 5, 944.

21. L. Bokobza. *Polymer*. **2007**. 48, 4907.

22. R. Jastia, C.R. Bertozzi. *Chem. Phys. Lett*. **2010**. 494, 1.

23. K. Hashimoto, H. Irie, A. Fujishima. *Jpn. J. Appl. Phys*. **2005**. 44, 12, 8269.

24. T. Kasuga, M. Hiramatsu, A. Hoson, T. Sekino, K. Niihara. *Langmuir*. **1998**. 14, 3160.

25. D.V. Bavykin, B.A. Cressey, F.C. Walsh. *Aust. J. Chem.* **2007**. 60, 95.

26. D.V. Bavykin, M. Carravetta, A.N. Kulak, F.C. Walsh. Chem. Mater. **2010**. 22, 2458.

27. D.V. Bavykin, F.C. Walsh. *Titanate, titanium dioxide and related materials. Synthesis properties and applications. Springer*. **In preparation**.

28. D.V. Bavykin, B.A. Cressey, M.E. Light, F.C. Walsh. *Nanotechnology.* **2008**. 19**,** 27, 275604.

29. D.V. Bavykin, J.M. Friedrich, F.W. Walsh. *Adv. Mater.* **2006.** 18, 2807.

30. D.V. Bavykin, V.N. Parmon, A.A. Lapkin, F.C. Walsh. *J. Mater. Chem*. **2004**. 14, 3370.

31. S. Zhang, L.-M. Peng, Q. Chen, G.H. Du, G. Dawson, W.Z. Zhou. *Phys. Rev. Lett.* **2003**. 91, 256103.

32. M.-J. Paek, H.-W. Ha, T. W. Kim, S.-J. Moon, J.-O. Baeg J.-H. Choy, S.-J. Hwang. *J. Phys. Chem. C.* **2008**. 112, 41, 15966.

33. Q. Chen, G.H. Du, S. Zhang, L.-M. Peng. *Acta Cryst*. **2002**. B58, 587.

34. D.V. Bavykin, K.E. Redmond, B.P. Nias, A.N. Kulak, F.C. Walsh. *Aust. J. Chem*. **2010**. 63, 270.

35. P. Herrasti, A.N. Kulak, D.V. Bavykin, C. Ponce de Léon, J. Zekonyte, F.C. Walsh. *Electrochimica Acta*. **2011**. 56, 1323.

36. D.V. Bavykin, E.V. Milsom, F. Marken, D.H. Kim, D.H. Marsh, D.J. Riley, F.C. Walsh, K.H. El-Abiary, A.A. Lapkin. *Electrochem. Comm*. **2005**. 7, 1050.

37. H. Niu, Y. Cai, Y. Shi, F. Wei, S. Mou, G. Jiang. *J. Chromatogr. A*. **2007**. 1172, 113.

38. D.V. Bavykin, S.N. Gordeev, A.V. Moskalenko, A.A. Lapkin, F.C. Walsh. *J. Phys. Chem. B*. **2005**. 109, 18, 8565.

39. D.V. Bavykin, A.A. Lapkin, P.K. Plucinski, L. Torrente-Murciano, J.M. Friedrich, F.C. Walsh. *Topics in Catalysis*. **2006**. 39, 151.

40. M.T. Byrne, J.E. McCarthy, M. Bent, R. Blake, Y.K. Gun'ko, E. Horvath, Z. Konya, A. Kukovecz, I. Kiricsi, J.N. Coleman. *J. Mater. Chem*. **2007**. 17, 2351.

41. D.V. Bavykin, F.C. Walsh. *J. Phys. Chem. C.* **2007.** 111, 40, 14644.

42. J. Geng, Z. Jiang, J. Wang, Y. Shi, D. Yang, L. Xiao. *Chem. Eng. Technol.* **2010**. *33*, 2, 244.

43. Z. Chang, J. Liu, X. Sun, J. Liu. *Front. Chem. China.* **2010**. 5, 1, 71.

44. L. Torrente-Murciano, A.A. Lapkin, D.V. Bavykin, F.C. Walsh, K. Wilson. *J. Catalysis*. **2007**. 245, 2, 272.

45. L. Yu, X. Zhang. *Mat. Chem. Phys*. **2004**. 87, 1, 168.

46. Z.-R. Tang, X. Yin, Y. Zhang , Y.-J. Xu. *Inorg. Chem*. **2013**. 52, 20, 11758.

47. C. Huang, X. Liu, L. Kong, W. Lan, Q. Su, Y. Wang. *Appl. Phys. A.* **2007**. 87, 781.

48. W. Zheng, Y.F. Zheng, K.W. Jin, N. Wang. *Talanta*. **2008**. 74, 1414.

49. H.-J. Song, Z.-Z. Zhang, X.-H. Men. *Eur. Polym. J.* **2008**. 44, 4, 1012.

50. P. Berthier. *Ann. Chim. Phys*. **1826**. 32, 332.

51. M. Du, B. Guo, D. Jia. *Polym. Int.* **2010**. 59, 574.

52. D. Rawtani, Y.K. Agrawal. *Rev. Adv. Mater. Sci*. **2012**. 30, 282.

53. E. Joussein, S. Petit, J. Churchman, B. Theng, D. Righi, B. Delvaux. *Clay Minerals*. **2005**. 40, 383.

54. K. Prashantha, M.F. Lacrampe, P. Krawczak. *Polym. Letters*. **2011**. 5, 4, 295.

55. M. Liu, B. Guo, M. Du, X. Cai, D. Jia. *Nanotechnology*. **2007**. 18, 455703.

56. S.R. Levis, P.B. Deasy. *Int. J. Pharm.* **2002**. 243, 125.

57. G. Tari, I. Bobos, C.S.F. Gomes, J.M.F. Ferreira. *J. Colloid Interf. Sci*. **1999**. 210, 360.

58. D.G. Shchukin, S.V. Lamaka, K.A. Yasakau, M.L. Zheludkevich, M.G.S. Ferreira, H. Mohwald. *J. Phys. Chem. C*. **2008**. 112, 958.

59. S. Baskaran, N.S. Bolan, N.A. Rahman, R.W. Tillman. *NZ J. Agric. Res.* **1996**. 39, 297.

60. Z. Lin, R.W. Puls. *Environmental Geology*. **2000**. 39, 7, 753.

61. D.G. Shchukin, G.B. Sukhorukov, R.R. Price, Y.M. Lvov. *Small*. **2005**. 1, 5, 510.

62. P. Liu, M. Zhao. *Appl. Surf. Sci*. **2009**. 255, 3989.

63. R.L. Parfitt. *Clay Minerals*. **2009**. 44, 135.

64. N. Yoshinaga, S. Aomine. *Soil Sci. Plant Nutr*. **1962**. 8, 114.

65. L.A. Bursill, J.L. Peng, L.N. Bourgeois. *Philosophical Magazine*. **2000**. 80, 1, 105.

66. K. Yamamoto, H. Otsuka, S.-I. Wada, D. Sohn, A. Takahara. *Soft Matter*. **2005**. 1, 372.

67. W. Ma, W.O. Yah, H. Otsuka, A. Takahara. *J. Mater. Chem*. **2012**. 22, 11887.

68. W.C. Ackerman, D.M. Smith, J.C. Huling, Y.-W. Kim, J.K. Bailey, C.J. Brinker. *Langmuir*. **1993**. 9, 1051.

69. K. Yamamoto, H. Otsuka, A. Takahara. *Polym. J*. **2007**. 39, 1, 1.

70. W. Ma, W.O. Yah, H. Otsuka, A. Takahara. *Beilstein J. Nanotechnol.* **2012**. 3, 82.

71. L. Guimarães, A.N. Enyashin, J. Frenzel, T. Heine, H.A. Duarte, G. Seifert. *ACS Nano*. **2007**. 1, 4, 362.

72. C. Levard, J. Rose, A. Masion, E. Doelsch, D. Borschneck, L. Olivi, C. Dominici, O. Grauby, J.C. Woicik, J.-Y. Bottero. *J. Am. Chem. Soc*. **2008**. 130, 5862.

73. S. Mukherjee, V.M. Bartlow, S. Nair. *Chem. Mater*. **2005**. 17, 4900.

74. S. Imamura, T. Kokubu, T. Yamashita, Y. Okamoto, K. Kajiwara, H. Kanai. *J. Catal.* **1996**. 160, 1, 137.

75. F. Ohashi, S. Tomura, K. Akaku, S. Hayashi, S.I. Wada. *J. Mat. Sci*. **2004**. 39**,** 1799.

76. I. Bottero, B. Bonelli, S.E. Ashbrook, P.A. Wright, W. Zhou, M. Tagliabue, M. Armandia, E. Garrone. *Phys. Chem. Chem. Phys*. **2011**. 13, 744.

77. D.-Y. Kang, N.A. Brunelli, G.I. Yucelen, A. Venkatasubramanian, J. Zang, J. Leisen, P.J. Hesketh, C.W. Jones, S. Nair. *Nat. Commun*. **2014**. 5, 3342.

78. M. Kobayashi, M. Nitanai, N. Satta, Y. Adachi. *Colloids and Surfaces A: Physicochem. Eng. Aspects*. **2013**. 435, 139.

79. J. Zang, S. Konduri, S. Nair, D.S. Sholl. *ACS Nano*. **2009**. 3, 6, 1548.

80. D. Sun, C.-C. Chu, H.-J. Sue. *Chem. Mater*. **2010**. 22, 3773.

81. D. Qian, E.C. Dickey, R. Andrews, T. Rantell. *Appl. Phys. Lett*. **2000**. 76, 20, 2868.

82. J. Hilding, E.A. Grulke, Z.G. Zhang, F. Lockwood. *J. Disp. Sci Tech*. **2003**. 24, 1, 1.

83. Z. Spitalsky, D. Tasis, K. Papagelis, C. Galiotis. *Prog. Polym. Sci*. **2010**. 35, 357.

84. Y. Lin, B. Zhou, K.A.S. Fernando, P. Liu, L.F. Allard, Y.P. Sun. *Macromol*. **2003**. 36, 7, 199.

85. B. Zhao, H. Hu, A. Yu, D. Perea, R.C. Haddon. *J. Am. Chem. Soc*. **2005**. 127, 8, 197.

86. M. Sano, A. Kamino, J. Okamura, S. Shinkai. *Langmuir*. **2001**. 17, 5125.

87. W.T. Wu, L. Shi, Y. Wang, W. Pang, Q. Zhu. *Nanotechnology*. **2008**. 19, 125607.

88. W. Wu, S. Zhang, Y. Li, J. Li, L. Liu, Y. Qin, Z.-X. Guo, L. Dai, C. Ye, D. Zhu. *Macromol*. **2003**. 36, 6286.

89. S. Qin, D. Qin, W.T. Ford, D.E. Resasco, J.E. Herrera. *Macromol*. **2004**. 37, 752.

90. Y.C. Jung, N.G. Sahoo, J.W. Cho. *Macromol. Rapid. Commun*. **2006**. 27, 126.

91. A. Koshio, A.M. Yudasaka, M. Zhang, S. Iijima. *Nano Lett*. **2001**. 1, 361.

92. Z. Yao, N. Braidy, G.A. Botton, A. Adronov. *J. Am. Chem. Soc*. **2003**. 125, 16015.

93. J. Cui, W.P. Wang, Y.Z. You, C. Liu, P. Wang. *Polym*. **2004**. 45, 8717.

94. F. Buffa, H. Hu, D.E.Resasco. *Macromol*. **2005**. 38, 8258.

95. Y. Liu, J. Tang, J.H. Xin. *Chem. Commun*. **2004**. 2828.

96. G. Viswanathan, N. Chakrapani, H. Yang, B. Wei, H. Chung, K. Cho, C.Y. Ryu, P.M. Ajayan. *J. Am. Chem. Soc*. **2003**. 125, 9258.

97. C. Gao, Y.Z. Jin, H. Kong, R.L.D. Whitby, S.F.A. Acquah, G.Y. Chen, H. Qian, A. Hartschuh, S.R.P. Silva, S. Henley, P. Fearon, H.W. Kroto, D.R.M. Walton. *J. Phys. Chem. B.* **2005**. 109, 11925.

98. H.J. Lee, S.J. Oh, J.Y. Choi, J.W. Kim, J. Han, L.S. Tan, J.B. Baek. *Chem. Mater*. **2005**. 17, 5057.

99. D. Tasis, K. Papagelis, M. Prato, I. Kallitsis, C. Galiotis. *Macromol. Rapid. Commun*. **2007**. 28, 1553.

100. A. Funck, W. Kaminsky. *Compos. Sci. Technol*. **2007**. 67, 906.

101. S. Cosnier, M. Holzinger. *Electrochim. Acta*. **2008**. 53, 3948.

102. V. Datsyuk, C. Guerret-Piecourt, S. Dagreou, L. Billon, J.C. Dupin, E. Flahaut, A. Peigney, C. Laurent. *Carbon*. **2005**. 43, 873.

103. A.V. Bazilevsky, K. Sun, A.L. Yarin, C.M. Megaridis. *Langmuir*. **2007**. 23, 7451.

104. Y.-C. Tsai, J.-D. Huang. *Electrochem. Commun*. **2006**. 8, 956.

105. H. Wang. *Curr. Opin. Coll. Interf. Sci*. **2009**. 14, 364.

106. R. Rastogi, R. Kaushal, S.K. Tripathi, A.L. Sharma, I. Kaur, L.M. Bharadwaj. *J. Coll. Interf. Sci*. **2008**. 328, 421.

107. R. Ramasubramaniam, J. Chen, H. Liu. *Appl. Phys. Lett*. **2003**. 83, 14, 2928.

108. F. Du, J.E. Fischer, K.I. Winey. *J. Polym. Sci. Part B: Polym. Phys*. **2003**. 41, 3333.

109. P. Pötschke, T.D. Fornes, D.R. Paul. *Polym*. **2002**. 43, 11, 3247.

110. M.J. Biercuk, M.C. Llaguno, M. Radosavljevic, J.K. Hyun, A.T. Johnson, J.E. Fischer. *Appl. Phys. Lett*. **2002**. 80, 15, 2767.

111. J. Bai. *Carbon.* **2003**. 41, 1309.

112. A. Allaoui, S. Bai, H.M. Cheng, J. Bai. *Compos. Sci. Technol*. **2002**. 62, 1993.

113. J.M. Park, D.S. Kim, J.R. Lee, T.W. Kim. *Mater. Sci. Eng. C*. **2003**. 23, 971.

114. C.H. Tseng, C.C. Wang, C.Y. Chen. *Chem. Mater*. **2007**. 19, 308.

115. I. O'Connor, H. Hayden, J.N. Coleman, Y.K. Gun'ko. *Small.* **2009**. 5, 4, 466.

116. K.Q. Xiao, L.C. Zhang, I. Zarudi. *Compos. Sci. Technol*. **2007**. 67, 177.

117. J. Gorrasi, M. Sarno, A. Di Bartolomeo, D. Sannino, P. Ciambelli, V. Vittoria. *J. Polym. Sci. B.* **2007**. 45, 597.

118. W.D. Zhang, L. Shen, I.Y. Phang, T. Liu. *Macromolecules.* **2004**. 37, 256.

119. J.B. Gao, M.E. Itkis, A.P. Yu, E. Bekyarova, B. Zhao, R.C. Haddon. *J. Am. Chem. Soc*. **2005**. 127, 11, 3847.

120. T. Liu, I.Y. Phang, L. Shen, S.Y. Chow, Y.D. Zhang. *Macromolecules*. **2004**. 37, 7214.

121. J. Gao, B. Zhao, M.E. Itkis, E. Bekyarova, H. Hu, V. Kranak, A. Yu, R.C. Haddon. J. *Am. Chem. Soc*. **2006**. 128, 7492.

122. H. Mahfuz, A. Adnan, V.K. Rangari, M.M. Hasan, S. Jeelani, W.J. Wright, S.J. DeTeresa. *Appl. Phys. Lett*. **2006**. 88, 083119.

123. S. Ruan, P. Gao, T.X. Yu. *Polym*. **2006**. 47, 1604.

124. H. Hou, J.J. Ge, J. Zeng, Q. Li, D.H. Reneker, A. Greiner, S.Z.D. Cheng. *Chem. Mater*. **2005**. 17, 967.

125. H.G. Chae, T.V. Sreekumar, T. Uchida, S. Kumar. *Polym*. **2005**. 46, 10925.

126. G.M. Spinks, V. Mottaghitalab, M Bahrami-Samani, P.G. Whitten, G.G. Wallace. *Adv. Mater*. **2006**. 18, 637.

127. S. Kumar, T.D.Dang, F.E. Arnold, A.R. Bhattacharyya, B.G. Min, X. Zhang, R. Vaia, C. Park, W.W. Adams, R.H. Hauge, R.E. Smalley, S. Ramesh, P.A. Willis. *Macromol*. **2002**. 35, 9039.

128. K.H. Kim, W.H. Jo. *Carbon*. **2009**. 47, 1126.

129. T. Chatterjee, C.A. Mitchell, R.A. Hadjiev, V.G. Krishnamoorti. *Adv. Mater*. **2007**. 19, 3850.

130. A. Mamedov, N.A. Kotov, M. Prato, D.M. Guldi, J.P. Wicksted, A. Hirsch. *Nature Materials*. **2002**. 1, 3, 190.

131. B.X. Yang, J.H. Shi, K.P. Pramoda, S.H. Goh. *Nanotech*. **2007**. 18, 125606.

132. S.H. Jin, Y.B. Park, K.H. Yoon. *Compos. Sci. Technol*. **2007**. 67, 3434.

133. J.J. Ge, D. Zhang, Q. Li, H. Hou, M.J. Graham, L. Dai, F.W. Harris, S.Z.D. Cheng. *J. Am. Chem. Soc*. **2005**. 127, 9984.

134. Q. Zhang, J. Li, X. Zhao, D. Chen. *Polym. Int*. **2009**. 58, 557.

135. G.L. Hwang, Y.T. Sheih, K.C. Hwang. *Adv. Funct. Mat*. **2004**. 14, 5, 487.

136. D. Blond, V. Barron, M. Ruether, K.P. Ryan, V. Nicolosi, W.J. Blau, J.N. Coleman. *Adv. Funct. Mater*. **2006**. 16, 1608.

137. L. Liu, D. Tasis, M. Prato, H.D. Wagner. *Adv. Mater*. **2007**. 19, 1228.

138. R. Haggenmueller, H.H. Gommans, A.G. Rinzler, J.E. Fischer, I. Winey. *Chem. Phys. Lett*. **2000**. 330, 219

139. M.A. López Manchado, L. Valentini, J. Biagiotti, J.M. Kenny. *Carbon*. **2005**. 43, 7, 1499.

140. T.E. Chang, L.R. Jensen, A. Kisliuk, R.B. Pipes, R. Pyrz, A.P. Sokolov. *Polym*. **2005**. 46, 439.

141. M.V. Jose, D. Dean, J. Tyner, G. Price, E. Nyairo. *J. Appl. Polym. Sci*. **2007**. 103, 3844.

142. D. McIntosh, V.N. Khabashesku, E.V. Barrera. *J. Phys. Chem. C*. **2007**. 111, 1592.

143. I. O'Connor, H. Hayden, S. O'Connor, J.N. Coleman, Y.K. Gun'ko. *J. Phys. Chem*. **2009**. 113, 20184.

144. R. Blake, J.N. Coleman, M.T. Byrne, J.E. McCarthy, T.S. Perova, W.J. Blau, A. Fonseca, J.B. Nagy, Y.K. Gun'ko. *J. Mater. Chem*. **2006**. 16, 4206.

145. R. Sen, B. Zhao, D. Perea, M.E. Itkis, H. Hu, J. Love, E. Bekyarova, R.C. Haddon. *Nano Lett*. **2004**. 4, 459.

146. H.C. Kuan, C.C.M. Ma, W.P. Chang, S.M. Yuen, H.H. Wu, T.M. Lee. *Compos. Sci. Technol*. **2005**. 65, 1703.

147. Y.C. Jung, N.G. Sahoo, J.W. Cho. *Macromol. Rapid Commun*. **2006**. 27, 126.

148. M. Xu, D. Zhang, B. Gu, J. Wu, Q. Chen. *Macromol*. **2006**. 39, 3540.

149. H. Xia, M. Song. *J. Mater. Chem*. **2006**. 16, 1843.

150. M. Cadek, J.N. Coleman, V. Barron, K. Hedicke, W.J. Blau. *Appl. Phys. Lett*. **2002**. 81, 27, 5123.

151. J.N. Coleman, M. Cadek, R. Blake, V. Nicolosi, K.P. Ryan, C. Belton, A. Fonseca, J.B. Nagy, Y.K. Gun'ko, W.J. Blau. *Adv. Funct. Mat.* **2004**. 14, 8, 791.

152. S. Bhattacharyya, J.P. Salvetat, M.L. Saboungi. *Appl. Phys. Lett*. **2006**. 88, 233119.

153. K.P. Ryan, M. Cadek, V. Nicolosi, D. Blond, M. Ruether, G. Armstrong, H. Swan, A. Fonseca, J.B. Nagy, W.K. Maser, W.J. Blau, J.N. Coleman. *Compos. Sci. Technol*. **2007**. 67, 1640.

154. Y. Wu, Y. Kan, L. Song, Y. Hu. *Polym. Adv. Technol*. **2012**. 23, 1612.

155. G.Zhao, T. Wang, Q. Wang. *J. Mater. Sci*. **2011**. 46, 6673.

156. F. Xin, W. Huaiyuan, S. Yijun, C. Donghui, L. Xiaohua. Mat. Sci. Eng. A. 2007. 448, 253.

157. Q. Cheng, V. Pavlinek, Y. He, C. Li, A. Lengalova, P. Saha. *Eur. Polym. J*. **2007**. 43, 3780.

158. L. Gai, G. Du, Z. Zuo, Y. Wang, D. Liu, H. Liu. *J. Phys. Chem. C*. **2009**. 113, 7610.

159. Q. Cheng, Y. He, V. Pavlinek, C. Li, P. Saha. *Synthetic Metals*. **2008**. 158, 953.

160. S. Wei, P. Mavinakuli, Q. Wang, D. Chen, R. Asapu, Y. Mao, N. Haldolaarachchige, D.P. Young, Z. Guo. *J. Electrochem. Soc*. **2011**. 158, 11, K205.

161. S.M.Z. Khaled, R.J. Miron, D.W. Hamilton, P.A. Charpentier, A.S. Rizkalla. *Dental Materials*. **2010**. 26, 169.

162. A.A. Haroun, A.M. Youssef. *Synthetic Metals*. **2011**. 161, 2063.

163. D. Kralova, M. Slouf, M. Klementova, R. Kuzel, I. Kelnar. *Mat. Chem. Phys.* **2010**. 124, 652.

164. P.I. Pontón, J.R.M. d'Almeida, B.A. Marinkovic, S.M. Savic, L. Mancic, N.A. Rey, E. Morgado Jr., F.C. Rizzo. *Appl. Surf. Sci*. **2014**. 301, 315.

165. Y. Wei, L. Shen, Z. Wang, W.-D. Yang, H. Zhu, H. Liu. *Int. J. Hyd. En*. **2011**. 36, 5088.

166. Q. Li, C. Xiao, W. Li, H. Zhang, F. Chen, P. Fang, M. Pan. *Colloid. Polym. Sci*. **2010**. 288, 1369.

167. X.Wu, K. Scott. *Fuel Cells*. **2013**. 13, 6, 1138.

168. Q. Li, H. Zhang, Z. Tu, J. Yu, C. Xiong, M. Pan. *J. Memb. Sci*. **2012**. 423, 284.

169. J. Geng, Z. Jiang, J. Wang, Y. Shi, D. Yang, L. Xiao. *Chem. Eng. Technol*. **2010**. 33, 2, 244.

170. J. Wang, Y. Zhao, W. Hou, J. Geng, L. Xiao, H. Wu, Z. Jiang. *J. P. Sour*. **2010**. 195, 1015.

171. X. Zhang, A.J. Du, P. Lee, D.D. Sun, J.O. Leckie. *J. Mem. Sci*. **2008**. 313, 44.

172. V.C. Ferreira, O.C. Monteiro. *Electrochim. Acta*. **2013**. 113, 817.

173. R. Ma, T. Sasaki, Y. Bando. J. *Am. Chem. Soc*. **2004**. 126, 10382.

174. H. Tang, H.A. Sodano. *Nano Lett*. **2013**. 13, 1373.

175. J. Xu, C. Jia, B. Cao, W.F. Zhang. Electrochim. Acta. 2007. 52, 8044.

176. J. Li, Z. Tang, Z. Zhang. *Electrochem. Communications*. **2005**. 7, 62.

177. S. Beke, R. Barenghi, B. Farkas, I. Romano, L. Kőrösi, S. Scaglione, F. Brandi. *Mat. Sci. Eng. C*. **2014**. 44, 38.

178. M. Liu, Z. Jia, D. Jia, C. Zhou. *Prog. Polym. Sci*. **2014**. 39, 1498.

179. M. Liu, B. Guo, M. Du, D. Jia. *Appl. Phys. A*. **2007**. 88, 391.

180. R.T. De Silva, P. Pasbakhsh, K.L. Goh, S.-P. Cha, H. Ismail. *Polym. Test*. **2013**. 32, 265.

181. H. Ismail, W. S. Khoo, A. Ariffin. *J. Vin. Add. Tech*. **2013**. 19, 1, 55.

182. M. Liu, C.Wu, Y. Jiao, S. Xiong, C. Zhou. *J. Mater. Chem. B*. **2013**. 1, 2078.

183. K. Fujii, A.Norio Nakagaito, H.i Takagi, D. Yonekura. *Comp. Interf*. **2014**. 21, 4, 319.

184. Y. Tang, D. Zhou, J. Zhang. *J. Nanomat*. **2013**. 542421.

185. W.Y. Zhou, B. Guo, M. Liu, R. Liao, A.B.M. Rabie, D. Jia. *J. Biomed. Mater. Res. A*. **2010**. 1574.

186. G. Cavallaro, G. Lazzara, S. Milioto. *Polym. Deg. Stab*. **2013**. 98, 2529.

187. S. Yang, Z. Liu, Y. Jiao, Y. Liu, C. Ji, Y. Zhang. *J. Mater. Sci*. **2014**. 49, 4270.

188. M. Du, B. Guo, Y. Lei, M. Liu, D. Jia. *Polym*. **2008**. 49, 4871.

189. S. Ebnesajjad. *Fluoroplastics. Elsevier*. **2015**.

190. L. Jiang, C. Zhang, M. Liu, Z. Yang, W.W. Tjiu, T. Liu. *Comp. Sci. Tech*. **2014**. 91, 98.

191. K. Prashantha, H. Schmitt, M.F. Lacrampe, P. Krawczak. *Comp. Sci. Tech.* **2011**. 71, 1859.

192. U.A. Handge, K. Hedicke-Höchstötter, V. Altstädt. *Polymer*. **2010**. 51, 2690.

193. D.C.O. Marney, L.J. Russell, D.Y. Wu, T. Nguyen, D. Cramm, N. Rigopoulos, N. Wright, M. Greaves. *Polym. Deg. Stab*. **2008**. 93, 1971.

194. B. Guo, Q. Zou, Y. Lei, D. Jia. *Polym. J*. **2009**. 41, 10, 835.

195. K. Prashantha, B. Lecouvet, M. Sclavons, M.F. Lacrampe, P. Krawczak. *J. Appl. Polym. Sci*. **2013**. 128, 3, 1895.

196. M. Du, B. Guo, D. Jia. *Eur. Polym. J*. **2006**. 42. 1362.

197. M. Liu, B. Guo, Q. Zou, M. Du, D. Jia. *Nanotechnology*. **2008**. 19, 205709.

198. Y. Ye, H. Chen, J. Wu, L. Ye. *Polymer*. **2007**. 48, 6426.

199. J. Zhang, D. Zhang, A. Zhang, Z. Jia, D. Jia. *J. Reinf. Plast. Comp*. **2013**. 32, 10, 713.

200. M. Liu, B. Guo, M. Du, Y. Lei, D. Jia. *J. Polym. Res*. **2008**. 15, 205.

201. M.T. Albdiry, B.F. Yousif. *Mater. Des*. **2013**. 48, 68.

202. L. Zhang, T. Wang, P. Liu. *Appl. Surf. Sci*. **2008**. 255, 2091.

203. J.H. Choi, Y.W. Cho, W.S. Ha, W. S. Lyoo, C. J Lee, B.C. Ji, S.S. Han, W.S. Yoon. *Polym. Int*. **1998**. 47, 237.

204. D.-Y. Kang, H.M. Tong, J. Zang, R.P. Choudhury, D.S. Sholl, H.W. Beckham, C.W. Jones, S. Nair. *Appl. Mater. Interfaces.* **2012**. 4, 965.

205. D.-Y. Kang, N.A. Brunelli, G.I. Yucelen, A. Venkatasubramanian, J. Zang, J. Leisen, P.J. Hesketh, C.W. Jones, S. Nair. *Nature Comm.* **2014**. 5, 3342.

206. I. Bottero, B. Bonelli, S.E. Ashbrook, P.A. Wright, W. Zhou, M. Tagliabue, M. Armandi, E. Garrone. *Phys. Chem. Chem. Phys*. **2011**. 13, 744.

207. B. Thomas, T. Coradin, G. Laurent, R. Valentin, Z. Mouloungui, F. Babonneau, N. Baccile. *RSC Advances*. **2012**. 2, 426.

208. W.O. Yah, A. Irie, N. Jiravanichanun, H. Otsuka, A. Takahara. *Bull. Chem. Soc. Jpn*. **2011**. 84, 9, 893902.

209. K. Yamamoto, H. Otsuka, A. Takahara, S.-I. Wada. *J. Adh*. **2002**. 78, 591.

210. W. Ma, J. Kim, H. Otsuka, A. Takahara. *Chem. Lett*. **2011**. 40, 159.

211. W. Ma, H. Otsuka, A. Takahara. *Chem. Commun*. **2011**. 47, 5813.

212. W. Ma, H. Otsuka, A. Takahara. *Polym*. **2011**. 52, 5543.

213. K. Yamamoto, H. Otsuka, S.-I. Wada, D. Sohn, A. Takahara. *Polym*. **2005**. 46, 12386.

214. M. Kobayashi, M. Nitanai, N. Satta, Y. Adachi. *Coll. Surf. A: Phys. Eng. Asp*. **2013**. 435, 139.

215. K. Shikinaka, Y. Koizumi, K. Shigehara. *J. Appl. Polym. Sci*. **2015**. 132, 12, 41691.

216. K. Shikinaka, Y. Koizumi, Y. Osada, K. Shigehara. *Polym. Adv. Tech*. **2011**. 22, 8, 1212.

217. G.N.B. Baroña, M. Choi, B. Jung. *J. Coll. Interf. Sci*. **2012**. 386, 189.

218. J. Doshi, D.H. Reneker. *J. Electrost*. **1995**. 35, 151.

219. D.H. Reneker, I. Chun. *Nanotechnology*. **1996**. 7, 216.

220. M.Z. Elsabee, H.F. Naguib, R.E. Morsi. *Mater. Sci. Eng*. **2012**. C 32, 1711.

221. X.-H. Qin, S.-Y. Wang. *J. Appl. Polym. Sci*. **2006**. 102, 1285.

222. Z. Su, J. Li, Q. Li, T. Ni, G. Wei. *Carbon*. **2012**. 50, 5605.

223. W.-J. Li, C.T. Laurencin, E.J. Caterson, R.S. Tuan, F.K. Ko. *J. Biomed. Mater. Res*. **2002**. 60, 613.

224. H. Yoshimoto, Y.M. Shin, H. Terai, J.P. Vacanti. *Biomaterials*. **2003**. 24, 2077.

225. T.J. Sill, H.A. von Recum. *Biomaterials*. **2008**. 29, 1989.

226. M.Y. Song, D.K. Kim, K.J. Ihn, S.M. Jo, D.Y. Kim. *Nanotechnology*. **2004**. 15, 1861.

227. S. Chuangchote, T. Sagawa, S. Yoshikawa. *Phys. Lett*. **2008**. 93, 033310.

228. P. Gibson, H. Schreuder-Gibson, D. Rivin. *Colloids and Surfaces A: Physicochem. Eng. Aspects*. **2001**. 187 469.

229. M. Faccini, C. Vaquero, D. Amantia. *J. Nanomaterials*. **2012**, 892894.

230. P. Rujitanaroj, N. Pimpha, P. Supaphol. *Polymer*. **2008**. 49, 4723.

231. J.-P. Chen, G.-Y. Chang, J.-K. Chen. *Colloids and Surfaces A: Physicochem. Eng. Aspects*. **2008**. 313, 183.

232. T. Tamura, H. Kawakami. *Nano Lett*. **2010**. 10, 1324.

233. D. Li, Y. Xia. *Adv. Mater*. **2004**. 16, 14, 1151.

234. G. Taylor. *Proc. R. Soc. Lond. A*. **1964**. 280, 383.

235. W.-E. Teo, R. Inai, S. Ramakrishna. *Sci. Tech. Adv. Mater*. **2011**. 12, 013002.

236. Q.P. Pham, U. Sharma, A.G. Mikos. *Tissue Eng*. **2006**. 12, 5, 1197.

237. S.L. Shenoy, W.D. Bates, H.L. Frisch, G.E. Wnek. *Polymer*. **2005**. 46, 3372.

238. W.E. Teo, S. Ramakrishna. *Nanotechnology*. **2006**. 17, R89.

239. C.D. Saquing, C. Tang, B. Monian, C.A. Bonino, J.L. Manasco, E. Alsberg, S.A. Khan. *Ind. Eng. Chem. Res*. **2013**. 52, 8692.

240. R.R. Klossner, H.A. Queen, A.J. Coughlin, W.E. Krause. *Biomacr*. **2008**. 9, 2947.

241. M.G. McKee, M.T. Hunley , J.M. Layman, T.E. Long. *Macromol*. **2006**. 39, 2, 575.

242. T. Lin, H. Wang, H.Wang, X. Wang. *Nanotechnology*. **2004**. 15, 1375.

243. Y. Aykut, B. Pourdeyhimi, S.A. Khan. *J. Appl. Polym. Sci*. **2013**. 130, 5, 3726.

244. S. Tripatanasuwan, Z. Zhong, D.H. Reneker. *Polymer*. **2007**. 48, 5742.

245. A. Baji, Y.-W. Mai, S.-C. Wong, M. Abtahi, P. Chen. *Comp. Sci & Tech*. **2010**. 70, 703.

246. D. Li, Y. Wang,Y. Xia. *Nano Letters*. **2003**. 3, 8, 1167.

247. W.E. Teo, S. Ramakrishna. *Nanotechnology*. **2005**. 16, 1878.

248. J.M. Deitzel, J.D. Kleinmeyer, J.K. Hirvonen, N.C. Beck Tan. *Polymer*. **2001**. 42, 19, 8163.

249. A.L. Yarin. *Polym. Adv. Technol*. **2011**. 22, 310.

250. A.L. Yarin, E. Zussman, J.H. Wendorff, A. Greiner. *J. Mater. Chem*. **2007**. 17, 2585.

251. M. Pakravan, M.-C. Heuzey, A. Ajji. *Biomacromolecules*. **2012**. 13, 412.

252. S.S. Ojha, D.R. Stevens, T.J. Hoffman, K. Stano, R. Klossner, M.C. Scott, W. Krause, L.I. Clarke, R.E. Gorga. *Biomacromolecules*. **2008**. 9, 2523.

253. I.G. Loscertales, A. Barrero, I. Guerrero, R. Cortijo, M. Marquez, A.M. Gañan-Calvo. *Science*. **2002**. 295, 1695.

254. D. Li, Y. Xia. *Nano Letters*. **2004**. 4, 5, 933.

255. R. Ramaseshan, S. Sundarrajan, R. Jose, S. Ramakrishna. *J. Appl. Phys*. **2007**. 102, 111101.

256. M. Rinaudo. *Prog. Polym. Sci*. **2006**. 31, 7, 603.

257. R. Jayakumar, M. Prabaharan, S.V. Nair, H. Tamura. *Biotech. Adv*. **2010**. 28, 142.

258. H. Zhang, S. Li. C.J.B. White, X. Ning, H. Nie, L. Zhu. *Electroch. Acta*. **2009**. 54, 5739.

259. K. Ziani, C. Henrist, C. Jerome, A. Aqil, J.I. Mate, R. Cloots. *Carbohydrate Polymers*. **2011**. 83, 470.

260. D. Terada, H. Kobayashi, K. Zhang, A. Tiwari, C. Yoshikawa, N. Hanagata. *Sci. Technol. Adv. Mater*. **2012**. 13, 015003.

261. J.L. Vondran, W. Sun, C.L. Schauer. *J. Appl. Polym. Sci*. **2008**. 109, 968.

262. M.S. Austero, A.E. Donius, U.G.K. Wegst, C.L. Schauer. *R. Soc. Interf*. **2012**. 9, 2551.

263. C. Huang, R. Chen, Q. Ke, Y. Morsi, K. Zhang, X. Mo. *Colloids and Surfaces B: Biointerfaces*. **2011**. 82, 307.

264. R.H. Sanatgar, S. Borhani, S.A.H. Ravandi, A.A. Gharehaghaji. *J. Appl. Polym. Sci*. **2012**. 126, 3, 1112.

265. U. Stachewicz, F. Modaresifar, R.J. Bailey, T. Peijs, A.H. Barber. *Appl. Mater. Interf*. **2012**. 4, 2577.

266. J. An, H. Zhang, J. Zhang, Y. Zhao, X. Yuan. *Coll. Polym. Sci*. **2009**. 287, 12, 1425.

267. A.T. Hang, B. Tae, J.S. Park. *Carbohyd. Polym*. **2010**. 82, 472.

268. C. Wang, Y. Li, G. Ding, X. Xie, M. Jiang. *J. Appl. Polym. Sci*. **2013**. 127, 4, 3026.

269. Y.Y. Qi, Z.X. Tai, D.F. Sun, J.T. Chen, H.B. Ma, X.B. Yan, B. Liu, Q.J. Xue. *J. Appl. Polym. Sci*. **2013**. 127, 3, 1885.

270. C.-L. Zhang, K.-P. Lu, H.-P. Cong, S.-H. Yu. *Small*. **2012**. 8, 648.

271. Y. Zhao, S. Wang, Q. Guo, M. Shen, X. Shi. *J. Appl Polym. Sci*. **2013**. 127, 4825.

272. L. Liu, Y. Zhou, S. Pan. *J. Reinforced Plastics Composites*. **2013**. 32, 823.

273. H. Liao, R. Qi, M. Shen, X. Cao, R. Guo, Y. Zhang, X. Shi. *Colloids and Surfaces B: Biointerfaces*. **2011**. 84, 528.

274. K. Wei, J.-H. Xia, B.-S. Kim, I.-S. Kim. *J. Polym. Res*. **2011**. 18, 579.

275. A. Baji, Y.-W. Mai, S.-C. Wong, M. Abtahi, X. Du. *Comp. Sci & Tech*. **2010**. 70, 1401.

276. R. Qi, R. Guo, M. Shen, X. Cao, L. Zhang, J. Xu, J. Yu, X. Shi. *J. Mater. Chem*. **2010**. 20, 10622.

277. H. Bang, M. Gopiraman, B.-S. Kim, S.-H. Kim, I.-S. Kim. *Colloids and Surfaces A: Physicochem. Eng. Aspects*. **2012**. 409, 112.

278. J.H. Park, H.W. Lee, D.K. Chae, W. Oh, J.D. Yun, Y. Deng, J.H. Yeum. *Colloid Polym. Sci*. **2009**. 287, 943.

279. C. Zhou, R. Chu, R. Wu, Q. Wu. *Biomacromolecules*. **2011**. 12, 2617.

280. F. Nanni, F.R. Lamastra, F. Pisa, G. Gusmano. *J. Mater. Sci*. **2011**. 46, 6124.

281. S.-C. Wong, A. Baji, S. Leng. *Polymer*. **2008**. 49, 4713.

282. A. Patlolla, G. Collins, T.L. Arinzeh. *Acta Biomaterialia*. **2010**. 6, 90.

283. Y. Dong, D. Chaudhary, H. Haroosh, T. Bickford. *J. Mater. Sci*. **2011**. 46, 6148.

284. L.D. Tijing, W. Choi, Z. Jiang, A. Amarjargal, C.-H. Park, H.R. Pant, I.-T. Im, C.S. Kim. *Curr. Appl. Phys*. **2013**. 13, 7, 1247.

285. Z. Wang, N. Cai, D. Zhao, J. Xu, Q. Dai, Y. Xue, X. Luo, Y. Yang, F. Yu. *Polym. Comp*. **2013**. 34, 10, 1735.

286. D.M. Rein, Y. Cohen, J. Lipp, E. Zussman. *Macromol. Mater. Eng*. **2010**. 295, 11, 1003.

287. Y.Y.S. Huang, E.M. Terentjev, T. Oppenheim, S.P. Lacour, M.E. Welland. *Nanotech*. **2012**. 23, 105305.

288. S. Chuangchote, A. Sirivat, P. Supaphol. *Nanotech*. **2007**. 18, 145705.

289. Q. Qin, Y. Liu, S.-C. Chen, F.-Y. Zhai, X.-K. Jing,Y.Z. Wang. *J. Appl. Polym. Sci*. **2012**. 126, 5, 1556.

290. J.S. Jeong, J.S. Moon, S.Y. Jeon, J.H. Park, P.S. Alegaonkar, J.B. Yoo. *Thin Solid Films*. **2007**. 515, 12, 5136.

291. Y.-W. Lin, T.-M. Wu. *J. Appl. Polym. Sci*. **2012**. 126, E123.

292. S.D. McCullen, D.R. Stevens, W.A. Roberts, S.S. Ojha, L.I. Clarke, R.E. Gorga. *Macromolecules*. **2007**. 40, 997.

293. J.R. Davis. *Tensile Testing. ASM International*. **2004**.

294. A.C. Fischer-Cripps. *Introduction to Contact Mechanics. MES, Springer*. **2007**.

295. A.C. Fischer-Cripps. *Nanoindentation. MES, Springer*. **2004**.

296. B.J. Briscoe, L. Fiori, E. Pelillo. *J. Phys. D: Appl. Phys*. **1998**. 31, 2395.

297. W.C. Oliver, G.M. Pharr. *J. Mater. Res.* **1992**. 7, 6, 1564.

298. S. Zhang. *Thin films and coatings. CRC Press*. **2015**.

299. B.D. Beake, G.J. Leggett, M.R. Alexander. *J. Mat. Sci*. **2002**. 37, 4919.

300. B.D. Beake, G.S. Fox-Rabinovich, S.C. Veldhuis, S.R. Goodes. *Surf. & Coat. Tech*. **2009**. 203, 1919.

301. B.D. Beake, S. Chen, J.B. Hull, F. Gao. *J. Nanosci. Nanotech*. **2002**. 2, 1, 73.

302. C.A.Schuh. *Materials Today*. **2006**. 9, 5, 32.

303. A.A. Elmustafa. *Modelling Simul. Mater. Sci. Eng.* **2007**, 15, 823.

304. D. Tranchida, S. Piccarolo, J. Loos, A. Alexeev. *Macromolecules*. **2007**. 40, 1259.

305. B.D. Beake, G.A. Bell, W. Brostow, W. Chonkaew. *Polym. Int.* **2007**. 56, 773.

306. B.D. Beake, S. Zheng, M.R. Alexander. *J. Mater. Sci*. **2002**. 37, 3821.

307. A.M. Díez-Pascual, M.A. Gómez-Fatou, F. Ania, A. Flores. Prog. Mater. Sci. 2015. 67, 1.

308. H. Assender, V. Bliznyuk, K. Porfyrakis. *Science*. **2002**. 297, 5583, 973.

309. B.N.J. Persson. *Phys. Review lett*. **2001**. 87, 11, 116101.

310. O.M. Braun, A.G. Naumovets. *Surf. Sci. Rep*. **2006**. 60, 79.

311. B. Bhushan. *J. Vac. Sci. Technol*. **2003**. 21, 6, 2262.

312. F.P. Bowden. *Mathematical and Physical Sciences*. **1952**. 212, 1111, 440.

313. N. Maeda, N. Chen, M. Tirrell, J.N. Israelachvili. *Science*. **2002**. 297, 379.

314. H. Yosbizawa, J. Israelachvili. *J. Phys. Chem*. **1993**. 97, 11300.

315. E. Rabinowicz. *Friction and wear of materials. Wiley*. **1995**.

316. M.A. Chowdhury, M.K. Khalil, D.M. Nuruzzaman, M.L. Rahaman. *Int. J. Mech. & Mechatronics Eng*. **2011**. 11, 1, 45.

317. M. van Drogen. *The transition to adhesive wear of lubricated concentrated contacts. PhD Thesis. University of Twenty.* **2005**.

318. A.Y. Suh, A.A. Polycarpou, T.F. Conry. *Wear*. **2003**. 255, 556.

319. Review of the wear and galling characteristics of stainless steel. Committee of stainless steel producers. *American Iron and Steel Institute*. **1978**.

320. N.P. Suh, S. Jahanmir, J. Fleming, E.P. Abrahamson, N. Saka, J.P. Texeira. *The delamination theory of wear II. National Technical Information Service.* **1975**.

321. S.C. Lim. *Tribology International*. **2002**. 35, 717.

322. S. Hironaka. *Three Bond Technical News*. **1984**. 9.

323. I.C. Faraon. *Mixed lubricated line contacts. PhD thesis. University of Twente*. **2005**.

324. Y. Wang, Z. Liu, S. Wang, L. Yang. *Lubrication Science*. **2010**. 22, 453.

325. W. Shen, J. Sun, Z. Liu, W. Mao, J.D. Nordstrom, P.D. Ziemer, F.N. Jones. *JCT Research*. **2004**. 1, 2, 117.

326. B.J. Briscoe, S.K. Sinha. *Mat.-wiss. u. Werkstofftech*. **2003**. 34, 10-11, 989.

327. B. Shi, J.L. Sullivan, B.D. Beake. *J. Phys. D: Appl. Phys*. **2008**. 41, 045303.

328. R. Consiglio, N.X. Randall, B. Bellaton, J. von Stebut. *Thin Solid Films*. **1998**. 332, 1–2, 151.

329. B.D. Beake, G.J. Leggett. *Polymer*. **2002**.43, 319.

330. D.L. Burris, B. Boesl, G.R. Bourne, W.G. Sawyer. *Macromol. Mater. Eng*. **2007**. 292, 4, 377.

331. M. Naffakh, A.M. Díez-Pascual, C. Marco, G.J. Ellis, M.A. Gómez-Fatou. *Prog. Polym. Sci*. **2013**. 38, 1163.

332. A.M. Rao, J. Chen, E. Richter, U. Schlecht, P.C. Eklund, R.C. Haddon, U.D. Venkateswaran, Y.K. Kwon, D. Tomanek. *Phys. ReV. Lett.* **2001**. 86, 3895.

333. Y.T. Shah, A.B. Pandit, V.S. Moholkar. *Cavitation reaction engineering. Kluwer Academic/Plenum Publishers*. **1999**.

334. K.L. Mittal, R. Jaiswal. *Particle Adhesion and Removal. Wiley*. **2015**.

335. G. Pagani, M.J. Green, P. Poulin, M. Pasquali. *PNAS*. **2012**. 109, 29, 11599.

336. A. Koshio, M. Yudasaka, M. Zhang, S. Iijima. *Nanoletters*. **2001**. 1, 7, 361.

337. K.S. Suslick, D.A. Hammerton, R.E. Cline. *J. Am. Chem. SOC.* **1986**. 108, 5641.

338. Q. Cheng, S. Debnath, E. Gregan, H.J. Byrne. *J. Phys. Chem. C.* **2010**. 114, 8821.

339. S. Niyogi, M.A. Hamon, D.E. Perea, C.B. Kang, B. Zhao, S.K. Pal, A.E. Wyant, M.E. Itkis, R.C. Haddon. *J. Phys. Chem. B.* **2003**. 107, 8799.

340. K.R. Moonoosawmy, P. Kruse. *J. Am. Chem. Soc*. **2008**. 130, 13417.

341. J. Hilding, E.A. Grulke, Z.G. Zhang, F. Lockwood. *J. Disp. Sci. Tech.* **2003**. 24, 1.

342. P. Rangarajan, D. Bhattacharyya, E.A. Grulke. *J. Appl. Polym. Sci.* **1998**. 70, 6, 1239.

343. M.T. Taghizadeh, H. Rad, R. Abdollahi. *J. Appl. Polym. Sci*. **2012**. 123, 1896.

344. M.W.A. Kuijpers, P.D. Iedema, M.F. Kemmere, J.T.F. Keurentjes. *Polymer*. **2004**. 45, 6461.

345. F. Hennrich, R. Krupke, K. Arnold, J.A. Rojas-Stu1tz, S. Lebedkin, T. Koch, T. Schimmel, M.M. Kappes. *J. Phys. Chem. B*. **2007**. 111, 1932.

346. Y.Y. Huang, T.P.J. Knowles, E.M. Terentjev. *Adv. Mater*. **2009**. 21, 3945.

347. A. Lucas, C. Zakri, M. Maugey, M. Pasquali, P. van der Schoot, P. Poulin. *J. Phys. Chem. C*. **2009**. 113, 20599.

348. H.B. Chew, M.-W. Moon, K.-R. Lee, K.-S. Kim. *Proc. R. Soc. A*. **2011**. 467, 1270.

349. R.D. White, D.V. Bavykin, F.C. Walsh. *J. Phys. Chem. C*. **2012**. 116, 8824.

350. G. Halsey. *J. Chem. Phys*. **1948**. 16, 10, 931.

351. Y.M. Issa, S.I.M. Zayed, I.H.I. Habib. *Ar. J. Chem*. **2011**. 4, 259.

352. S.A. Vanapalli, S.L. Ceccio, M.J. Solomon. *PNAS*. **2006**. 103, 45, 16660.

353. B. Arash, Q. Wang, V.K. Varadan. *Scientific Reports*. **2014**. 4, 6479.

354. S.J. Gregg, K.S.W. Sing. *Adsorption, Surface Area and Porosity, 2nd ed. Academic Press: London.* **1982**.